**UNIVERSIDAD COMPLUTENSE DE MADRID**
FACULTAD DE CIENCIAS FÍSICAS
Departamento de Física de la Tierra y Astrofísica

**TESIS DOCTORAL**

# Fast-timing investigation with $\mathrm{LaBr_3(Ce)}$ arrays detector optimization and measurements in $^{136}$Te

# Coincidencias ultrarrápidas con matrices de $\mathrm{LaBr_3(Ce)}$ : optimización de detectores y aplicación al núcleo $^{136}$Te

MEMORIA PARA OPTAR AL GRADO DE DOCTOR

PRESENTADA POR

**María Victoria Vedia Fernández**

Directores

**Luis Mario Fraile Prieto**

Madrid
Ed. electrónica 2019

Universidad Complutense de Madrid
Facultad de Ciencias Físicas

Departamento de Estructura de la Materia, Física Térmica
y Electrónica

UNIVERSIDAD
COMPLUTENSE
MADRID

# Fast-timing investigation with $LaBr_3$(Ce) arrays: detector optimization and measurements in $^{136}$Te

# Coincidencias ultrarrápidas con matrices de $LaBr_3$(Ce): optimización de detectores y aplicación al núcleo $^{136}$Te

MEMORIA PARA OPTAR AL GRADO DE DOCTOR PRESENTADA POR

María Victoria Vedia Fernández

Director: Luis Mario Fraile Prieto

October 2018

**A mi familia y amigos**

# Summary

Nuclei with few valence particles outside of a doubly-magic core provide valuable information about single-particle energies, nucleon-nucleon effective interactions and may give insight into the onset of collectivity. The region around $^{132}$Sn draws particular attention because of the unexpected modifications of the shell structure and the sudden collective behaviour that arises. The $^{136}$Te nucleus, with two protons and two neutrons coupled to the doubly-magic $^{132}$Sn (Z=50 and N=82) constitutes an excellent testing ground for the study of these phenomena, and so it is studied in this PhD thesis.

One of the best means to study exotic nuclei is through lifetime measurements of excited states since they allow direct and model independent access to electromagnetic transition probabilities, which are key quantities for the study of single-particle configurations, nuclear collectivity, and make it possible to test theoretical models. Thus, this PhD thesis investigates the $^{136}$Te nucleus through the lifetime measurements of its excited states.

Among the different techniques for lifetime measurements, the fast-timing methods are the best suited in the range from tens of picoseconds to few nanoseconds, which is the range of interest in this thesis. Fast-timing methods are electronic timing techniques that make use of fast coincidences between the radiation populating and de-exciting a nuclear energy level. They rely on the use of very fast inorganic scintillators ($LaBr_3$(Ce) detectors in this case) for measuring the time differences, and on the use of HPGe detectors for selecting the appropriate decay branch. Fast-timing methods need very precise time calibrations for the $\gamma$-rays deposing their full energy in the detectors, and for $\gamma$-rays being Compton scattered, and their sensitivity is directly related to the time resolution of the setup in use. Therefore, it is important to optimize the time response of the setup, to obtain a good sensibility.

This is why, in addition to study the $^{136}$Te nucleus, this PhD thesis also presents an in-depth characterization of the standard fast-timing setup, and explains in detail the optimization procedure, which has lead to excellent values of time resolution.

The setup optimization entailed the best selection of the $LaBr_3$(Ce) detectors, by investigating the crystal size, shape and doping, in addition to the fine tuning of the analogue electronics with especial attention to the ORTEC 935 Constant Fraction Discriminator (CFD), which plays a key role [FMV$^+$13, FMP$^+$13]. The $LaBr_3$(Ce) crystals were coupled to a Hamamatsu R9779 photomultiplier tube (PMT), with excellent timing performance [FMO$^+$11] and characterized by coincidence measurements against a well-tested reference $BaF_2$ detector. The most relevant setup parameters to be optimized are the PMT bias voltage, and the CFD settings of external delay and zero-crossing (Z). The optimization led to excellent values of time resolution below 100 ps at $^{60}$Co energies for a standard 1-inch cylindrical crystal, which is the best-reported value to date for crystals of this size.

The best instruments available nowadays for lifetimes measurements are highly performing $LaBr_3$(Ce) arrays. They are the evolution of the standard fast-timing setups, and their good time response can be complemented with the high-efficient spectroscopic capabilities of HPGe arrays, or with the tracking abilities of silicon strip detectors, resulting in a powerful spectroscopic tool. Thus, their development and optimization is of great relevance. The most important requirements for the construction of a highly performing $LaBr_3$(Ce) array, are good time response, reasonable good energy resolution in addition to modular and flexible geometry, covering sufficient solid angle. Consequently, the crystal size should keep a good balance between the intrinsic timing resolution and the $\gamma$-ray detection efficiency.

To this end, two innovative geometries of $LaBr_3$(Ce) crystals were designed and tested in this PhD thesis. The work, which is the continuation of the setup optimization previously mentioned, was motivated by the development and construction of a highly-efficient $LaBr_3$(Ce) array, FATIMA (FAst TIMing Array), that will be part of the HISPEC-DESPEC experiments [DH, RPG$^+$] in the FAIR facility [FAI].

The first innovative geometry is a truncated cone crystal, with a nominal height of 38.1 mm and bases of $\oslash$= 38.1 mm and $\oslash$=25.4 mm. The second design is a hybrid-tapered crystal with a total height of 47 mm, and composed of a cylindrical section of $\oslash$=38.1 mm in the base and 16.5 mm in height, and a 30.5 mm long conical section with ⊘=19 mm in the small base. It was shown that the truncated cone geometry is a perfect candidate for the construction of high-efficient $LaBr_3$(Ce) arrays, since it has excellent time response while maintaining good energy resolution, and its geometry makes it a versatile crystal that can be highly packed in rings with a high solid angle coverage. The optimized time resolutions for the two special geometries of $LaBr_3$(Ce) crystals also stand as the best values achieved to date.

The experimental data for the $^{136}$Te study were obtained during the EXILL-FATIMA campaign [JBdF$^+$, RSB$^+$14], which was the first time that a hybrid spectrometer composed of a $LaBr_3$(Ce) array, FATIMA [LBB$^+$15] and a HPGe-array, EXOGAM [EXO] was used to measure picosecond to nanosecond lifetimes in neutron induced fission products.

Due to the production of many $\gamma$ emitting nuclei in the fission process a high level of Compton background is present under the full-energy peaks in the spectra, attaining a similar order of magnitude. Hence, to account for this background effect in the timing measurements, Compton correction procedures have been developed in this thesis to be implemented in the data analysis.

The present analysis required the use of an extension to large $LaBr_3$(Ce) arrays of the original Advanced Time-Delayed $\beta\gamma\gamma$(t) method by H. Mach [MGM89, MM89], based on HPGe-gated-$\beta$-$\gamma$ coincidences. It is called GCD method [RMS$^+$13] and relies on triple $\gamma$-coincidences to perform HPGe-gated $\gamma$-$\gamma$ timing.

The lifetimes of the $^{136}$Te yrast rotational band have been measured. The value derived for the first $2^+$ state is consistent with recent measurements and helps to solve the existing discrepancies about this value. Lifetimes of higher-lying states have been measured here for the first time. All experimental measurements are compared with the theoretical values available in the literature and with recent shell-model calculations performed by A. Gargano and coworkers.

# Resumen en Castellano

El estudio de núcleos con unos pocos nucleones de valencia fuera de la estructura de un núcleo doblemente mágico proporciona información muy relevante sobre los estados de partícula independiente, sobre las interacciones entre nucleones, y puede ayudar a comprender el comportamiento colectivo. Debido a las modificaciones que aparecen en la estructura de capas y los comportamientos colectivos observados en la región cercana al doblemente mágico $^{132}$Sn, el núcleo $^{136}$Te atrae gran interés, siendo un caso representativo para el estudio de estos fenómenos, ya que cuenta con dos protones y dos neutrones acoplados al $^{132}$Sn (Z=50 and N=82), por ende es estudiado en esta tesis.

Una de las mejores maneras para estudiar estas características es la medida de las vidas medias de estados nucleares excitados, ya que permiten el acceso directo a las probabilidades de transición electromagnética, que son magnitudes clave en la física nuclear. Las probabilidades reducidas de transición son especialmente adecuadas para obtener información sobre configuraciones de partícula independiente, sobre efectos colectivos y configuraciones deformadas, además de permitir poner a prueba los modelos teóricos. Los tiempos de vida de estados excitados son observables directos que pueden ser medidos con buena precisión, lo que nos permite obtener probabilidades de transición independientes de modelo.

Los métodos de coincidencias ultrarrápidas, o métodos de Fast Timing, son los más indicados para medir vidas medias en el rango de decenas de picosegundos a unos pocos nanosegundos, siendo este el rango de interés para el estudio del $^{136}$Te. Estos métodos se basan en el uso de centelleadores inorgánicos muy rápidos, cuya sensibilidad viene directamente determinada por la resolución temporal del sistema experimental, siendo su optimización determinante para alcanzar la mejor sensibilidad posible. El uso de matrices de $LaBr_3(Ce)$ de última generación combinadas con detectores de semiconductor es una herramienta muy potente. Su buena respuesta temporal puede ser complementada con las propiedades espectroscóspicas de los detectores de HPGe, o con la capacidad para detectar partículas de los detectores de silicio, resultando en una combinación de alto rendimiento. Por tanto el desarrollo y optimización de estos montajes experimentales es de gran importancia.

En esta tesis se ha llevado a cabo la caracterización exhaustiva de los principales elementos de un montaje experimental para la medida de vidas medias, junto a la optimización de la respuesta temporal de cada uno de ellos. El proceso de optimización fue parcialmente motivado por el desarrollo e implementación de la matriz de detectores de $\mathrm{LaBr_3}$(Ce) FATIMA (FAst TIMing Array) que formará parte de los experimentos HISPEC-DESPEC [DH, RPG$^+$] en la instalación FAIR-GSI [FAI]. Las características más importantes que debe tener una matriz de $\mathrm{LaBr_3}$(Ce) son: buena respuesta temporal, resolución energética aceptable y geometría modular y flexible que permita disponer los detectores en configuraciones eficientes. Para cumplir estos requisitos, se desarrollaron y caracterizaron dos geometrías inovadoras de cristales de $\mathrm{LaBr_3}$(Ce). La primera de ellas es un cono truncado de 38.1 mm de altura y bases de $\oslash$= 38.1 mm y $\oslash$=25.4 mm. La segunda cuenta con una sección cilíndrica de 16.5 mm de altura y base de $\oslash$=38.1 mm junto a una parte cónica de 30.5 mm de altura y bases de $\oslash$=38.1 mm y $\oslash$=19 mm.

Para su optimización, los cristales fueron acoplados a un fotomultiplicador Hamamatsu R9779 PMT, con un excelente rendimiento temporal [FMO$^+$11]. Se realizaron medidas en coincidencia contra un detector de referencia $\mathrm{BaF_2}$ perfectamente caracterizado. La optimización experimental implica la mejor selección de los detectores de $\mathrm{LaBr_3}$(Ce) atendiendo al tamaño, forma y dopaje, y el ajuste fino de la electrónica asociada con especial atención al "Discriminador de Fracción Constante" (CFD) ORTEC 935, que juega un papel clave [FMV$^+$13, FMP$^+$13]. Los parámetros más relevantes a optimizar son la tensión de polarización aplicada al tubo fotomultiplicador (PMT) y el retardo externo y el paso por cero (Z) en el CFD.

Además del estudio con las nuevas geometrías, se realizó la caracterización de un cristal cilindríco de 25.4 mm de altura y diámetro $\oslash$=25.4 mm.

Gracias al trabajo de optimización se han alcanzado valores de resolución temporal por debajo de los 100 ps a las energías del $^{60}$Co para el cristal cilíndrico estándar de 1 pulgada, que es el mejor valor medido hasta la fecha para cristales de este tamaño. La caracterización de distintas geometrías de $\mathrm{LaBr_3}$(Ce), permite concluir que la forma de cono truncado es excelente para la construcción de matrices de $LaBr_3$(Ce), ya que este diseño presenta buena respuesta temporal, buena resolución energética y geometría versátil. Los valores de resolución temporal para las dos geometrías inovadoras de $LaBr_3$(Ce) son también los mejores valores alcanzados hasta la fecha.

Esta tesis también presenta el estudio del núcleo $^{136}$Te a través de la medida de las vidas medias los estados excitados de la banda rotacional *yrast*. Los datos experimentales fueron tomados durante la campaña EXILL-FATIMA [JBdF$^{+}$, RSB$^{+}$14] que tuvo lugar en el ILL (Grenoble), en la que se utilizó un espectrómetro híbrido compuesto de una matriz de $LaBr_3$(Ce), FATIMA [LBB$^{+}$15], y de una matriz de HPGe, EXOGAM [EXO], en un experimento de fisión inducida por neutrones.

El análisis de los datos de $^{136}$Te se llevó a cabo mediante la aplicación de técnicas de fast-timing que se basan en coincidencias retardadas entre los rayos-$\gamma$ que pueblan y desexcitan los niveles nucleares. Estos métodos requieren de calibraciones temporales muy precisas, las llamadas PRD y la CRD (Prompt and the Compton response distributions) que expresan la respuesta temporal del sistema para los rayos gamma que depositan toda la energía en los detectores y para los que sufren dispersión Compton, en un intervalo amplio de energías. La técnica original se basa en coincidencias $\beta\gamma\gamma$(t) y fue inventada y desarrollada por H. Mach [MGM89, MM89]. El desarrollo de matrices de $LaBr_3$(Ce) estimuló la implementación de un método de fast-timing para la aplicación a un gran número de $LaBr_3$(Ce). El método GCD [RMS$^{+}$13] fue desarrollado por J.-M. Régis y se fundamenta en coincidencias triples $\gamma\gamma\gamma$(t) (HPGe-gated-$\gamma$-$\gamma$) aprovechando la simetría de las distribuciones temporales.

Debido a la producción de muchos núcleos en el proceso de fisión en la campaña EXILL-FATIMA, hay un alto nivel de fondo Compton bajo los picos de energía total, que puede llegar a contribuir en la misma magnitud que los eventos de energía total y emborronar los resultados. Esta cantidad de fondo Compton llega a afectar a las distribuciones temporales. Para poder lidiar con esta situación, se ha desarrollado un procedimiento de análisis que cuenta con una serie de correciones detalladas que permiten cuantificar la influencia de las posibles contribuciones derivadas del fondo. Se han desarrollado métodos de corrección de que se implementan en el análisis de datos.

Las vidas medias de los estados excitados de la banda rotacional *yrast* del $^{136}$Te se presentan en esta tesis, habiendo sido algunas de ellas medidas por primera vez. El valor obtenido para el primer estado $2^{+}$ ayuda a desenmarañar la actual inconsistencia de resultados experimentales, aunque está sujeto a incertidumbres. Por vez primera se han medidos tiempos de vida de otros estados de mayor excitación. Las medidas experimentales se comparan con los valores teóricos disponibles en la literatura y con cálculos recientes de modelo de capas realizados por A. Gargano y colaboradores.

# Contents

**Summary** **iii**

**Resumen en Castellano** **vii**

**Introduction** **1**

**1 Motivation of this work** **5**

- 1.1 The nuclear shell model . . . . 7
  - 1.1.1 Pairing and the seniority scheme . . . . 11
- 1.2 Electromagnetic transition probabilities . . . . 12
  - 1.2.1 Weisskopf estimates . . . . 14
  - 1.2.2 Transition probabilities and collectivity . . . . 15
  - 1.2.3 Collectivity vs. single particle states . . . . 17

**2 Lifetime measurements with fast scintillators** **21**

- 2.1 The Advanced Time-Delayed $\beta\gamma\gamma(t)$ method . . . . 22
  - 2.1.1 The Convolution Technique . . . . 23
  - 2.1.2 The Centroid Shift Method . . . . 24
- 2.2 The Mirror Symmetric Centroid method . . . . 25
- 2.3 The impact of the experimental setup for fast-timing methods . . . . 28
- 2.4 Towards the construction of large $\mathrm{LaBr_3(Ce)}$ arrays . . . . 30

**3 Optimization of the fast-timing setup** **33**

- 3.1 Characterization and optimization of $\mathrm{LaBr_3(Ce)}$ detectors . . . . 34
  - 3.1.1 Characterization procedure . . . . 34
  - 3.1.2 Choice of photodetector . . . . 36
  - 3.1.3 Spectroscopic features: energy resolution . . . . 37

3.1.4 Spectroscopic features: energy linearity . . . . . . . . . . . . . . 39
3.1.5 Spectroscopic features: $\gamma$-ray detection efficiency . . . . . . . . . 39
3.1.6 Time response: time resolution and time walk . . . . . . . . . . . 39
3.2 The ORTEC 935 Constant Fraction Discriminator . . . . . . . . . . . . 40
3.3 Experimental setup for crystals characterization . . . . . . . . . . . . . . 43
3.4 Analysis of the list-mode data . . . . . . . . . . . . . . . . . . . . . . . . 45
3.5 The $LaBr_3$(Ce) detectors . . . . . . . . . . . . . . . . . . . . . . . . . 47
3.5.1 Cylindrical $LaBr_3$(Ce) crystals . . . . . . . . . . . . . . . . . . . . 47
3.5.2 Innovative designs of $LaBr_3$(Ce) crystals: Truncated cone and hybrid-tapered geometries . . . . . . . . . . . . . . . . . . . . . . . . 48
3.6 Study of the cylindrical $LaBr_3$(Ce) detectors . . . . . . . . . . . . . . . . 50
3.6.1 Energy resolution . . . . . . . . . . . . . . . . . . . . . . . . . . 50
3.6.2 Energy linearity . . . . . . . . . . . . . . . . . . . . . . . . . . . 52
3.6.3 Gamma-ray detection efficiency . . . . . . . . . . . . . . . . . . . 53
3.6.4 Time response: time resolution . . . . . . . . . . . . . . . . . . . 54
3.6.5 Time response: time walk . . . . . . . . . . . . . . . . . . . . . . 60
3.7 Performance evaluation of innovative $LaBr_3$(Ce) geometries . . . . . . . 62
3.7.1 Energy resolution and linearity . . . . . . . . . . . . . . . . . . . 62
3.7.2 Gamma-ray detection efficiency . . . . . . . . . . . . . . . . . . . 64
3.7.3 Time response: time resolution . . . . . . . . . . . . . . . . . . . 65
3.7.3.1 Conical crystal . . . . . . . . . . . . . . . . . . . . . . . 65
3.7.3.2 Hybrid-tapered crystal . . . . . . . . . . . . . . . . . . . 67
3.7.3.3 Comparison of the time response of both crystals . . . . 70
3.7.4 Time response: time walk . . . . . . . . . . . . . . . . . . . . . . 72
3.8 Conclusions of this chapter . . . . . . . . . . . . . . . . . . . . . . . . . 75

**4 The EXILL-FATIMA campaign 79**
4.1 The ILL, the H113 neutron guide and the PF1 . . . . . . . . . . . . . . 80
4.2 Targets and the target chamber . . . . . . . . . . . . . . . . . . . . . . . 82
4.3 Detectors of the EXILL-FATIMA spectrometer . . . . . . . . . . . . . . 85
4.3.1 Spectroscopic measurements with EXILL . . . . . . . . . . . . . 86
4.3.2 Hybrid configuration of the EXILL-FATIMA spectrometer . . . . 87
4.4 Electronics and data acquisition . . . . . . . . . . . . . . . . . . . . . . . 88

**5 Data Analysis of EXILL-FATIMA campaign 93**
5.1 Data structure and the SOCOv2 software . . . . . . . . . . . . . . . . . 93
5.2 Event Builder . . . . . . . . . . . . . . . . . . . . . . . . . . . . . . . . 94
5.2.1 Time-stamp offsets . . . . . . . . . . . . . . . . . . . . . . . . . . 95
5.2.2 Coincident time window . . . . . . . . . . . . . . . . . . . . . . . 96
5.2.3 Energy calibration . . . . . . . . . . . . . . . . . . . . . . . . . . 96
5.2.4 Detectors drifts . . . . . . . . . . . . . . . . . . . . . . . . . . . . 97
5.2.5 Event multiplicity . . . . . . . . . . . . . . . . . . . . . . . . . . 97
5.3 Coincident spectra . . . . . . . . . . . . . . . . . . . . . . . . . . . . . 100
5.3.1 Exclusion of certain detector combinations . . . . . . . . . . . 102
5.3.2 Anti-Compton . . . . . . . . . . . . . . . . . . . . . . . . . . . . 102
5.3.3 Add-back in Clovers . . . . . . . . . . . . . . . . . . . . . . . . . 103
5.3.4 Alignment of the time distributions . . . . . . . . . . . . . . . . 103
5.4 The Fast-Timing Matrix . . . . . . . . . . . . . . . . . . . . . . . . . . 103
5.5 Choice of the best conditions for the analysis . . . . . . . . . . . . . . 105
5.5.1 Target selection . . . . . . . . . . . . . . . . . . . . . . . . . . . 105
5.5.1.1 Fission Yields . . . . . . . . . . . . . . . . . . . . . . . 105
5.5.1.2 Fission Partners . . . . . . . . . . . . . . . . . . . . . . 106
5.5.2 Strategies for background reduction . . . . . . . . . . . . . . . . 108
5.5.2.1 Exclusion of $LaBr_3$(Ce) detector pairs . . . . . . . . . . 109
5.5.2.2 Add-Back reconstruction . . . . . . . . . . . . . . . . . . 110
5.5.2.3 Subtraction of events coincident with background under FEPs . . . . . . . . . . . . . . . . . . . . . . . . . . 112
5.5.3 Event multiplicity . . . . . . . . . . . . . . . . . . . . . . . . . . 116
5.6 Analysis procedure . . . . . . . . . . . . . . . . . . . . . . . . . . . . . 118
5.6.1 Conditions for the analysis of $^{136}$Te . . . . . . . . . . . . . . . . 118
5.6.2 Gating procedure and analysis using triple events . . . . . . . . . 119
5.6.2.1 Energy. Clover-Clover-Clover . . . . . . . . . . . . . . . 119
5.6.2.2 Energy. Clover-$LaBr_3$(Ce)-Clover . . . . . . . . . . . . 120
5.6.2.3 Timing. Clover-$LaBr_3$(Ce)-$LaBr_3$(Ce) . . . . . . . . . . 122
5.6.2.4 Example of the analysis procedure using triple events . 124
5.6.3 Quadruple events . . . . . . . . . . . . . . . . . . . . . . . . . . 128
5.7 Timing Calibrations . . . . . . . . . . . . . . . . . . . . . . . . . . . . 129

5.7.1 Time calibration for FEPs: the PRD . . . . . . . . . . . . . . . . 130
5.7.1.1 Construction of the PRD . . . . . . . . . . . . . . . . . . 130
5.7.2 Compton Response Time Distributions . . . . . . . . . . . . . . . 137
5.7.2.1 Compton Response using calibration sources . . . . . . 138
5.7.2.2 Internal Compton Response distribution: CRD$_{feeder}$ and CRD$_{decay}$ . . . . . . . . . . . . . . . . . . . . . . . . . 140
5.7.2.3 Internal Compton Response distribution: CCRD . . . . 143
5.8 Implementation of the background corrections . . . . . . . . . . . . . . . 145
5.8.1 First-order background corrections . . . . . . . . . . . . . . . . . . 146
5.8.2 Compton correction implemented in this thesis . . . . . . . . . . . 149
5.8.3 Verification of the analysis procedure using $^{100}$Zr . . . . . . . . . 151
5.9 Summary and conclusions of this chapter . . . . . . . . . . . . . . . . . 156

**6 Lifetime measurements in $^{136}$Te 157**
6.1 Previous information on $^{136}$Te . . . . . . . . . . . . . . . . . . . . . . . . . 158
6.2 Lifetime measurements of excited states in $^{136}$Te . . . . . . . . . . . . . 161
6.2.1 Partners and contaminants . . . . . . . . . . . . . . . . . . . . . . . 161
6.2.2 Lifetime values in $^{136}$Te measured in triple coincidences . . . . . 164
6.2.2.1 Lifetime of the first excited $2^+$ state . . . . . . . . . . . 164
6.2.2.2 Lifetime of the first excited $4^+$ state . . . . . . . . . . . 178
6.2.2.3 Lifetime of the first excited $6^+$ state . . . . . . . . . . . 183
6.2.2.4 Lifetime of the first excited $8^+$ state . . . . . . . . . . . 189
6.2.3 Lifetime values measured in quadruple coincidences . . . . . . . 193
6.2.3.1 Lifetime of the first excited $2^+$ . . . . . . . . . . . . . . 194
6.3 Theoretical calculations for $^{136}$Te . . . . . . . . . . . . . . . . . . . . . . . 199
6.4 Discussion of lifetime values . . . . . . . . . . . . . . . . . . . . . . . . . . 204

**Conclusions and Outlook 211**

**List of Figures 217**

**List of Tables 223**

**References 225**

**Main contributions 237**

# Introduction

The atomic nucleus is a many-body quantum system where three of the fundamental forces are in action: the electromagnetic, the strong nuclear and the weak nuclear interaction. It is a compound of strongly correlated fermions, the nucleons (neutrons and protons), which are the relevant degrees of freedom for the description of nuclear physics phenomena. However, the main interaction between the nucleons is not completely understood yet: there are still some important questions to be answered *i.e.* the dramatic changes in the nuclear properties that arise with the increase of the neutron excess, or the unexpected behaviour of the nuclear systems away from the stability valley. In other words, the actual interaction of the nucleon-nucleon behaviour and its evolution far from the stability valley remains to be totally explained.

To address these questions many experimental and theoretical efforts have been dedicated to the study of exotic nuclei far from stability, whose properties provide the key ingredients for elaborating nuclear models that can be successfully applied at the limits of the nuclear chart.

The development of nuclear forces based on chiral effective field theory and the ability to expand the calculation model spaces has triggered a quantitative leap forward in the last decade. This is also the case for large-scale shell-model calculations based on configuration interactions, which are able nowadays to explain in a quantitative manner many of the properties of stable nuclei and exotic ones.

However, there are some aspects such as the collective behaviour that is still not completely reproduced by theory. In the nuclear shell model, each nucleon (proton or neutron) is moving in a mean field potential that determines the single-particle motion, the nuclear shells and the quantum energy levels. However, collective behaviours are due to correlations and configuration mixing from the residual interactions beyond the average field, entailing a different nucleon-nucleon interaction. Therefore, understanding the interplay between single-particle states and collective phenomena is a subject of great interest.

Thanks to the continuous development of the radioactive ion Beam facilities it has been possible to explore nuclear observables further and further off stability, putting to more stringent test the theoretical models and investigating important aspects such as the collective phenomena or the unexpected structural modifications that appear far from the stability. The development of nuclear models is intimately connected to the progress of experimental techniques.

In this work, we aim to understand the interplay between single particle-states and collective behaviour in neutron-rich exotic nuclei. This is done through the application of the so-called Ultra Fast Timing method for the measurement of excited level lifetimes. Lifetime measurements of excited states give direct access to electromagnetic transition probabilities, which are key quantities in nuclear physics. Transition rates provide unique knowledge about the nuclear structure and information about aspects such as the ground state deformation of even-even nuclei, collective quadrupole and octupole behaviour and shape coexistence. In addition, electromagnetic transition probabilities play an important role in the investigation of the nucleon-nucleon effective interactions and allow to test different theoretical models. Since lifetime values are direct observables that can be measured with good accuracy using different experimental techniques, their measurements allow deriving model independent determinations of the transition probabilities.

The aim of this PhD thesis is two-fold. Firstly we focus on the choice and optimization of experimental parameters of fast scintillating detectors in order to achieve the best performance in terms of their time response. The ultimate aim is to apply the fast-timing method and to construct efficient fast-timing arrays able to operate in stand-alone mode or within hybrid configurations with high-resolution Ge detectors. Secondly, we apply the fast-timing method to the measurement of excited level lifetimes in the exotic nucleus $^{136}$Te, in the vicinity of the doubly-magic $^{132}$Sn, in order to better understand its structure.

Striking modifications to the standard ordering of the single-particle energies have been observed in exotic nuclei that have a large disparity in proton and neutron numbers, giving rise to the disappearance of the conventional magic numbers and the appearance of new shell gaps. These structural modifications are more prominent in neutron-rich exotic nuclei, and therefore these are critically scrutinized with the aim of realizing a predictive model for atomic nuclei that is valid across the nuclear chart.

The regions around doubly magic nuclei attract a strong interest from both experimental and theoretical points of view. Nuclei with few valence particles outside of a doubly magic core are very well suited to test the shell-model effective Hamiltonian and allow important parameters such as single-particle energies, two-body matrix elements and effective electromagnetic operators to be obtained. They provide valuable information about nucleon-nucleon effective interactions and give an insight into the onset of collectivity. In particular, electromagnetic transition connecting nuclear states, provide important guidance for a better understanding of nuclei. Nuclei in the vicinity of $^{132}$Sn isotope are of special interest because they exhibit unexpected modifications of the shell structure and sudden collective phenomena. This is the case of the $^{136}$Te nucleus, with two protons and two neutrons above the doubly magic $^{132}$Sn (Z=50 and N=82), an excellent testing ground to probe the onset of collectivity and the nucleon-nucleon interaction in the region north-west of $^{132}$Sn.

Our tool to tackle the study of is the measurement of excited level lifetimes, which together with the $\gamma$-decay branching ratios and transition multipolarity, provide the electromagnetic transition rates. Despite the strong impact of accurate lifetime measurements data is still scarce and new high-quality measurements are needed.

The lifetime measurements in the 10 ps to several ns regime can be achieved by electronic timing with very fast detectors, such as the Advanced Time-Delayed method applied to beta-decay studies. This method can be extended to large mixed arrays combining fast scintillator detectors and high-resolution HPGe. FATIMA, the *FAst TIMing Array*, is the instrument based on LaBr3(Ce) detectors devoted to the measurement of excited level lifetimes in the sub-nanosecond regime. The main FATIMA requirement is a good time resolution over an extended energy range. Sufficient detection efficiency and reasonable energy resolution are also required.

In this work, the hybrid FATIMA-EXOGAM array has been used to the study of the exotic $^{136}$Te, two protons and two neutrons away from the doubly-magic $^{132}$Sn, within the fast-timing FATIMA-EXILL campaign performed at the Institut Laue Langevin (ILL) in Grenoble. The nucleus $^{136}$Te is of importance to study proton and neutron configurations outside the Z=50 N=82 double shell closure. In $^{136}$Te, an anomalous behaviour of the B(E2; $2_1^+ \rightarrow 0_1^+$) transition probability with respect to the lighter Te isotopes have been observed. Contrary to the semi-empirical trends for collective quadrupole states, in this nucleus both the $2_1^+$ state energy and the reduced transition probability to the ground state decrease compared to neighbouring isotopes, pointing to a significantly different structure of this particular state. Lifetime measurements provide model-independent information to derive the transition rates and in this work, we have extended the measurements to the higher excited states in the ground state rotational band.

In Chapter 1 we motivate this work by describing the theoretical framework of the study. Some general characteristics of $\gamma$ spectroscopy and fast-timing methods are discussed in Chapter 2, together with the impact of the experimental setup for the application of the fast-timing methods. Chapter 3 describes the optimization of the detector parameters in order to achieve the best performance for fast-timing measurements. Chapter 4 contains the technical details of the production of $^{136}$Te at ILL and the fission process. We illustrate the experimental setup and properties of the detectors used in our experiment. The description of the data analysis together with the analysis procedures developed in this work are presented in Chapter 5. Chapter 6 addresses the main results of the analysis of transition rates in $^{136}$Te. The results are compared to theoretical calculations. Finally, the conclusions and possible future lines of work are shown in the last Chapter of the thesis.

# 1

# Motivation of this work

The atomic nucleus is an excellent playground to study three of the interactions of Nature: the electromagnetic, the strong nuclear and the weak nuclear forces. A large variety of phenomena takes place in the nucleus, including the emission of particles and radiation, collective excitations, deformation and many other. Although nuclei were discovered more than a century ago, and many experimental and theoretical efforts have been put forward to try and understand their proprieties, no unified nuclear theory exists to date and the basic interaction between their constituents is not fully understood.

Much of our knowledge of the complex problem of the nucleus relies on the shell structure, an arrangement similar to those of electrons in atoms, by which the nucleons (protons and neutrons) are organized. Nuclei having special numbers of protons and neutrons, the so-called magic numbers, acquire extra binding energy. This was early recognized by observing isotopic abundances and binding energies. In the pioneering work of W.M. Elsasser [Els33, Els34] the first attempt to establish an independent-particle model was presented. In this picture, each nucleon moves in a global potential, independent of the of each other. In spite of the successful explanation based on closed shells of the magic numbers for light nuclei, not all of them could be successfully accounted for neither by his model nor by the similar ones that followed.

The introduction of the spin-orbit coupling by Maria Göppert Mayer [May49] provided the solution to this puzzle and the successful interpretation of the known magic numbers in the valley of stability: 2, 8, 20, 28, 50, 82 and 126.

Nevertheless, it has been known for years that shell structure changes far off stability, new magic numbers appear and the existing ones disappear [SP08], giving rise to exciting features.

The nucleon-nucleon interaction and how its evolution affects the properties of the nucleus when moving away from stability is one of the most fundamental standing questions in nuclear physics. The regions around doubly-magic nuclei (those that correspond to both proton and neutron magic numbers) far from stability play a very important role in our understanding of the evolution of nuclear structure. They have been subject of many experimental and theoretical studies in the last decades [SGJ+14, KBU+15, OKK+10, Zuk03, KEHJO07, OSH+10, SS10, CCGI13, CCGI13, NNB17] as they have come experimentally more accessible thanks to the development of new facilities and production methods, and to the advancement of nuclear instrumentation.

Regions around doubly-magic nuclei provide the best way to test the shell-model effective Hamiltonian, namely the single particle energies and two-body matrix elements of the residual interaction, as well as the effective electromagnetic operators. Single-particle energies in the vicinity of these nuclei are the key input to models trying to describe the nuclear structure in exotic regions of the nuclear chart. Proton and neutron excitations across shell gaps and the evolution of the proton-neutron interaction can be investigated in these exotic nuclei. In addition, gross properties of these nuclei play a role in the astrophysical rapid neutron capture process.

During the last two decades, there has been a substantial effort in gaining experimental information on nucleon-rich nuclei far from the stability line, which has given evidence for changes in the shell structure when approaching the neutron drip line. In this context, nuclei in the regions of the shell closures with a large $N/Z$ ratio are of great interest, opening the opportunities for a better understanding of the forces that bind nucleons together. For the vast region of the medium-heavy nuclei, there are only two doubly-magic nuclei, the stable $^{208}$Pb and the *exotic* $^{132}$Sn, which can be reached and studied with some detail.

The nuclear structure around $^{132}$Sn has been recently tackled both experimentally and theoretically. Realistic shell-model calculations have proved to lead to a good description of nuclei in this region [CCGI13]. In these particular calculations, the two-body matrix elements of the shell-model effective Hamiltonian are constructed by means of many-body perturbation theory starting from a low-momentum interaction derived from the high-precision CD-Bonn nucleon-nucleon potential. The chosen model space includes the 6 neutron-particle orbitals $0h_{9/2}$ $1f_{7/2}$, $1f_{5/2}$, $2p_{3/2}$, $2p_{1/2}$, $0i_{13/2}$, and the 5 neutron-hole orbitals $0g_{7/2}$, $1d_{5/2}$, $1d_{3/2}$, $2s_{1/2}$, $0_{11/2}$ for tin isotopes with N >82 and N<82, respectively. The values of the single-particle and single-hole energies are taken from experimental values, specifically from the spectra of $^{133}$Sn and $^{131}$Sn if available. Proton and neutron excitations across the 50 and 82 shells are not explicitly included in the calculations but are accounted for by the core polarization contributions to the effective interaction.

Although new data have been acquired for nuclei around $^{132}$Sn, no clear evidence for changes in the shell structure has been observed, as was the case in lighter mass regions. However, the available data have shown some anomalies, one of the most notable ones being the asymmetry in the behaviour of the properties of the *yrast* $2^+$ state in Sn and Te isotopes with respect to the 82 neutron shell closure. Further information is needed to clarify the nature of this feature. A proposed explanation for the asymmetry in the energy behaviour of the $2^+$ state is the reduction of the neutron pairing when crossing N=82 and in this connection it may be useful to investigate the magic Sn isotopes, which may give direct information on the neutron-neutron interaction.

In this thesis, we concentrate on the measurement of nuclear lifetimes in neutron-rich $^{136}$Te isotope (Z=52) with just two protons and two neutrons outside the doubly-magic $^{132}$Sn. Dynamic information, such as electromagnetic moments, provides a very stringent test of the theoretical models, and allow the systematic inter-comparison of nuclei in the region around $^{132}$Sn. This information can be directly obtained by the measurement of lifetimes of excited nuclear states, with the knowledge of the level structure. The measurement of the lifetimes of excited states in $^{136}$Te will serve as input for the mapping of the collectivity for Te isotopes and will allow the comparison to other nuclides in the region, including Xe isotopes with Z=54.

## 1.1 The nuclear shell model

The independent-particle model is one of the most successful theoretical approaches to address the nuclear many-body problem, certainly close to stability, but also nuclei in exotic regions of the nuclear chart. The main components are discussed below.

The fundamental hypothesis of the nuclear shell-model is that each nucleon moves independently in a mean-field describing the average interaction with the other nucleons. Although this description arises from the analogy to the atomic shell model, major differences exist, the main one being that the dynamics of atomic electrons are due to the central Coulomb potential created by the nucleus, while in the nucleus the nucleons themselves create the central mean field potential. This makes the description of the nuclear properties much more challenging.

The many-body (A) Schrödinger equation for the nucleus can be written in general as a function of the kinetic and potential terms, by assuming that the potential consists of two-body interactions. This is in most of the cases a good description, at least close to stability, because higher order interactions are smaller and can be effectively included into a two-body term. Nonetheless, two-body interactions have been shown to be limited far off stability and the addition of a three-body term has been argued to provide better agreement with the experimental data in certain regions of the nuclear chart.

With the hypothesis of the mean-field potential, the dynamics of the nucleon can be written with a Hamiltonian dependent on a one-body potential term $V_i$ to describe the effect of the nucleons and a residual potential term $W_i$ to account for the residual interaction, which can be neglected in the extreme single-particle model. It is customary to use a Woods-Saxon type potential for $V_i$ as stems from the short-range nature of the nuclear forces, or an approximation such as a harmonic oscillator potential. With the addition of the spin-orbit term discussed above the harmonic oscillator magic numbers leading to shell gaps at 2, 8, 20, 40, 70, etc. are modified to match the known nuclear magic numbers at the stability line.

The validity of the independent-particle description is limited to nuclei one nucleon away from closed shells, but the residual two-body interaction has a prominent role as soon as we depart from magic numbers by adding more nucleons. In addition, the magic numbers are now known to shift in exotic regions of the nuclear chart.

The nucleon-nucleon interaction contains in addition to the central part spin and isospin terms to fulfil the general properties of the nuclear force, the spin-orbit term and a tensor term in order to reproduce experimental observations, acting on nucleons coupled to S=1 (like the spin-orbit term). But the nucleon-nucleon interaction needs to be constrained to the valence space, and therefore one needs to deal with an effective interaction, which can be derived from the (free) nucleon-nucleon interaction by correcting by anti-symmetrization and by in-medium effects that are accounted for in perturbation theory. These are, in fact, contradicting requirements since the antisymmetrization due to the Pauli principle needs to take into account the repulsive core of the nuclear interaction, which diverges at short distance, while the perturbation cannot work under this assumption. Therefore renormalization methods need to be applied. But effective interactions built out of the nucleon-nucleon potentials are not capable of completely reproducing nuclear properties, including the saturation of the nuclear force and the magic numbers. It is generally argued that two-body forces are not enough to treat complex nuclei and that adding a three-body term provides better agreement with the experimental data [Zuk03].

In order to perform shell-model calculations, the configuration space needs to be reduced to a handful of valence orbitals above where the calculations are numerically possible since, otherwise, the basis dimensions explode. To this end, a closed core is defined, with orbitals completely filled and no exchange of particles with higher-lying orbitals allowed. The valence space is made up of orbitals where valence nucleons evolve. A forbidden space at higher energies, where particles cannot be promoted, can also be defined.

A way around the lack of effective three-body interactions available for certain valence spaces is the multipole decomposition of the Hamiltonian, which factorizes it in a monopole part and a multipole component. The monopole part contains the spherical mean field and can be adjusted to describe experimental data. It is a function of the proton and neutron single-particle energies and the monopole component of the two-body interaction obtained as the average over all possible magnetic sub-states of two nucleons (protons or neutrons) in the orbits $j$ and $j'$ that couple to a two-body state with total angular momentum J:

$$V_{jj'}^{nn'} = \frac{\sum_J (2J+1) < jj'|V|jj' >}{\sum_J (2J+1)} ,$$

where the indexes $n$ and $n'$ indicate the type of nucleon $\pi$, $\nu$. Therefore protonneutron, neutron-neutron and proton-proton monopole interactions can be defined.

Using the monopole term of the Hamiltonian one may quantify the effect on a given nucleon in an orbital by the rest of the nucleons by the so-called effective single-particle energies (ESPE). They represent the energy when correlations are removed, and thus they cannot be directly observed. For a nucleon in an occupied orbital, the ESPE is the opposite of the nucleon separation energy. Around a closed core characterized by A nucleons, the ESPE can be obtained from the single-particle energy $\epsilon_j^n$

$$E_j^n = \epsilon_j^n(A) + \sum_{j'n'} V_{jj'}^{nn'} \hat{N_{j'}^{n'}} \ ,$$

being $\hat{N_{j'}^{n'}}$ the occupation number of the valence $j'$ orbitals above the A core.

The monopole drift is given by the difference with $\epsilon_j^n(A)$,

$$\Delta\epsilon_j^n(A) = \sum_{j'n'} V_{jj'}^{nn'} \hat{N_{j'}^{n'}} \ .$$

and it is responsible for the evolution of the shell structure in several regions of the nuclide chart. To what extent the different components of the monopole interaction contribute to shell evolution is subject of strong debate [OFU$^+$01, OSF$^+$05, OSH$^+$10], since it is not easy to track down the origin of the effects due to the renormalization procedures and the fit of the monopole term to experimental data. Nonetheless, in several investigations, the effective interaction is decomposed in central, spin-orbit and tensor terms, which allows to isolate the effects and compare to experimental data. The general agreement is that the evolution of the ESPE is driven by the central part of the nucleon-nucleon interaction, while the tensor part affects the splitting of spin-orbit partners.

The monopole part of the tensor force makes that the neutron orbital affects proton spin-orbit partners orbitals, and vice-versa. The sign of the interaction depends on whether $j_\downarrow = l + 1/2$ or $j_\uparrow = l - 1/2$ is being filled, with repulsive interaction for spin orbit partners ($j_\downarrow$-$j'_\uparrow$) and attractive for the same type of orbit ($j_\uparrow$-$j'_\uparrow$ and $j_\downarrow$-$j'_\downarrow$). It has no effect on completely full orbitals.

The multipole term of the Hamiltonian takes care of correlations between nucleons in the valence space, such as quadrupole interaction and pairing, and it drives particle-hole excitations across the shell gaps (such as the $^{132}$Sn core). Correlations are more relevant in the case of diminished shell gaps due to monopole drifts, where they can even favour intruder deformed configurations at low energy if their correlation energy is larger than the energy needed to make them. This effect leads to what have been coined "island of inversion". The multipole term is thus triggering deformation, contrary to the monopole one that tries to make the nucleus spherical. The effect of correlations can be sizeable already very close to the shell closures, due to the presence of only a few particles above the shell gap. Therefore the study of nuclei close to shell closures, such as $^{136}$Te, with only 2 protons and 2 neutrons above $^{132}$Sn, is of the greatest interest to characterize these effects. Dynamical information, like transition probabilities, provides a more stringent test to nuclear models than only spectroscopic information. The former can be obtained by direct, model-independent, measurements of level lifetimes as those described in this PhD work.

### 1.1.1 Pairing and the seniority scheme

When multiple particle configurations are into play, a simplistic interpretation in terms of the shell model it is not able to correctly describe nuclear properties. Nevertheless, there are features and symmetries that may help interpret spectroscopic features. Pairing correlations are one of the most important ones. Pairing is responsible for the energy gain for even-even nuclei, giving rise to the J=$0^+$ spin-parity of the ground state. It is also the case of odd-even mass staggering. The pairing interaction favours spherical shapes because it tends to couple pairs of particles to a total magnetic angular momentum projection 0. This is why in the vicinity of closed shells the strong pairing interaction opposes deformation.

The tendency of particles to pair to J = $0^+$ makes it possible to develop angular momentum coupling schemes for systems with several particles outside closed shells, where the symmetries are used to take care of a large amount of configurations that can be involved. One of these schemes is *seniority*. Let's consider a multi-particle configuration of $n$ particles in a shell-model orbital with total angular momentum $j$, denoted by $\mathrm{j}^n$. For a state with total angular momentum $J$, we can identify the number of pairs of particles that couple to 0 angular momentum. Let us call seniority $\nu$ the number of unpaired particles, that is, those that contribute to the total angular momentum $J$ into the state. Therefore the total number of paired particles that couple to $J = 0$ is $n - \nu$ and the number of pairs $(n - \nu)/2$. Then $\nu$ is the minimum number of nucleons that can couple to $J$, and the state has a seniority $\nu$. For a given $J$ value it is possible to find states with higher seniority than $\nu$.

Seniority is a good quantum number to label states due to the fact that some nuclear interactions conserve seniority, and the seniority scheme can be used in the proximity of closed shells to describe spectroscopic properties and electromagnetic transitions of nuclei. It can be applied to Sn isotopes, but also to $^{136}$Te if one assumes a dominant contribution of neutron pairs. One of the most important consequences of the seniority scheme is that, once states are labelled by the seniority quantum number, it is possible to derive the properties of transition operators between them.

## 1.2 Electromagnetic transition probabilities

Nuclei in excited states normally decay to more stable states (of lower energy) by the emission of $\gamma$-rays (photons) whose energy corresponds to the energy difference between the initial and the final states; this process is called $\gamma$-decay.

Transition probabilities of $\gamma$-rays that connect nuclear states provide unique information about the atomic nucleus. They give an insight of the nuclear structure and inform about aspects such as the ground state deformation of even-even nuclei, collective quadrupole and octupole behaviour or shape coexistence. In addition, transition rates play an important role in the investigation of the nucleon-nucleon effective interactions and allow to test different theoretical models. The study of the $\gamma$-rays emitted by a nucleus is one of the main means to learn about nuclear structure.

The transition probabilities of $\gamma$-ray emission between an initial state $|J_iM_i\rangle$ to a final state $|J_fM_f\rangle$ are described by the Fermis's golden rule (Equation 1.1), where $\rho$ defines the density of final states and $\langle J_fM_f|\, H_{int}\, |J_iM_i\rangle$ is the matrix element of the interaction.

$$\Gamma_{i\to f} = \frac{2\pi}{\hbar} |\, \langle J_fM_f|\, H_{int}\, |J_iM_i\rangle\, |^2 \rho \tag{1.1}$$

Fermis's golden rule states that the number of transitions per unit of time is proportional to the square of the transition matrix element $\langle J_fM_f|\, H_{int}\, |J_iM_i\rangle$, where the initial and final states are characterized by the quantum numbers of the total angular momentum J, its projection M, and the parity $\pi$, and $H_{int}$ is the Hamiltonian that describes the interaction connecting the initial and final states.

The interaction of the electromagnetic field with the nucleons can be expressed as an infinite series of electric and magnetic terms (multipoles), where the most significant contribution is given by the lowest moments (dipole, quadrupole and octupole). The electric and magnetic multipole operators that entails the transition from the initial to the final state can be expressed with Equations 1.2 and 1.3, where $\rho(\mathbf{r})$ refers to the charge distribution, $\overrightarrow{j(\mathbf{r})}$ is the current distribution and $Y_{\lambda\mu}$ are the spherical harmonics of order $\lambda, \mu$. The two equations are derived considering the nuclei as point charges and the wavelength of the emitted photons larger than the nuclear radius. The distinct electric or magnetic multipoles of order $\lambda$ (E$\lambda$, M$\lambda$) have definite angular distributions and different parity properties.

$$\mathcal{M}(E\lambda, \mu) = \int \rho(\mathbf{r}) r^{\lambda} Y_{\lambda\mu}(\hat{\mathbf{r}}) dr \tag{1.2}$$

$$\mathcal{M}(M\lambda, \mu) = \frac{-1}{c(\lambda+1)} \int \overrightarrow{j(\mathbf{r})} \cdot (\overrightarrow{\mathbf{r}} \times \overrightarrow{\boldsymbol{\nabla}}) r^{\lambda} Y_{\lambda\mu}(\hat{\mathbf{r}}) dr \tag{1.3}$$

To evaluate the matrix elements $\langle J_f M_f | \, H_{int} \, | J_i M_i \rangle$, it is convenient to write them as a function of the reduced transition matrix elements $\langle \psi_f | \, | \mathcal{M}(X\lambda) \, | \psi_i \rangle$. This is done by averaging the initial magnetic substates M$_i$ and summing over the final substates M$_f$ and the third component $\mu$ of the electromagnetic multipole $\lambda$ (Equation 1.4). The reduced transition probability has the advantage of not depending on the third component of the nuclear spin, the magnetic quantum number.

$$B(X\lambda; J_i \rightarrow J_f) = \sum_{\mu, M_f} | \, \langle J_f M_f | \, \mathcal{M}(X\lambda, \mu) \, | J_i M_i \rangle \, |^2 \tag{1.4}$$

$$B(X\lambda; J_i \rightarrow J_f) = \frac{1}{2J_i + 1} | \, \langle J_f | \, | \mathcal{M}(\mathcal{X}\lambda) | \, | J_i \rangle \, |^2 \tag{1.5}$$

The Winger-Eckart theorem allows to derive Equation 1.5 from 1.4 by factoring out the dependence of M$_i$ and M$_f$. Out of Equation 1.5 one can derive Equation 1.6 that relates the backwards and forwards transition rates:

$$B(X\lambda; J_i \rightarrow J_f) = \frac{2J_f + 1}{2J_i + 1} B(X\lambda; J_f \rightarrow J_i). \tag{1.6}$$

The total transition rate of an electric or magnetic transition of multipolarity $\lambda$ that connects an initial state of total spin J$_i$ to a final of J$_f$ corresponds to Equation 1.7.

$$P_\gamma(X\lambda; J_i \rightarrow J_f) = \frac{8\pi(\lambda+1)}{\lambda[(2\lambda+1)!!]^2\hbar}\left(\frac{E_\gamma}{\hbar c}\right)^{2\lambda+1} B(X\lambda; J_i \rightarrow J_f) \tag{1.7}$$

Since the total transition rate $\mathrm{P}_\gamma$ is the inverse of the partial lifetime $\tau_\gamma$, the reduced electromagnetic transition rates can be expressed as a function of the transition energy and the partial lifetime with Equation 1.8:

$$B_\gamma(X\lambda; J_i \rightarrow J_f) = \frac{\lambda[(2\lambda+1)!!]^2\hbar}{8\pi(\lambda+1)}\left(\frac{\hbar c}{E_\gamma}\right)^{2\lambda+1} \tau_\gamma^{-1}. \tag{1.8}$$

The partial lifetime $\tau_\gamma$ is related with the total lifetime $\tau$ of the nuclear level by the gamma branching $br_\gamma$ ratio as $\tau_\gamma = \frac{\tau}{br_\gamma}$. Therefore, the measurement of the levels lifetimes $\tau$ together with the gamma branching ratio $br_\gamma$ provide a model-independent access to the reduced transition probabilities.

### 1.2.1 Weisskopf estimates

The Weisskopf estimates or single particle estimates give a measure of the transition probability in the case that just only one particle is the responsible of the transition. The estimates are derived under the assumptions of a constant radial wavefunction with a nuclear radius of $R_o = 1.2A^{1/3}$ fm, and with only one nucleon going from one single particle orbit to another without affecting the remaining nucleons.

$$B_w(E\lambda) = \frac{1}{4\pi}\left(\frac{3}{\lambda+3}\right)^2 \cdot (1.2)^{2\lambda} \cdot A^{2\lambda/3} \quad e^2 fm^{2\lambda} \tag{1.9}$$

$$B_w(M\lambda) = \frac{10}{\pi}\left(\frac{3}{\lambda+3}\right)^2 \cdot (1.2)^{2\lambda-2} \cdot A^{(\lambda-2)/3} \quad {\mu_N}^2 fm^{2\lambda-2} \tag{1.10}$$

Weisskopf units (W.u.) works as a benchmark for both theoretical and experimental values indicating the magnitude of the collectivity of the transition. If a transition is greater than an order of magnitude or more than the Weisskopf estimate, it indicates that many nucleons have been acting together in a coherent collective manner.

Seniority makes it possible to systematically map spectroscopic properties in a given shell model configuration across different isotopes or isotones when changing the number of $n$ particles that occupy a $j$ orbital. In particular dipole moments and any other one-body matrix element do not depend on $n$, and should be constant for a given $j$ shell. On the contrary, two-body interactions are directly proportional to the number of pairs, given by $(n-\nu)/2$, and should peak in the middle of the shell. Within a given nucleus, odd-tensor single-particle operators such as electromagnetic $M1$ transitions can only connect states with the same seniority, while in the case of $E2$ transitions $\Delta\nu = 0,\pm 2$ changes are possible. Algebraic relations make it possible to relate B(E2) rates between seniority conserving and seniority changing transitions as a function of the number of nucleons $n$ in a given configuration (typically in a chain of isotopes), and also for a different transition within the same nucleus for different total angular momentum and seniority change.

### 1.2.2 Transition probabilities and collectivity

The single-particle space for a nucleus such as $^{136}$Te, in the framework of the nuclear shell model, has a large dimension with many valence particles, whose collective motion is driven by quadrupole correlations, giving rise to quadrupole collective states. How these states evolve as we depart from the shell closure is of great interest, and consequently, several phenomenological models have been developed in order to describe the quadrupole collective states.

For even-even nuclei, there is an empirical relation between the excitation energy of the first $2^+$ state and the transition rate B(E2) of the de-exciting ground state transition that is so-called the Grodzins rule [Gro62]. This formulation establishes that the product of the energy and the transition rate from the $2^+$ are directly proportional to $Z^2/A$, being the transition rates of the first $2^+$ state and the excitation energy a clear signature of the quadrupole collectivity. Figure 1.1 shows the empirical relation between the lifetimes of the first excited $2^+$ states in the even-even nuclei as a function of the excitation energy. The plot is directly taken from [Gro62] and gather the experimental data that was available when L. Grodzins formulated the empirical relation.

Later global fits to existing data confirmed the Grodzins empirical relation and lead to a modified version [RNT01] that is expressed in Equation 1.11 and is called Raman version of the Grodzins rule.

$$B(E2;0^+\rightarrow 2^+)[e^2b^2] = (2.57\pm 0.45)\cdot E^{-1}\cdot Z^2\cdot A^{-2/3} \tag{1.11}$$

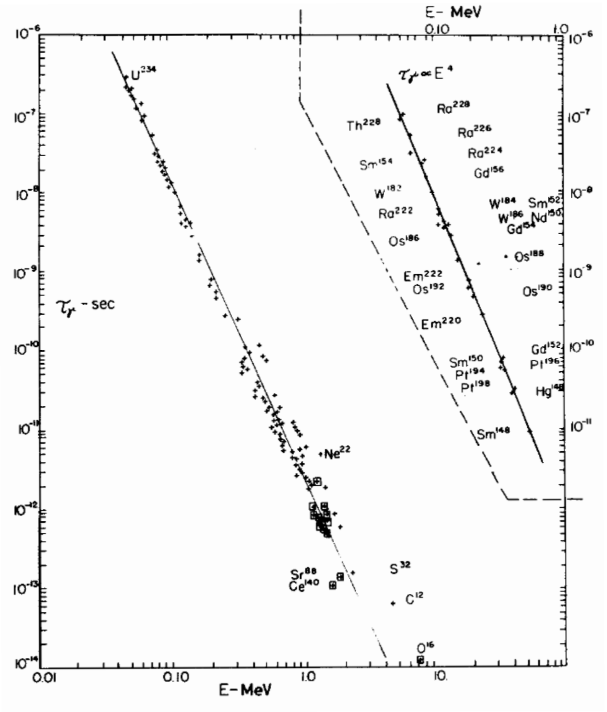

**Figure 1.1: Empirical Grodzins rule for even-even nuclei.** - Empirical relation between the measured lifetimes of the first $2^+$ state as a function of its excitation energy [Gro62].

In Equation 1.11, the $B(E2)\uparrow$ value is the transition rate upwards from the ground state to the excited $2^+$ state, connected with the $B(E2)\downarrow$ via Equation 1.6. In this case, the relation between the transition rates upwards from the ground state to the first excited $2^+$ state, $B(E2)\uparrow$, and the transition rate from the $2^+$ state to the ground state, $B(E2)\downarrow$, is $B(E2)\uparrow = 5 \cdot B(E2)\downarrow$. Alternatively, the lifetime of the $2^+$ state, which is a direct observable, can be expressed with the relation presented in Equation 1.12. Assuming quadrupole deformation, the deformation parameter $\beta$ is readily obtained as Equation 1.13 express, where E is the transition energy and A the atomic number.

$$\tau_\gamma = (1.59 \pm 0.28) \cdot 10^{14} \cdot E^{-4} \cdot Z^{-2} \cdot A^{2/3} \tag{1.12}$$

$$\beta = (466 \pm 41) \cdot E^{-1/2} \cdot A^{-1} \tag{1.13}$$

Therefore, lifetime values give direct access to the B(E2) reduced transition probabilities, providing valuable information about quadrupole collectivity and nuclear deformation.

### 1.2.3 Collectivity vs. single particle states

The collective behaviour that arises in nuclei far from the stability is a paradigm still to be understood in the description of finite many-body quantum systems. The influence of the residual interactions becomes more and more important when approaching the mid-shell regions, giving rise to collective behaviour that indicates that the wavefunction spreads over multiple coherent particle-hole components with vibrational or rotational degrees of freedom. A good approach to understand collective behaviour is the study of quadrupole electric transition probability B(E2) and its evolution. B(E2) transition rates provide key information about the wavefunction of the lowest lying excited states and the ground state. In addition, they are directly accessible by measurements of lifetimes of excited states.

The excitation energies of the first $2^+$ and $4^+$ excited states together with the related lifetime values in even-even nuclei constitute an excellent benchmark for testing the available nuclear models, from the "single-particle" to the collective regime. The evolution of the B(E2;$2^+_1 \rightarrow 0^+_{gs}$) strength along isotopic chains gives a measure on how collectivity evolves. The normal trend is a gradual increase from the minimum value of the spherical nuclei situated at closed shells, which are governed by the single-particle degrees of freedom, towards higher values in mid-shell regions, where developing deformations, rotational and vibrational excitations develop as the number of valence nucleons increases. Therefore, an enhanced B(E2) transition rate is a clear indication of collective behaviour.

Within of a nucleus the B(E2) strength normally increases with the spin for low lying states in a rotational or vibrational band. Hence, it is possible to express the degree of collectivity by the quantity $B_{4/2}$=B(E2; $4^+ \rightarrow 2^+$)/ B(E2; $2^+ \rightarrow 0^+_{gs}$) which gives a good measure of the collective excitations. For an ideal rotor, the strength ratio is $B_{4/2}$=10/7=1.43, whereas for a harmonic vibrator $B_{4/2}$=2, reflecting the ratio between the number of phonons in the initial and the final state.

The trend of the excitation energy of the first $2^+$ and $4^+$ excited states is opposite to the B(E2) strength, there is a gradual lowering of the excitation energy as the number

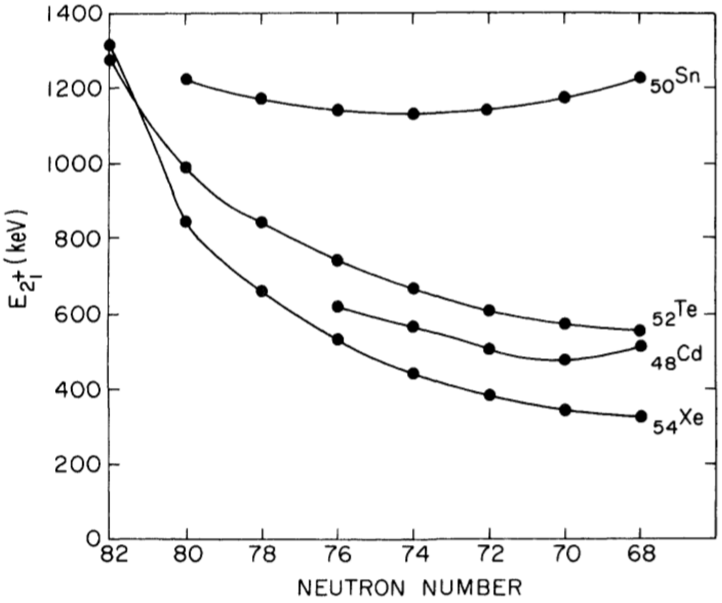

**Figure 1.2: Excitation energy of the $2_1^+$ states in the $^{132}$Sn region.** - Excitation energy of the first excited $2^+$ states for nuclei in the $^{132}$Sn region [Cas00].

of valence nucleons increases. The energy of the first excited states increases towards closed shells, whereas the probability to excite a nucleus is enhanced with the number of valence nucleons that are available to create the excited state. Figure 1.2 shows the energy levels of the Sn, Xe, Te, and Cd nuclei. The singly magic Sn nuclei with $Z \sim 50$ and $N \neq 82$ display a typical shell model behaviour independent of the number of valence neutrons. The energy of the $2^+$ remains high, however as valence nucleons are added the energy of the $2^+$ drops sharply, like for Te and for Cd nuclei, (where the two valence protons are counted as holes). The drop is even more pronounced for Xe, which has four valence protons.

The degree and the type of collectivity can be also expressed in terms of the energy ratio of the first $4^+$ state to the first $2^+$state, i.e. $R_{4/2}=E(4_1^+)/E(2_1^+)$. This ratio ranges from values $< 2$ for spherical nuclei (shell model), between 2.0 and 2.5 for nuclei with vibrational excitations. Through $\sim$2 for nuclei reasonably close to closed shells and up to 3.33 for nuclei with purely rotational excitations near mid-shell. Values near 2.0, 2.5, and 3.33 are typical of different types of macroscopic collective shapes: spherical harmonic vibrator, axially asymmetric rotor, and axially symmetric rotor, respectively.

However, there is a smooth progression from one to another of these idealized collective limits.

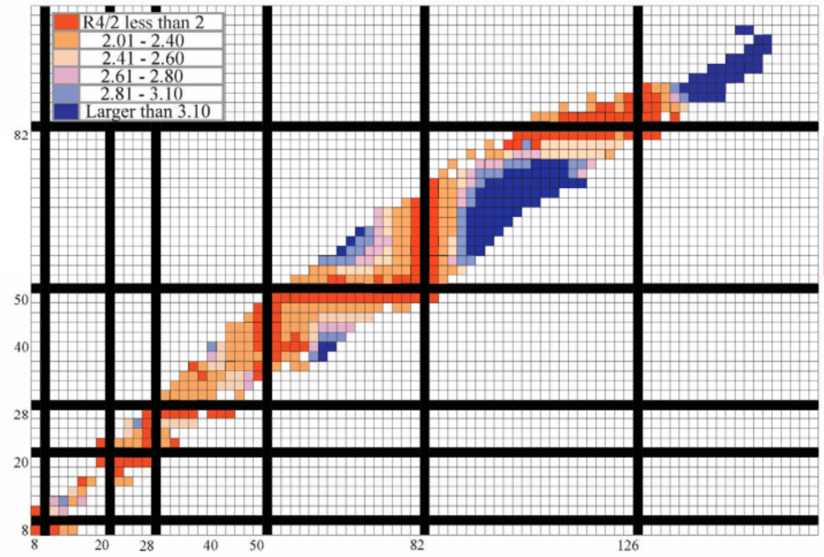

**Figure 1.3: Structural evolution in regard to the $R_{4/2}$ ratio.** - Perspective of the structure evolution along the nuclear chart in relation to the $R_{4/2}$ ratio [Cas00].

# 2

# Lifetime measurements with fast scintillators

As discussed in the previous Chapter, lifetime values give direct access to the reduced transition probabilities, allowing a better understanding of nuclear structure, including nuclear deformation and collectivity. The experimental accessible range of nuclear lifetimes spans forty-five orders of magnitude. Several experimental techniques are employed, their choice depending on the production mechanism and lifetime value. Delayed coincidence methods using HPGe detectors cover the microsecond and nanosecond range. In the femtosecond and picosecond ranges techniques such as the recoil distance method and the Doppler shift attenuation method may be used. Delayed coincidence methods using fast scintillators, generally labelled as *fast timing*, such as the Advanced Time Delayed (ATD) method or the Generalized Centroid Shift (GCD) method, are the best suited to measure lifetimes from tens of picoseconds to several nanoseconds. The sensitivity of the fast-timing techniques is directly proportional to the time resolution of the setup in use, which becomes a determining factor in this type of measurements.

In what follows we, therefore, refer to fast-timing methods as the set of delayed-coincidence techniques for lifetime measurements down to the few picoseconds range that rely on coincidence between fast, typically $LaBr_3(Ce)$ scintillators, gated by HPGe detectors.

## 2.1 The Advanced Time-Delayed $\beta\gamma\gamma(t)$ method

The Advanced Time Delayed method (ATD) is an electronic timing method that allows the measurement of lifetimes of excited states populated in $\beta$-decay in the range of few nanoseconds down to tens of picoseconds and even below. It was invented by Henryk Mach in 1996 at the TRISTAN facility in Brookhaven National Laboratory, and later developed and published by H. Mach, M. Moszyński and R. Gill [MGM89, MM89, MWM+91]. It relies on triple coincidences $\beta\gamma\gamma$(t), where the time information is obtained from $\beta$-$\gamma$ delayed coincidences between the fast timing scintillators (plastic and $BaF_2$ at that time) and the lack of energy resolution of the $BaF_2$ crystals is overcome by the selection of the desired decay branch by imposing a high resolution $\gamma$ condition on the HPGe detectors. In this manner, lifetimes are derived by measuring the time differences between the arrival of the $\beta$ particles following the $\beta$-decay of the parent nucleus and the $\gamma$-rays that de-excite the level of interest. Nowadays, the $\beta$-particles are measured with a fast and thin plastic detector, and the de-exciting $\gamma$-rays are recorded with fast $LaBr_3$(Ce) scintillators. The third condition applied on a HPGe (High Purity Germanium) detector, taking advantage of its good energy resolution, selects the decay cascade.

The measured time distributions assuming no background contributions can be expressed with a function $F(t_j)$ of the form of Equation 2.1, where $N$ is the total number of counts in the spectrum, $P(t_j)$ characterizes the system response at a given energy and the $f(t)$ function is of the form $f(t) = e^{-\lambda t}$ for t > 0, where $\lambda$ is the time constant of the level, $\lambda = \frac{ln(2)}{T_{1/2}}$.

$$F(t_j) = N \int_0^{+\infty} P(t_j - t) f(t) dt \tag{2.1}$$

To derive lifetime values using the ATD method the intrinsic system response is deconvoluted from the total delayed spectrum. The energy-dependent system response $P(t_j)$ comprises all experimental uncertainties such as the rise time of the scintillator crystals the timing performance of the PMT or the electronics contributions. It is derived by measuring the time distributions of prompt $\gamma$-rays that de-excite short-lived states of $\tau < 1$ ps, and it is generally assumed quasi Gaussian. The ability to measure short lifetimes is directly proportional to the time resolution of the system in use and to the available statistics.

In the frame of the ATD method, there are two different techniques for lifetime determination: the Convolution technique and the Centroid Shift technique. Each works for a different time range and, especially the second one, relies on precise time calibrations. Both are explained in the following subsections.

### 2.1.1 The Convolution Technique

If the level lifetime is long enough to appear as a slope on the delayed part of the time distribution, it is possible to derive the level half-life by fitting the time distribution to a convolution function that is composed of a Gaussian in addition to an exponential decay as expressed in Equation 2.2. The quasi-Gaussian component corresponds to the system prompt response function at a given energy, while the exponential decay is caused by the level half-life.

$$F(t_j) = N \int_A^{+\infty} e^{-\delta(t_j - t)^2} e^{-\lambda t} dt \tag{2.2}$$

In Equation 2.2, $N$ refers to a normalisation factor, the $\delta$ parameter is related to the Gaussian width of the prompt distribution and $A$ is related to the centroid position of prompt distribution. The FWHM of the quasi-Gaussian function that corresponds to the prompt distribution comprises all experimental uncertainties related to the scintillator crystal, PMT and electronics.

Figure 2.1 presents two time distributions as an example. The spectrum in red with a Gaussian shape corresponds to the time distribution of a short-lived state, whose half-life is short enough for not being visible at the spectrum as a slope in the delayed side. The distribution in blue corresponds to a long-lived level, whose half-life is long enough to appear as a slope in the time spectrum. The distribution is well represented as a convolution of a Gaussian function and an exponential decay. In some cases, it is possible to directly derive the level half-life by fitting the slope to an exponential decay in the region outside of the influence of the prompt. The time resolution of the setup in use is defined by the width of the prompt Gaussian distribution and therefore influences the range of applicability of the slope method.

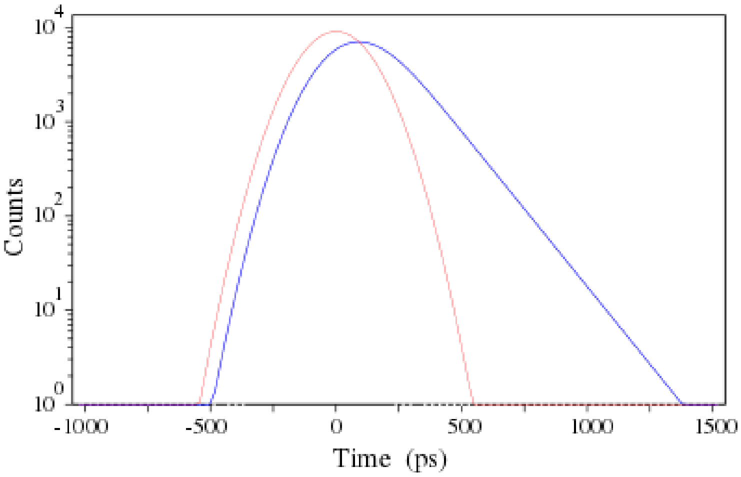

**Figure 2.1: Time distributions of long-lived and a short-lived states.** - Time distributions corresponding to a short-lived level in red with a quasi-Gaussian shape, and a long-lived state in blue with the form of a convoluted function of Gaussian plus exponential decay. The half-life of the long-lived state can be clearly seen as a slope at the right side of the distribution. The picture is taken from [Ola13].

### 2.1.2 The Centroid Shift Method

The Centroid Shift method is employed when the level lifetime is much shorter than the FWHM time resolution of the quasi-Gaussian component of the prompt time distribution (See Equation 2.1), about one third of the width of the peak given as the FWHM. In these cases, there is no visible slope at the delayed part of the spectrum. The application of this technique is also limited by the available statistics in the time spectrum.

The Centroid Shift Method method consists in the determination of the first moment (centroid) of the time spectrum originated by the time differences between the coincident events in the fast timing detectors. Equation 2.3 provides the definition of the centroid as the mean value of the time distribution, where $\sum_i n_i$ is the number of total events at the time spectrum and $t_i$ corresponds to the time channel. The standard error $(\delta C)^2$ is given in Equation 2.3.

$$C^D = \bar{t} = \frac{\sum_i t_i n_i}{\sum_i n_i} \qquad (\delta C)^2 = (\delta_i)^2 = \frac{\sum_i \left(t_i - \bar{t}\right)^2}{\left(\sum_i n_i\right)^2} \tag{2.3}$$

The lifetime of interest is deduced from the relative shift the measured centroid of the delayed time spectrum with respect to the prompt response at the same energy, which is given by a prompt curve that describes the system response as a function of energy, the relation is given at Equation 2.4.

$$\tau = C^{D} - C^{Prompt} \tag{2.4}$$

The Centroid Shift Method method relies on precise time calibrations, which are the Full-Energy-Peak (FEP) curve and the Compton distribution. The FEP-curve or prompt response accounts for the energy-dependent system response to the full-energy events, *i.e.* $\gamma$-rays that have fully deposited their energy in the fast scintillators. The FEP-curve is aimed at de-convoluting the intrinsic system response from the total time spectrum and is measured using prompt $\gamma$-rays that de-excite short-lived states of $\tau \leq 1$ ps. The Compton curve provides the system response to the $\gamma$-rays that have lost part of their energy through Compton scattering around the setup and is aimed at correcting the Compton contribution to the total time spectrum. For very precise timing measurements a further correction taking care of the different Compton response at a given energy arising from FEP of different energies can be implemented [MGM89].

## 2.2 The Mirror Symmetric Centroid method

The fast-timing methods can be expanded to measure level lifetimes of states by electronic timing between feeding and de-populating transition using fast scintillators, such as it was implemented in beam in the Jyväskylä accelerator laboratory, or in GANIL [MKG+17] where the measurement of lifetimes below $8^{+}$ isomers in N=50 isotones was achieved at the LISE3 spectrometer via $\gamma$-$\gamma$ fast timing. Thanks to the discovery and development of scintillator crystals such as $LaBr_3$(Ce) that exhibit good energy resolution in addition to fast response and high-efficiency for $\gamma$-ray detection, the extension of fast-timing methods has been handed on a silver platter. Prior to $LaBr_3$(Ce) crystals the fast timing detectors that were in used were based on $BaF_2$ crystals, with an excellent time response but with an energy resolution of about 9-10% that did not allow to resolve full-energy peaks in energy spectra.

The Mirror Symmetric Centroid method (MSC) is a delayed coincidence technique for lifetime measurements down to the few-picosecond range that relies on triple $\gamma\gamma\gamma$(t) coincidences. Lifetime values in the MSC technique are derived from the time differences between two fast $LaBr_3$(Ce) scintillator detectors [RPJR10] with a high-resolution energy condition applied on HPGe detectors for the selection of the decaying branch. That is to say, lifetimes are measured from the time difference between the arrival of $\gamma$-rays that populate a nuclear level and the $\gamma$-rays that de-excite it.

The method distinguishes between two types of time distributions: the delayed and the anti-delayed. The delayed is obtained when the $\gamma$-rays that populate the level (feeder) work as the start signals in the measurement of the time differences (typically using a Time to Amplitude Converter or TAC), while the transitions that de-excite (decay) the level act as the stop. The centroid position of the measured distribution $C^{delayed}$ is delayed (shifted to the right) from the centroid position of the prompt distribution $C^P(E_{feeder}, E_{decay})$ by the lifetime of the level. The anti-delayed distribution is measured when the $\gamma$-rays that de-excite the level (decay) work as the start in the TAC and the transitions that populate it acts as the stop (feeder). Consequently, the measured centroid position of the anti-delayed time distribution $C^{Anti-delayed}$ is anti-delayed (shifted to the left) from the centroid position of the prompt distribution $C^P(E_{decay}, E_{feeder})$ the lifetime of the level. The MSC method takes advantage of the symmetry from the time distributions when the start and stop signals are reversed for fast detectors of the same characteristics.

Instead of dealing with the individual time responses of feeding and de-exciting transitions as a function of energy, this method employs a combined time response curve for energy differences. The method thus defines a magnitude called the centroid increment, which is derived at a certain energy increment as expressed in Equation 2.5.

$$\Delta C(\Delta E_\gamma) = C^{delayed} - C^{Anti-delayed} \qquad \Delta E_\gamma = E_{feeder} - E_{decay} \tag{2.5}$$

For prompt transitions, the centroid increment yields the Prompt Response Difference, PRD, which describes the combined $\gamma - \gamma$ zero-time versus energy time-walk of the setup. For a level with a mean life $\tau$ the centroid increment is then given by

$$\Delta C(\Delta E_\gamma) = PRD(\Delta E_\gamma) + 2\tau \, . \tag{2.6}$$

To construct the PRD a reference is chosen by gating constantly on a $\gamma$-ray that populates or de-excites a level; then the other detectors select the coincident $\gamma$-transitions.

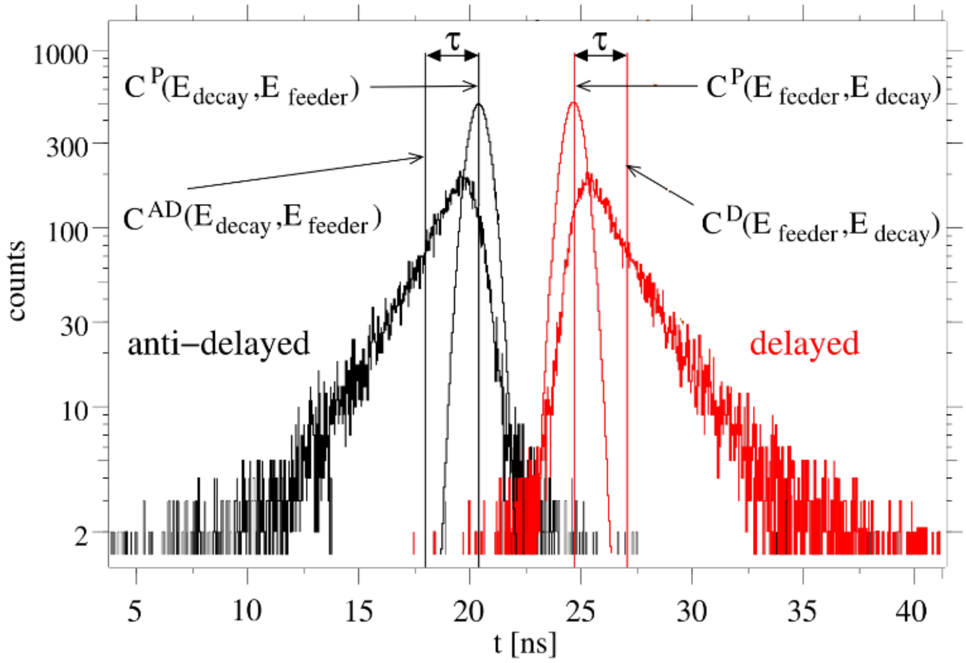

**Figure 2.2: Examples of delayed and anti-delayed time spectra.** - Examples of delayed (red) and anti-delayed (black) time spectra for the application of the MSC method.

Ideally, these transitions should be prompt to obtain the actual system response. Nevertheless, the level lifetimes in $^{152}$Eu are well known and measured, so by subtracting from the centroids twice the known lifetimes the system response is obtained. It is useful to notice that the PRD verifies the following relation:

$$PRD(\Delta E_\gamma) = PRD(E_{feeder}) - PRD(E_{decay}) \,. \tag{2.7}$$

## 2.3 The impact of the experimental setup for fast-timing methods

The development and implementation of the Advanced time Delayed (ATD) technique was initially possible thanks to the technical developments of the fast $BaF_2$ inorganic scintillators and to the state-of-the-art fast photomultipliers tubes (PMTs) [MGM89]. $BaF_2$ crystals have a fast response of the same order as plastic scintillators and show moderate energy resolution for discrete $\gamma$-ray energies. The dynode timing ability of fast PMTs resulted in an improvement of the 20% of the timing performance [MGM89].

The more recent discovery of $LaBr_3$(Ce) scintillators has led to a major breakthrough in the application of the ATD technique, since $LaBr_3$(Ce) crystals unite excellent time response with good energy resolution [LDvE$^+$02, Gob]. $LaBr_3$(Ce) crystals are one of the fastest scintillators commercially available nowadays [LDvE$^+$02, SGK$^+$03, Gob], their energy resolution at 662 keV is measured to be as good as 2.8% [Gob], and their photon yield corresponds to 63 photons/keV [Gob], which is much higher than the light output of other inorganic scintillators [Dor02]. Hence, due to their superb properties, $LaBr_3$(Ce)-based detectors have been the option of choice for the application of the Advanced Time-Delayed (ATD) method since 2005 [WMF$^+$07], being now the current standard in *fast-timing* spectroscopy [MuuBB$^+$10, ARM$^+$13, OFM$^+$13, RSB$^+$14]. The much superior energy resolution of $LaBr_3$(Ce) crystals compared to $BaF_2$, allows to disentangle complex decay schemes and provides higher peak-to-background ratios, which results in smaller time corrections due to the Compton contribution under full-energy peaks.

During the last 15 years, several new types of inorganic scintillators apart from $LaBr_3$(Ce) crystals have been produced and tested, mainly halides and lutetium-based compounds, which were activated by cerium or praseodymium doping such as $LaCl_3$(Ce). Despite some of them (*i.e.* $CeBr_3$) showing very competitive performance in terms of time response [FMV$^+$13], $LaBr_3$(Ce) scintillators remain as the best suited detectors for the application of fast-timing techniques.

The sensitivity of the fast-timing methods is directly proportional to the time resolution of the setup in use, where time resolution is the capacity of distinguishing between two events that have occurred close in time.

In the frame of the fast-timing measurements, the time resolution of a setup is expressed with the FWHM (Full Width at Half Maximum) of the quasi-Gaussian prompt distribution, where FWHM=$2.35\cdot\sigma$ for a Gaussian. The prompt distribution is measured using short-lived levels that are de-excited and populated by prompt $\gamma$-rays. The time spectra are energy dependent and its FWHM varies with the energy, therefore there is a need to define a standard energy when expressing the time resolution. In this work, the time resolution is given at $^{60}$Co energies (1173-1332 keV) and 511 keV.

The total time resolution of a fast-timing setup is determined by several factors, where the main contribution arises from the scintillator detector. It strongly depends on the rise time of the generated pulses and has two contributions: one coming from the crystal itself and a second one coming from the photodevice in use, which is a photomultiplier tube (PMT) in this work.

The crystal contribution is determined by the lifetime of the excitations inside the crystal, which marks the decay time of the pulse, by the size and the shape of the crystal, which influences the internal reflections and the interaction points and the internal absorption, and by the amount of photons produced per keV (photon yield). The PMT contribution is determined by the photocathode efficiency, *i.e.* the number of photo-electrons generated at the photocathode, by the time spread of the electrons from the photocathode to the first dynode and by the spread of the electrons in the dynode system.

Apart from the scintillators detectors, the contribution of certain components of the electronic chain such as the Constant Fraction Discriminator (CFD), which directly determines the time walk, are also significant factors regarding the timing performance of the setup.

Therefore, to obtain the maximum sensibility when using fast timing techniques, it is of key relevance to optimize the time resolution of the setup achieving the best possible timing performance. This effect becomes more and more relevant as the measured lifetimes are shorter and shorter, being of the highest importance in the few-picoseconds range.

The optimization of the setup entails the best choice of crystal type ($LaBr_3$(Ce) in this case), size, shape and doping, the right selection of the coupling photosensor [FMO$^+$11] and the optimization of the electronic circuit [FMV$^+$13, FMP$^+$13]. In addition, the systematic investigation of the fast-timing setup provides useful knowledge for the design and construction of large fast-timing arrays such as the FATIMA array that will be part of HISPEC-DESPEC experiments [DH, RPG$^+$] at the FAIR-GSI facility [FAI]. The FATIMA array is meant to be used as a standalone or a hybrid $\gamma$-ray array dedicated to $\beta$-$\gamma$ and $\gamma$-$\gamma$ spectroscopy.

## 2.4 Towards the construction of large $LaBr_3$(Ce) arrays

Highly performing $LaBr_3$(Ce) arrays are nowadays one of the best means to study the atomic nucleus. Their good time response can be complemented with high-efficient spectroscopic capabilities of HPGe arrays, or with the tracking abilities from silicon strip detectors. This combination results in a powerful tool to understand the nuclear matter. Therefore, the development and optimization of mixed arrays are of great relevance for applications in experimental nuclear physics studies in the present and future facilities.

Different geometries of the $LaBr_3$(Ce) detectors have been used for fast timing, the most common one being the cylindrical one, with crystals of different sizes. However, a highly suitable shape for the construction of big arrays the big arrays construction is one that makes it possible to build rings of detectors around the source, increasing the solid angle and the $\gamma$-ray detection efficiency due to the good packing factor. Examples of these special geometries are provided in this thesis, namely the truncated cone geometry and the hybrid-tapered design inspired on $BaF_2$ reference crystals. Both geometries favour the light collection inside the crystal, enhancing the time resolution and compensating intrinsic efficiency losses. The results presented in this work indicate that the truncated cone geometry is an excellent candidate for the construction of large $LaBr_3$(Ce) arrays. In addition to its versatile geometry that allows to placing the crystals in several different configurations, it has an excellent time resolution comparable to the much smaller 1 in. cylindrical crystals. And therefore much better than a cylindrical crystal of similar size. It has sufficiently good energy resolution and high $\gamma$-ray detection efficiency.

To date, interesting results have been obtained by the use of $LaBr_3$(Ce) arrays such as ROSPHERE [BCDC$^+$16] placed in the IFIN-HH laboratory (Bucharest) [MuuBB$^+$10, KLM$^+$11, MAR$^+$12, MPM$^+$13, NBM$^+$14]. The first time that a large array of $LaBr_3$(Ce) detectors in combination with a high-efficiency HPGe-clover array was used in neutron-induced spectroscopy, was during the EXILL-FATIMA experiment in 2013 that took place in the nuclear reactor of the ILL [JBdF$^+$, RSB$^+$14]. The experimental will be described in detail in Section 4. Another example is the recent experiment performed at the Argonne National Laboratory in December 2015 and January 2016, measuring decay radiation of fission products from a $^{252}$Cf source, with the purpose of investigating neutron-rich nuclei in the mass region around A=110 and A=150 by measuring lifetimes of low-lying excited states. The source was placed at the focus of one hemisphere of the GAMMASPHERE array, with 51 HPGe detectors, which was coupled to 25 $LaBr_3(Ce)$ from the FATIMA collaboration. Besides the milestones reached until today, the continuous development of radioactive beam facilities together with the implementation of state-of-the art hybrid spectrometers is a powerful strategy to push forward the limits of nuclear physics.

The optimization work presented in Chapter 3 was triggered by the design and construction of the FAst TIMing Array (FATIMA) that will be placed at FAIR facility [F$^+$]. The FATIMA (FAst TIMing Array) spectrometer has been designed as an integral component of the DESPEC setup within the NUSTAR@FAIR collaboration. The NUSTAR (NUclear STructure, Astrophysics and Reactions) is an international collaboration aimed at the study of astrophysics, nuclear structure and reactions of nuclei far from the stability. It is one of the main physics pillars of FAIR [FAI], the facility for Antiproton Ion Research. The spectrometer will be placed at the focal plane of the Super-FRS in combination with the HISPEC/DESPEC setup [DH]. The HISPEC/DESPEC (High-resolution In-flight SPECtroscopy/DEcay SPECtroscopy) experiments will obtain radioactive ions beam from the Low Energy Branch (LEB) of the Super-FRS (the new Superconducting Fragment Separator). DESPEC is focused on decay experiments. It is a modular experiment equipped with AIDA, a set of highly segmented silicon-based detectors (DSSSD), where the beam is slowed down and implanted. There is a set of detectors around it, such as highly efficient HPGe spectrometers or the FATIMA $LaBr_3(Ce)$ array for lifetime determination, and there are also ancillary detectors for charged particle and neutron detection.

FATIMA may operate as a standalone $\gamma$ spectrometer in coincidence with Super-FRS tracking detectors and AIDA, or as hybrid spectrometer working in combination with plastic scintillators for fast-timing with $\beta$-particles in the case of $\beta$-spectroscopy and with high-resolution $\gamma$ detectors such as DEGAS. The main aim of FATIMA is to perform lifetime measurements from few ns to few ps ranges below isomers and follows $\beta$-decay. In addition to excellent time response in an extended energy range, FATIMA needs a good energy resolution together with sufficient $\gamma$-ray detection efficiency.

The following Chapter 3 explains in detail the most relevant elements of a fast-timing setup together with their influence on the total timing performance. Chapter 3 also presents the optimization procedure of the total time response of the system carried out through a systematic investigation of the setup parameters, namely the PMT bias voltage, the CFD external delay and the zero-crossing (Z). A comparison of $LaBr_3$(Ce) crystals of different sizes, shapes and Ce concentration is also provided.

# 3

# Optimization of the fast-timing setup

As discussed in the previous chapter, $LaBr_3(Ce)$-based detectors unite fast response and good energy resolution. Therefore they have been the preferred ones for the application of the Advanced Time-Delayed (ATD) technique since 2005 [WMF$^+$07] and they are the current standard in fast-timing spectroscopy, and the choice for large high-performance arrays for *fast-timing* spectroscopy [MuuBB$^+$10, ARM$^+$13, OFM$^+$13, RSB$^+$14, F$^+$]. In addition, their potential for medical imaging is under exploration [DWSP$^+$10].

The ability to measure lifetimes in the few-picosecond range by fast timing techniques such as the ATD method or the GCD method is directly related to the time resolution of the fast-timing setup in use, and proportional to the available statistics in the time-difference peak. This fact can be quantified by a figure of merit as

$$FoM = \frac{FWHM}{\sqrt{N}} C, \tag{3.1}$$

where $FWHM$ is the coincidence time resolution, $N$ is the number of counts in the time peak and $C$ is a correction factor related to the peak to background ratio and to our ability to select the timing peak. Both the optimization of the time resolution of the setup and the acquisition of sufficient statistics play an important role to maximize the figure of merit.

In this Chapter, the most relevant elements of the fast-timing $LaBr_3(Ce)$ setup contributing to the enhancement of the time resolution are discussed. A simple fast-timing setup consisting of $LaBr_3$(Ce) crystals coupled to fast photomultipliers tubes and a readout by means of analog electronics is used. The description of the in-depth characterization of the components of the setup is provided, together with their optimization to achieve the best timing performance. The most sensitive parameters to fine tune are the external delay in the Constant Fraction Discriminator (CFD), the CFD zero-crossing value (Z) and the photomultiplier tube (PMT) bias voltage.

In view of the construction of highly-performance $LaBr_3$(Ce) arrays for fast-timing studies like the one used during the EXILL-FATIMA campaign, or the one that will be placed in combination with HISPEC-DESPEC detectors in the FAIR facility [Pod08, F$^+$] (see previous Chapter), different $LaBr_3$(Ce) detectors equipped with crystals of different shape, size and composition has been tested and compared.

The Chapter is largely based on the work published in references [VMF$^+$15] and [VCGF$^+$17]. Some of the procedures are also discussed in [FMP$^+$13] and [FMV$^+$13].

## 3.1 Characterization and optimization of $LaBr_3$(Ce) detectors

The setup optimization for fast-timing measurements entails three main parts, namely: the best choice of scintillator crystals (size, shape and doping), the selection of the most performing coupling photosensor and the optimization of the electronic components for signals treatment.

### 3.1.1 Characterization procedure

In this thesis we refer to a $LaBr_3$(Ce) detector as the assembly of a $LaBr_3$(Ce) scintillator crystal coupled to a photomultiplier tube. Consequently, the time contribution of a $LaBr_3$(Ce) detector to the total time resolution of the fast timing setup is the combination of the $LaBr_3$(Ce) crystal contribution in addition to the contribution of the PMT, and both should be considered. The time response of the scintillator detectors represents the main contribution to the total time resolution of the setup, being its optimization a key aspect in the process of maximizing the timing performance. To this aim, we have systematically characterized and optimized the time response of different $LaBr_3$(Ce) crystals attending to important factors such as the Ce dopant concentration, the size and the shape of the scintillator crystals.

The main factor regarding the $LaBr_3$(Ce) crystal contribution is the internal structure of the crystal itself. It determines the amount of photons produced per keV and the lifetime of the excitations inside of the crystal, which directly influences the decay time constant of the scintillator. It has been reported that the Ce doping concentration strongly influences the time response and the energy resolution of $LaBr_3$(Ce) detectors [GMH$^+$05]. Up to 5% Ce concentration the photon yield of $LaBr_3$(Ce) crystals increases and hence the energy resolution and the time response as well [GMH$^+$05]. However, further Ce increase leads to a constant energy resolution [DDB$^+$08]. Contrary to the trend measured for the energy resolution it is believed a gradual improvement of the time response as the Ce doping concentration increases. In order to investigate the Ce influence on the time response and the energy resolution, we have studied in depth three identical $LaBr_3$(Ce) crystals of cylindrical shape commercially manufactured with different Ce concentration.

The size and the shape of the crystal is also an important factor. It influences the interaction points of the $\gamma$-rays inside of the crystal, the internal reflections of the photons and the $\gamma$-ray detection efficiency. Crystals of large size have obviously higher $\gamma$-ray detection efficiency than those of the same shape but smaller in dimensions. However, due to the amount of internal reflections, bigger crystals exhibit worse values of energy and time resolution. Certain $LaBr_3$(Ce) geometries favour the light collection inside of the crystal enhancing the time resolution and the spectroscopic features, despite having bigger dimensions. Over the last ten years, different geometries of $LaBr_3$(Ce) detectors have been used: cylindrical $LaBr_3$(Ce) scintillators of different dimensions and truncated cone $LaBr_3$(Ce) crystals, inspired in former geometries of $BaF_2$ detectors which exhibited very good timing performance. The dimensions of the cylindrical crystals range from 1 in. in height and 1 in. in diameter for the smallest ones, to 2.5 in. in height and 2.5 in. in diameter for the biggest crystals. In this work, the cylindrical crystals of 1 in. x 1 in. are taken as the standard reference detector for crystal characterization and benchmarking.

The first step in the study corresponds to a detailed characterization of a cylindrical 1 in. in height and 1 in. in diameter $LaBr_3$(Ce) detector that will be taken as a reference. The performance evaluation of the 1 in. $LaBr_3$(Ce) entails the optimization of the time response of the analog electronics as the main objective. The energy resolution and linearity of the $LaBr_3$(Ce) detectors in use are relevant factors to be considered when applying fast-timing methods, so the aim is to achieve the best time resolution while maintaining good energy resolution and linearity. The study explores the time response as a function of the working parameters of the Constant Fraction Discriminator (CFD) employed, ORTEC model 935, the external delay and the zero-crossing parameter Z. Two working regimes of the ORTEC 935, the Constant Fraction Discriminator (CFD) and the Leading Edge Discriminator (LE) are also studied.

Once the best setup conditions that maximize the timing performance are found, it is possible to investigate different sizes and geometries of $LaBr_3$(Ce) crystals, assessing the geometry influence on their time response and spectroscopic features. Innovative geometries specially designed to enhance the scintillation light collection inside of the crystal may yield time resolution values as good as those delivered by crystals of smaller sizes, while providing much higher $\gamma$-ray detection efficiency. The second step in the study corresponds to the characterization of two innovative geometries of $LaBr_3$(Ce) crystals specially designed to this end. The first design is a truncated cone crystal of 1.5 in. in height an diameters of 1.5 and 1 in in the bases. The second one is inspired in the advantageous Studsvik design for $BaF_2$ crystals. It is a tapered hybrid crystal composed of a conical part with a cylindrical section. Section 3.5.2 presents the two crystal geometries in detail and provide the technical drawings. In addition to their improved capabilities, the two innovative geometries are very convenient regarding the construction of highly-performance $LaBr_3$(Ce) arrays. The cone-like structures provide a good packing factor making it possible to cover larger solid angles than those covered by cylindrical crystals of similar dimensions, improving in $\gamma$-ray detection efficiency.

### 3.1.2 Choice of photodetector

The photodetectors best suited for the $LaBr_3$(Ce) crystals of the sizes mentioned above are fast photomultiplier tubes. The PMT contribution to the total time resolution of the set up is determined by the number of photo-electrons generated at the photocathode (photocathode efficiency), by the time spread of the electrons from the photocathode to the first dynode and by the spread of the electrons in the dynode system. In addition to the timing performance, high light-yield scintillators such as $LaBr_3$(Ce) may cause non-linear responses due to space-charge effects in the photomultiplier tube (PMT) [Mos06]. Hence, the right selection of the coupling PMT is a key aspect when optimizing the total time resolution.

In this study, the selected PMT model for crystal operation is the Hamamatsu R9779 in assembly number H10570. It is a high speed head-on 8-stage device with a window of 2 in. in diameter, optimized for timing measurements [Ham09], with a rise time of 1.8 ns [Ham09, FMV+13]. It is equipped with a bialkali photocathode. It has been specially designed for the most time efficient collection of photo-electrons and it is furnished with an accelerating grid at the front end in order to get all photo-electrons simultaneously arrive at the first dynode. In this way output signals have a typical transit time of 20 ns and transit time spread (TTS) of only 250 ps FWHM.

It has been proven that the Hamamatsu R9779 is the best suited PMT model currently available in the market for fast-timing spectroscopy with $\mathrm{LaBr_3(Ce)}$ crystals [FMO+11, FMV+13]. In addition to the excellent timing capabilities, it also shows good spectroscopic features: the measured energy resolution values are only slightly worse than those reported with PMT models especially aimed to spectroscopic applications, and the energy linearity is preserved when biasing the PMT to the voltage that provides the best time response.

The PMT bias voltage is another important factor to be considered when optimizing the performance of $\mathrm{LaBr_3(Ce)}$ detectors. It influences the electron multiplication and collection, and secondary emissions inside the PMT. Not only affects the time resolution but also influences the energy resolution and linearity. In principle, the time resolution is not as sensitive to this parameter as it is to the external CFD delay, but it is important concerning the energy resolution and linearity. The initial values for optimizing the PMT bias voltage were chosen in the way to obtain a 1 V anode amplitude for 1 MeV incident $\gamma$-rays in the crystal. The optimal HV value is selected by considering three factors: linearity, energy resolution and time resolution.

### 3.1.3 Spectroscopic features: energy resolution

In addition to the time response, which directly determines the sensitivity of the fast-timing methods, the energy resolution is also an important characteristic to be evaluated. A reasonably good energy resolution favours the proper selection of the decay branches and contributes to minimizing the time corrections due to the Compton background under the full-energy $\gamma$-peaks. A bad energy resolution may hamper transition selection when deriving timing differences (see Chapter 5). The energy resolution of

$LaBr_3(Ce)$ crystals has been measured to be as good as 2.8% at 662 for small cylindrical crystals of 1 in. in height and 1 in. of diameter [VMF$^+$15].

In this thesis, we provide the relative energy resolution of the $LaBr_3(Ce)$ detectors as the ratio between the FWHM of the $\gamma$-ray full energy peak (FEP) and its energy as $E_R = \Delta E/E_o$, where $\Delta E$ correspond with the FWHM of the FEP and $E_o$ with the energy centroid. If the values of FWHM and centroid position are considered in channels instead of keV, one obtains the *apparent* energy resolution, which does not account for non-linear effects. The actual energy resolution involves the determination of the functional relation $f(p)$ between the peak position in channels, which is proportional to the signal amplitude and the $\gamma$-ray energy, $E_i = f(p_i)$. Values of the real energy resolution are normally higher than apparent ones. Assuming that to first order the relation between channels and energy is locally linear, the energy resolution can be obtained from the expression in Equation 3.2

$$E_R = \frac{\Delta p}{E_o} \times \left. \frac{df}{dp} \right|_{p=p_o} \tag{3.2}$$

For a relatively small non-linear behaviour, where the energy relation can be expressed with a second order polynomial of the form $f(p) = a + bp + cp^2$, the energy resolution corresponds to the expression in Equation 3.3.

$$E_R = \frac{b + 2cp_o}{a + bp_o + cp_o^2} \Delta p \tag{3.3}$$

One should note that the apparent energy resolution is equal to the actual resolution for a perfect linear fit with zero offset, $a = c = 0$.

As the energy resolution is energy dependent, all values of energy resolution reported in this thesis are given at 662 keV ($^{137}$Cs source), which is taken as the energy standard. The bias voltage applied to the Hamamatsu R9779 PMT that provides the best time response ranges from $-1200$ V to $-1300$ V. This voltage range also preserves good energy resolution and linearity. As discussed before, the Hamamatsu R9779 is optimized for timing applications at the expense of slightly worse energy resolution. That is why the energy resolution of the reference 1 in. $LaBr_3(Ce)$ cylindrical crystal has also been tested by means of a second PMT model that is aimed at spectroscopic measurements, the Hamamatsu R6231. In this chapter, the energy resolution of $LaBr_3(Ce)$ crystals of different geometries at 662 keV is also measured with this second PMT model.

### 3.1.4 Spectroscopic features: energy linearity

The energy linearity is a relevant factor when applying fast-timing methods since a non-linear energy response may hinder the selection of the full-energy peaks in the energy spectra, and a non-linear response implies high-order polynomial energy corrections. High photon-yield crystals such as $LaBr_3(Ce)$ may display non-linear response due to intrinsic pulse height non-proportionality and to space-charge effects that arise in the PMT [Mos06]. In the later case, the non-linear response could appear even with good light yield proportionality. In order to assess the energy linearity of the $LaBr_3(Ce)$ detectors, the functional relationship between the peak position (signal amplitude) and the real $\gamma$-ray energy was measured in the voltage range from $-900$ V to $-1700$ V. To this aim a $^{152}$Eu source with many usable $\gamma$-rays was employed.

### 3.1.5 Spectroscopic features: $\gamma$-ray detection efficiency

High $\gamma$-ray detection efficiency is a required feature for the construction of fast-timing arrays based on $LaBr_3(Ce)$ detectors [$F^+$, $RBR^+14$]. The photopeak efficiency is calculated as the ratio of the number of events that have deposited their full energy in the crystal and the total number of emitted $\gamma$-rays.

In the present work, the absolute full-energy peak efficiency of the different $LaBr_3(Ce)$ crystals was measured with an absolutely calibrated $^{152}$Eu source placed at several distances from the crystal housing end-cap. The $\gamma$-ray efficiency was measured at PMT bias voltage that gives the optimal time response while preserving good energy resolution and linearity.

### 3.1.6 Time response: time resolution and time walk

The time response of every $LaBr_3(Ce)$ detector depends on the applied photomultiplier bias voltage, as discussed above, and on the Constant Fraction Discriminator parameters, mainly the zero-crossing (Z) and external CFD delay. Hence, the time resolution is optimized by the choice of the photomultiplier bias voltage and by an iterative procedure starting by the external CFD delay and following by a fine tune of the zero-crossing value (Z).

Once the most performing CFD external delay is found the zero crossing Z value is investigated by firstly observing the bipolar pulses in the oscilloscope in order to define a valid operational range, and secondly by fine tuning the Z parameter, while measuring the time walk. One should note that the time resolution does not significantly vary for different Z values, while the time walk may be considerably be modified. The aim of the Z parameter modification is to obtain a smooth time walk curve without compromise of the time resolution. Section 3.2 explains the operation of the Constant Fraction Discriminator employed in this work. Section 3.2 also provides the details of the optimization procedure of the zero-crossing (Z) and external CFD delay parameters. List-mode timing data were collected at $^{60}$Co energies and at $^{22}$Na (511 keV) for every LaBr$_3$(Ce) detector, and sorted and analyzed off-line as described in Section 3.4.

## 3.2 The ORTEC 935 Constant Fraction Discriminator

The signals from the LaBr$_3$(Ce) detectors are fed into an analog processing chain. Despite digital CFD triggering methods do exist since many years ago, analog CFD modules remain as the preferred option due to their superior timing performance. Nevertheless, recent work [STVC$^+$16] shows very competitive timing results using fully digital systems in combination with triggering algorithms optimized by machine learning methods.

For the timing signals, the Constant Fraction Discriminator (CFD) plays an important role. It determines the precise arrival time of the incoming signals independently of their amplitude with a low time walk. Pulses are always triggered at the same signal rise time fraction. In the experimental setups discussed in this thesis, the selected CFD units are analog ORTEC 935 modules. They were selected because of their proven capability of working with very fast scintillators yielding excellent time resolution in addition to time walk below +50 ps over a 100:1 dynamic range [ORT]. The ORTEC 935 CFD is furnished with extra features that considerably broaden its utility, such as the leading edge (LE) triggering mode, the low-level threshold for noise rejection, the walk adjustment control (Z) and the zero-crossing monitor [ORT]. The most relevant parameters regarding the timing performance are the external CFD delay and the CFD zero-crossing value (Z). To deal with the very fast pulses providing optimal time resolution, the ORTEC 935 CFD is equipped with an especial transformer (XFMR) for constant-fraction shaping and a selectable internal delay of −1 ns (W1). The total shaping delay corresponds to the sum of the external delay, which is implemented as a LEMO cable at the CFD front panel and the internal delay selected with the W1 jumper. The use of very short total delays of 0.6 ns or shorter has made it possible to obtain time resolution values never achieved before. Contrary to other CFD models, the attenuation fraction is fixed to a value of 20 %.

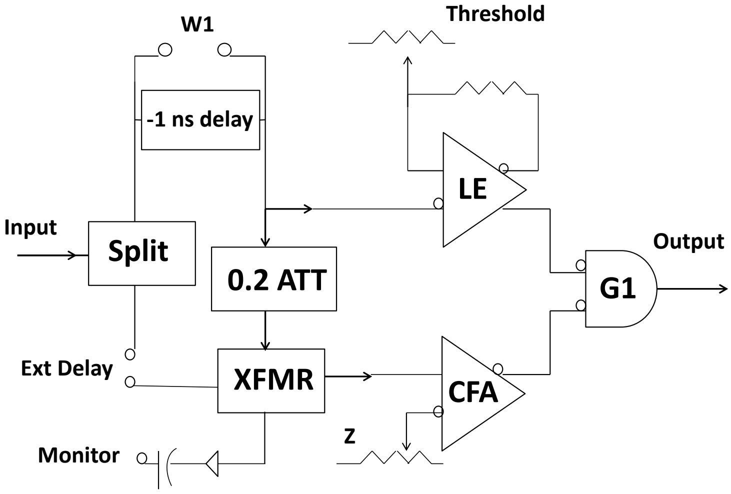

**Figure 3.1: Simplified block diagram of the ORTEC 935 CFD.** - Simplified block diagram illustrating the operation of the ORTEC 935 CFD, adopted from [ORT, VMF$^{+}$15].

Figure 3.1 is a simplified block diagram of the ORTEC 935 that explains in a schematic way how the ORTEC 935 works. The input signal is split into two pulses: the first one is attenuated by the 20% fixed factor and "delayed" by −1 ns when the W1 jumper is removed, while the second one is inverted and retarded by the CFD external delay before entering the constant fraction transformer. Inside the XFMR comparator, both signals are added together resulting in a bipolar pulse whose zero crossing indicates the arrival time of the incoming signal. When the external delay is shorter than 1 ns, there is no bipolar output from the XFMR, and consequently, the module operates as a leading edge (LE) comparator, triggering the incoming signals when they cross the adjusted threshold.

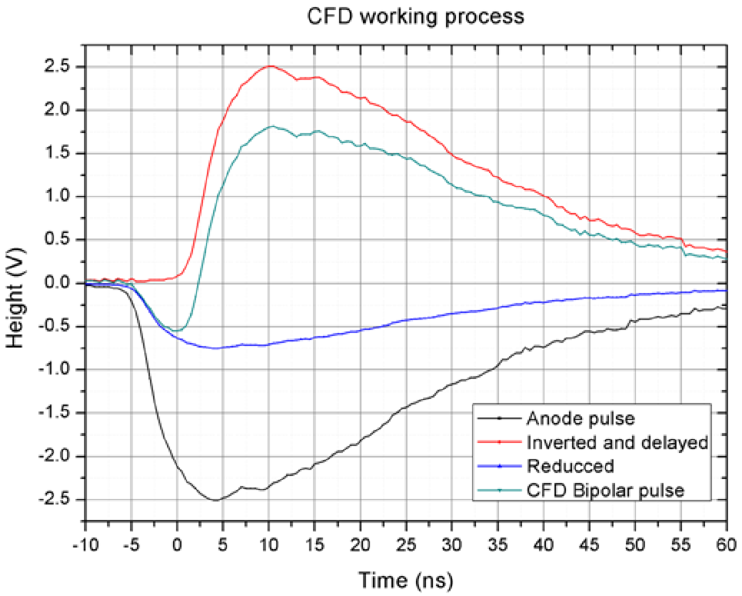

**Figure 3.2: Example of working principle of the Constant Fraction Discriminator.** - An illustrative example of the Constant Fraction triggering method. The negative incoming signal (black) is divided in two signals. The first one is attenuated by 20% and "delayed" $-1$ ns (blue). The second one is inverted and retarded by the CFD external delay (red). The pulse in green is the CFD bipolar signal that corresponds to the sum of the blue and the red signals and whose zero crossing indicates the arrival time incoming signal.

Time walk, drifts and time jitter are the most common problems that deteriorate time resolution when a leading edge discriminator methods are used. Nevertheless, when the pulse rise time is sharp enough with no jitter, the leading edge triggering method may be very efficient. This fact has been investigated in detail for one of the cylindrical 1 in. × 1 in. crystals by the operation of the ORTEC 935 in either LE or CFD mode.

To adjust the external CFD delay and zero-crossing we have followed an iterative procedure, starting by the external CFD delay and followed by a fine tune of the zero-crossing value (Z). During the optimization process the internal delay $W1$ jumper was removed, setting an internal delay of $-1.0$ ns, *i.e.* when the external delay is set at

4.0 ns, the total CFD delay used for the CFD triggering procedure corresponds to 3.0 ns. The starting value of the external CFD delay for the optimization procedure was taken as the anode rise time at 662 keV, which is typically a value of the order of 5 to 6 ns (measured from 10 to 90% of the signal amplitude), see Figure 3.2. The range of tested external delays in this work is wide, ranging from 0.5 to 20 ns. Care must be taken when very short external delays like 1.5 ns are set since the time walk becomes very sensitive to the Z value. Despite that the time resolution does not significantly vary for different Z values, important modifications may happen on the time walk. The aim was to obtain a smooth time walk curve without compromise of the time resolution.

## 3.3 Experimental setup for crystals characterization

The time characterization of the $LaBr_3$(Ce) detectors was performed by coincidence measurements against a well-known $BaF_2$ crystal that acted as a reference. The $BaF_2$ detector is a small truncated cone crystal with an ultra-fast response of ∼80 ps FWHM time resolution for $^{60}$Co. It is coupled to the Photonis XP2020-URQ PMT model by silicon grease to favour light transmission and wrapped into opaque tape to avoid photon losses. The high voltage applied to the XP2020-URQ photomultiplier tube has been tuned to the best performance in terms of time response, −2300 V.

The time resolution of the reference $BaF_2$ detector was measured by the use of three identical $BaF_2$ detectors with an equal response coupled to XP2020-URQ photomultipliers chosen with very similar parameters. The use of three $BaF_2$ detectors measuring their combine time resolution in pairs allow to derive the time resolution of every individual $BaF_2$ detector. By assuming a Gaussian time response for the detectors, the time resolution of one unit is 83±2 ps at $^{60}$Co energies and 125±2 ps at $^{22}$Na energies (511 keV ). These values were used to de-convolute the time resolution of the $LaBr_3$(Ce) detectors under study. Slight deterioration of the time response may arise in the long term due to noise, ageing and other factors. Therefore the time resolution of the reference detector was monitored throughout the entire period of measurements (which spanned over months). The monitoring measurements at $^{60}$Co energies yielded time resolution for a single detector ranging from 81.5±1.5 ps at the beginning of the measurements to 84.4±1.5 ps. The stability of the setup against short-term electronic drifts was monitored as well. When it was necessary, it was corrected in the off-line analysis, but in any case instability corrections were found to be below 2 ps.

Both detectors, the reference and the one under study, were fixed to an aluminium frame aligned and held very close to each other, with the radioactive source placed in between them. Figure 3.3 illustrates part of the test bench used for crystals characterization. The detector on the left corresponds to the one under test, which is composed of a $LaBr_3(Ce)$ crystal and the Hamamatsu R9779 PMT model. The one on the right-hand side is the $BaF_2$ reference crystal coupled to the Phonics XP2020-URQ.

The negative anode signals from both PMT are used for timing measurements, directly fed to an ORTEC 935 Constant Fraction Discrimination (CFD), where the timing of every signal is determined by the constant fraction or by the leading edge methods. The CFD outputs were sent to an ORTEC 567 Time to Amplitude Converter (TAC), which provides square pulses whose height corresponds to the time difference between the start and the stop signals. The ORTEC 567 TAC allows performing timing spectroscopy in the range from 10 ns to 2 ms with a FWHM time resolution below 0.01% of the full scale plus 5 ps for all ranges, that is 10 ps for the 50 ns range. It has an excellent temperature stability and integral linearity. In this setup, the $BaF_2$ signals act as the start at the TAC, while the pulses from $LaBr_3(Ce)$ detectors work as the stop. The intrinsic resolution of the TAC and ADC electronics was measured to be of the order of 16 ps. For this purpose, the same signal was split and used as the start and stop of the TAC module. This makes the time resolution of the electronics negligible with respect to that of the scintillator detectors and it will be ignored in the following.

The last dynode signals were used for energy measurement. They were processed firstly by an ORTEC 113 preamplifier and then by a TENNELEC TC 247 spectroscopic amplifier module. The output TAC pulses and the two energy signals out of the amplifiers are digitized by standard NIM ADC modules. The digitization in the three peak ADCs is controlled by a window generated by means of a Gate and Delay Generator triggered by valid events in the TAC. Figure 3.3 includes the schematics of the setup.

The data were stored in list-mode for the analysis. Timing measurements were performed at $^{60}$Co and $^{22}$Na $\gamma$-ray energies, while the energy resolution of the crystals was calculated by using a $^{137}$Cs source (662 keV).

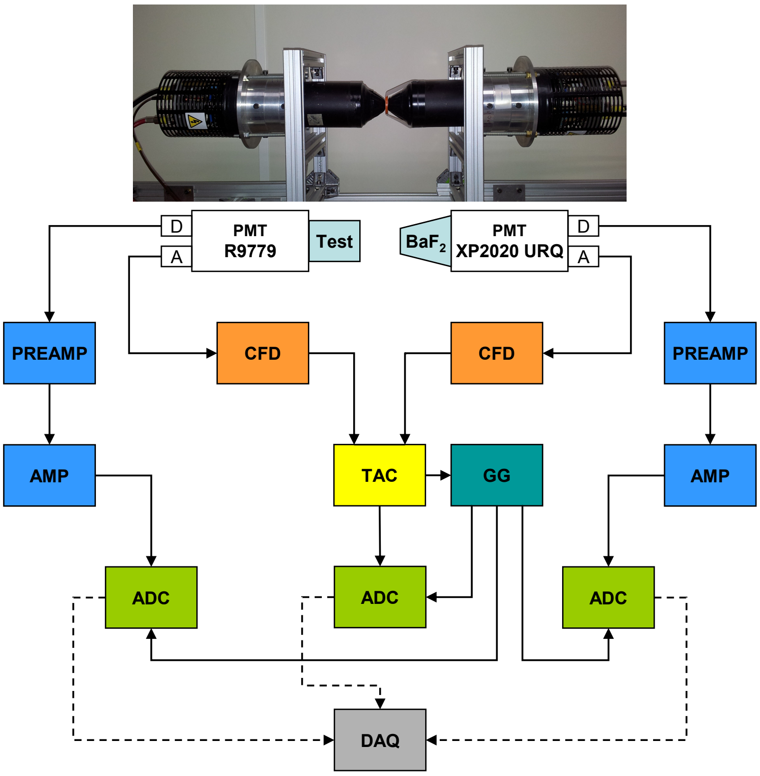

**Figure 3.3: Test bench for crystal characterization.** - Picture of the experimental setup with the crystal under test on the left and the truncated cone $BaF_2$ reference detector on the right. The schematics of the experimental setup for crystal characterization is below. The anode signals (negative) from both detectors, the one under test and the reference are directly connected to the ORTEC 935 (CFD). Both output signals from the CFD are directly fetched into the ORTEC 567 (TAC). The signal from the reference detector acts as the start in the TAC, while the crystal under test as the STOP. The dynode signal (positive) is used for energy measurements, once preamplified in an ORTEC 113 preamplifier and amplified in a Tennelec TC amplifier.

## 3.4 Analysis of the list-mode data

The timing analysis of the list mode data was performed by means of the SORTM software, which was especially programmed by Henryk Mach for this purpose [Mac12]. Because the electronics are temperature sensitive, the first step consists in the correction of possible drifts that may arise due to temperature variations. To address this problem, the correction procedure consists firstly in setting a broad energy gate in the energy spectra on both detectors and secondly in calculating the FWHM and centroid position of the coincidence time spectrum. For $^{60}$Co, the initial broad energy windows include both the 1173- and 1332-keV peaks in the energy spectra on both detectors. For the $^{22}$Na source, the broad gate comprises the 511 keV peak. Afterwards, the calculated coincidence time spectrum is subdivided into consecutive data groups each composed at least of 1000 events in its partial time spectrum. For every partial spectrum, typically 7 to 10, the FWHM and centroid are determined and compared to the values measured for the total time distribution. The differences give an indication of the pattern of instability shifts due to short-term drifts of the electronics. Instabilities are corrected by shifting the partial spectra by its position and summing spectra together. For about 80% of the cases, the partial drifts were below 3 ps, the instability correction was minor and therefore the FWHM for the shifted summed spectrum was the same as for the initial uncorrected spectrum. Regarding the rest of the cases, the correction produced effects below the sigma uncertainty of the measurement. For the cases where the calculated shifts were significant the measurements were simply repeated.

The second step in the analysis procedure after having to correct by the temperature drifts consists in the offline energy gate selection on full energy peaks (FEP) in each detector. For the $^{60}$Co source, gates are set at the 1173 and 1332-keV peaks, by setting the width at a tenth of the maximum. Consequently, there are two time spectra calculated, one for each of the two possible combinations: when the 1173-keV FEP is selected in the $BaF_2$ and the coincident 1332-keV FEP is measured by the $LaBr_3$(Ce) detector, and when the reversed combination is selected. The reported time resolution for $^{60}$Co energies is given for the summed spectrum. For the $^{22}$Na source, narrow gates are set at the full width at half maximum (FWHM) of the 511-keV peak, generating only one time spectrum.

The FWHM values measured out of $^{60}$Co and $^{22}$Na time spectra corresponds to the coincidence resolution time (CRT), and encompasses the time contribution of the reference $BaF_2$ detector and the $LaBr_3$(Ce) detector under test. Hence, to calculate the individual $LaBr_3$(Ce) time resolution it is necessary to deconvolute the CRT by the $BaF_2$ contribution. The reported values of $LaBr_3$(Ce) time resolution in this thesis refers to the individual $LaBr_3$(Ce) FWHM time resolution.

## 3.5 The LaBr$_3$(Ce) detectors

Due to their hygroscopicity, the LaBr$_3$(Ce) crystals are hermetically sealed inside an aluminium housing with a thin aluminium window at the entrance and a glass light guide fitted at the coupling side to the photosensor. In order to protect the crystal, there are several layers of light reflector and shock absorbing material inside the housing case to assure the stability of the crystal and minimize photon losses. Crystals were coupled to the R9779 PMT window by Viscasil silicon grease and wrapped into opaque tape. To ensure the detector assembly crystals were held to the PMT by a coupling aluminium ring, which fixes the crystal position.

In this work, we study three cylindrical crystals of the standard size of 1 inch, with different nominal Ce doping, and two crystals of specially designed geometries, a truncated-cone crystal and a hybrid tapered crystal with a cylindrical and a conical section.

### 3.5.1 Cylindrical LaBr$_3$(Ce) crystals

The three cylindrical crystals were labeled as $A$, $B$ and $C$, an increasing amount of Ce doping. The first one to be produced by company Saint-Gobain was Crystal $C$, it was grown in 2006 as a test crystal with enhanced Ce doping concentration of 10%, while standard LaBr$_3$(Ce) crystals are commercially produced with a 5% of Ce doping. The purpose of the Ce enhancement was to study the Ce effect on the scintillating properties since it was reported that the time resolution of the LaBr$_3$(Ce) crystals improves with the amount of Ce doping [GMH$^+$05]. Crystal $A$ was produced by Saint-Gobain in the same year as Crystal $C$ as a standard crystal of 5% of doping concentration using the conventional crystal growth and production techniques. Due to this fact crystal $A$ can be considered as the standard LaBr$_3$(Ce) reference for benchmarking other crystals. Finally, crystal $B$ was the latest to be manufactured, by company EPIC. It was grown at the end of 2012 with 8% of Ce doping. This crystal was aimed at achieving a good balance between increased doping and homogeneity for medium-sized crystals. Figure 3.4 provides an example of the anode pulses of Crystal $A$ when coupled to the Hamamatsu R9779 PMT.

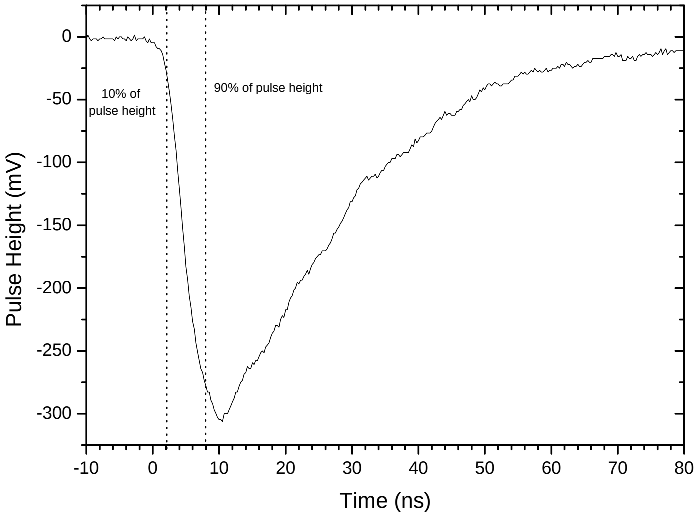

**Figure 3.4: Anode pulse of Crystal *A* coupled to Hamamatsu R9779 PMT model.** - Anode pulse of Crystal *A*+Hamamatsu R9779 acquired with 2 Gsa/s 1 GHz oscilloscope. The used source is a standard $^{137}$Cs and the PMT bias voltage $-1000$ V. The anode rise time taken from 10% to 90% of the maximum pulse height is about 6 ns.

### 3.5.2 Innovative designs of LaBr$_3$(Ce) crystals: Truncated cone and hybrid-tapered geometries

The two innovative geometries of LaBr$_3$(Ce) crystals presented in this work were specially designed to enhance the collection of the scintillation light inside of the crystal, and thus the timing features. The two geometries are also aimed at the construction of efficient LaBr$_3$(Ce) arrays thanks to their versatility and the packing factor. It is important to underline that that LaBr$_3$(Ce) crystals of this size and geometry were produced for the first time for this purpose, representing a challenge for the manufacturer (Saint-Gobain) to machine them out of the raw material and to properly polish them before encapsulation.

The first design is a truncated cone shape crystal, with a nominal height of 38.1 mm (1.5 in.) and bases of $\oslash$= 38.1 mm (1.5 in.) and $\oslash$=25.4 mm (1 in.). Figure 3.5 shows the geometry of the truncated cone crystal and the dimensions as provided by the manufacturer. In order to obtain precise geometric information, a detailed CT scan of the LaBr$_3$(Ce) crystal has been performed, also presented in Figure 3.5. The dimensions measured from the CT scan are marginally smaller than the nominal ones, with a reduction of at most 1 mm in the diameter of the bases, which is the estimated uncertainty in the measurement of distances in the CT images. The CT image also reveals the presence of Silicon-based disks placed just below the entrance window of the crystal case. It is believed that the disks have a protective and packing function, however, they were not reported by the manufacturer and they may influence the absorption of low-energy $\gamma$-rays.

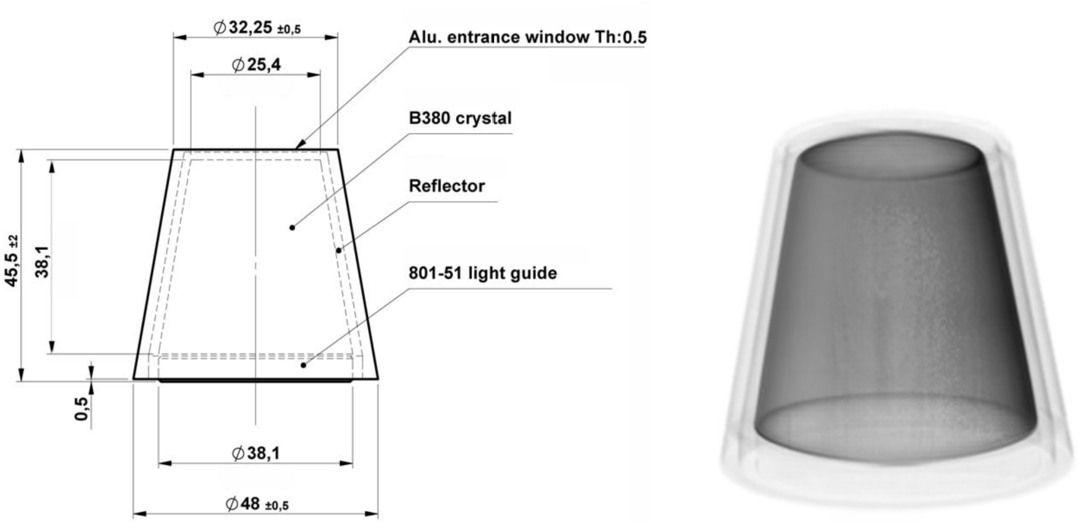

**(a)** **(b)**

**Figure 3.5: Truncated cone LaBr$_3$(Ce) crystal.** - LaBr$_3$(Ce) crystal with the shape of a truncated cone. The dimensions of the crystals in mm are given as provided by the manufactured. On the right hand side a CT scan of the crystal is shown.

The second geometry is based on the advantageous "Studsvik" design for BaF$_2$ crystals [MF14]. It is a tapered hybrid crystal with a total height of 47 mm, a cylindrical section of nominal $\oslash$=38.1 mm in the base and 16.5 mm in height, and a 30.5 mm long conical section with $\oslash$=19 mm in the small base. Figure 3.6 illustrates the geometry of the detector and shows the nominal dimensions as provided by the manufacturer. A CT image is also shown on the right-hand side of Figure 3.6. For the tapered LaBr$_3$(Ce) crystal it was found that the actual dimensions turn out to be significantly smaller than the nominal ones, with bases of $\oslash$=36.5 mm and $\oslash$=16.5 mm, and the length of the conical section of 29.5 mm. Despite the differences between the nominal and actual dimensions are apparently not very significant, they have a sizeable effect in the detection efficiency, as discussed below. The CT of this crystal also shows Si disks under the entrance window.

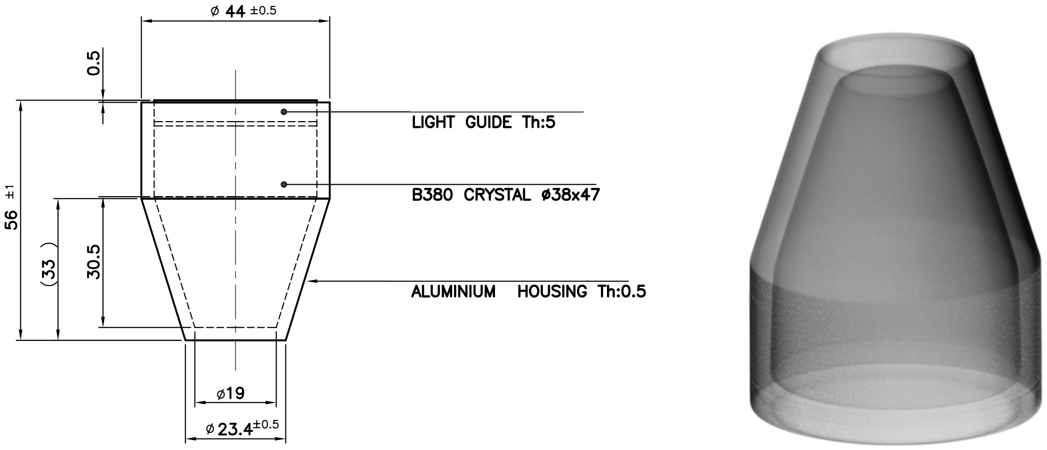

**(a)** **(b)**

**Figure 3.6: Hybrid LaBr$_3$(Ce) crystal.** - Tapered geometry of the LaBr$_3$(Ce) crystal (Studsvik's design) with a conical and a cylindrical section. The dimensions of the crystal in mm are given by Saint-Gobain. On the right hand side a CT scan of the crystal is shown.

## 3.6 Study of the cylindrical LaBr$_3$(Ce) detectors

In this section, we present the performance characterization of the cylindrical LaBr$_3$(Ce) detectors, identical in shape but produced with distinct Ce doping concentration. The objective is finding the optimal parameters that yield the best time response in terms of resolution, without spoiling the performance regarding energy resolution and linearity. As discussed above a suitable high voltage to bias the PMT is in the range from −1200 V to −1300 V. In this voltage range, the energy resolution and the linearity are well preserved in addition to the good time response.

### 3.6.1 Energy resolution

The energy resolution of the three LaBr$_3$(Ce) detectors was measured at the PMT bias voltages that provide the best time resolution using a standard $^{137}$Cs source (662 keV). This source is used because it possesses a single $\gamma$-ray, and it serves as a good reference.

We report here the energy resolution of the three $LaBr_3(Ce)$ detectors as the ratio between the FWHM of the $\gamma$-ray full energy peak and its corresponding energy corrected by non-linearity (Section 3.1.3. The measured values for Crystals $A$, $B$ and $C$ are 3.4 %, 3.4 % and 4.0 % respectively. These values are slightly worse than the 2.8% quoted by the manufacturer as a consequence of the use of the R9779 PMT, which is optimized for timing measurements and provides the best time response at the expense of worse energy resolution. As mentioned before to obtain a measure of this effect, Crystal $A$ was also tested by means of Hamamatsu R6231 PMT, which has been designed for energy measurements. The energy resolution measured at 662 keV is 2.9%, matching the specifications. Table 3.1 summarizes the relative energy resolution values of the three crystals and the two PMT models that were employed (R9779 and R6231). The values are expressed in per cent with an estimated error of 0.1 %.

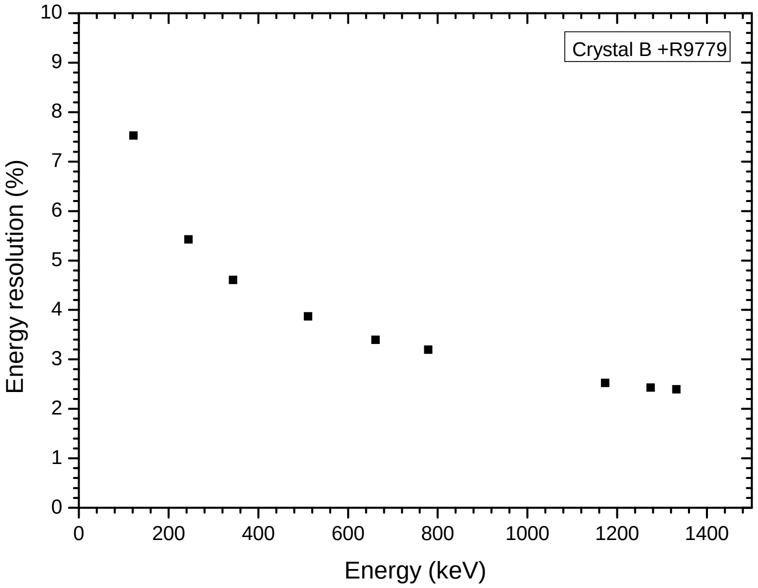

**Figure 3.7: Relative energy resolution of Crystal $B$ coupled to R9779 PMT as a function of the energy.** - Relative energy resolution of Crystal $B$ coupled to Hamamatsu R9779 as a function of the energy. The PMT is operated at the PMT bias voltage that provides the best timing performance, $-1300$ V.

In addition to 662 keV, the energy resolution of the $LaBr_3(Ce)$ crystals was also measured at different energies, in the range from 122 to 1332 keV, using standard calibration sources. Figure 3.7 presents the energy resolution of Crystal *B* coupled to Hamamatsu R9779 PMT at different energies. The measured trend is almost identical for the three crystals (A, B and C), therefore it is significant enough to provide data from one of the detectors.

| Crystal | Ce (%) | PMT | HV(V) | Er (%) |
|---|---|---|---|---|
| A | 5 | R9779 | 1300 | 3.4 |
| A | 5 | R6231 | 1000 | 2.9 |
| B | 8 | R9779 | 1300 | 3.4 |
| C | 10 | R9779 | 1200 | 4.0 |

**Table 3.1: Relative energy resolution of cylindrical crystals at 662 keV.** - Relative energy resolution (Er) of Crystals A, B and C measured at $^{137}$Cs energy (662 keV). The uncertainty in the values is 0.1%. The crystals were coupled to Hamamatsu R9779 and R6231 PMT models.

Regarding the Ce concentration, Crystals *A* (5% of Ce) and *B* (8% of Ce) display the same energy resolution value, while Crystal *C*, with a 10% nominal Ce concentration, shows the worst value among the three, 4.0%. The photon yield for crystal *C* is ∼8% lower than for crystal *A*, in agreement with [GMH$^+$05], but also the photon yield for crystal *B* with 8% Ce doping and same energy resolution as *A* is higher than for crystal *A* by ∼10%. Given that the contributions to the intrinsic resolution are the non proportional response (which is low for $LaBr_3$(Ce) [SGK$^+$03]) and the inhomogeneities, which cause local variations in the scintillation light output [DdHvE95], the main reason for the worse energy resolution for the highly doped crystal *C* might be explained by Ce inhomogeneities inside the crystal.

### 3.6.2 Energy linearity

The three $LaBr_3$(Ce) detectors behave linearly over the analyzed energy range, and especially at PMT voltage values from −900 V to −1300 V. Small deviations from linear behaviour appear at −1300 V, where the best time resolution is achieved. At higher voltages than −1300 V the behaviour deviates significantly from linearity. It can be seen that the three detectors display the same response, supporting the idea that the main contribution is the PMT gain variance [DdHvE95].

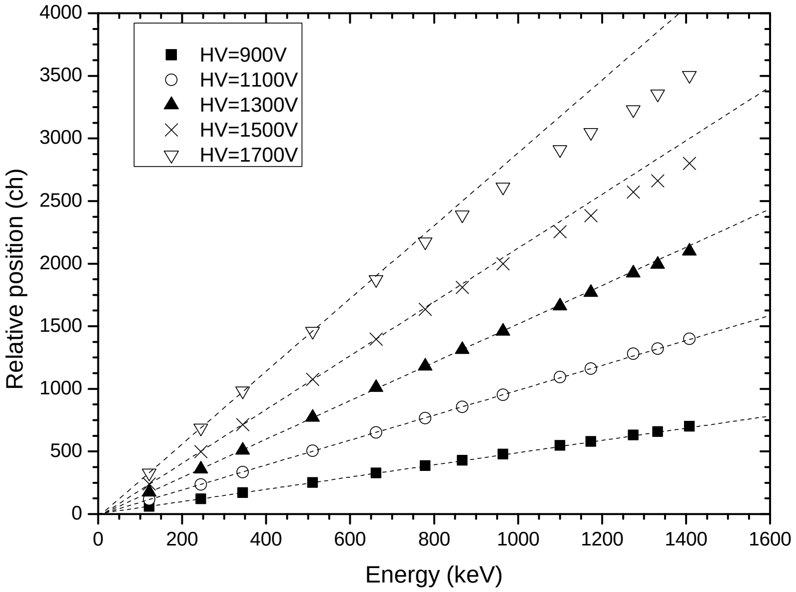

**Figure 3.8: Functional relation between the peak position and the $\gamma$-ray energy that illustrates the detector linearity.** - Functional relation between the peak position and the $\gamma$ energy measured at five different PMT bias voltage. The detector in use corresponds to the assembly of Crystal B coupled to R9779 PMT that was operated at $-1300$ V. To give a measure of the deviation from linear behaviour the first 4 points of each data set were linearly fitted.

Figure 3.8 shows the signal amplitude (peak position) versus the $\gamma$-ray energy for Crystal $B$ measured at different PMT voltages. To illustrate the departure from the linear behaviour only the first four points of each data set were linearly fitted, and the fit was extrapolated up to 1600 keV. It should be underlined that at the operational voltage giving the best timing performance, both the energy resolution and linearity of the LaBr3(Ce)+R9779 detectors are good, and thus well suited for spectroscopic experiments.

### 3.6.3 Gamma-ray detection efficiency

The $\gamma$-ray detection efficiency has been measured for the three crystals (A, B and C) at several distances from the entrance window. Since the result is almost identical for the three detectors Figure 3.9 illustrates the results for one of them, Crystal B, coupled to the R9779 PMT at the distances of 20, 40, 100 and 150 mm. The energy range spans 122 to 1408 keV, using the standard $^{152}$Eu source.

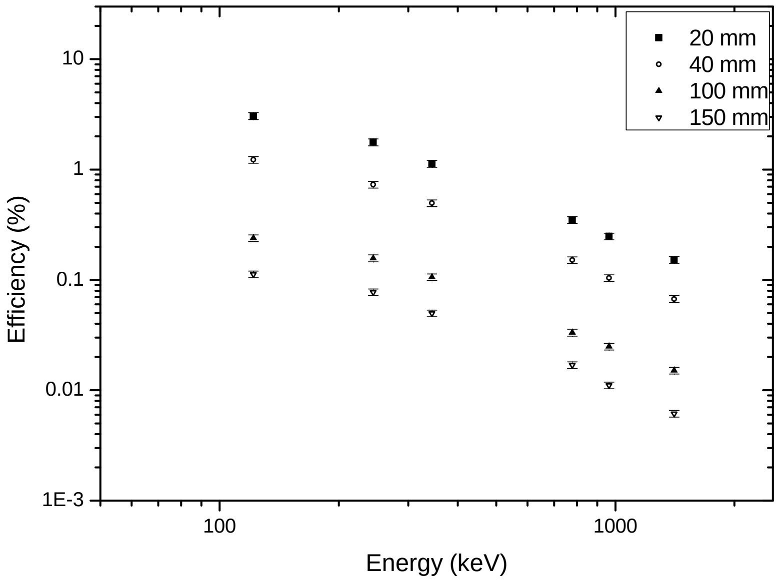

**Figure 3.9: Full-energy peak (FEP) detection efficiency of a 1-inch cylindrical crystal.** - Full-energy peak detection efficiency measured at 20, 40, 100 and 150 mm from the entrance window, in the range from 122 to 1408 keV. The detector is Crystal B coupled to Hamamatsu R9779 PMT, which was operated at −1300 V.

### 3.6.4 Time response: time resolution

The three detectors achieve the best timing performance when the Hamamatsu R9779 PMT is operated in the bias range from −1200 to −1300 V. It was found that the time resolution is not considerably affected by the PMT bias voltage, the response is nearly flat. There is only a small variation below 5 ps between the best and the worse values in the ample range from −1100 to −1700 V. In the following, the time resolution is reported for the optimal high voltage.

The time resolution of crystals $A$, $B$ and $C$ has been optimized through an iterative procedure, leading to the outstanding values of 106±2, 98±2 and 107±2 ps respectively. These values are achieved when very short CFD external delays around 1.6 ns are set at the ORTEC 935 (see below). Table 3.2 summarizes the aforementioned values, which were measured at $^{60}$Co energies, together with those obtained at 511 keV ($^{22}$Na).

| **Crystal** | **External Delay (ns)** | **HV (V)** | **ORTEC MODE** | **FWHM $^{60}$Co (ps)** | **FWHM $^{22}$Na (ps)** |
|---|---|---|---|---|---|
| A | 1.6 | 1300 | CFD | 110±2 | 164±2 |
| A | 0.8 | 1300 | LE | 106±2 | 158±2 |
| B | 1.6 | 1300 | CFD | 98±2 | 148±2 |
| C | 1.6 | 1200 | CFD | 107±2 | - |

**Table 3.2: Best time resolution values (FWHM) of Crystals A, B and C at $^{60}$Co and $^{22}$Na (511 keV) energies.** - Best values of FWHM time resolution for Crystals A, B and C at $^{60}$Co and $^{22}$Na (511 keV) energies. The zero crossing value (Z) is set at 2.0 mV and the CFD threshold at $-508$ mV.

The best time resolution among the three crystals is achieved with Crystal *B*, which was the last one produced and contains 8% of Ce. The excellent value of 98±2 ps at $^{60}$Co energies is the best time resolution value quoted to date for crystals of this size. It is expected that this figure could be further improved with full-fledged digital algorithms for signal processing. Figures 3.10 and 3.11 present the time spectra of Crystal B coupled to R9779 for $^{60}$Co and $^{22}$Na (511 keV) energies. For these measurements, the reference BaF$_2$ detector gave FWHM resolutions of 81±2 ps and 120±2 ps for $^{60}$Co and $^{22}$ Na, respectively. The FWHM resolution of Crystal *B* is deconvoluted from the total FWHM resolution of 190 ps for $^{22}$Na source and 127 ps using a $^{60}$Co source.

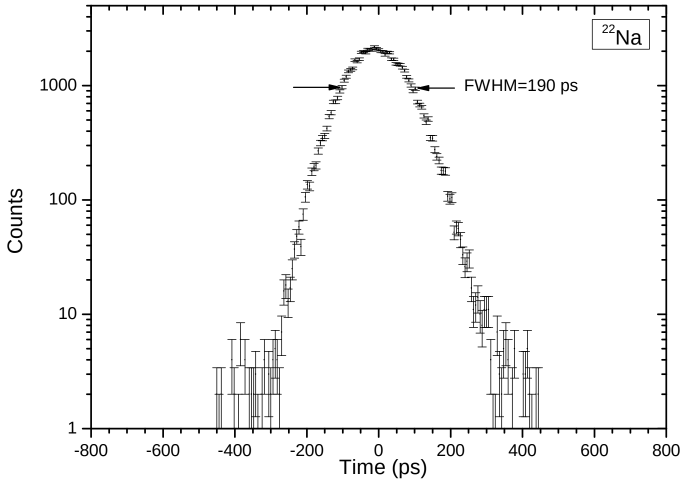

**Figure 3.10: Time resolution of 1-in LaBr$_3$(Ce) detector at 511 keV. -** Time spectrum for Crystal B+R9779 against the reference BaF$_2$ detector measured at 511 keV with a $^{22}$Na source. The FWHM resolution of 190 ps is the convolution of 120±2 ps from the reference detector and the 148±2 ps from the LaBr$_3$(Ce) unit.

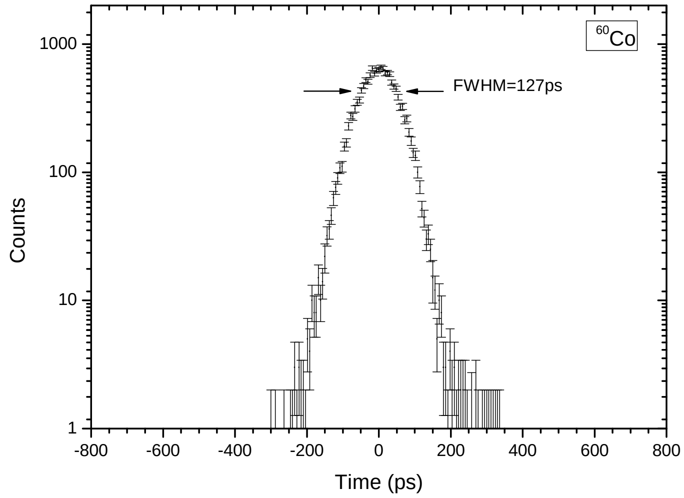

**Figure 3.11: Time resolution of 1 in LaBr$_3$(Ce) detector at $^{60}$Co energies.** Time spectrum for Crystal B+R9779 against the reference BaF$_2$ detector measured at $^{60}$Co energies. The FWHM resolution of 190 ps is the convolution of the contributions from the reference detector of 120±2 ps and the LaBr$_3$(Ce) unit of 148±2 ps.

Concerning the CFD external delay, a wide range going from 0.5 to 20 ns was explored. The best time resolutions are measured for very short CFD external delays, which are longer than 1.4 ns and shorter than 1.8 ns, and the optimal value is achieved at 1.6 ns. To measure these values in steps of 0.1 ns cables and connectors of different lengths have put together and calibrated by measuring the centroid position of the time spectrum in the TAC. For longer values of external CFD delay, this good value deteriorates by more than 50%. One should keep in mind that the W1 jumper from the ORTEC 935 was removed during the entire measuring (Section 3.2). Hence, the total delay for the CFD triggering is 1 ns shorter than the selected external delay.

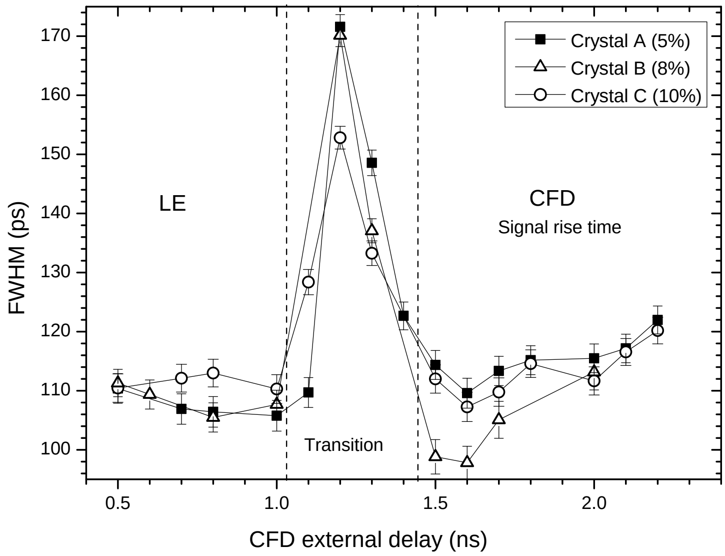

**Figure 3.12: Time resolution of Crystals *A*, *B* and *C* as a function of the CFD external delay at $^{60}$Co energies.** - Time resolution of Crystals *A*, *B* and *C* as a function of the external delay measured at $^{60}$Co energies. The plot shows the values obtained when using very short delays. Detectors *A* and *B* were operated at −1300 V and *C* at −1200 V. The CFD settings correspond to Z=2.0 mV and Th=−508 mV.

Figure 3.12 presents the FWHM time resolution of the three crystals *A*, *B* and *C* as a function of the CFD external delay from 0.5 to 2.2 ns. The time resolution in the total explored range is shown in Figure 3.13 for Crystal B, as representative of the three similar detectors. Depending on the selected value of external delay there are

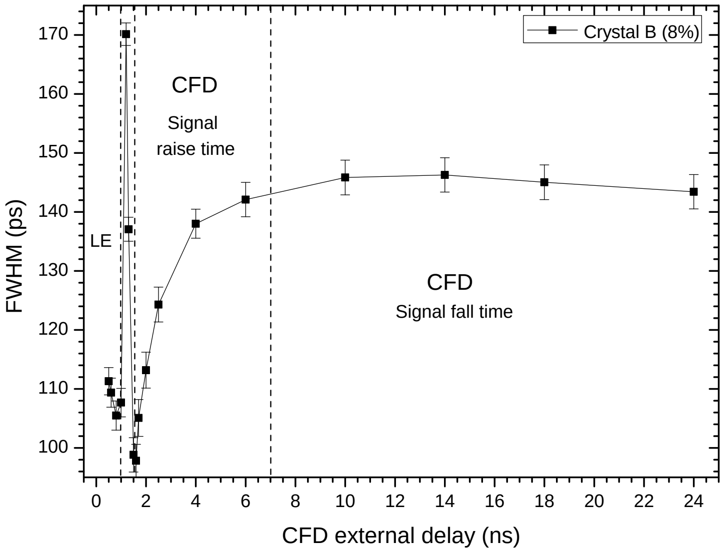

**Figure 3.13: Time resolution of Crystal *B* as a function of the CFD external delay at $^{60}$Co energies.** - Time resolution of Crystal *B* as a function of the CFD external delay measured at $^{60}$Co energies. The plot presents the full range of CFD external delays explored in this work. Detector *B* was operated at −1300 V and the CFD settings correspond to Z=2.0 mV and Th=−508 mV.

four distinct operation regions of the ORTEC 935, as one can identify from Figures 3.12 and 3.13.

When the external delay is shorter than 1 ns (0.5−0.8 ns) the 935 unit triggers as a level discriminator providing good time resolutions independently of the external delay and comparable to that obtained by the CFD triggering procedure. This is possible because the incoming pulses have a sharp rise time and low level of jitter. The leading edge triggering fractions were also investigated here in order to achieve the best values of FWHM time resolution. The optimal leading edge triggering level is reached when the threshold control at the ORTEC 935 is set at −508 mV, equivalent to a real input voltage level of 64 mV. At our operation bias, this corresponds to a 3.75% of the anode pulse height for $\gamma$-rays of 1332 keV. Secondly, there is an unstable region between 0.9 and 1.3 ns where the time resolution severely increases, as a consequence of the regime transition. The operation of the module in this mode should be avoided. Thirdly, for external delays longer than 1.4 ns, the ORTEC 935 operates as a CFD discriminator. As already discussed, in this regime the time resolution achieves a minimum at 1.6 ns for the three crystals, and afterwards, it smoothly increases until it reaches a fairly constant value of FWHM for external delays larger than 7 ns (effective shaping delay equal to the pulse rise time, 6 ns). Finally, for large delays the CFD triggers on the decay of the time pulses, yielding an almost flat behaviour of the time resolution, but at the expense of worse values, which reach (146±2 ps) at 14 ns for Crystal *B*.

We note that the best time resolution of Crystal *A*, which is 106±2 ps, is obtained when the ORTEC 935 triggers as a LE discriminator, while the value increases up to 110±2 ps when the module works as CFD discriminator. This is due to the anode pulses that lack of time jitter and present very steep rise time (see Figure 3.4). Hence, in this case, the LE trigger mode performs as good as the CFD. For crystals *B* and *C* the values in LE operation mode are close to the best CFD mode FWHM values, showing that leading edge operation is viable whenever the time walk is not relevant.

If we now turn to the comparison of these LaBr$_3$(Ce) crystals of the same size, and the influence of the Ce concentration, it is expected that, in contrast to the energy resolution, the time response improves when Ce doping is increased above 5% [GMH$^+$05]. Crystal *B*, which contains an 8% of dopant, gives a superior time resolution (about 10% better) than Crystals *A* and *C*, even though the nominal doping concentration of crystal *C* is higher (10%). In connection with the influence on the energy resolution discussed above a possible explanation may be a non-uniform distribution of the Ce inside the scintillator, since it was grown as a test crystal when the production technique was not as developed as it is now. Local variations in the scintillation light output may affect the timing response.

The values of time resolution achieved in the present thesis for Crystals A, B and C are the best reported to date for a standard cylindrical 1-inch LaBr$_3$(Ce) crystal [Mos06]. This has been possible thanks to the use of the Hamamatsu R9779 PMT in conjunction with the ORTEC 935 CFD at very short delays. The excellent time resolution of 98±2 ps at $^{60}$Co energies may push forward the application of fast-timing methods in nuclear spectroscopy.

### 3.6.5 Time response: time walk

The time adjustment of the zero crossing potentiometer in the 935 CFD only produces minor changes in the width of the time distribution. The systematic analysis yields very similar time resolutions for zero crossing parameters from Z=0.0 mV to Z=2.0 mV for a fixed energy value. The best time resolution is measured for Z=2.0 mV.

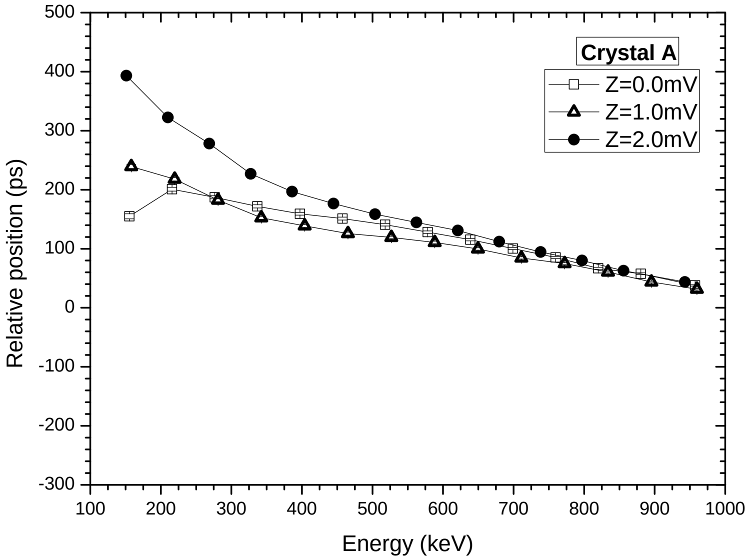

**Figure 3.14: .** - Compton time walk of Crystal *A* coupled to the Hamamatsu R9779 PMT. The detector is powered at $-1300$ V and the external CFD delay is set to 1.6 ns. The zero time reference is given by the position of 1173-keV full energy peak.

However, the Z value does affect the time walk, which needs to be corrected for when the detectors are used in a real experiment in a wide energy range. In order to understand the suitable operational values, it is useful to examine the position of the time spectrum as a function of energy for the different settings. For this purpose, the Compton time walk provides a good approximation of the FEP time walk when using crystals such as those under study here [MWM$^+$91]. Figures 3.14 and 3.15 shows the centroid position of the time distribution as a function of energy for Compton events arising from the 1173-keV $\gamma$-ray from $^{60}$Co, for Crystals *A* (standard) and *B* (enhanced doping of 8%), respectively. As depicted in the figure, positive values of Z yield a smooth time walk, which can be taken care of in the measurements. At the best

Z value for time resolution, the Compton walk is of the order of 300 ps over 1 MeV for Crystal *B*, which is manageable in experimental conditions, specially when a large number of detectors need to be put together in a big array. Although smaller walk can be obtained at a setting of Z=1.0 mV, this is at the expense of a steeper curve at low energies. Crystal *A* has a similar behaviour, but in this case, it is possible to achieve walk of the order of 150 ps/MeV for settings Z=1.0 mV or Z=0.5 mV.

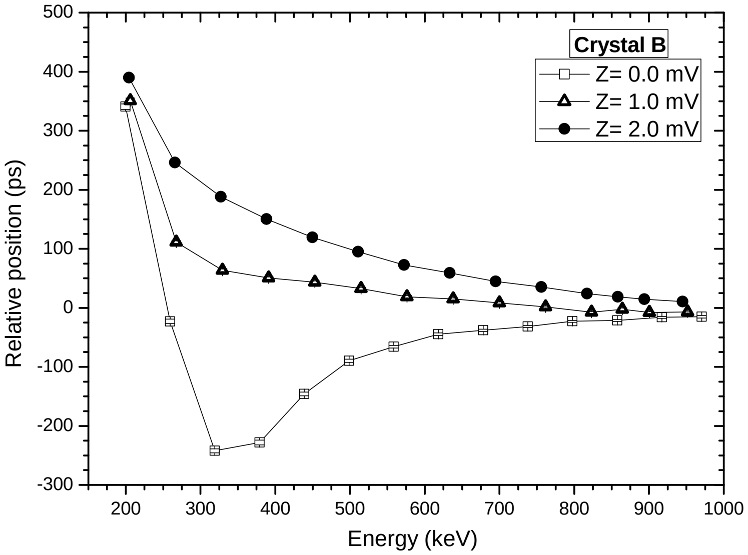

**Figure 3.15: Compton time walk of Crystal *B*.** - Compton time walk of Crystal *B* coupled to the Hamamatsu R9779 PMT. The detector is powered at −1300 V and the external CFD delay is set to 1.6 ns. The zero time reference is given by the position of 1173-keV full energy peak.

## 3.7 Performance evaluation of innovative $LaBr_3(Ce)$ geometries

This section presents the evaluation of the overall performance of the two innovative $LaBr_3(Ce)$ geometries: the truncated-cone crystal and the tapered crystal. Both designs are aimed at enhancing the scintillation light collection and therefore they are expected to provide better timing performance than that of $LaBr_3(Ce)$ crystals of their size. Regarding the energy resolution of both geometries, it is expected that the size of the crystals, which deteriorates the energy resolution, would be compensated by the improved light collection procedure, which enhances it. The $\gamma$-ray detection efficiency of both designs is also evaluated in this section. All these features are relevant for the construction of large arrays of $LaBr_3(Ce)$ detectors.

### 3.7.1 Energy resolution and linearity

The energy resolution of both geometries is characterized with both the Hamamatsu R9779 timing PMT, and the R6231 PMT model, better suited for spectroscopic measurements, as already discussed. Relative energy resolution values ($E_r$) are given here as the ratio between the FWHM of the $\gamma$-ray full energy peak and its energy, corrected for non-linearity effects as explained above in this section. Values reported in this PhD Thesis were measured at PMT bias voltages that provides the best time response. For the R6231 model, it ranges from −900 V to −1000 V and for the R9779 PMT from −1200 V to −1300 V.

| Geometry | Er R9779 (%) | Er R6231 (%) |
|---|---|---|
| Tapered | 4.3 | 3.8 |
| Truncated cone | 4.0 | 3.3 |
| 1-in.. cylinder | 3.4 | 2.8 |

**Table 3.3: Relative energy resolution (Er) of the conical and tapered detectors measured with the Hamamatsu R9779 and R6231 PMT models.** - The Er is given at 662 keV as the ratio between the full width at half maximum (FWHM) and the energy (keV), with absolute uncertainties of the order of 0.1%. Both PMTs were operated at the best performing bias voltage, −1300 V for the R9779 and −1000 V for the R6231. The result for a 1 in. cylindrical crystal is given for comparison.

The best values of relative energy resolution measured at 662 keV are 4.0 % FWHM for the conical LaBr$_3$(Ce) crystal and 4.3% FWHM for the tapered one when the crystals are coupled to the Hamamatsu R9779 PMT. Both values are higher than the 3.4 % measured with the standard 1-in. cylindrical LaBr$_3$(Ce) crystal (Section 3.6.1). This effect was expected, as a result of their larger volume.

Regarding the R6231 PMT, the best relative energy resolutions are 3.3 % for the truncated cone LaBr$_3$(Ce) and 3.8% for the tapered detector. The measured values are much larger than the 2.9% obtained with the standard 1-in. cylindrical LaBr$_3$(Ce) (Section 3.6.1). It is not evident whether the higher values can only be attributed to a volume effect. Figure 3.16 displays the $^{137}$Cs energy spectra measured with the tapered, the truncated cone and the 1-in. cylindrical LaBr$_3$(Ce) crystals coupled to the Hamamatsu R9779 PMT.

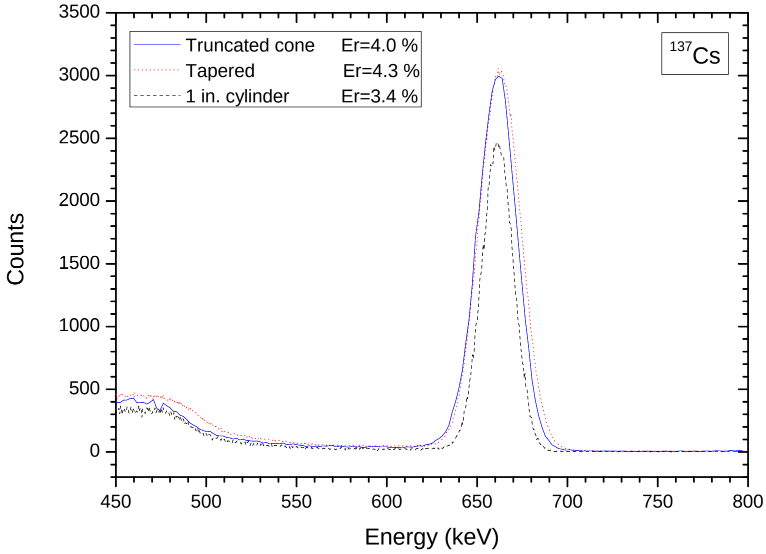

**Figure 3.16: Energy spectra of $^{137}$Cs measured with the truncated cone, the hybrid-tapered and the standard LaBr$_3$(Ce) detectors.** - Energy spectra of $^{137}$Cs measured with the tapered detector (red dots), the truncated cone crystal (solid blue line) and with a reference 1-in. cylindrical crystal (black dashes). All of them were coupled to the R9779 PMT, which was operated at −1300 V. The relative energy resolution values, given as the ratio between FWHM and energy, are provided in the plot.

The energy linearity of the two detectors has also been investigated through the analysis of the functional relation between the peak position (signal amplitude) and the corresponding $\gamma$-ray energy using a $^{152}$Eu source. The dependence is linear up to 1400 keV for high voltages below 1300 V.

### 3.7.2 Gamma-ray detection efficiency

The absolute photopeak efficiencies of the two detectors were measured using the absolutely-calibrated $^{152}$Eu source placed at 100 mm distance from the entrance window of the crystal capsules. Figure 3.17 shows the comparison for both detectors. The experimental error stems from the contribution of 5% in the source activity plus 7% uncertainty from the integration of the peak areas. The uncertainty in the distance from the source to the detector is of the order of 1 mm. The solid lines in Figure 3.17 show the simulated efficiency for the truncated cone (dashed line) and tapered geometries (solid line) taken from [VCGF$^+$17]. They are included in the plot to compare to the experimental measurements. In comparison with the absolute photopeak efficiencies of the standard 1-in. crystals (Section 3.6.3), both geometries are much efficient yielding similar values of time resolution. This feature makes them excellent candidates for the construction of large LaBr$_3$(Ce) arrays.

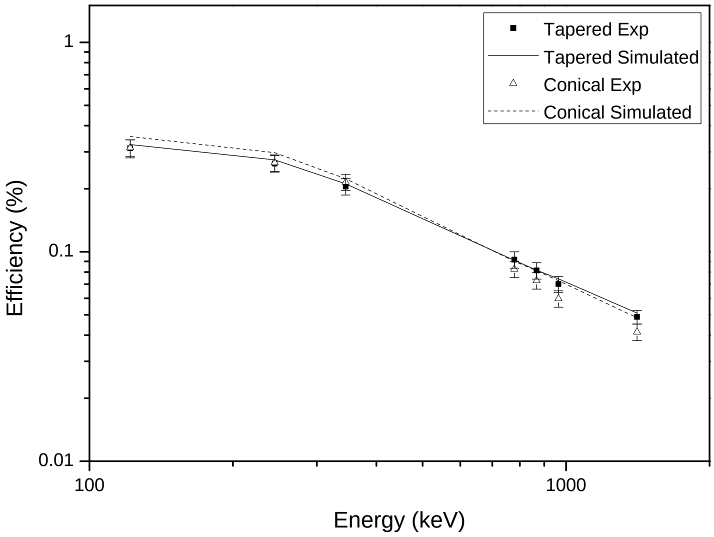

**Figure 3.17: Absolute photopeak efficiencies of the truncated cone and hybrid-tapered LaBr$_3$(Ce) detectors.** - Absolute photopeak efficiencies for the truncated cone (empty triangles) and hybrid-tapered detector (filled squares) measured with an absolutely-calibrated $^{152}$Eu source placed at 100 mm from the detectors. The lines represent Geant4-simulated efficiency taken from [VCGF$^+$17].

### 3.7.3 Time response: time resolution

The time resolution for the two novel LaBr$_3$(Ce) crystals was optimized following the procedure described in Section 3.1 and taking advantage of the results found for the 1 in. cylindrical crystals (Section 3.6.4). In that case, it was observed that the best time resolutions are obtained when very short CFD external delays of the order of 1.5 ns are set at the ORTEC 935. Therefore, the region from 1.4 to 1.8 ns was carefully explored for both geometries. In addition to the short values, the analyzed range of CFD delays ranges from 0.5 to 20.0 ns. The time response was measured at $^{60}$Co energies and 511 keV ($^{22}$Na). For the study, the PMT voltage was also set in the range $-1200$ to $-1300$ V, although a much wider range has been investigated.

#### 3.7.3.1 Conical crystal

As it was expected, the best time resolution is achieved in the region of very short CFD external delays; for longer delays the time resolution deteriorates as the length of the cable increases, being a 30% worse for delays longer than 10 ns.

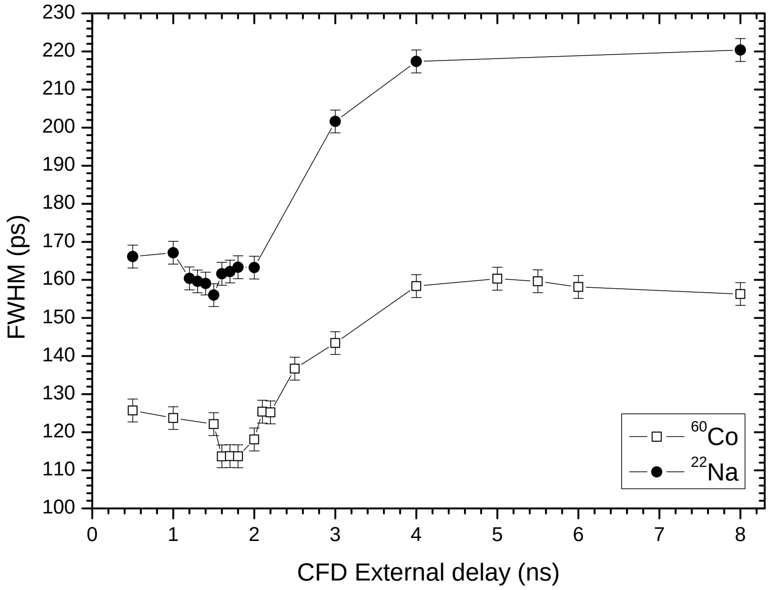

**Figure 3.18: Time resolution of the truncated cone crystal as a function of the CFD external delay for $^{60}$Co and 511 keV energies.** - Time resolution of the truncated cone detector as a function of the CFD external delay at $^{60}$Co and 511 keV ($^{22}$Na) energies. The Hamamatsu R9779 PMT was operated at $-1200$ V.

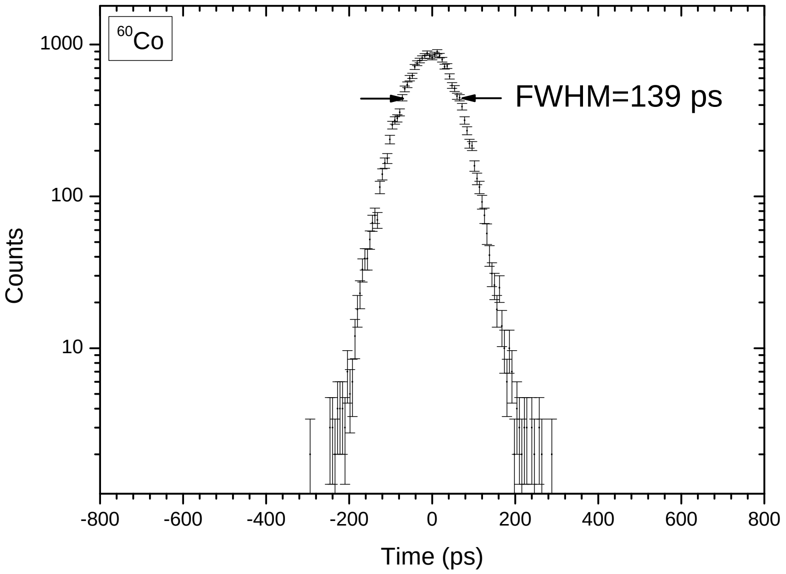

**Figure 3.19: Time spectrum of the conical crystal vs. the reference detector at $^{60}$Co energies.** - Time spectrum of the conical LaBr$_3$(Ce) coupled to R9779 versus the reference detector at $^{60}$Co energies. The FWHM CRT of 139 ps is the convolution of the contributions of the reference detector and the LaBr$_3$(Ce) unit, yielding 110±3 ps.

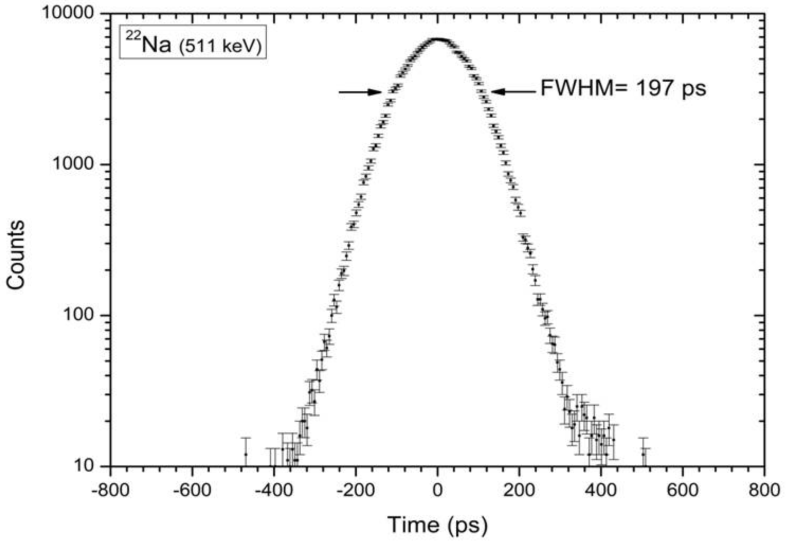

**Figure 3.20: Time spectrum of the conical crystal vs. the reference detector at 511 keV ($^{22}$Na).** - Time spectrum of the conical LaBr$_3$(Ce) coupled to R9779 versus the reference detector at at 511 keV ($^{22}$Na) energies. The FWHM CRT of 197 ps is the convolution of the reference detector 120(3) ps and the LaBr$_3$(Ce) unit, yielding 158±3 ps.

This behaviour has been already observed for the cylindrical crystals (Section 3.6.4). The influence of the CFD external delay on the time resolution is depicted in Figure 3.18 at the energies of $^{60}$Co and $^{22}$Na (511 keV). Figures 3.19 and 3.20 show the time spectra corresponding to the best time resolutions of the conical crystal at $^{60}$Co and 511 keV energies, respectively. The best values of time resolution of the conical LaBr$_3$(Ce) measured at $^{60}$Co and 511 keV energies correspond to 110±3 ps and 158±3 ps FWHM, respectively. These values are obtained when an external delay of 1.7 ns is set at the ORTEC 935, and the R9779 PMT is biased with −1200 V. The FWHM of 139 ps displayed in Figure 3.19 contains the contribution of the reference detector with a resolution of 85±2 ps and the LaBr$_3$(Ce) crystal, with 110±3 ps. The 197 ps of FWHM presented in Figure 3.20 contains the contribution of 120±3 ps from the reference BaF$_2$ and the time resolution of the conical LaBr$_3$(Ce) of 158±3 ps.

#### 3.7.3.2 Hybrid-tapered crystal

The same analysis has been performed for the tapered-hybrid crystal. The best time resolutions for the at $^{60}$Co and $^{22}$Na (511 keV) energies correspond to 111±3 ps and 160±3 ps, respectively. The optimal parameters are 1.5 ns of CFD external delay and −1300 V of PMT bias voltage. Nonetheless, these promising values are somewhat misleading. Figure 3.21 presents the time resolution of the hybrid-tapered detector as a function of the CFD external delay measured at $^{60}$Co and 511 keV ($^{22}$Na) energies. For this crystal, the time resolution rapidly deteriorates when the CFD external delay gets longer and longer. Values increase by more than a 60% and, more worryingly, asymmetries appear in the time peak. These facts suggest the presence of a double component in the output, which can be produced by a non-optimal photon reflection in the inner layers or at the interface between the conical and cylindrical sections. Time peaks begin to be asymmetric when using CFD external delays longer than only 2.0 ns, and even more asymmetric, close to an unresolved doublet, for delays longer than 4.0 ns. It is important to underline that the machining and polishing procedures to produce these innovative geometries represented a challenge and that this was the first time that LaBr$_3$(Ce) crystals of this size and geometry were produced.

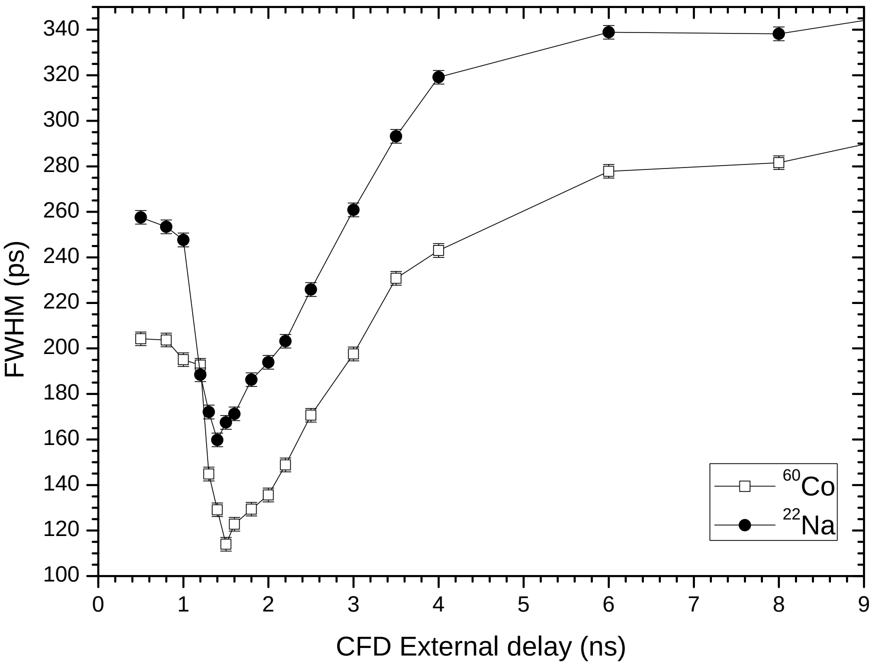

**Figure 3.21: Time resolution of the hybrid-tapered crystal as a function of the CFD external delay for $^{60}$Co and 511 keV energies.** - Time resolution of the hybrid-tapered detector as a function of the CFD external delay measured at $^{60}$Co and 511 keV ($^{22}$Na) energies. The Hamamatsu R9779 PMT was operated at −1300 V.

Figure 3.22 illustrate these problems. The upper panel shows the time spectrum corresponding to the best time resolution achieved for the hybrid-tapered LaBr$_3$(Ce) crystal at $^{60}$Co energies. The time peak is symmetric and the FWHM of 140 ps contains the contribution of the reference detector with a resolution of 85±2 ps and the LaBr$_3$(Ce) crystal, with 111±3 ps. The lower panel displays the spectrum measured with a long external CFD delay of 8.0 ns for the LaBr$_3$(Ce) detector. In this case, the peak is clearly asymmetric, probably an unresolved doublet. The FWHM of the non-Gaussian distribution is 293 ps, which corresponds to ∼280 ps FWHM for the tapered detector. Clearly, the settings are not very stable for the hybrid-tapered detector since the time response strongly gets worse when moving slightly outside of the local minimum where the time resolution is good. This comes in addition to the degraded energy resolution for this crystal and suggests that the design of this type hybrid crystals needs to be improved before they can be used for nuclear spectroscopy.

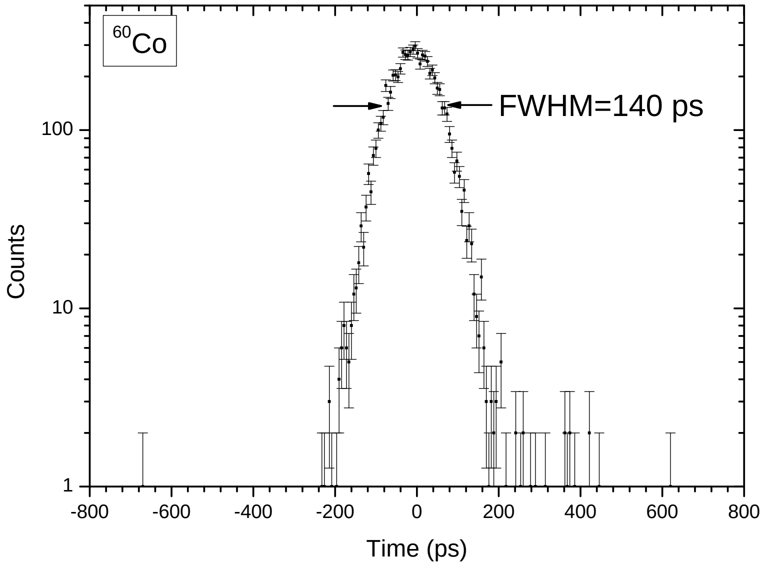

(a)

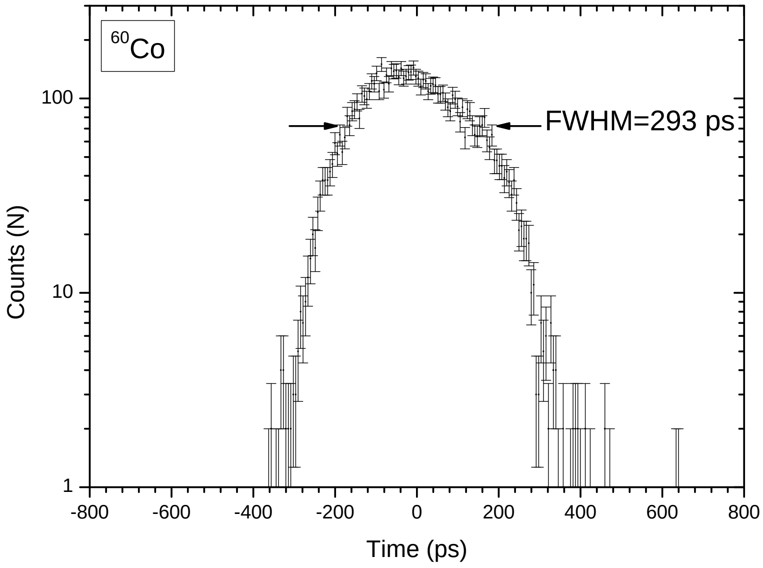

(b)

**Figure 3.22: Time spectra of the tapered crystal at $^{60}$Co energies for different CFD delays.** - Time spectrum of the hybrid-tapered LaBr$_3$(Ce) coupled to R9779 versus the reference BaF$_2$ detector at $^{60}$Co energies. Plot (a) displays the time peak when a short delay of 1.5 ns is set at the ORTEC 935. The FWHM CRT of 140 ps is the convolution of the contributions of the reference detector and the LaBr$_3$(Ce) unit, yielding 111±3 ps. This spectrum corresponds to the best time resolution achieved. Plot (b) shows the spectrum measured with a longer external CFD delay of 8.0 ns for the LaBr$_3$(Ce) detector. As can be seen in this case the peak is asymmetric and looks like an unresolved doublet. The FWHM of the non-Gaussian distribution is 293 ps, which corresponds to ~280 ps FWHM for the tapered detector.

#### 3.7.3.3 Comparison of the time response of both crystals

Figures 3.23 and 3.24 present the FWHM time resolution as a function of the CFD external delay for the two crystals, the truncated cone and the hybrid-tapered. Figure 3.23 displays the response at $^{60}$Co energies and 3.24 at 511 keV using a $^{22}$Na source. For comparison, the time response of 1-inch cylindrical crystal B (Section 3.5.1) is also plotted in both graphs. The inset in each plot is a zoom in the short values region, where the best FWHM is achieved. These plots show how the best values are also achieved for very short CFD delays, and how the time resolution deteriorates with the length of the cable.

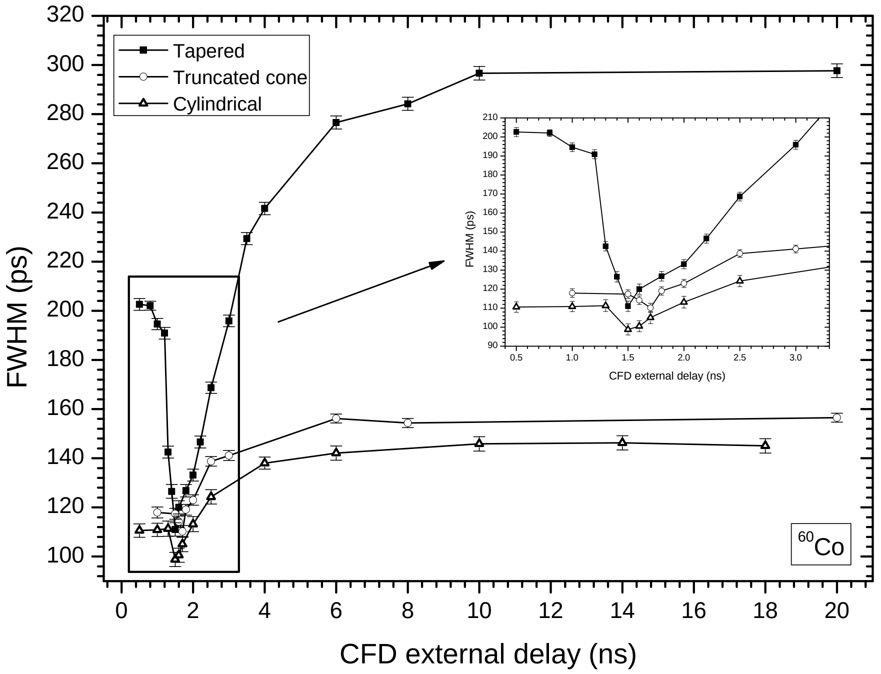

**Figure 3.23: FWHM time resolution as a function of the CFD external delay at $^{60}$Co energies.** - Time resolution of the truncated cone and hybrid-tapered crystals as a function of the CFD external delay. Both crystals were coupled to a Hamamatsu R9779 PMT, operated at −1200 V and −1300 V respectively. As a comparison the time resolution of a 1-in. cylindrical LaBr$_3$(Ce) crystal with 8% doping is also included. The inset shows the region of short CFD external delays, where the best FWHM time resolution is achieved for both geometries. The time resolution displayed in the plot was measured at $^{60}$Co energies.

Table 3.2 summarizes the best individual FWHM time resolutions for the two crys-

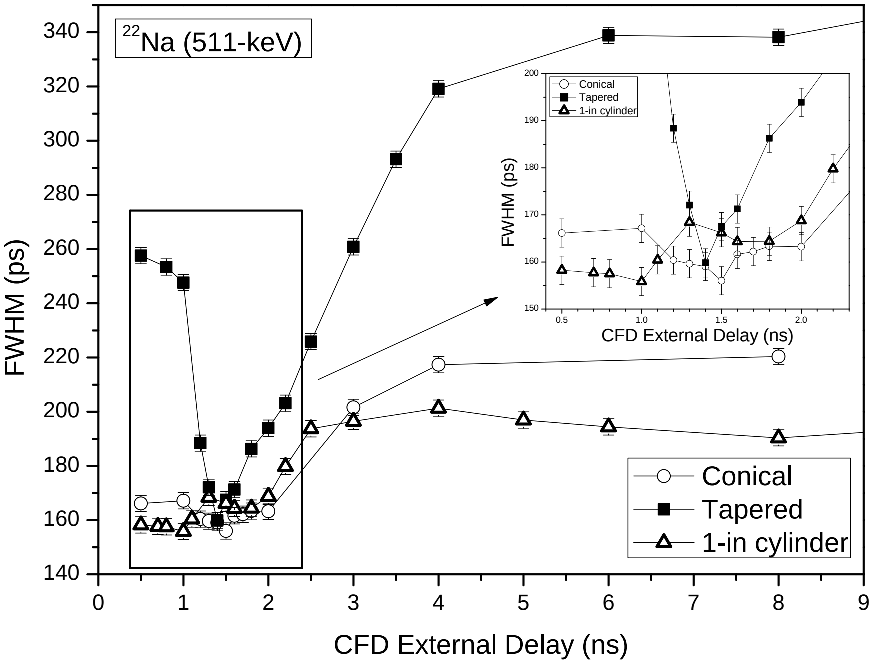

**Figure 3.24: FWHM time resolution as a function of the CFD external delay at 511 keV ($^{22}$Na)** - Time resolution of the truncated cone and hybrid-tapered crystals as a function of the CFD external delay for 511 keV. Both crystals were coupled to Hamamatsu R9779 PMT, operated at −1200 V and −1300 V respectively. As a comparison the time resolution of a 1-in. cylindrical LaBr$_3$(Ce) crystal with 8% doping is also included. The inset shows the region of short CFD external delays, where the best FWHM time resolution is achieved for both geometries. The time resolution displayed in the plot was measured at 511 keV ($^{22}$Na).

tals, with the values of Crystal B for comparison. The excellent values of 110±3 ps for the truncated cone LaBr$_3$(Ce) and the 111±3 ps for the tapered detector has been possible due to the new geometry designs in combination with the use of the ORTEC 935 CFD at very short delays, and the good performance of the Hamamatsu R9779 PMT. The time resolution is almost independent on the high voltage applied to the photomultiplier, with a small variation below 6 ps in the range −1100 V to −1500 V. The optimal HV, which is −1200 V for the conical LaBr$_3$(Ce) and −1300 V for the tapered one, preserves the energy linearity. This behaviour was already observed for the cylindrical crystals (Section 3.6.4). The values reported in this thesis for the time resolution of conical and tapered LaBr$_3$(Ce) detectors are the best results reported to date for crystals of these sizes.

| **Geometry** | **External Delay (ns)** | **HV (V)** | **FWHM $^{60}$Co (ps)** | **FWHM $^{22}$Na (ps)** |
|---|---|---|---|---|
| Tapered | 1.5 | $-1300$ | 111±3 | 160±3 |
| Truncated cone | 1.7 | $-1200$ | 110±3 | 158±3 |
| 1-in. cylinder | 1.5 | $-1300$ | 98±2 | 148±2 |

**Table 3.4: Best time resolution values (FWHM) of the truncated cone and hybrid-tapered crystal at $^{60}$Co and $^{22}$Na (511 keV) energies.** - Best results of FWHM time resolution for the two innovative LaBr$_3$(Ce) geometries, the truncated cone and the hybrid-tapered detector compared to the 1-in. cylinder. The time resolution was measured at $^{60}$Co energies and 511 keV ($^{22}$Na). The zero crossing value (Z) is set at 2.0 mV and the CFD threshold at $-508$ mV.

In spite of the good time resolution of the tapered hybrid LaBr$_3$(Ce) crystal for specific settings, it is observed that the time response strongly deteriorates as a function of the external CFD delay. At longer delays, the time peaks have a double structure, which may arise from the inner cylindrical and conical surfaces. This is confirmed by the measurement of the energy spectra, where strong asymmetries emerge, deteriorating the energy resolution to the point of displaying double full-energy peaks. At the present stage this rends this (otherwise promising) crystal not suitable for fast-timing measurements.

On the contrary, the truncated cone LaBr$_3$(Ce) crystal is very well suited for fast-timing applications since it exhibits excellent time response while maintaining good energy resolution and small time walk. Furthermore, it can be highly packed in rings covering large solid angles. Due to its geometry it is very versatile, so it is possible to efficiently group detectors to build high-performance LaBr$_3$(Ce) fast-timing arrays.

### 3.7.4 Time response: time walk

The dependence of the time response as a function of energy was also investigated for these two innovative geometries, following the same procedure used for cylindrical crystals (Sections 3.2 and 3.6.5). Using the precise zero-crossing adjustment of the ORTEC 935, a good time walk with a total span of about 300 ps in an energy range of 1 MeV for both crystals was obtained when for Z=2.0 mV. Figure 3.25 illustrates the time walk for the two types of crystals. For very short delays in the CFD the measured walk is smooth, but in the case of the hybrid LaBr$_3$(Ce) the walk becomes unstable for CFD delays above 2.0 ns. Although it is not shown in the plot In fact, for delays longer than 8.0 ns the time walk seems to be composed of two distributions. It is possible that this effect is also caused by the presence of a double component in the output signal, which may be produced by an irregular photon reflection at the crystal surface, or at the interface between the conical and cylindrical sections.

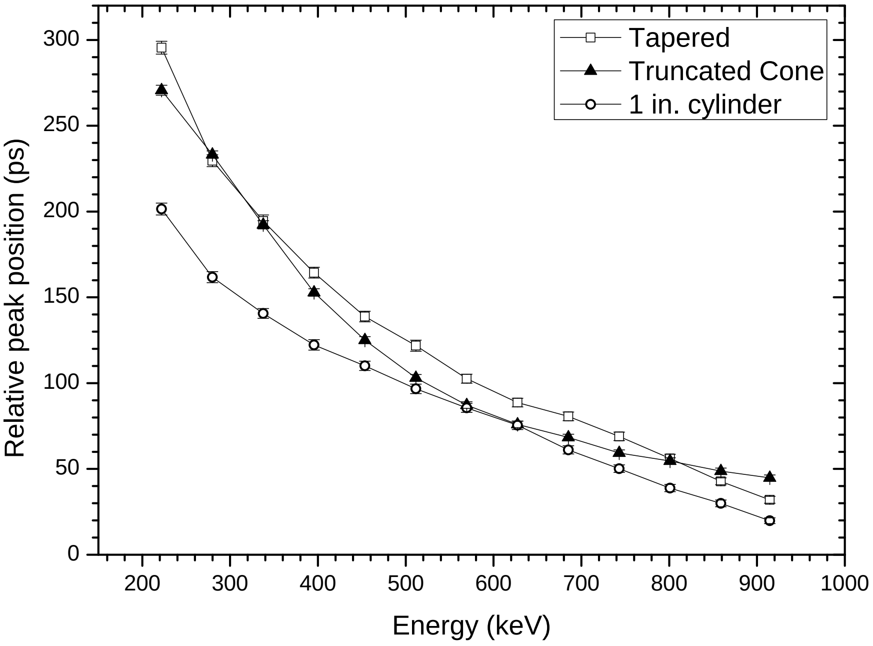

**Figure 3.25: Compton time walk of conical and tapered crystals coupled to the Hamamatsu R9779 PMT.** - Compton time walk of conical and tapered crystals coupled to the Hamamatsu R9779 PMT. The walk response from the standard 1 in. x 1 in. cylindrical LaBr$_3$(Ce) is also included for comparison. The relative peak positions refer to the shift of the time peak with respect to the position of the time peak for the 1173-keV full energy peak (zero in the x-axis). Detectors are operated at $-1200$ V and $-1300$ V respectively with a CFD external delay set as 1.7 ns for the truncated cone and 1.5 ns for the tapered LaBr$_3$(Ce). Regarding the cylindrical crystal, the detector is operated at 1300 V with a 1.6 ns external delay. The zero crossing parameter for all of them corresponds to Z=2.0 mV.

The measured time walk distribution for the LaBr$_3$(Ce) truncated-cone geometry is shown in Figure 3.26 for a fixed optimized CFD external delay of 1.7 ns as a function of the CFD zero-crossing value, Z. Positive values of Z yield a monotone behaviour with no minimum and are very well suited for fast-timing spectroscopy. Specifically, at Z=2.0 mV, the walk dependence is of the order of 300 ps in the range from 200 to 1000 keV.

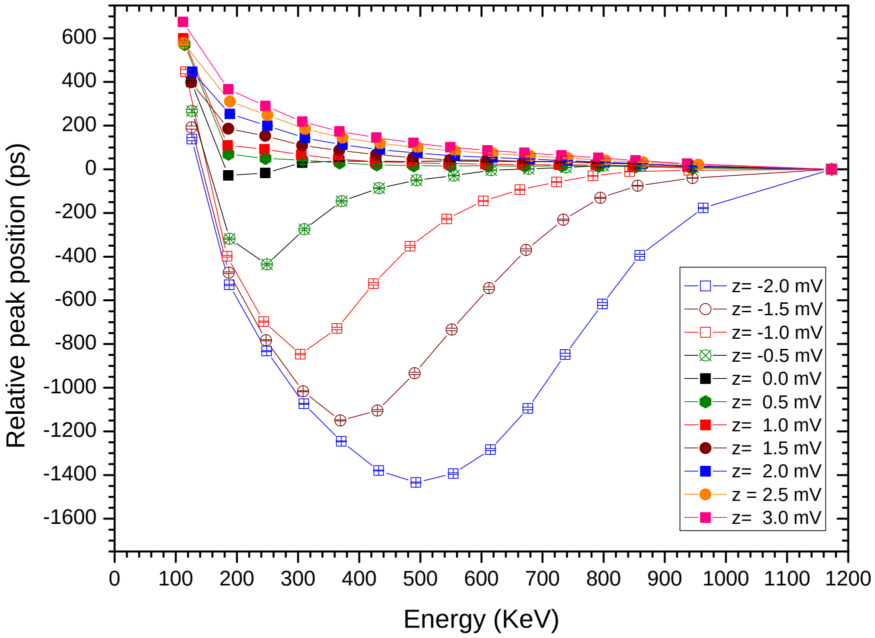

**Figure 3.26: Compton time walk of the conical LaBr$_3$(Ce) crystal for different Z values.** - Compton time walk of the truncated cone LaBr$_3$(Ce) for different values of the zero-crossing parameter Z. The crystal is coupled to the Hamamatsu R9779, which was powered with −1200 V. The relative peak positions refer to the shift of the time peak with respect to the 1173-keV full energy peak (zero in the x-axis). The external delay set at the CFD was 1.7 ns for all the measurements.

## 3.8 Conclusions of this chapter

$LaBr_3$(Ce)-based crystals are the best-suited detectors for the application of fast-timing spectroscopy since they combine excellent time response with good energy resolution and high $\gamma$-ray detection efficiency. The sensitivity of the fast-timing methods directly depends upon the time resolution of the setup, the main contributor being the $LaBr_3$(Ce) detectors. It is therefore of importance to optimize their time response.

In this work, we have characterized standard cylindrical crystals of 1 inch in height and 1 inch in diameter, and two newly designed crystals with the shape of a truncated cone and of a hybrid conical plus cylindrical shape. All of them were coupled to the Hamamatsu R9779 photomultiplier tube, specially designed for fast response. Signal processing was performed using NIM electronic modules. We have implemented an iterative procedure to optimize the PMT bias voltage and the CFD external delay and zero crossing in order to achieve the best possible time resolution.

Concerning the cylindrical crystals three $LaBr_3$(Ce) scintillators 1 inch in height and 1 inch in diameter manufactured with different Ce concentration were studied. Very short external delays around 1.6 ns set at the ORTEC 935 and a high voltage range of −1200 to −1300 V for the Hamamatsu R9779 PMT yield the best time resolution results. FWHM values of 106±2, 98±2 and 107±2 ps for crystals with standard 5% Ce doping ($A$), 8% Ce ($B$) and 10% Ce ($C$), respectively, were obtained for $^{60}$Co energies. The differences reflect the effect of the Ce doping concentration but, in contrast to former studies [GMH$^+$05], the time resolution of the crystal with 10% Ce is worse than the resolution of the crystal with 8% Ce. This could be understood as inhomogeneities in the doping distribution when the crystal was manufactured.

The time resolution values are the best reported so far for crystals of this size. In particular, for Crystal $B$, with enhanced Ce doping of 8%, we have found that a bias voltage of −1300 V on the PMT, together with the optimal ORTEC 935 parameters of Z= 2.0 mV and external delay of 1.6 ns, yield the best time resolutions at $^{60}$Co and $^{22}$Na energies. The time resolution measured at $^{60}$Co energies has been pushed below 100 ps to 98±2 ps, which should be compared to the best resolution available to date with a similar cylindrical 1-inch $LaBr_3$(Ce) crystal of 107±4 ps, reported by Moszyński *et al.*, using the Photonis XP20D0 PMT [Mos06]. This is achieved while preserving a reasonable energy resolution and time walk. Indeed, for the operation in the CFD regime, the time walk has been assessed by taking advantage of the good ORTEC 935 qualities and the possibility of precise zero-crossing adjustment. We have shown that a very smooth Compton time walk is obtained for energies below 1 MeV. Additionally, we show that the operation of the ORTEC 935 CFD in leading-edge mode provides similar or even better time resolution values than the CFD operation at a given energy. This is the case of Crystal $A$ after the optimization of the triggering fraction by the modification of the threshold control value of the CFD module. This mode of operation can only be applied when the time walk is not relevant or when it can be corrected.

Concerning the novel geometries, the two other crystals that have been investigated, a truncated cone crystal of 25.4 mm in height, with bases of $\oslash$=38.1 mm and $\oslash$=25.4 mm, and a hybrid tapered crystal, with a cylindrical section of nominal $\oslash$=38.1 mm in the base and 16.5 mm in height, and a 30.5 mm long conical section narrowing down to $\oslash$=19 mm diameter base. The idea behind these designs was on one side enhancing the scintillation light collection inside the crystals and consequently their timing performance and, on the other side, providing crystals to build fast-timing arrays with a modular and versatile geometry, and with sufficient solid angle coverage and thus $\gamma$-ray detection efficiency.

The best FWHM time resolution values measured for the truncated cone and the tapered $LaBr_3$(Ce) crystals at $^{60}$Co energies are 110±3 ps and 111±3 ps respectively. At 511 keV they are measured to be 158±3 and 160±3 ps. These values are the best reported to date for $LaBr_3$(Ce) crystals of this shape and size, being comparable to the results obtained for the smaller 1-inch cylindrical crystal.

In spite of the good time resolution of the hybrid-tapered $LaBr_3$(Ce) crystal achievable for specific settings, it is observed that the time response strongly deteriorates as a function of the external CFD delay. At longer delays, the time peaks have a double structure, which may arise from the light reflection in the inner cylindrical and conical surfaces. This is confirmed by the measurement of the energy spectra, where strong asymmetries emerge, deteriorating the energy resolution to about 4.3%. At the present stage, this rends this crystal not suitable for fast-timing measurements. Nevertheless, this problem might be solved with an improved manufacturing technique.

On the contrary, the truncated cone $LaBr_3$(Ce) crystal is very well suited for fast-timing applications since it has excellent time response while maintaining good energy resolution. Additionally, it can be densely packed in rings or other arrangements with sufficient efficiency to construct high-efficiency $LaBr_3$(Ce) fast-timing arrays. One of them is FATIMA [F$^+$], a standalone or a hybrid $\gamma$-ray array dedicated to $\beta$-$\gamma$ and $\gamma$-$\gamma$ spectroscopy that will be placed at the focal plane of the SuperFRS at the FAIR facility in GSI [FAI]. This work may be further extended by studying larger crystals and different geometries of relevance for the construction of future fast timing arrays.

# 4

# The EXILL-FATIMA campaign

The use of high-purity germanium (HPGe) clover detectors efficiently arranged in geometries is one of the most powerful tools nowadays in nuclear spectroscopy. Their excellent energy resolution in combination with a substantial solid angle coverage, make it possible to disentangle complex level schemes in nuclear structure, providing high isotopic selectivity and giving access to angular correlations, allowing the assignment of spin and parities to nuclear states. The spectroscopic information can be nicely complemented with lifetime measurements of nuclear excited states providing a direct insight into the nuclear structure through the determination of the reduced transition probabilities. Therefore, the combination of HPGe detectors with ultra-fast scintillators detectors efficiently arranged in arrays holds a strong potential in Nuclear Physics.

The nice results obtained in the past using HPGe detectors arrays, like GAMMASPHERE [Lee97, HRZ$^+$95] in spontaneous fission studies with $^{252}$Cf and $^{248}$Cm sources, encourage the performance of complementary experiments such as neutron-capture reactions and prompt $\gamma$-ray spectroscopy on induced fission products using HPGe arrays. Consequently, in 2013, it was performed for the first time an experiment of prompt $\gamma$-ray spectroscopy on induced fission fragments using a large array of HPGe and $LaBr_3$(Ce) detectors built up like an hybrid spectrometer [RSB$^+$14]. The experiment was named EXILL-FATIMA and the experimental campaign took place at the research nuclear reactor of the Institute Laue-Langevin (ILL) [RSB$^+$14, ILL], in Grenoble (France).

The experiment ran during 100 days, which corresponds to two reactor cycles, and it was composed of two blocks: the spectroscopic part, named EXILL (EXOGAM@ILL) [JBdF$^+$], which was mainly focused on $\gamma$-ray spectroscopy and angular correlation measurements, and the EXILL-FATIMA part, that incorporated the FAst TIMing Array array, FATIMA, providing the spectrometer with the capability of measuring lifetimes down to the few picoseconds range.

## 4.1 The ILL, the H113 neutron guide and the PF1

The institute Laue-Langevin (ILL), located in Grenoble (France), is an international research centre at the leading edge of neutron science. It counts with a nuclear reactor devoted to science that provides a high flux of neutrons feeding some 40 state-of-the-art instruments covering a wide range of research topics.

**Figure 4.1: Nuclear reactor of the institute Laue-Langevin (ILL).** - Institute Laue-Langevin (ILL) and the related nuclear reactor where the EXILL-FATIMA campaign took place. The facility is located in Grenoble (France).

The ILL reactor is equipped with several neutron guides that transport the high flux of neutrons to the experimental areas. The most intense one is the ballistic super mirror guide H113 that feeds the cold neutron beam facility PF1B, where the EXILL-FATIMA spectrometer was placed [RSB+14]. The PF1B facility is enclosed in between casemates and specially shielded to reduce the $\gamma$ and neutron background.

Right before the PF1, the H113 guide delivers a thermal neutron capture-equivalent flux density of $2.2{\cdot}10^{10}$ cm$^{-2}$ s$^{-1}$ at the nominal reactor power of 58.3 MW, with a

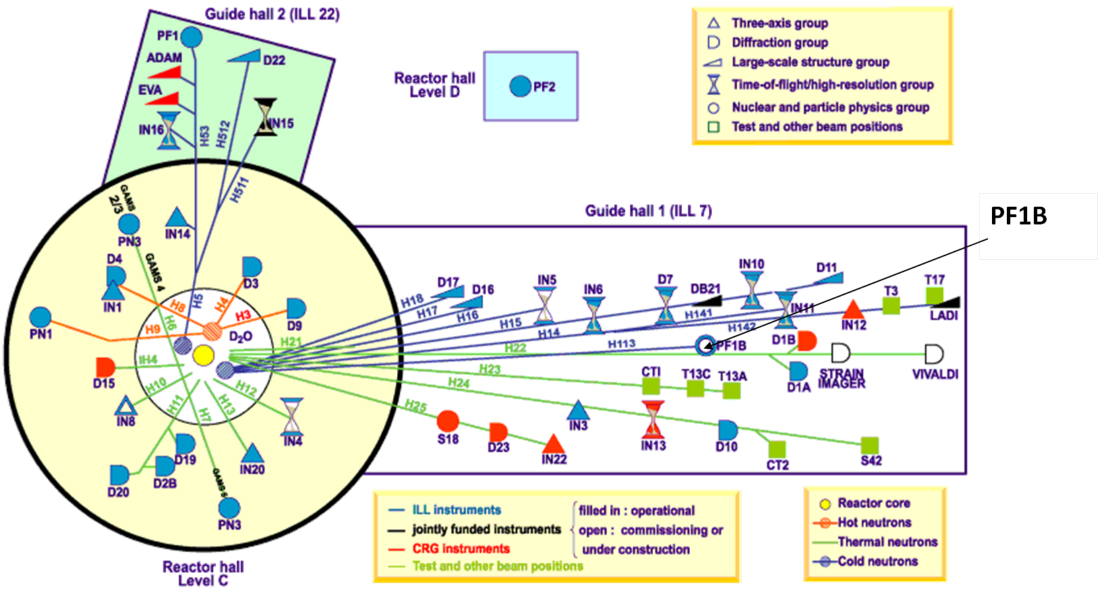

**Figure 4.2: Schematics of the nuclear reactor of ILL.** - Illustrative scheme of the different neutron guides and the setup distribution at the ILL nuclear reactor facility [ILL].

relatively large divergence of 7 mrad FWHM [ADH$^+$06]. This large beam profile is not well suited for $\gamma$-ray spectroscopy and angular correlations, and therefore to achieve a pencil beam with 1 cm diameter and negligible neutron halo, the neutron flux was collimated by a system, that is composed of a sequence of circular apertures of 1 cm in diameter made of neutron absorbing materials such as boron carbide and sintered enriched $^6$LiF. The apertures were shielded with 5-cm-thick lead absorbers in order to suppress $\gamma$-ray background coming from boron. The apertures were inserted inside a cylindrical vacuum tube made of aluminium and covered with an inner layer of borated plastic to absorb scattered neutrons that were not absorbed by the apertures. The total length of the collimation system is 4 m, followed by a free flight path section of 1 m with vacuum pump access, and the target chamber attached at the end. Right after the chamber, there is a dump pipe of 1 m that is finished in a stopper of 5-mm-thick $^6$LiF [HKF$^+$02, ADH$^+$06, JBdF$^+$]. Figure 4.3 provides a schematic layout of the collimation system.

The neutron beam position and profile was verified with RTQA and EBT2 radiochromic films [JBdF$^+$] and the H113 collimation system was simulated using McSTAS package for neutron transport [LN99, WFL04].

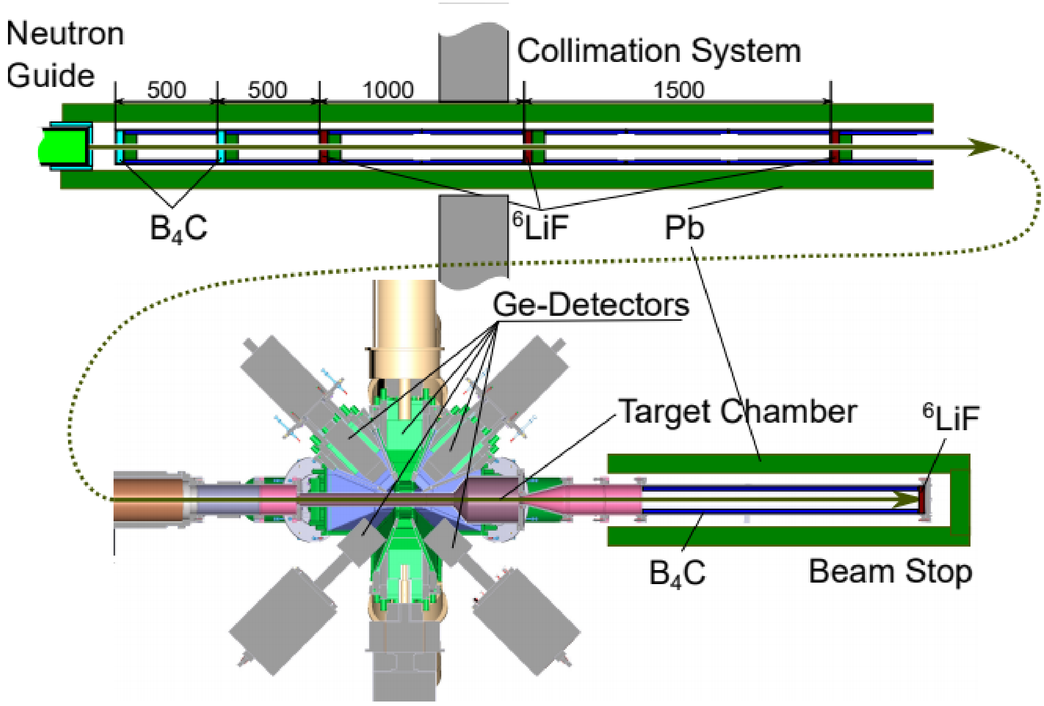

**Figure 4.3: Schematic layout of the collimation system placed at the H113 neutron guide.** - Schematic layout of the collimation system to achieve neutron pencil beams of about 1 cm diameter. The sequence of apertures made of boron carbide and sintered enriched $^6$LiF are sketched and explained in the layout. At the end of the collimation system the target chamber is placed followed by a beam dump. Figure taken from [JBdF$^+$].

## 4.2 Targets and the target chamber

Along the EXILL-FATIMA campaign two targets of fissile $^{241}$Pu and $^{235}$U were used. After the neutron impact fission products are produced with a recoil energy from 50 to 110 MeV, therefore targets were sandwhiched between materials that work as stoppers in order to reduce the Doppler broadening of the emitted $\gamma$-rays.

The $^{235}$U target was enriched to 99.7%, with the remaining 0.3% composed of non-fissile isotopes $^{234}$U, $^{236}$U, $^{238}$U. Therefore, considering the use of cold neutrons and the target composition the total fission rate is dominated by the $^{235}$U(n,f) reaction. Assuming an average prompt neutron multiplicity of $\nu_p$=2.42, the average N/Z ratio of the fission pairs is 1.539 and 2.539 for A/Z. The Uranium target was built with a sandwich structure of Zr and Sn.

The $^{241}$Pu contained an enrichment of 78%, with a 5% of $^{240}$Pu and 16% of $^{242}$Pu.

The fissile $^{239}$Pu represented only the 0.02%. At the beginning of the experiment, the amount of $^{241}$Am corresponded to 0.2% (10 kBq), while at the end it reached a 0.5% (23 kBq). Considering the target composition and the use of cold neutrons, the fission is mainly dominated by the $^{241}$Pu(n,f) reaction. For this case, with a prompt neutron multiplicity of $\nu_p$=2.929, the average N/Z ratio for fission fragment pairs is 1.543, being slightly higher than that of the $^{235}$U. The plutonium target was produced with Be backing stopper.

The target chamber was carefully designed in order to achieve optimal $\gamma$-ray spectroscopy. It was made of materials that do not absorb the emitted $\gamma$-rays and do not produce $\gamma$-ray scatter. Its structure favours the placement of the spectrometer detectors in a configuration very close to the target position, and makes it handy to load and unload the target. Figure 4.4 provides a schematic layout of the target chamber. It also displays the target position inside the spectrometer. The chamber was designed with a double-wall target chamber system that can be operated in two configurations in regard of the radiotoxicity of the targets.

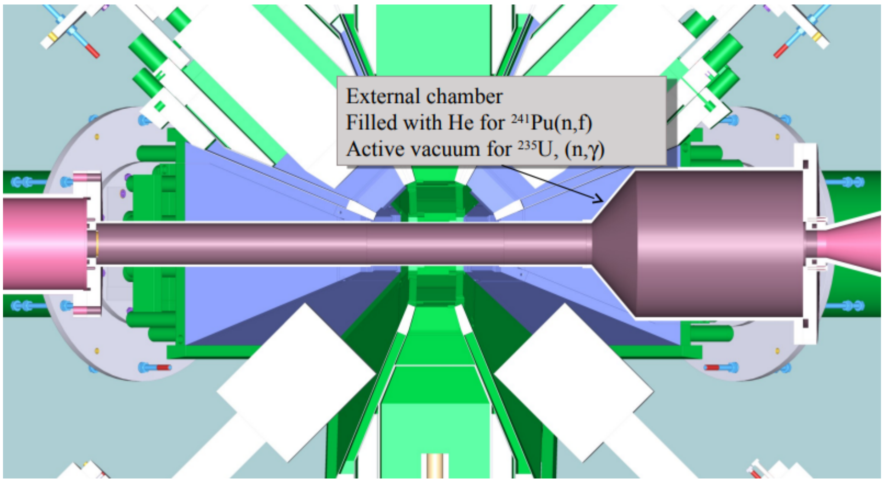

**Figure 4.4: Schematic layout of the target chamber.** - A schematic layout of the target chamber and its position inside the EXILL-FATIMA spectrometer. Its structure favours the placement of the Ge and LaBr$_3$(Ce) detectors in a close-geometry configuration. Figure taken from [JBdF$^+$].

The first configuration uses the outer shell of the chamber and it is optimized for (n,$\gamma$) and $^{235}$U(n,f) reactions, with low radio-toxic targets. The chamber was made in aluminium with a 2 mm wall thickness and a 50 mm pipe that is directly connected to the collimator and the beam stop vacuum system. Samples were inserted with teflon bags and held to the metallic frame with teflon wires.

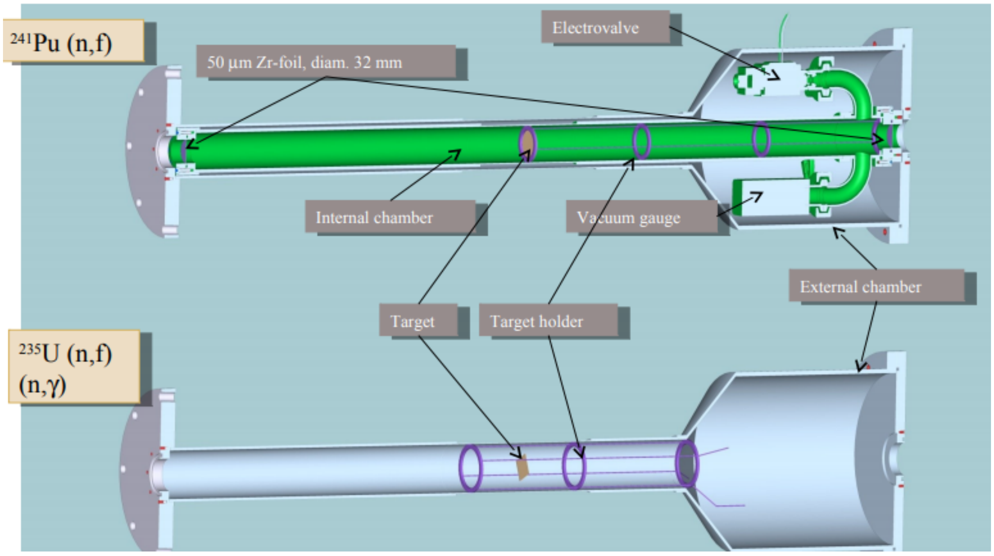

**Figure 4.5: Schematic view of the target chamber structure showing the two operating configurations.** - Schematic view of the two operating configurations of the target chamber. The scheme shown at the bottom corresponds to the single wall configuration used for (n,$\gamma$) and $^{235}U$(n,f) experiments. The target holder frame is drawn in purple and the target teflon bag in beige. The upper part of the layout shows the double wall configuration used with high radio-toxicity targets or samples. The second chamber, which is inserted into the outer chamber, is drawn in green. It is a completely independent chamber equipped with a vacuum gauge allowing to monitor its tightness during operation. Samples are loaded into the inner chamber in ILL alpha activity laboratory and the chamber is vacuum pumped and sealed. Figure taken from [JBdF$^+$].

For the case of higher radio-toxicity, there is a second configuration that includes an inner target chamber that is inserted instead of the target holder frame. The second chamber is made of an aluminium tube of 35 mm inner diameter and 2 mm thickness. It was loaded, sealed and vacuum pumped at the ILL alpha activity laboratory. The neutrons travel through a 200-$\mu$m thick Zr window to minimize neutron scattering. The collimation system and the outer vacuum pipe as well as the beam stop tube were filled with helium gas and pumped to a pressure of 50 mbar. The inner chamber was provided with a vacuum gauge to ease the chamber manipulation during the experiment. Figure 4.5 illustrates the two operating configurations.

In addition to $^{235}$U and $^{241}$Pu targets, sources of $^{133}$Ba, $^{60}$Co, and $^{152}$Eu (420 kBq) were employed for calibrations in the low energy range, for higher energies the neutron capture reaction $^{35}$Cl(n,$\gamma$)$^{36}$Cl was used.

## 4.3 Detectors of the EXILL-FATIMA spectrometer

The result of merging together a highly efficient Ge array with cutting-edge LaBr$_3$(Ce) detectors results in the EXILL-FATIMA setup, a hybrid spectrometer with excellent timing capabilities in addition to the good spectroscopic features. Figure 4.6 shows the hybrid spectrometer placed at the end of the H113 neutron line.

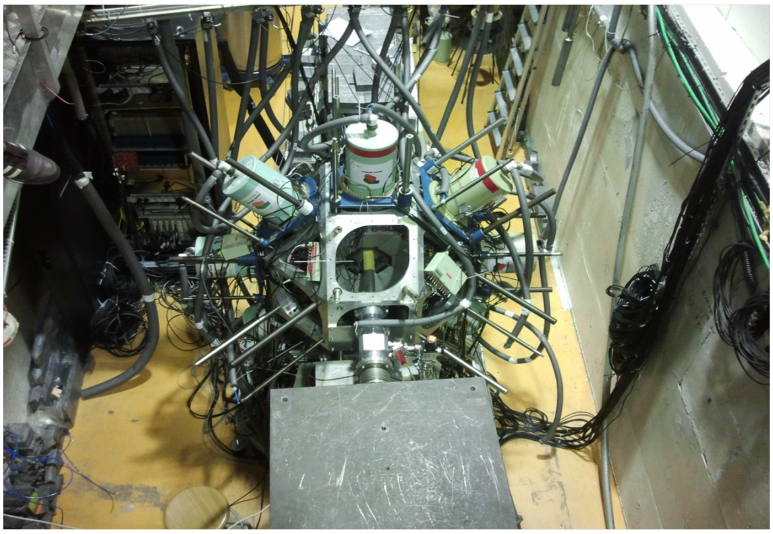

**Figure 4.6: Hybrid spectrometer developed for the EXILL-FATIMA experiment.** - Photograph of the hybrid spectrometer of the EXILL-FATIMA campaign. The central ring of the frame is composed of Ge-Clover detectors. LaBr$_3$(Ce) detectors are distributed along two rings around the central one. The spectrometer is placed in the H113 neutron beam line at the ILL nuclear reactor. Picture taken from Vadym Paziy [Paz].

A close view of the target region is provided in Figure 4.7. The target position is indicated with the yellow structure in the center of the image. The picture displays the BGO-shielded Ge clovers (green rhomboid structures) and the LaBr$_3$(Ce) detectors encased in aluminium, which are arranged in close geometry around the target position.

**Figure 4.7: Setup picture of the target area.** - Photograph of the setup in the target area showing some of the BGO-shielded Ge clovers and the $LaBr_3(Ce)$ detectors placed in a close-geometry configuration around the target position. The yellow structure corresponds to the target.

### 4.3.1 Spectroscopic measurements with EXILL

As mentioned above, a spectroscopic campaign, EXILL was performed first. The spectrometer was composed of HPGe detectors equipped with active Compton-suppression shields made of BGO (Bismuth Germanate). The detectors were arranged in a rhombicuboctahedron geometry, with the aim of performing very precise angular and directional-polarization correlation measurements. The frame in use was designed in GANIL to hold 16 EXOGAM clovers, and it was adapted to place all types of detectors around the target chamber in the PF1 area. Regarding HPGe detectors, germanium crystals of three different types were at play: ten EXOGAM Clover detectors from GANIL (Grand Accelerateur National des Iones Lourdes) [EXO, Aza99, SAF$^+$00], six GASP detectors from LNL (Legnaro National Laboratory) [GAS, C93] and two Clover detectors form LOHENGRIN-ILL [DBT$^+$99]. Depending on the campaign needs, different combinations of the three types of HPGe detectors were mounted on the frame [JBdF$^+$]. Figure 4.8 presents the different types of Ge detectors employed along the EXILL campaign together with their placement in the frame. The configuration shown corresponds to the spectroscopic part of the campaign, named EXILL. To keep the germanium detectors refrigerated an automatic auto-filling system that pumped in liquid nitrogen was specially designed for the EXILL campaign. The system filled in the Ge detectors three times per day and the temperature of each single clover detector was continuously monitored.

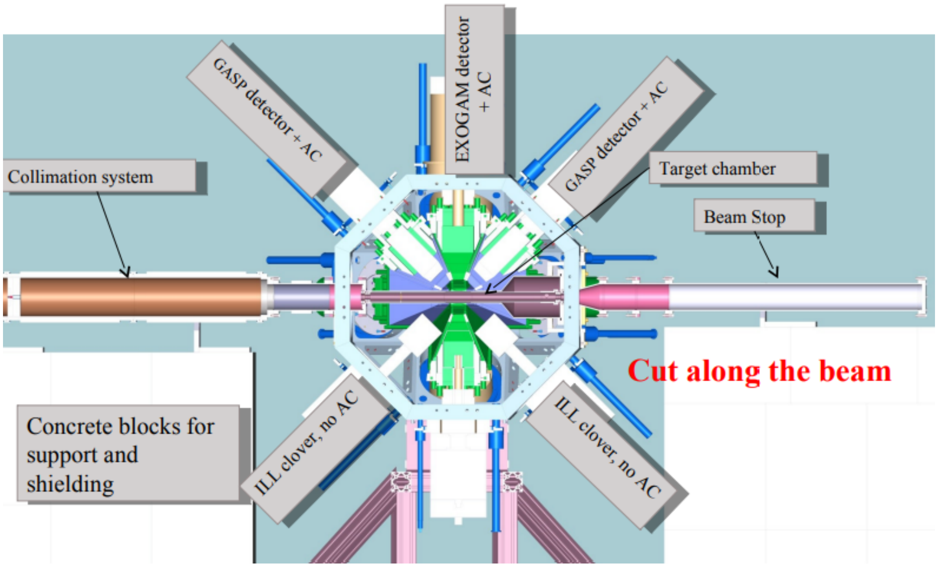

**Figure 4.8: Schematic view of the different Ge detectors employed during the EXILL-FATIMA campaign and their placement.** - A schematic layout of the different Ge detectors used during the EXILL-FATIMA campaign and their placement in the frame [BdFD+13, JBdF+]. The drawing also displays the collimation system, the target chamber and the concrete blocks for supporting the shielding. The configuration shown corresponds to the spectroscopic part of the campaign, EXILL. Sketch taken from [JBdF+].

### 4.3.2 Hybrid configuration of the EXILL-FATIMA spectrometer

During the second part of the campaign, the FAst Timing Array FATIMA was mounted around the central octagon of EXILL, keeping in the spectrometer eight BGO-shielded EXOGAM clovers placed at a distance of 14.5 cm from the target. The FATIMA array counted with 16 $LaBr_3$ (Ce) detectors that were arranged into two rings at both sides of the central octagon, with detectors angles of 40° and 140° relative to the beam direction. All $LaBr_3$(Ce) crystals were 1.5 inch in diameter, but eight were 1.5 inch in length while the other eight were 2 inch in length. To obtain the highest $\gamma\gamma$ coincidence efficiency in $LaBr_3$(Ce)-$LaBr_3$(Ce), the faces of the shorter crystals (1.5 in.) were fixed at a distance of 8.5 cm relative to the target almost touching each other. All $LaBr_3$(Ce) crystals were commercially produced with a 5% of Ce doping concentration and were coupled to Hamamatsu R9779 photomultiplier tubes (PMT) [Ham09, Gob]. The anode pulses from all PMTs were used for timing measurements and the dynode signals for energy. As reported in Chapter 3 the Hamamatsu R9779 is the best suited photomultiplier tube for the use of $LaBr_3$(Ce) crystals and has become the current standard in the application of the fast-timing methods. It exhibits superior timing capabilities than any other PMT model currently available at the market [FMV+13, VMF+15]. In addition to its excellent timing performance, it delivers relatively good energy resolution and conserves energy linearity.

The procedure followed to set the PMT bias voltages consisted in selecting the HV values that provides anode output signals of 1 V in amplitude for 1 MeV photons. The HV values range between 1100 and 1200 V for all the PMTs. Setting the bias voltage in this way assures that all detectors have the same transfer function, *i.e.* the same amplitude vs. energy characteristics, which favours a similar time walk for all the $LaBr_3$(Ce). One should note that the bias voltage values that provide the best time response are around 1200 V. Therefore, powering the Hamamatsu R9779 PMTs with 1100-1200 V should provide very good timing performance. The time resolution of the setup is limited by the $LaBr_3$(Ce) detectors, which has two contributions one coming from the crystal itself and a second one coming from the PMT, as discussed in Chapter 3.

Figure 4.9 provides a schematic layout of the hybrid EXILL-FATIMA spectrometer on the left hand side of the image. The Ge-Clover detectors are drawn in orange with the BGO-shielding highlighted in red. $LaBr_3$(Ce) detectors are marked in gray indicating the aluminium cases in which they are arranged.

## 4.4 Electronics and data acquisition

The electronic scheme of the hybrid spectrometer can be divided into two branches. The first one corresponds to the spectroscopic part of the setup composed of BGO-shielded HPGe detectors [JBdF+], and the second one to the EXILL-FATIMA arrangement [RSB+14], which includes 16 $LaBr_3$(Ce) detectors to the central ring of eight EXOGAM clovers. Consequently, the second branch is composed of the electronics related to the EXOGAM clovers in addition to and the ones related to the $LaBr_3$(Ce) detectors.

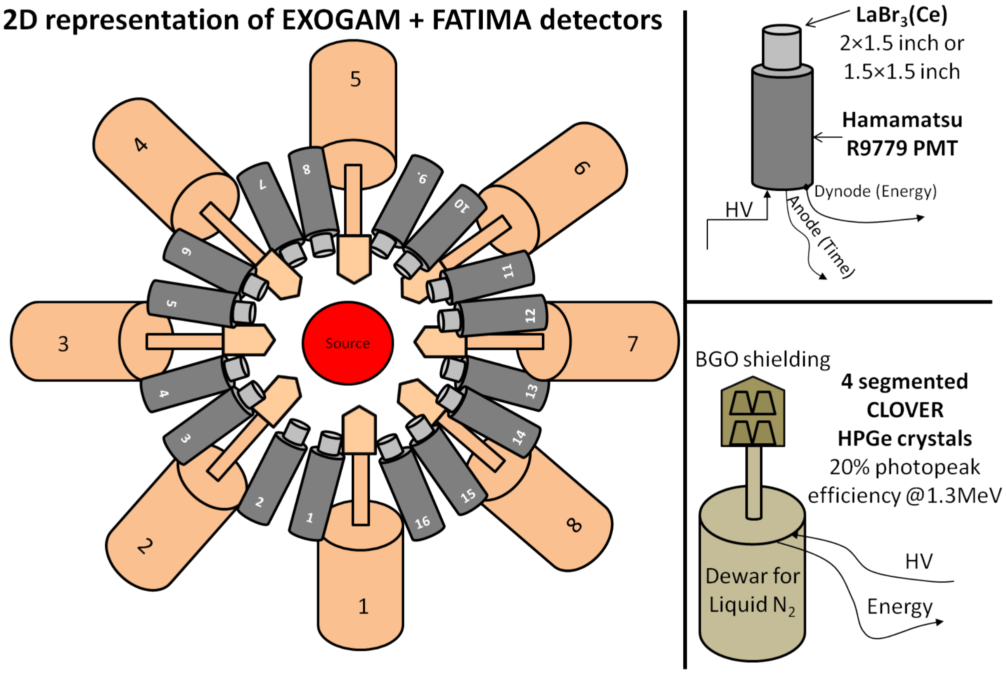

**Figure 4.9: Schematic layout of the EXILL-FATIMA spectrometer and the employed detectors.** - The left part of the drawing shows a sketch of the EXILL-FATIMA spectrometer. The Ge-Clover detectors are drawn in orange with the BGO-shielding highlighted in red and LaBr$_3$(Ce) detectors are marked in gray. All detectors are labeled with their assigned numbers and the target position is marked with a red circle in the middle of the spectrometer. On the right hand side of the drawing a schematic description of the Ge and LaBr$_3$(Ce) detectors is provided. The image is taken from Vadym Paziy [Paz].

In the branch relative to the HPGe-Clovers, the analog signals coming from the HPGe preamplifiers were digitised by ten VME CAEN V1724. Each 1-unit wide VME module contains 8 channels of 14 bits and 100MS/s digitizers [CAE]. All modules were phase locked to an external clock provided by a master V1724 card, with a sampling time of 10 ns and an uncertainty of 1 channel (10 ns). The information relative to the amplitude of the pulses and the arrival time processed by the VME V1724 cards was collected by two RIO3 Power-PC-based VME single board computer and wrote into a hard disk in list mode, the boards worked as data concentrator and were provided with a 256 MB memory. The total event rate achieved was 900 kHz with 7.2 MB/s of data.

All germanium detectors except the LOHENGRIN-ILL ones were shielded with active BGO Compton-suppression structures. The signals from the segments of a BGO shield covering each germanium detector were daisy-chained together and saved with those from the HPGe crystal in list mode. The anti-coincidence discrimination procedure was performed off-line.

The electronic branch relative to the FATIMA array entails the electronics associated to the $LaBr_3$(Ce) detectors. The negative anode signals from all PMTs were used for timing measurements, they were directly fed into an analogue ORTEC 935 Constant Fraction Discrimination (CFD) [ORT], where the arrival time of every signal was determined by the constant fraction triggering method. In this complex setup with 16 $LaBr_3$(Ce) detectors using a time processing channel for every detector pair would imply a total of 120 channels. The solution adopted here is the multiplexing of Stop signals using logic fan-in/fan-out modules. The CFD outputs were sent to analog Time to Amplitude Converter (TAC) modules model ORTEC 567. Each TAC module is started by a single detector i, but stopped by j detectors, with j>i and 1≤i, j≤16. Each individual time peak for the 120 detectors combinations is individually adjusted to fit in the center of the 50 ns TAC range by tuning the cable length between the electronic modules.

The TAC modules deliver square pulses whose height corresponds to the time difference between the start and the stop signals. Each start-stop combination can be selected by imposing extra conditions on the $LaBr_3$(Ce) detectors. The TAC output signals containing the time differences information are digitized by VME CAEN V1724 cards [CAE]. The intrinsic resolution of the TAC and ADC electronics was measured to be below 16 ps. The last dynode signals of all PMTs were used for the energy measurement. The fast pulses were shaped by home-made RC circuits that provide signals with a decay time of about 2 $\mu$s and afterwards were sent to the VME CAEN V1724 modules [CAE] for digitization. Every signal was processed and stored in triggerless mode in a triple list-mode containing the information of the channel ID, the amplitude and the arrival time. All passive electronic components such as coaxial cables were carefully tested in advance to avoid systematic errors.

Figure 4.10 provides an illustrative scheme of the FATIMA electronics. Since the scheme could result complicated to follow due to the big amount of components Figure 4.11 provides a simplified version of the electronics scheme.

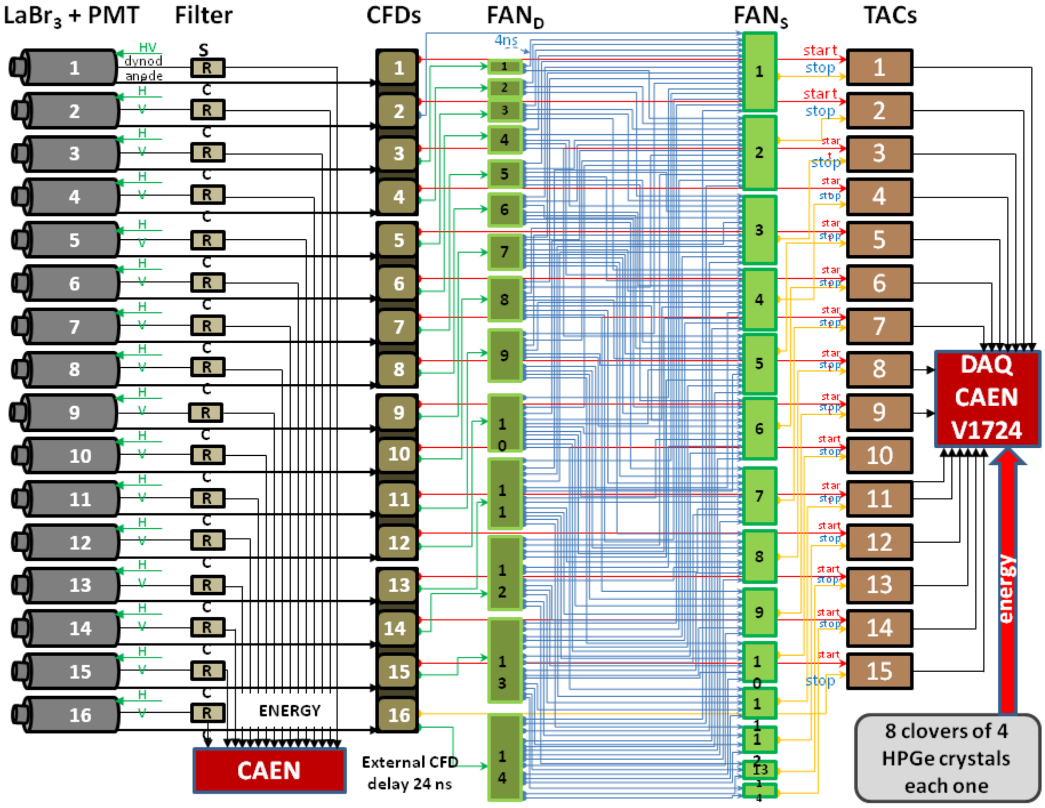

**Figure 4.10: Electronics scheme of the FATIMA branch of the hybrid spectrometer.** - A schematic layout of the electronics setup for the FATIMA branch. The negative anode signals of the $LaBr_3$(Ce) detectors were used for timing measurements, while -dynode pulses were used for energy determinations. The arrival time of every anode pulse is given by the use of analogue Constant Fraction Discriminators (CFD) ORTEC 935, and the time differences are calculated by analogue Time to Amplitude converters (TACs). For pulse digitization several VME CAEN V1724 modules were employed. The scheme is taken from Vadym Paziy [Paz].

Despite it was found that the best values of time resolution when using $LaBr_3$(Ce) detectors and the ORTEC 935 CFD are achieved for short delays of around 1.5 ns (Chapter 3), in the current setup we prefer to trade time resolution and time walk stability and the CFD external delay was set at 24 ns. The reason for this is to obtain a very stable time walk distribution with the smoothest possible trend. Very short shaping delays provide the best values of time resolution, however, the time walk may become sensitive to variations of the zero-crossing parameter Z, slight changes may cause substantial variations in the time walk. Long shaping delays that trigger in the decay part of the signal provide smooth and stable time walk distributions at expenses of 30% worse values of time resolution.

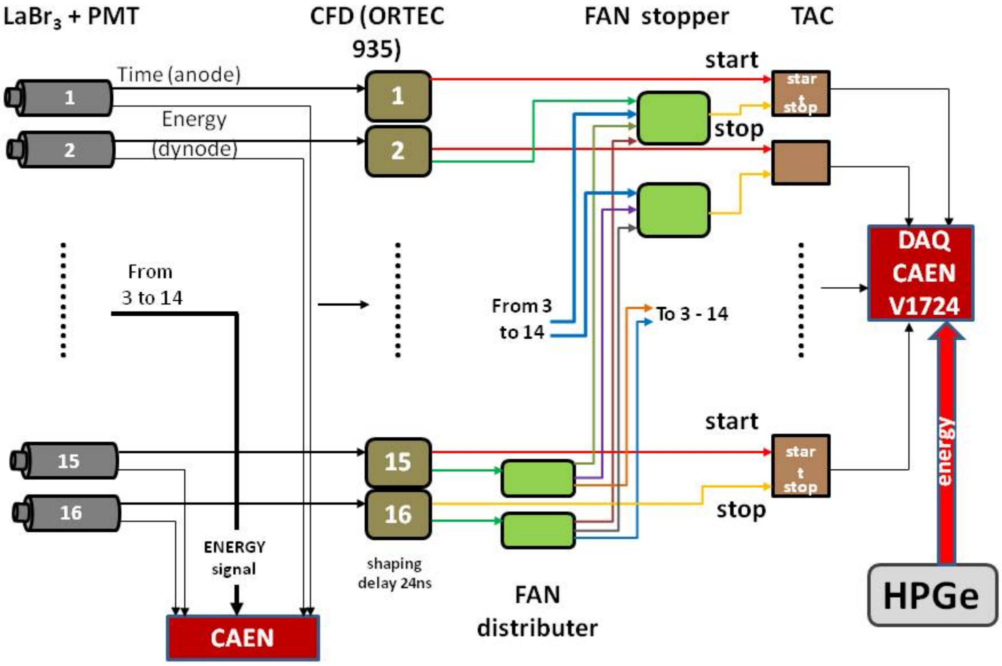

**Figure 4.11: Simplified electronics scheme of the FATIMA branch.** - A simplified layout of the electronics setup relative to the FATIMA branch. The negative anode signals of the $LaBr_3$(Ce) detectors were used for timing measurements, while the last dynode pulses were used for energy. The arrival time of every anode pulse is determined by the use of analogue Constant Fraction Discriminators (CFD) ORTEC 935, and the time differences are calculated by analogue Time to Amplitude converters (TACs). For pulse digitization several VME CAEN V1724 modules were employed. The scheme is taken from Vadym Paziy [Paz].

Data taking was triggerless and divided in short runs of around 2 GB each, with a normal count rate of 10-20 KHz per channel, and time intervals of 7-15 minutes. Every run contained enough statistics to monitor the system performance. During the EXILL campaign about 60 GB data were recorded.

# 5

# Data Analysis of EXILL-FATIMA campaign

Data collected during the EXILL-FATIMA campaign involves a large number of detectors, and different detectors combinations, being therefore, a rather complex set of data that needs to be sorted and analyzed. In addition, there is an extra level of complexity involved by the delicate time calibrations of the fast-timing detectors, which are required as a consequence of the time response of the system. This Chapter describes the data handling and the preparation together with the analysis tools employed and the analysis procedures.

## 5.1 Data structure and the SOCOv2 software

Data recorded during the EXILL-FATIMA campaign were arranged in a list-mode structure containing the information relative to pulse amplitude, arrival time and detector type. Data were recorded triggerless without any intrinsic grouping among the list-mode files, being necessary to sort the hits from the detectors into valid events.

For the data analysis of the EXILL-FATIMA campaign, a special software called SOCOv2 was developed at the Institute of Nuclear Physics of Cologne (IKP) by N.Saed-Samii *et al.* [SSb]. The program is C++ based, works following a command scheme and was tailored to handle big data sets such as the 60 TB of triggerless data measured in the current experiment. In principle, SOCOv2 is able to utilize the full computer power by extensive parallel processing and allows the implementation of new commands, being extensible to future analysis methodologies.

For the task of event building, SOCOv2 is equipped with Listmode-reader classes and an Event-Builder tool. Concerning coincident projections, SOCOv2 contains the Gate Spectra command for building $\gamma$-$\gamma$ matrices and the Ft-Matrix tool for the timing analysis [SSb]. The SOCOv2 software requires certain input files such as the channel configuration, the energy calibration or the drift corrections, whose structure and contents are explained in the following sections. A complete set of the configuration files containing tested examples was internally distributed by J.-M. Régis to the EXILL-FATIMA collaboration [Rég].

## 5.2 Event Builder

An event is defined as a set of hits having occurred within a pre-determined coincidence window, with a valid configuration of channels and with only one hit per channel. The Event-Builder tool of SOCOv2 reads the information from the list-mode files and groups the hits following given conditions into events, providing output files in the .evt format. Additionally, SOCOv2 also provides calibrated and uncalibrated total projections. After this step, the amount of data is reduced by approximately one order of magnitude. Before sorting the events, there are several important considerations that should be taken into account, such as the time-stamp offsets, the coincidence time window, the channel configuration, the energy calibrations and the detectors drifts. The Event-Builder tool needs the following inputs for an optimal working:

- Requirements-configure file: Sets the coincidence conditions.
- Coincidence window size: Indicates the window size for grouping the hits.
- Channel-configure file: Provides the information on the channels in use.
- Calibration file: Includes the calibration of every channel (optional).
- Shifts-dir: Contains the information for correcting detectors drifts.
- Runlist: A list containing all the list-mode files that will be sorted.

A common collection of requirements for the analysis of the EXILL-FATIMA data set containing the Channel-configure file, the Calibration files, Shifts-dir and examples of Requirements-configure files, were provided by J.-M. Régis within the internally distributed set of the configuration files [Rég]. The following Figures 5.1, 5.2 and 5.3 have been taken form the SOCOv2 manual [SSb].

### 5.2.1 Time-stamp offsets

Before sorting the events, it is important to consider whether coincident hits from different types of detectors do not reach the digitizer at the same time because of the divergent electronic pathways (CFD, TAC) and the different detector nature (HPGe, $LaBr_3$(Ce) and BGO). Hence, it is necessary to determine the timestamp offsets and to align the incoming signals before sorting the events. To address this issue, SOCOv2 includes the command "timestamp-shift", which reads list-mode files and calculates the time differences between every detector and a reference that is defined by the user. All the information provided by the Timestamp-shift tool is summarized in the output file summary.info, and it will be incorporated into the channel configuration file that is required to build the events. Figure 5.1 presents four timestamps distributions of different types of detectors: a HPGe-Clover, a BGO, a $LaBr_3$(Ce) and TAC with respect to the reference channel zero, which is Clover 0-0. The plots have been taken from the SOCOv2 manual [SSb].

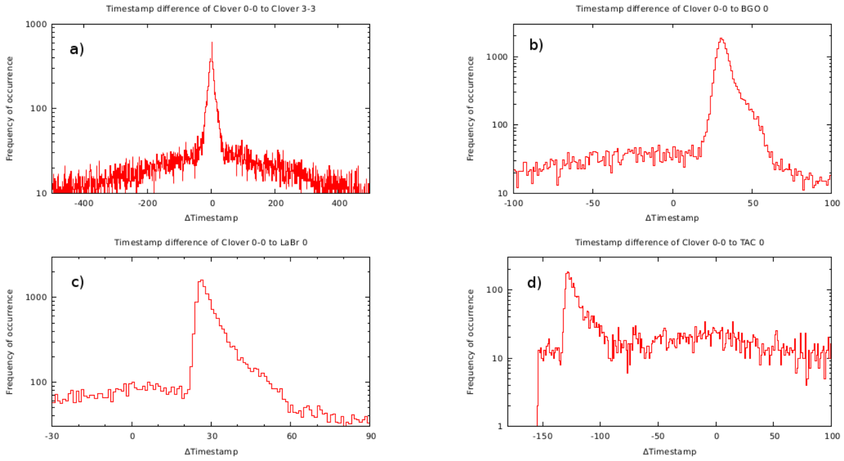

**Figure 5.1: Time-stamps offsets.** - Time-stamps offsets of four different types of detectors with respect to the Clover 0-0 that is taken as the reference channel. The a) panel plots the offset between the Clover 3-3 and the Clover 0-0, while the plot b) the offset between the BGO 0 and the reference Clover 0-0. The lower panels c) and d) display the offsets between a $LaBr_3$(Ce) and a TAC with respect to the Clover 0-0 reference.

### 5.2.2 Coincident time window

The size of the coincident window when grouping the hits into events is a key factor since a small window will contain too few true events while a too large window will include too many random hits. Hence, to determine the optimal window size, SOCOv2 has the command Multiplicity-info that provides a matrix containing the information of valid events and the multiplicity as a function of the window size. It is important to correct the timestamp offsets before determining the coincidence window, otherwise, it would be much larger than required. The current analysis has been performed with a coincidence window of 120 ns.

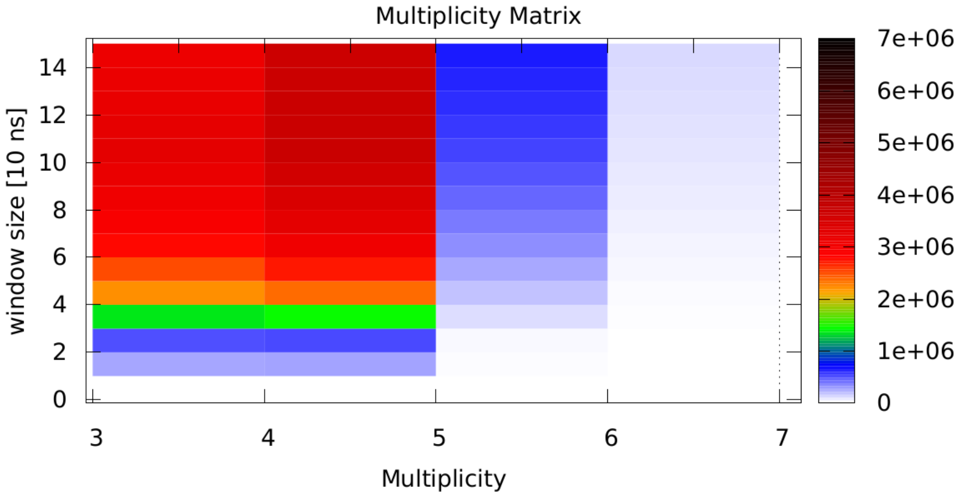

**Figure 5.2: Multiplicity Matrix.** - An illustrative example of a multiplicity matrix. The data corresponds to the $^{152}$Eu source sorted with the requirements of two LaBr$_3$(Ce) detectors and one TAC in a range from 10 to 140 ps. The X-axis provides the multiplicity information, while the Y-axis the window size.

### 5.2.3 Energy calibration

In order to calibrate the detectors in energy, SOCOv2 incorporates the Dump tool that provides raw spectra, i.e. counts vs channels, for every detector that appears in the list-mode file. Once the calibration functions are calculated they are saved in the input calibration file for further steps in the analysis. SOCOv2 can handle polynomial calibrations of any degree thanks to the Polynomial class that is implemented.

### 5.2.4 Detectors drifts

In experiments that span over long periods, detector signals may suffer from gain shifts as a consequence of electronic drifts, temperature changes and the continuous bombardment of particles. This effect worsens the energy resolution and makes calibration functions only valid for few runs. Hence, SOCOv2 is equipped with the Shift-Tracker tool that uses the raw spectra obtained with the Dump command and creates polynomial fits that map the drifted peaks back to the corresponding position with respect to a given reference. This task is done for every detector in every list-mode file.

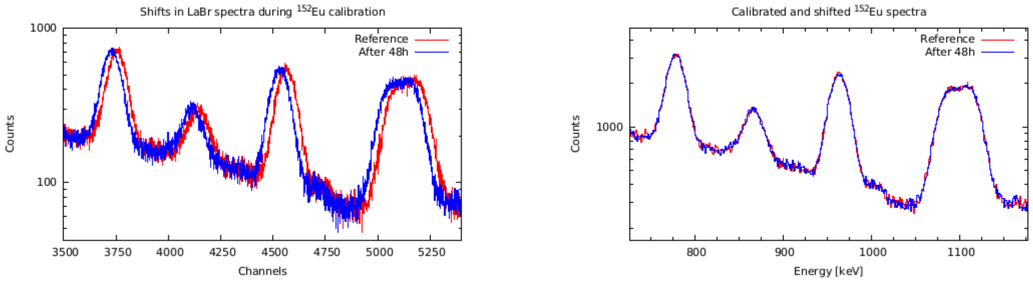

**Figure 5.3: Detectors drifts.** - Drift example of two LaBr$_3$(Ce) detectors over 48h (left). The panel on the right shows the two of them after drift corrections.

### 5.2.5 Event multiplicity

A valid event is composed of a set of hits that have occurred following certain given conditions within a coincidence time window. In the present analysis, these conditions are indicated to SOCOv2 through the requirement-configure file which contains the maximum and the minimum amount of channels firing, as well as the detector type. An example of the requirements-configure inputs is shown in Table 5.1.

The condition for a double event is the arrival of two $\gamma$-rays to two different detectors, such as two LaBr$_3$(Ce). Out of these events, it is possible to measure half-lives of nuclear-excited states through the time differences between the arrival of a $\gamma$-ray that populates a level and the arrival of the $\gamma$-ray that de-excites it. Table 5.1 provides the requirements for sorting double $\gamma$-$\gamma$(t) events, with two LaBr$_3$(Ce) and a TAC.

| type | min | max |
|---|---|---|
| CLOVER | 0 | 0 |
| LaBr | 2 | 2 |
| TAC | 1 | 1 |

**Table 5.1: Double events.** - Requirement-configure file for sorting double events. The number of Clovers is zero as there are only $\gamma$-$\gamma$(t) coincidences required. The number of $LaBr_3$(Ce) is two for lifetime measurements. The sorting also includes one TAC to extract the timing information.

In fission studies of exotic nuclei, such as the present experiment, it is not possible to uniquely select two $\gamma$-rays in $LaBr_3$(Ce) detectors belonging to a given nucleus, due to the high number of $\gamma$-rays simultaneously emitted by the fission products, being therefore necessary an extra coincident condition. To this end, we take advantage of the good energy resolution of the HPGe-clovers, setting one or more high-resolution energy gates in a $\gamma$-transition from the nucleus of interest. An event containing three $\gamma$-rays in coincidences is coined Triple event. Triple events consisting of one HPGe-Clover and two $LaBr_3$(Ce) hits will be referred as $\gamma\gamma\gamma$(t). These events contain also the time information provided by the TAC. For the analysis of the contents of the gates and in the cases when the level structure of the nuclei under study is not known triple clover events, $\gamma\gamma\gamma$, are used.

In the present analysis double events have been used when dealing with calibration sources like $^{60}$Co, while a substantial part of the complete analysis has been performed using triple events. Tables 5.1 and 5.2 show examples of the requirement-input files for sorting double and triple events. In table 5.1 there are only conditions on the $LaBr_3$(Ce) and on the time (TAC), while in 5.2 the extra condition of a $\gamma$-ray hitting a HPGe-Clover is included. In this case, the requirement file accounts for a minimum of one HPGe crystal and a maximum of four HPGe crystals to allow add-back reconstruction within of a HPGe-Clover. The add-back reconstruction procedure is explained in detail in the following Section 5.5.2.2.

| type | min | max |
|---|---|---|
| CLOVER | 1 | 4 |
| LaBr | 2 | 2 |
| TAC | 1 | 1 |

**Table 5.2: Triple events.** - Requirement-configure file for sorting triple events. The minimum number of Clovers is one to account for $\gamma$-$\gamma$-$\gamma$(t) coincidences and the maximum is four to allow for add-back reconstruction. The number of $LaBr_3$(Ce) is two as in the former example for lifetime measurements.

In fission experiments like the EXILL-FATIMA campaign, as a consequence of the numerous fragments that are produced, the amount of $\gamma$-rays present is very high with a substantial background, with the fission partners contributing to the level complexity. Hence, the use of two high-resolution HPGe-gates for sorting the events instead of only one may prove convenient. However, one should find the right balance between the background reduction and the statistics, as the probability of recording quadruple $\gamma$-$\gamma$-$\gamma$-$\gamma$ events is 1-5% of the efficiency for triple events. Table 5.3 provides an example of the requirement-file for sorting quadruple events. In this example, the maximum number of Clovers is eight to allow for add-back reconstruction.

| type | min | max |
|---|---|---|
| CLOVER | 2 | 8 |
| LaBr | 2 | 2 |
| TAC | 1 | 1 |

**Table 5.3: Quadruple events.** - Requirement-configure file for sorting quadruple events. The minimum number of Clovers is two to account for $\gamma$-$\gamma$-$\gamma$-$\gamma$(t) coincidences and the maximum is eight to allow for add-back reconstruction. There are two $LaBr_3$(Ce) detectors and one TAC for lifetime measurements.

The examples of requirement-configuration files shown in this work only contain three types of detectors: HPGe-Clovers, $LaBr_3$(Ce) and TACs, because they are the options of interest. Nevertheless, SOCOv2 has the possibility to work with a wider range of detectors, for further information see [SSb].

## 5.3 Coincident spectra

Coincident spectra provide the necessary information to construct the nuclear level scheme and to measure the lifetime of excited states. Therefore, the next step after sorting the events is to build coincident spectra applying conditions on the detectors firing. The Gate-spectra command provides the coincident projection of every channel when a defined set of conditions are selected through the gate-configuration file. There are three types of gates that can be accepted: detector type, detector ID and add-back gate. In the ID type, the coincident conditions are applied only to the selected detectors according to their ID, in the detector type the conditions are applied to all detectors of a given type and the add-back gate allows for add-back reconstruction. The following Tables 5.4, 5.5 and 5.6 show examples of the Gate-configure files.

| #channel ID | min | max |
|---|---|---|
| 138 | 340 | 360 |
| 140 | 413 | 433 |

**Table 5.4: ID type Gate-configure file.** - Gate-configure file where the coincident conditions are applied only to the selected detector according to their ID. In this example, there are two conditions on the energy of two $LaBr_3$(Ce) detectors, with ID numbers 138 and 140.

| # Gate type | min | max |
|---|---|---|
| LABR | 340 | 360 |
| LABR | 413 | 433 |
| CLOVER | 604 | 608 |

**Table 5.5: Detector type Gate-configure file.** - Gate-configure file where the coincident conditions are applied to types of detectors. In this example, there are conditions on two energies of $LaBr_3$(Ce) detectors and one energy of Clover detectors.

| #Addback | type | threshold | min | max |
|---|---|---|---|---|
| Addback | CLOVER | 20 | 604 | 608 |
| Addback | CLOVER | 20 | 350 | 355 |

**Table 5.6: Add-back type Gate-configure file.** - Gate-configure file that allows for the add-back reconstruction in the Clovers. It contains the minimum threshold for the reconstruction which in this example is 20 keV and the energy range of interest in keV for the reconstruction.

In addition to the Gate-configure files, the Gate-spectra command requires the following input:

- Calibration-configure: Includes the calibration of every channel.
- Channel-configure file: Provides all information regarding the channels.
- Gate configure: Indicates de coincident conditions.
- Shifts-dir: Contains the information for correcting detectors drifts.
- BGO-Threshold: Sets the thresholds for the anti-Compton subtraction.
- Exclude-configure: Contains the detectors combinations that should be excluded.
- TAC-shifts-configure: Provides the shifts for TAC alignment (optional).

The Calibration-configure file, which contains the energy calibration of every channel, the Channel-configure file with all information relative to channel configuration, and the Shifts-dir file with the drift corrections are the same inputs as those used for building the events (See Section 5.2). These SOCOv2 requirements together with the BGO-Threshold, the Exclude-configure file and the TAC-shifts-configure are (in principle) common to the analysis of the full set of EXILL-FATIMA data [Rég].

When selecting an energy region that contains a Full Energy Peak (FEP), the background underneath the FEP influences the results, being the time distributions especially affected. Considering the large amount of $\gamma$-rays produced in this experiment, it is likely that many of them would scatter around the setup contributing to a high level of background. It is therefore, an important issue to consider. To this aim, there are several useful strategies for background reduction.

In the present analysis the approaches that are listed in the following are used:

*a*) Exclude some detectors combinations.

*b*) Perform add-back full-energy reconstruction.

*c*) Compton suppression of Ge-events that are in coincidence with BGO-shielding.

*d*) Subtraction of the events that are in coincidence with background under. FEPs.

The *a)*, *b)* and *c)* approaches complement each other and can be easily implemented using the SOCOv2. The *d)* strategy is not implemented in the software, and therefore needs to be carried out after performing the sortings (Gate-spectra or Ft-matrix). Details are presented in subsection 5.5.2.

### 5.3.1 Exclusion of certain detector combinations

One of the principal drawbacks of experiments performed with detectors positioned in a compact geometry is the inter-detector Compton-scattering. As the detectors are placed very close to each other to increase the solid angle covered, there is a high probability that (depending on the energy) a $\gamma$-ray impacts first on one detector not leaving its full energy, hitting afterwards a neighbour clover detector leaving part of its energy or the totality. This effect results in unwanted satellite and phantom peaks next to the full-energy peaks and is of particular relevance for the $LaBr_3$(Ce) detectors. To address this problem, the Gate-spectra command accepts a list of the detector combination that should be excluded if they fired simultaneously. The most performing detector combinations regarding the excluding procedure are provided in Table 5.11.

### 5.3.2 Anti-Compton

The HPGe detectors used in this experiment, the EXOGAM clovers, are equipped with active Compton-suppression shields made of BGO detectors [Aza99, SAF$^+$00, EXO]. The procedure works in the way that when there is a coincidence between one HPGe crystal and the corresponding BGO, the hit stored in the Clover is discarded, because it corresponds to a Compton-scattering event: the $\gamma$-ray has not deposited all its energy in the Clover, only a fraction, that contributes to the background instead of to FEP events. The Compton suppression strategy becomes more efficient as the energy of the incoming $\gamma$-ray increases, especially in the high energy region, where Compton effect dominates over photoelectric effect.

### 5.3.3 Add-back in Clovers

EXOGAM clovers are comprised of four Ge-crystals with the aim of increasing the granularity to provide the ability of add-back reconstruction. When a $\gamma$-ray scatters from one crystal to second crystal inside of the same Clover, it is possible to get the initial energy of the $\gamma$-ray by adding the two energies. The add-back reconstruction works for the combination of two to four crystals within the same Clover, but it is better implemented for two crystals at energies around 1 MeV. The specific instructions for the reconstruction are given to the Gate-spectra tool through the add-back type gate configure file, an example is shown in Table 5.6. This type of gate can be combined with the other types.

### 5.3.4 Alignment of the time distributions

Although during the setting up of the Time to Amplitude Converter modules, the length of the cables that feed the signals into the TACs from the Constant Fraction Discriminator, and Fan in/out modules, has been carefully selected in order to align all the centroids of the fifteen TACs, there are still some small misalignments. Thus, when considering the superposition of the valid time distributions the individual shifts produce a broadening of the total Gaussian time peak, leading to spurious asymmetries to appear. To solve this issue, TACs should be proof-aligned one by one. The information related is listed in the TAC-shifts-configure file, that works as an input for the Gate-Spectra and Ft-matrix command.

## 5.4 The Fast-Timing Matrix

A key part of the lifetime analysis is the construction of fast-timing matrices. They are tridimensional objects that contain the energy information about the coincident $LaBr_3$(Ce), namely the $\gamma$-ray energies of the transitions that populate and de-excite a level together with the associated time differences in the third axis. To this end, SOCOv2 is featured with the Ft-Matrix tool that provides two output matrices called “Start” and “Stop”. The first step to build the matrices is to select the gating conditions. It consists in setting a $LaBr_3$(Ce)-type gate in one energy transition that could be the feeding or the decaying $\gamma$-ray of the level of interest and certain additional high-resolution gates in different transitions of the cascade for cleaning the events in coincidences. The gating conditions are provided to the Ft-Matrix tool through the Gate-configuration file and similar to Gate-Spectra. The background and the amount of Compton underneath the Full Energy Peaks (FEPs) can be reduced by excluding some detectors combinations, performing add-back reconstruction and discarding Ge-events in coincidences with the BGO shielding (see section 5.3). The Start and Stop matrices contain the energy of the second-selected $\mathrm{LaBr_3(Ce)}$ in the rows and the corresponding TAC information in the columns, and they are produced with the assumption that a $\mathrm{TAC}_i$ can only be started by a $\mathrm{LaBr_3(Ce)}_i$ and stopped by a $\mathrm{LaBr_3(Ce)}_j$, where i< j. The Start matrix is filled up with the coincident events that have started the TACs when the $\gamma$-ray selected in the input file has stopped them while the Stop matrix is composed of all of the events that have stopped the TACs when the selected $\gamma$-ray has started them. Regarding the input files, the Ft-Matrix command requires the same inputs as the Gate-spectra command, listed in section 5.3 [SSb]. Once the Start and Stop matrices are built, the next step is to calculate the time distributions that contain the time differences between the $\gamma$-transition that populates the level and the one that de-excites it. This is done by selecting the coincident $\gamma$-ray on the energy axes and projecting into the time axis. The coincident $\gamma$-ray can either be the feeding or the decaying transition depending on what was selected in the gating-input file. The obtained time distribution is composed by the sum of the individual TAC spectra coming from the valid combinations of feeder-decay $\gamma$-rays working as start-stop in the TACs. The procedure described in subsection 5.3.4 for the alignment of every single time distribution results crucial at this point.

In the present analysis, the projections on the time and the second gating step were performed using the program Tv [Fit]. The Tv-Software was developed by Andreas Fitzler and colleges at the Institut fr Kernphysik of Cologne (IKP), with the aim of spectra visualization and data analysis for nuclear experiments. Although this particular Tv-Software was used in the current analysis, the SOCOv2 outputs are compatible with a wide range of programs [SSb]. For operating with the output matrices and vectors the set of programs provided by N. Saed-Samii [SSa] has been also used.

## 5.5 Choice of the best conditions for the analysis

As discussed earlier, in induced fission experiments with the characteristics of the EXILL-FATIMA campaign, the amount of fission fragments and the $\gamma$-rays produced is considerably high, being therefore very probable to find two or more $\gamma$-transitions so close in energy that cannot be resolved. With these conditions, the selection of the relevant nuclei turns into a very difficult task. In addition to the high $\gamma$-ray multiplicity, the large background produced by the Compton scattering of the numerous $\gamma$-rays around the setup also hampers the accurate selection of the nucleus of interest. Besides the $\gamma$-multiplicity and the prominent background, one should consider that the data were recorded triggerless during 100 days, constituting a total amount of 60 TB. Hence, it is very important to wisely select the analysis conditions.

### 5.5.1 Target selection

During the EXILL-FATIMA campaign, two different fission targets made of $^{241}$Pu and $^{235}$U were used, providing good access to production regions that were not reached before for fast-timing measurements [JBdF$^{+}$, RSB$^{+}$14]. The combination of $^{241}$Pu and $^{235}$U materials provide several advantages regarding the production rates, the fission partners and the contaminants. The technical details of the targets were explained in depth in Section 4.2.

#### 5.5.1.1 Fission Yields

The use of two different fission targets has certain advantages such as the complementarity of the production, due to the different fission yields, and the presence of distinct fission partners. Depending on the production of the isotope of interest and the partners that are produced, it may be more favourable to select the data set measured either with the $^{241}$Pu or the $^{235}$U target. In the present analysis, as we focus on tellurium isotopes the preferred target considering the production cross-section is $^{241}$Pu [EXI]. Nevertheless, for cases when the fission yield is sufficient, such as $^{136}$Te, the analysis can be performed using both of them, and in addition, this provides a good cross-check of the results. Tables 5.7 and 5.8 show the thermal neutron fission yields in % for tellurium isotopes when using a $^{241}$Pu and $^{235}$U targets.

| **Isotope** | $^{136}$**Te** | $^{137}$**Te** | $^{138}$**Te** | $^{139}$**Te** |
|---|---|---|---|---|
| **Yield from JEFF3.3 (%)** | 2.1(4) | 5.5(17)$\times10^{-1}$ | 1.5(5)$\times10^{-1}$ | 1.9(7)$\times10^{-2}$ |
| **Yield from ENDF/B VIII.0 (%)** | 1.7(4) | 5.0(3)$\times10^{-1}$ | 1.1(7)$\times10^{-1}$ | 1.9(7)$\times10^{-2}$ |

**Table 5.7: Thermal neutron fission yields of the $^{241}$Pu target for Te.** - Thermal fission yields of the $^{241}$Pu target for the $^{136,137,138,139}$Te isotopes. Values are given in percent and were extracted from the JEFF3.3 and ENDF/B VIII.0 databases and [LAdB$^+$10].

| **Isotope** | $^{136}$**Te** | $^{137}$**Te** | $^{138}$**Te** | $^{139}$**Te** |
|---|---|---|---|---|
| **Yield from JEFF3.3 (%)** | 1.7(3) | 4.9(15)$\times10^{-1}$ | 1.1(4)$\times10^{-1}$ | 1.7(6)$\times10^{-2}$ |
| **Yield from ENDF/B VIII.0 (%)** | 1.34(11) | 4.5(5)$\times10^{-1}$ | 6.6(21)$\times10^{-2}$ | 6.7(21)$\times10^{-2}$ |

**Table 5.8: Thermal neutron fission yields of the $^{235}$U target for Te.** - Neutron-induced fission yields of the $^{235}$U target for the $^{136,137,138,139}$Te isotopes, in percent. Values were extracted from the JEFF3.3 and ENDF/B VIII.0 databases and [LAdB$^+$10].

In view of the fission yields, we conclude that the most performing strategy for the $^{136}$Te analysis is to use both targets. The approach would consist firstly in deriving the lifetime for each target separately, if possible, and secondly in a comparison of the results.

#### 5.5.1.2 Fission Partners

An important concern in the analysis is the presence of fission-partners. They are produced simultaneously with the nuclei of interest, appearing in coincidence within the gating conditions. Fission partners may even contain $\gamma$-transitions with energy close to those under inspection, being an important source of background. They might also have long-lived states that hamper the timing analysis and induce errors. Therefore, a careful investigation of the fission partners that come together with the isotopes under study is important before selecting the most suitable fission target.

The nuclear composition of the partners is determined by the atomic (Z) and mass (A) numbers of the targets in use and by the isotope of interest, hence, for the Te isotopes with Z=52, when considering the $^{241}$Pu target (Z=94), different Molybdenum isotopes (Z=42) would come as the fission partners, while for the $^{235}$U case (Z=92), the Zirconium isotopes (Z=40) are produced. Then, one needs to consider that the number of neutrons evaporated in the fission reaction ranges from one to eight, being the average for $^{241}$Pu $\overline{\nu}_{\nu}$= 2.94 and $\overline{\nu}_{\nu}$= 2.42 for $^{235}$U [GSI84]. Table 5.9 summarizes the most common fission partners of $^{136}$Te considering the number of evaporated neutrons.

| | **Products** | | | |
|---|---|---|---|---|
| | $^{136}_{84}\mathbf{Te}_{52}$ | | $^{137}_{85}\mathbf{Te}_{52}$ | |
| **Target** | **Partners** | **Most likely** | **Partners** | **Most likely** |
| $^{241}_{147}\mathbf{Pu}_{94}$ | $^{97}$Mo $\leq$ X $\leq$ $^{105}$Mo | $^{103,104}$Mo | $^{98}$Mo $\leq$ X $\leq$ $^{106}$Mo | $^{104,105}$Mo |
| $^{235}_{143}\mathbf{U}_{92}$ | $^{91}$Zr $\leq$ X $\leq$ $^{99}$Zr | $^{97,98}$Zr | $^{92}$Zr $\leq$ X $\leq$ $^{100}$Zr | $^{98,99}$Zr |

**Table 5.9: Fission partners of $^{136}$Te and $^{137}$Te.** - Summary of the fission partners for $^{136}$Te attending to the number of protons and neutrons of the two targets and $^{136}$Te and $^{137}$Te, and the number of evaporated neutrons.

For the case of $^{136}$Te, the most likely partners are $^{103,104,105}$Mo and $^{97,98,99}$Zr with a lower probability of presence of $^{100,101,102}$Mo and $^{93,95}$Zr. Table 5.10 provides the thermal neutron fission yields of the $^{136}$Te partners for the $^{241}$Pu and $^{235}$U targets, taken from [LAdB$^{+}$10]. Regarding the partners, the Molybdenum isotopes do not seem to represent a problem, since their most intense $\gamma$-transitions are not close in energy to the $\gamma$-rays under study in $^{136}$Te, and they can be resolved when applying narrow energy gates in the LaBr$_3$(Ce) detectors. However, one should be cautious because there are long-lived excited states in some Molybdenum isotopes such as $^{104}$Mo [NND]. The situation is more delicate regarding Zirconium partners; in principle, the Zr $\gamma$-rays do not overlap with those in $^{136}$Te, but in Zr isotopes, there are several excited states whose lifetimes are in the ns range [NND].

Therefore, regarding the fission partners, the $^{241}$Pu target is the best option as a starting point. Nevertheless, the $^{235}$U target can also be used to extract an independent value of the lifetimes in $^{136}$Te following the strategy explained in subsection 5.5.1.1 above.

| **Production yields of $^{136}$Te partners** | | | | | | | | |
|---|---|---|---|---|---|---|---|---|
| **$^{241}$Pu** | **Most likely** | | | | **Less likely** | | | |
| **Isotope** | $^{106}$Mo | $^{105}$Mo | $^{104}$Mo | $^{103}$Mo | $^{102}$Mo | $^{101}$Mo | $^{100}$Mo | $^{99}$Mo |
| **Yield(%)** | 3.89 | 4.13 | 3.61 | 1.72 | 0.54 | 0.11 | 0.02 | $1.33\times10^{-3}$ |
| **$^{235}$U** | **Most likely** | | | | **Less likely** | | | |
| **Isotope** | $^{100}$Zr | $^{99}$Zr | $^{98}$Zr | $^{97}$Zr | $^{95}$Zr | | $^{93}$Zr | |
| **Yield(%)** | 4.98 | 3.58 | 2.57 | 1.09 | $1.27\times10^{-1}$ | | $1.37\times10^{-4}$ | |

**Table 5.10: Fission yields of the $^{136}$Te partners when using $^{241}$Pu and $^{235}$U targets.** - Production rates of the $^{136}$Te partners for the $^{241}$Pu and $^{235}$U targets. Values were taken from [LAdB$^{+}$10].

### 5.5.2 Strategies for background reduction

In experiments such as the EXILL-FATIMA campaign that present a considerable number of $\gamma$-rays and with detectors in close-geometry configurations the probability for multiple scattering of a $\gamma$-ray before losing its full-energy is not negligible, giving rise to inter-detector Compton scattering. This yields a high level of background that complicates the proper selection of the Full Energy Peaks (FEP). As background events are also selected when setting energy gates, the time distributions may be significantly influenced, being seriously affected in some cases. In the present experiment, the background level is still high even after having selected three gating conditions (triple coincidences), there are peak to background ratios (P/B) of about one. This is true for triple Ge conditions but even more for germanium-lanthanum-lanthanum(time). Therefore, taking actions to reduce the background is crucial. However, imposing stringent conditions would lead to a significant loss in the statistics, which would yield high statistical uncertainties. For these reasons, it is necessary to reach the optimal balance that minimizes the background while maintaining sufficient statistics. In this analysis, we employed four strategies for background reduction, namely: *a)* exclusion of some detectors combinations, *b)* add-back reconstruction, *c)* discarding Ge-events in coincidence with the BGO shielding and *d)* subtraction of the coincident events with background underneath the Ge-gated FEPs. These corrections were discussed in Section 5.3 above, and explained in detail in the following sections.

In the present work, add-back reconstruction and background subtraction of the Ge-gated FEP-peaks are not used simultaneously to avoid potential over-subtractions. This is due to the manner that the add-back reconstruction is implemented in the analysis software. On the contrary, the exclusion of some detector combinations and the BGOs anti-coincidences are assumed compatible and both are implemented at the same time. In the current analysis, we employ either the add-back reconstruction or the background subtraction, in combination with the exclusion of some detector combinations and the BGOs anti-coincidences.

#### 5.5.2.1 Exclusion of $LaBr_3$(Ce) detector pairs

The inter-detector Compton-scattering increases the background in the $LaBr_3$(Ce) detectors, but it may also produce satellite peaks next to the actual FEPs. We have investigated the effect of excluding some detectors combinations to reduce the unwanted effects and to improve the peak to background ratio while keeping good enough statistics. Tests have been performed using standard $^{60}$Co and $^{152}$Eu sources and the $^{241}$Pu data. For the exclusion procedure, the detectors are grouped in pairs accordingly to the geometry and are labeled as channel ID 1 and channel ID 2. The correspondence between the channel ID and the actual detectors can be found in the schematic diagram from Figure 4.9 in Section 4.3. The best combination of detectors to be excluded is actually the one proposed to the collaboration for the analysis [Rég]. Here, we have verified that this is the most suitable option. Both the peak to background ratio and the time distributions improve when applying the excluding option with these settings. Table 5.11 shows the best combination of detectors to be excluded. Depending on the detector location in the array there are one to four nearest neighbours that need to be excluded. In most of the cases, the total amount of counts is reduced by a 30%, however, the FEPs in the energy spectra are cleaner and the corresponding time distributions sharper.

| Chn ID 1 | Chn ID 2 | Chn ID 1 | ChnID 2 | Chn ID 1 | ChnID 2 |
|---|---|---|---|---|---|
| 128 | 129 | 132 | 133 | 137 | 138 |
| 128 | 130 | 132 | 134 | 138 | 139 |
| 128 | 134 | 133 | 134 | 138 | 140 |
| 128 | 135 | 134 | 135 | 139 | 140 |
| 129 | 130 | 136 | 137 | 140 | 141 |
| 130 | 131 | 136 | 138 | 140 | 142 |
| 130 | 132 | 136 | 142 | 141 | 142 |
| 131 | 132 | 136 | 143 | 142 | 143 |

**Table 5.11: Excluded LaBr$_3$(Ce) combination.** - The most performing combination of detectors to be excluded when gating with SOCOv2. The exclusion is performed in pairs according to the geometry, where detectors are labelled with channel ID 1 and channel ID 2. The correspondence between the channel ID and the actual detectors can be found in the schematic diagram in Section 4.3.

#### 5.5.2.2 Add-Back reconstruction

The add-back reconstruction allows recovering the initial energy of a $\gamma$-ray that has scattered inside a HPGe-Clover detector from one crystal to another. This procedure makes it possible to reduce the background level and to increase the number of true counts in the Full-energy-peaks (FEPs). The Compton events that otherwise will be lost in the background, contribute now to the reconstructed FEP energy. The effect is more relevant as the energy increases, when the Compton effect becomes dominant.

The add-back option may be of help to compute the Ft-matrix since the Compton contribution is reduced while the full-energy response (FEP-FEP) is enhanced. Figure 5.4 illustrates the add-back effect by showing two HPGe-Clover spectra. Both were Ge-gated in the 607-keV $\gamma$-ray and LaBr$_3$(Ce)-gated in the 423-keV transition, with the aim of measuring the lifetime of the $4^+$ state in $^{136}$Te (a partial level scheme is provided in Figure 5.6). The plot in Figure 5.4 shows the reduction of the coincident Compton events at low energies and the enhancement of the counts in the coincident FEPs such as the one at 353 keV.

A similar graph for LaBr$_3$(Ce) spectra is given in Figure 5.5, where two coincident LaBr$_3$(Ce) spectra with the same conditions as those used in Figure 5.4 are shown.

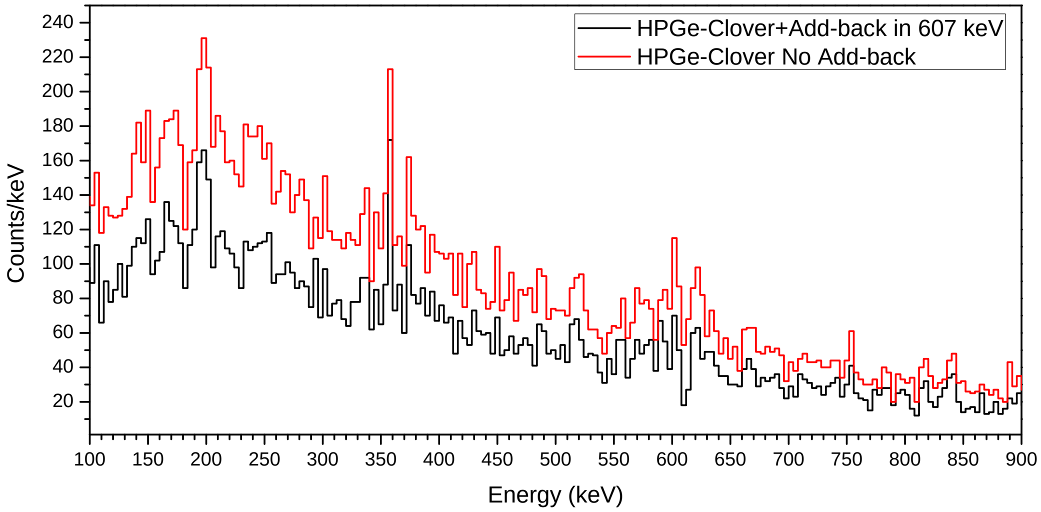

**Figure 5.4: Coincident HPGe-Clover spectra that illustrate the add-back reconstruction.** - Coincident HPGe-Clover spectrum obtained with add-back reconstruction in the 607-keV $\gamma$-ray (black) and without any add-back procedure (red). Both spectra are Ge-gated in the 607 keV transition and LaBr$_3$(Ce)-gated in 423 keV $\gamma$-ray. The multiplicity of the data set is three (triple coincidences) and the selected target is $^{241}$Pu.

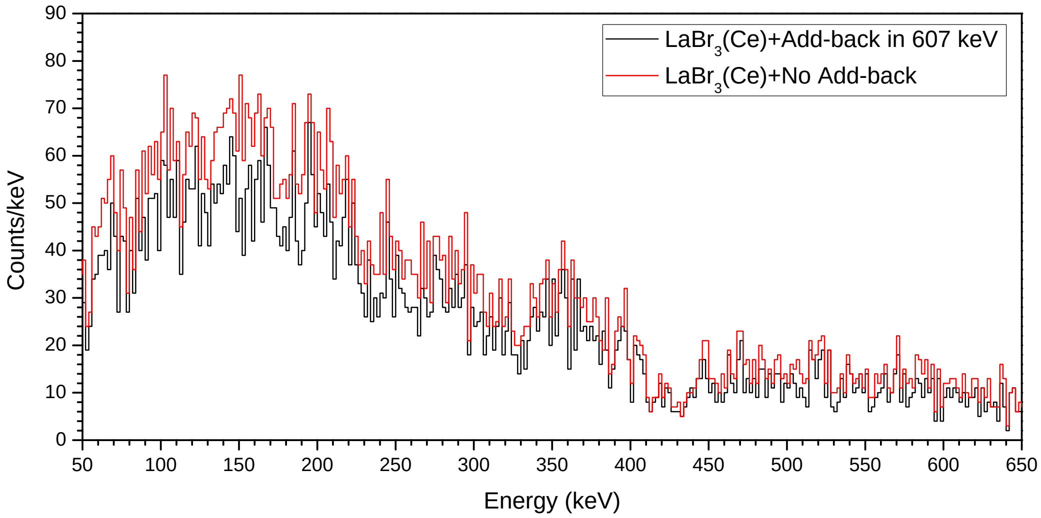

**Figure 5.5: Coincident LaBr$_3$(Ce) spectra illustrating the add-back reconstruction procedure.** - Coincident LaBr$_3$(Ce) spectra obtained with add-back reconstruction in the 607-keV $\gamma$-ray (black) and without any add-back procedure (red). Both spectra are Ge-gated in the 607 keV transition and LaBr$_3$(Ce)-gated in 423 keV $\gamma$-ray. The multiplicity of the data set is three ($\gamma\gamma\gamma$) and the selected target is $^{241}$Pu.

In this case, the reduction of the background level is not as obvious as in the case of the HPGe-Clovers. Anyhow, the peak-to-background ratio of the 353-keV peak, defined as $P/B = (A_T - A_{Bkg})/A_{Bkg}$, improves from 0.51 to 0.68 when the add-back reconstruction is performed for the 607-keV $\gamma$-ray.

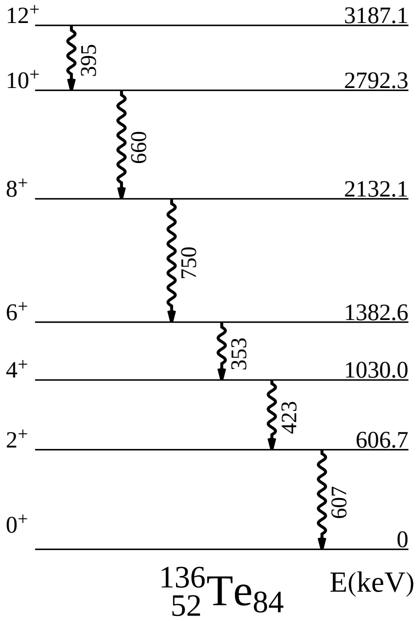

**Figure 5.6: Partial level scheme of $^{136}$Te.** - Partial level scheme of $^{136}$Te showing the ground-state yrast rotational band.

#### 5.5.2.3 Subtraction of events coincident with background under FEPs

One of the primary contributions to the background level of the EXILL-FATIMA data is the Compton scattering of the numerous $\gamma$-rays that are produced. Due to this effect, the FEP peaks are sitting on a high Compton continuum of the same energy, but different nature. When applying energy gates on the FEPs, the events correlated with the Compton underneath also appear in coincidence, blurring the coincident spectra with "deceptive" counts. Hence, it becomes necessary to correct for this effect. A good strategy to discard part of this contribution is to subtract the events that appear in coincidence with the background underneath the FEPs selected in the HPGe-Clovers. Since the background under the peaks (C) cannot be directly measured, it is selected on the right hand side of the FEP, by choosing a region with the same number of channels that only contains background (C′). Figure 5.7 presents a HPGe-Clover spectrum with no gating conditions, from the $^{241}$Pu data set. In this plot, one can observe the high level of background and the numerous $\gamma$-rays that are produced. The inset illustrates the manner of selecting the background in the Ge detectors on the right hand side of the FEPs. In this case, the 607 keV peak is taken as an example because it will be used for gating the HPGe-Clovers detectors in the following plots.

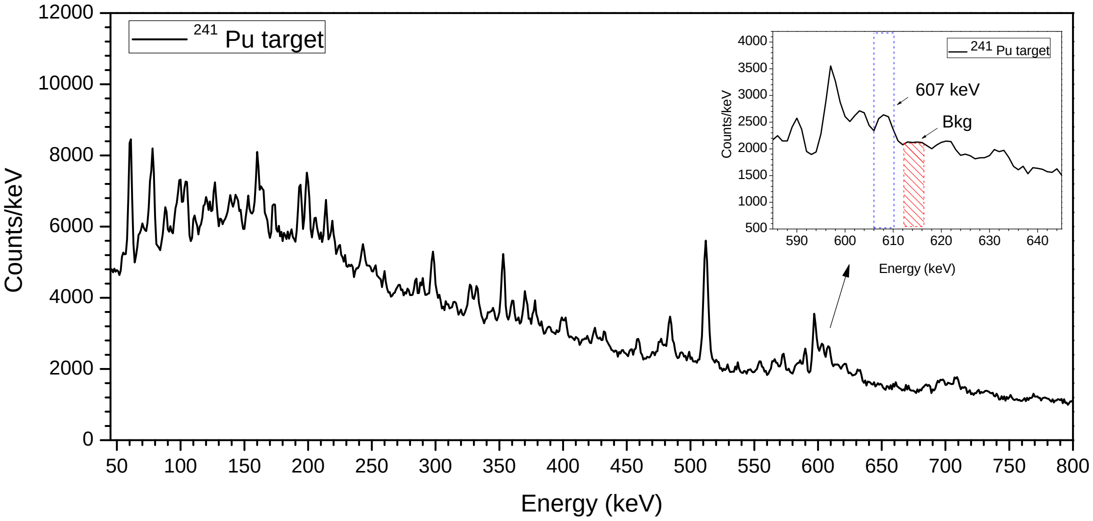

**Figure 5.7: HPGe-Clover spectrum non-gated.** - HPGe-Clover spectrum measured for the $^{241}$Pu data set without any kind of gates. The inset of the figure zooms in the 607-keV peak and shows the way of selecting the background. The region marked with blue lines corresponds to the 607-keV energy gate, while the region in red is the background gate (C′) selected for the background subtraction.

Figure 5.8 provides an example of the magnitude of the effect by showing two coincident spectra of the $^{241}$Pu data set. To investigate the optimal conditions for the analysis of $^{136}$Te, a condition is set on the 607-keV $\gamma$-ray. The plot in black is a coincident HPGe-Clover spectrum Ge-gated by the 607-keV transition, and the plot in red is a HPGe-Clover spectrum Ge-gated on the right hand side background (C′) of the 607-keV transition.

The plot in blue from Figure 5.8 is the difference between the black and the red spectra. It presents the events that are in coincidence with the full-energy events that constitute the 607-keV peak, since the counts that are in coincidence with the background have been subtracted. It can be noted that the blue spectrum is mainly

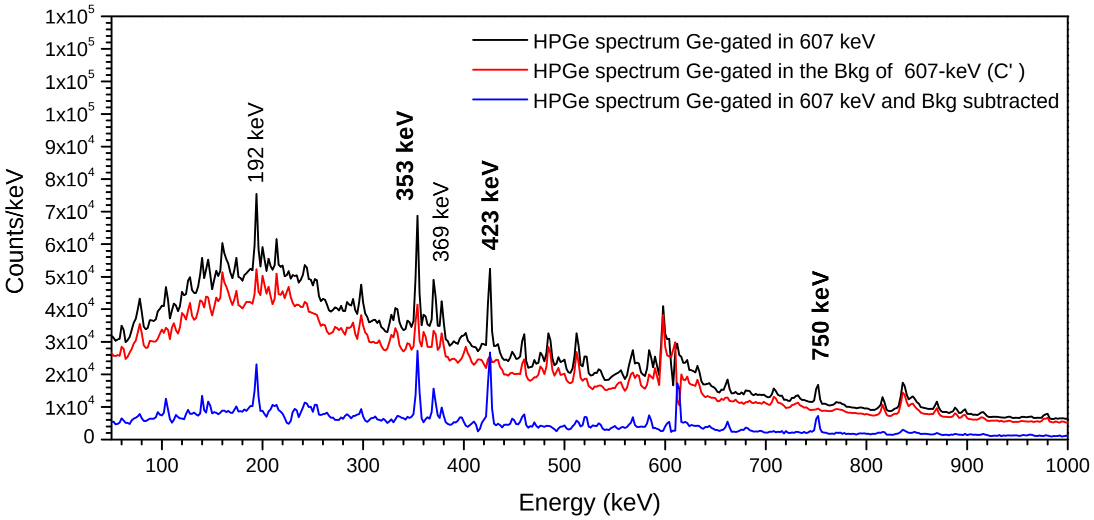

**Figure 5.8: Coincident HPGe spectra that illustrate the effect of background subtraction under the FEP peaks in the HPGe-clovers.** - Coincident HPGe-Clover spectra obtained by Ge-gating in the 607-keV $\gamma$-ray (black) and in the background at the right hand side of the 607-keV FEP (red). The plot in blue is the subtraction of the black and red spectra. The $\gamma$-rays from $^{136}$Te are labeled in bold font, and the $\gamma$-transitions from the $^{104}$Mo, which is one of the most produced partner, in Arial font. The multiplicity of the data set is three (triple coincidences) and the selected target is $^{241}$Pu.

composed by the $^{136}$Te $\gamma$-rays, which is the isotope of interest in the present analysis, and some of the most abundant fission partners, such as $^{104}$Mo, while the contribution of other nuclei is almost negligible. Figure 5.8 shows that it is worthwhile to subtract the background contribution of the Ge-gated peaks because the resulting spectrum is much cleaner.

Figure 5.9 presents the same effect but on the LaBr$_3$(Ce) spectra. One can see that the high level of background in the low energy region disappears as expected; the spectrum is mainly composed by the most intense $\gamma$-rays from $^{136}$Te and the partners (Mo isotopes). The question is whether this effect on energy spectra is also relevant for the fast-timing analysis.

Thus, the effect of background subtraction on the Ge-gated peaks is also investigated for the fast-timing matrices. Figure 5.10 shows the coincident LaBr$_3$(Ce) spectra derived from three Ft-matrices. The plot in black provides the energy spectrum of the matching LaBr$_3$(Ce) detectors with a Ge-gate in the 607-keV transition and a

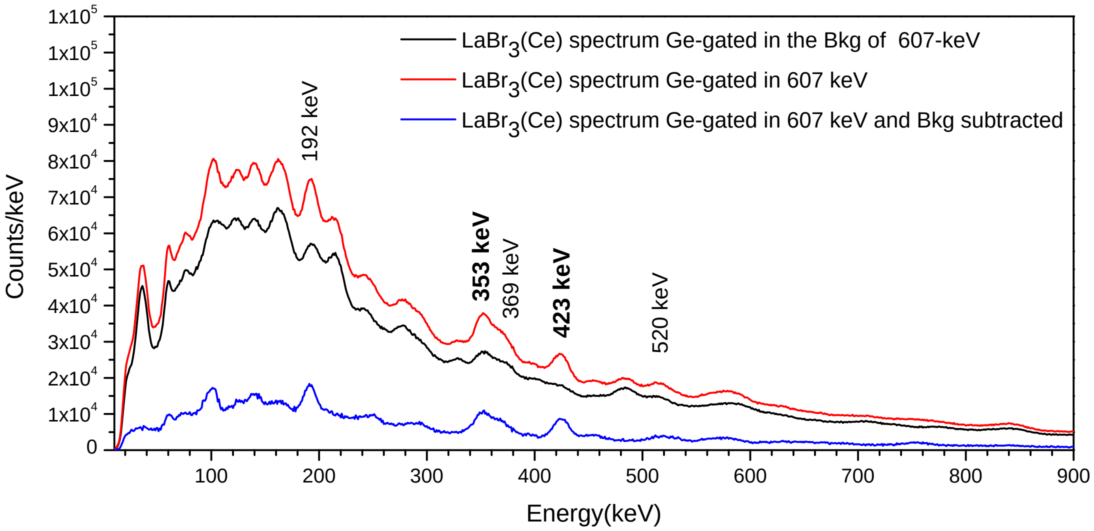

**Figure 5.9: Coincident LaBr$_3$(Ce) spectra that show the effect of the background subtraction under the gated peaks on the HPGe-clovers.** - Coincident LaBr$_3$(Ce) spectra obtained by gating on the HPGe-Clovers in the 607-keV $\gamma$-ray (black) and in the background on the right hand side (C') of the 607-keV FEP (red) projected from the Ft-matrix. The plot in blue corresponds to the difference between the red and the black spectra, and it shows the effect of subtracting the events that are in coincidence with the background of the Ge-gated peaks. Apart from some minor contributions, the blue plot is mainly composed by the $^{136}$Te and the $^{104}$Mo $\gamma$-rays. The $^{104}$Mo isotope is one of the most abundant fission partners of $^{136}$Te. The $\gamma$-rays from $^{136}$Te are labeled in bold font, and the $\gamma$-transitions from the $^{104}$Mo in Arial font. Unlabelled FEPs corresponds to isotopes that are not of our interest. The selected target is $^{241}$Pu.

LaBr$_3$(Ce) gate in the 423-keV $\gamma$-ray projected from the Ft-matrix. The plot in red shows the coincident events that are in coincidence with the right hand-side background of the 607-keV transition and the 423-keV $\gamma$-ray in the LaBr$_3$(Ce) detectors. It can be noted that the large amount of peaks and background that appear in the low energy region arises from the Compton background under the HPGe peak. As in the previous cases, the plot in blue corresponds to the spectrum subtraction, showing essentially the events that are in coincidence with the full-energy events at 607 keV. In the present example, the peak-to-background (P/B) has improved from 0.49 when using the add-back reconstruction to 1.7 when subtracting the background under the Ge-gated peak. In addition to excellent improvement in the (P/B), Figure 5.10 also shows that it is worthwhile to subtract the events that are in coincidence with the background underneath the Ge-gated peak because the spectrum obtained is much cleaner. It basically contains the $\gamma$-rays from $^{136}$Te and its partners ($^{104}$Mo), the contaminants have faded. In spite of the loss of statistics, this analysis points to the fact that the background subtraction procedure may be a good analysis strategy.

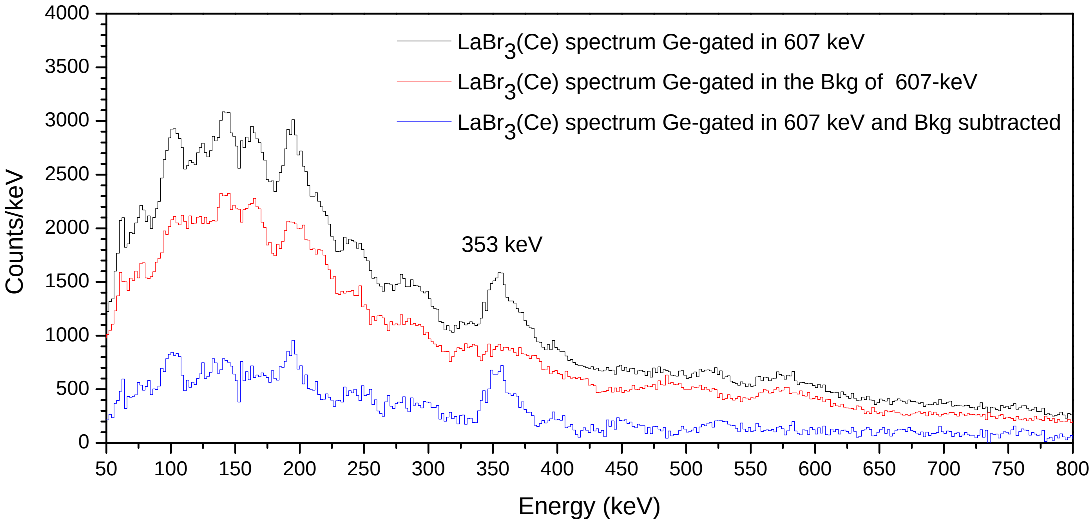

**Figure 5.10: Coincident $LaBr_3$(Ce) spectra that display the effect of the background subtraction under the gated peaks on the HPGe-clovers.** - Coincident $LaBr_3$(Ce) spectra obtained by gating the HPGe-Clovers on the 607-keV $\gamma$-ray (black) and in the background on the right hand side of the 607-keV FEP (red). The plot in blue is the difference between the red and the black ones. This plot (blue) shows the effect of subtracting the events that are in coincidence with the background under the Ge-gated peaks. In addition to the 607-keV Ge-gate, the three spectra are $LaBr_3$(Ce)-gated in the 423-keV transition. The matching $LaBr_3$(Ce) energy for deriving the lifetime of the $4^+$ state, which is 353 keV, is labeled at the plot. The used target is $^{241}$Pu.

### 5.5.3 Event multiplicity

A valid event is composed of a set of hits that have occurred following certain given conditions within a coincidence time window. The sorting conditions define the event multiplicity and are imposed on the number of $\gamma$-rays that are detected in the different types of detectors. As mentioned before (Section 5.2.5), a triple $\gamma\gamma\gamma$(t) timing event is composed of one $\gamma$-ray detected on the HPGe-Clover detectors and two $\gamma$-rays detected on the $LaBr_3$(Ce) crystals. It also contains the timing information, provided by the TACs, with the time difference between $LaBr_3$(Ce) hits.

An extra coincident condition imposed on the number of detected $\gamma$-rays, making a total of four, may be applied, leading to quadruple $\gamma\gamma\gamma\gamma$(t) events. In this case two $\gamma$-rays recorded in the Ge-detectors and two in the $LaBr_3$(Ce) crystals. Quadruple events also contain the relevant time information provided by the TACs. The main advantage of performing the analysis with four coincident conditions is the considerable reduction of the level of background, the peak to background ratio improves more than a factor of three with respect to triple events. However, the coincidence efficiency is much lower causing a reduction of the statistics of the time spectra in a factor of more than three. For the case of $^{136}$Te where the amount of statistics is good enough to impose more than three coincident conditions, it is possible to extract lifetime information from quadruple events. In the present study, the approach followed consists in firstly analyzing triple events to derive the lifetime values taking advantage of the good statistics and secondly in cross-checking the results by investigating quadruple events. In some cases, due to the presence of contaminants or as a consequence of not sufficient available statistics, the lifetime value has been only measured using one of the methods. The coincidence time window for the present analysis has been optimized to the value of 120 ns, being the most suitable time window for both triple and quadruple events.

## 5.6 Analysis procedure

As discussed in previous sections, the first step in the analysis consists in selecting the best conditions for every case, being the target, the background reduction and the event multiplicity the most relevant factors. The second step is the optimal selection of the energy gates together with the investigation of the projected spectra. It is important to identify the contaminants or fission partners that potentially could affect the results and to adjust the width of the energy gates according to the detector type and the background underneath the FEPs. The third step entails the timing analysis through the fast timing matrices and the Generalized Centroid Difference method (GCD) [RMS+13]. A correction to the effect of the background component in the time distributions is needed.

### 5.6.1 Conditions for the analysis of $^{136}$Te

The best strategy regarding the target selection is to investigate both targets separately to extract independent values and compare them afterwards (Section 5.5.1). This is possible because the two of them produce good yields and the fission partners do not represent a problem, in principle. However, there are some Zr isotopes with long-lived states that may be produced as fission partners of the $^{235}$U target.

Concerning the background reduction, the best approach is to combine the background subtraction of the Ge-gated peaks with the exclusion of some detector combinations and rejecting the events in coincidence with the BGO shields. The three actions were explained above. Concerning the event multiplicity, triple and quadruple events provide suitable results, allowing us to cross-check the results. The optimal conditions for the $^{136}$Te analysis are summarized below:

- **Targets:** Both $^{241}$Pu and $^{235}$U used separately and compared afterwards.
- **Background reduction:** Combination of the background subtraction of the Ge-gated peaks with the rejection of the coincident BGO events and the exclusion of some timing detectors combinations.
- **Multiplicity:** Triple events are preferred due to the higher statistics; quadruple events also perform fine at the expense of statistical losses.

### 5.6.2 Gating procedure and analysis using triple events

When using a triple timing event $\gamma$-$\gamma$-$\gamma$(t) the high-resolution gate set on the Ge detector is an indispensable condition in the present analysis of neutron-induced fission data. The gating procedure comprises three steps: the first one consists in the investigation of the contents of the coincident spectra. The second one is devoted to properly set the energy gates in the $LaBr_3$(Ce) detectors, taking care of the peak width. The third one is focused on the construction of the fast-timing matrices.

1. **Investigation of the coincident spectra:** By using two or three high-resolution energy gates (Ge-gates) and projecting into the coincident HPGe-Clover spectra.
2. **Gate assessment at the $LaBr_3$(Ce) detectors:** Evaluating the best combinations and the optimal width of the $LaBr_3$(Ce) gates, to avoid contaminants and unresolved FEPs.
3. **Construction of the fast-timing matrices:** Sorting of the Start and Stop matrices by using the best combination of gates.

These steps are explained in detail in the coming subsections. When the subtraction of events in coincidence with the background ($C'$) in the Ge-gated peaks is implemented, the same energy gates are used for the $LaBr_3$(Ce) detectors (step two) and fast-timing matrices are also constructed for the background-gated coincident $LaBr_3$(Ce) peaks (step three). Then either the fast-timing matrices or the projections are subtracted to arrive to the final time distributions that provide the timing information. The procedures are illustrated with the measurement of the half-life $4^+$ state in $^{136}$Te.

#### 5.6.2.1 Energy. Clover-Clover-Clover

Taking advantage of the excellent energy resolution of the HPGe-clover detectors, the first step in the gating strategy consists in selecting two known $\gamma$-transitions in the Ge detectors and investigating the contents of the coincident spectra. In this part, two energy conditions are applied on the Clover detectors for gating and projecting while the coincident third HPGe-clover projection is used to investigate the components that appear in coincidences. The two high-resolution gates allow the identification of possible contaminants and fission partners that hamper the subsequent analysis. The Clover-Clover-Clover data sorting may also provide new spectroscopic information about the level scheme of the isotope under study. For this step, the Gate-Spectra command with the corresponding gate-configuration file is used in the SOCOv2 software (Section 5.3). Figure 5.11 provides an example of a coincident HPGe-Clover spectrum with the gating conditions set at the 750- and 352-keV $\gamma$-rays, a partial level scheme of $^{136}$Te is shown on the right hand side for clarification. The plot shows the $\gamma$-transitions from the ground-state rotational band, but also other $\gamma$-rays that are in coincidence with the gating transitions.

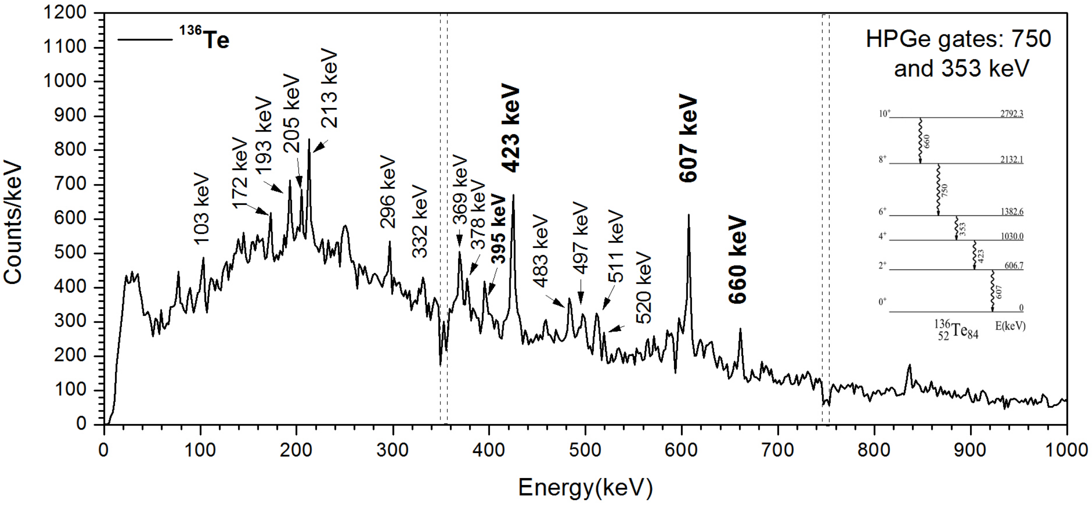

**Figure 5.11: Coincident HPGe energy spectrum gated in the 750- and 353-keV $\gamma$-transitions.** - Energy spectrum of the HPGe-Clover detectors in coincidence with the 750 and 353 keV $\gamma$-transitions ($\gamma\gamma\gamma$) gated in the high-resolution HPGe-clovers for the $^{241}$Pu target. The width of the gates is indicated in the plot with dashed lines, while prominent peaks are labeled. The $\gamma$-rays in the $^{136}$Te yrast rotational band are marked in bold with their energy, and a scheme of the band is included on the right hand side of the graph.

#### 5.6.2.2 Energy. Clover-LaBr$_3$(Ce)-Clover

The selection of the energy gates in the LaBr$_3$(Ce) detectors is crucial for lifetime measurements through Fast-Timing methods [MGM89]. If the selected regions contain something else apart from the $\gamma$-rays of interest, the measured time distributions are influenced, being sometimes considerably affected. In some cases, FEPs that appear as single peaks in the LaBr$_3$(Ce) spectra are in reality unresolved doublets, due to the energy resolution of this type of detectors [Gob, VMF$^+$15]. Therefore, the second step consists in the careful inspection of the coincident $LaBr_3$(Ce) spectra and the comparison with the equivalent Clover projection, after having imposed energy conditions on two known $\gamma$-transitions from the decay of interest. One of the condition is applied to the Clover detectors and the other one to the $LaBr_3$(Ce) crystals (Clover-$LaBr_3$(Ce)-Clover). The reason for this step in the analysis is to investigate the actual contents of the non-resolved peaks in the $LaBr_3$(Ce) gates that will be used for sorting the fast timing matrix, taking advantage of the excellent energy resolution of the Ge detectors. Since there are two $\gamma$-rays involved in the fast timing matrix, namely the feeding and the de-exciting transition, this procedure is carried out twice, one for each of them.

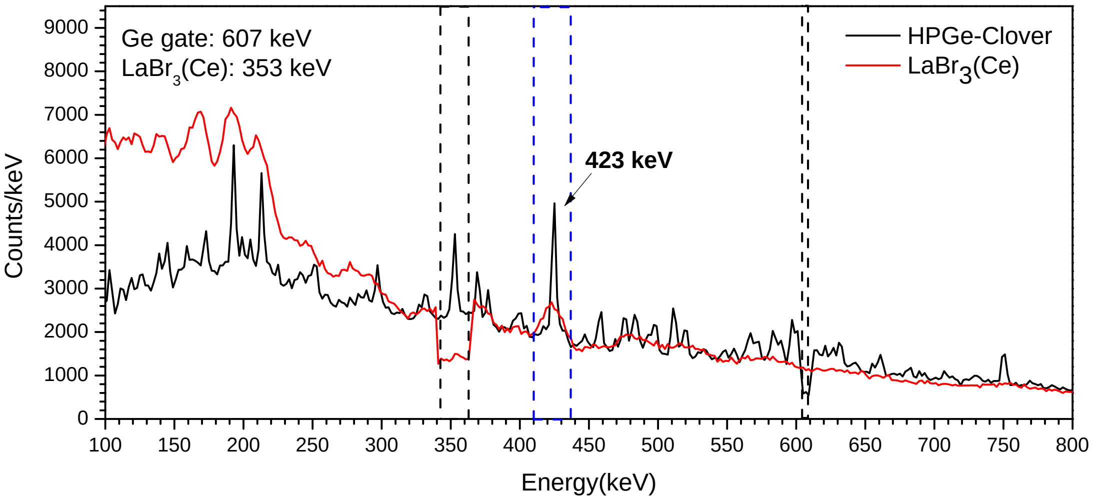

**Figure 5.12: Coincident HPGe-Clover and $LaBr_3$(Ce) spectra gated in the 607- and 353-keV transitions.** - Energy spectra of HPGe-Clover detectors (black) and $LaBr_3$(Ce) crystals (red), in coincidence with the 607 keV $\gamma$-ray selected in the Ge detectors and the 352 keV in the $LaBr_3$(Ce) detectors. The width of the chosen gates is indicated in the plot with black dashed lines, while the size of the second selected gate in the $LaBr_3$(Ce) crystals is plotted in blue. The used target is $^{241}$Pu.

Figure 5.12 provides an example of two coincident HPGe-Clover (black) and $LaBr_3$(Ce) (red) spectra gated by the 607-keV $\gamma$-ray in the Ge detectors and by the 352-keV transition in the selected $LaBr_3$(Ce) crystals. The width of the gates is marked in black dashed lines, while the selected size for the second $LaBr_3$(Ce) gate is marked in blue. The usual size of the selected gates in the Clovers is about 3 keV, while the width at the $LaBr_3$(Ce) ranges from 15 to 20 keV. The SOCOv2 command used for sorting the events is the same as the one used in the former Section 5.6.2.1, namely Gate-Spectra, but with different conditions in the gate-configuration file (Section 5.3).

#### 5.6.2.3 Timing. Clover-LaBr$_3$(Ce)-LaBr$_3$(Ce)

The last step corresponds to the lifetime measurements through the use of the fast-timing matrices, which are tridimensional objects containing the coincident energy of the LaBr$_3$(Ce) detectors in the $x$ and $y$ axes and the related time information in the $z$ axis. The time distributions are obtained by imposing energy gates in the LaBr$_3$(Ce) detectors and projecting onto the time. The fast-timing matrices may have extra external conditions set on one or more energies in the HPGe-clovers detectors or other parameters.

To build the fast-timing matrices, SOCOv2 is equipped with the Ft-matrix command that provides the Start and the Stop matrices as outputs (Section 5.4). The gating conditions are given to SOCOv2 through the gate-configure file that contains one high-resolution gate of a typical width of 3 keV set in the Clovers to select the decay cascade, and a LaBr$_3$(Ce) gate set in the $\gamma$-ray that feeds or de-excites the level under study. The second gate for time projecting would correspond to the feeder or the decay transition depending on what was selected in the input file. The energy gates were previously optimized (subsections 5.6.2.1 and 5.6.2.2 above).

After gating and projecting, two time distributions will be obtained; the one corresponding to the Start matrix and the one relative to the Stop matrix. The Start projection is the superposition of all the time distributions coming from the TACs started by the second-selected $\gamma$-ray and stopped by the first-selected $\gamma$-transition at input file. Conversely, the Stop distribution is the superposition of all the time distribution from the TACs stopped by the second-selected $\gamma$-ray and started by the first-selected $\gamma$-transition in the input file. Figure 5.13 shows an example of two time distributions, delayed and anti-delayed, for measuring the lifetime of the first $4^+$ state in $^{136}$Te. The centroids of the time distributions carry the information on the lifetime of the level. Once the centroids of the Start and Stop distributions have been measured, the last step corresponds to calculating the centroid difference. It is defined as $\Delta C_{Exp}(\Delta E_\gamma) = C_{Exp}^{Stop} - C_{Exp}^{Start}$. According to the GCD method [RMS$^+$13], prior to Compton corrections, the lifetime value is given by:

$$\tau = \frac{1}{2}[\Delta C_{Exp}(\Delta E_\gamma) - PRD(\Delta E_\gamma)]. \qquad (5.1)$$

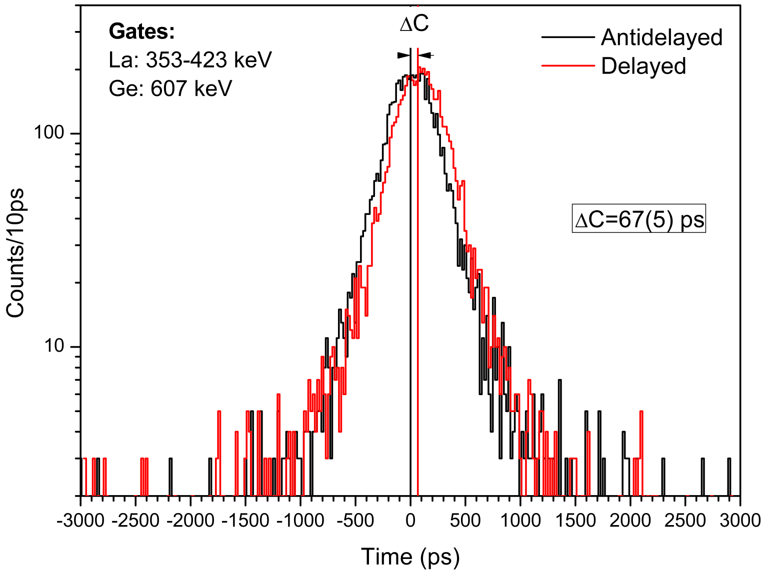

**Figure 5.13: Delayed and anti-delayed time distributions of the $4^+$ state in $^{136}$Te.** - Delayed (red) and anti-delayed (black) time distributions for the lifetime measurement of the first $4^+$ state in $^{136}$Te using the $^{241}$Pu target. The high-resolution energy gate of the HPGe-Clover detectors is set at 607 keV. The LaBr$_3$(Ce) gates were selected for the delayed distribution at 353 keV for start and 423 keV for stop and for the anti-delayed spectrum at 423 keV for start and 353 keV for stop.

For the lifetime measurement it is very important to ensure the absence of long-lived partners and contaminants that have $\gamma$-rays in coincidence with those under study having similar energy. Otherwise, the time distribution would be affected being centroid shifted by the lifetime of the long-lived isotope that is present. In some cases, setting very narrow energy gates on the LaBr$_3$(Ce) detectors solves this problem. Selecting a proper width of the energy gate is also important regarding the influence on the time distribution of the amount of background under the peaks. The Compton continuum under the FEP also shifts the centroid of the time spectrum.

In spite of the strategies to reduce the background contribution (Sections 5.5.2), the amount that is still present influences the timing analysis, shifting the total spectrum from the net time distribution up to tens of picoseconds in some cases, being therefore necessary to apply timing background correction. The Compton corrections can be performed by using a Compton curve built with calibration sources, such as $^{152}$Eu and

$^{60}$Co, or by an internal background curve taking advantage of the available statistics and the energy resolution of the LaBr$_3$(Ce) detectors. The corrections are explained in detail in Section 5.7.

#### 5.6.2.4 Example of the analysis procedure using triple events

An illustrative example following all the steps explained above is provided hereafter. It corresponds to the lifetime measurement of the $4^+$ state in $^{136}$Te using the $^{241}$Pu target. The lifetime of the $4^+$ level is given by the time difference between the arrival of the populating 423-keV $\gamma$-transition and the de-exciting 353-keV $\gamma$-ray (See Figure 5.6). Hence, a good gating strategy is to select the 607-keV transition as Ge-gate and the 353-423 keV $\gamma$-rays as LaBr$_3$(Ce)-gates.

**A. Contents of the coincident spectra: Clover-Clover-Clover**

The first step in the analysis consists in the investigation of the contents of the coincident spectra. To this aim, two sets of high-resolution energy gates in the HPGe-Clovers were set, while the third coincident HPGe-Clovers spectrum is examined. In this example, the two sets of gates are 607-423 keV and 607-353 keV. Figures 5.14 and 5.15 present the coincident Clover spectra gated in 607-423 keV and 607-353 keV respectively. The $\gamma$-rays from $^{136}$Te are labeled in bold font. The size of the gates, chosen with a typical width of 3 keV, is also marked with dashed lines. These two plots are used for the identification of fission partners and potential contaminants.

**B. Selection of the LaBr$_3$(Ce) gates: Clover-LaBr$_3$(Ce)-Clover**

Due to the energy resolution of the LaBr$_3$(Ce) detectors, which is poorer than the one from the HPGe-Clovers, the LaBr$_3$(Ce)-gated peaks for constructing the Ft-matrices may contain some other FEPs that come together with the one of interest as unresolved doublets. Other FEPs in their vicinity might also be selected within the energy gate. This may affect the total time distribution. To minimize this problem the contents of the LaBr$_3$(Ce) gates profiting from the better energy resolution of the Ge-detectors. In this step, the most suitable size of the LaBr$_3$(Ce) gates is also determined.

Figures 5.16 and 5.17 provide the coincident HPGe-Clover and LaBr$_3$(Ce) spectra Ge-gated by the 607-keV and LaBr$_3$(Ce)-gated by the 423-keV and 353-keV transitions respectively. From the inset of Figure 5.17 it can be seen that the 423-keV peak does not

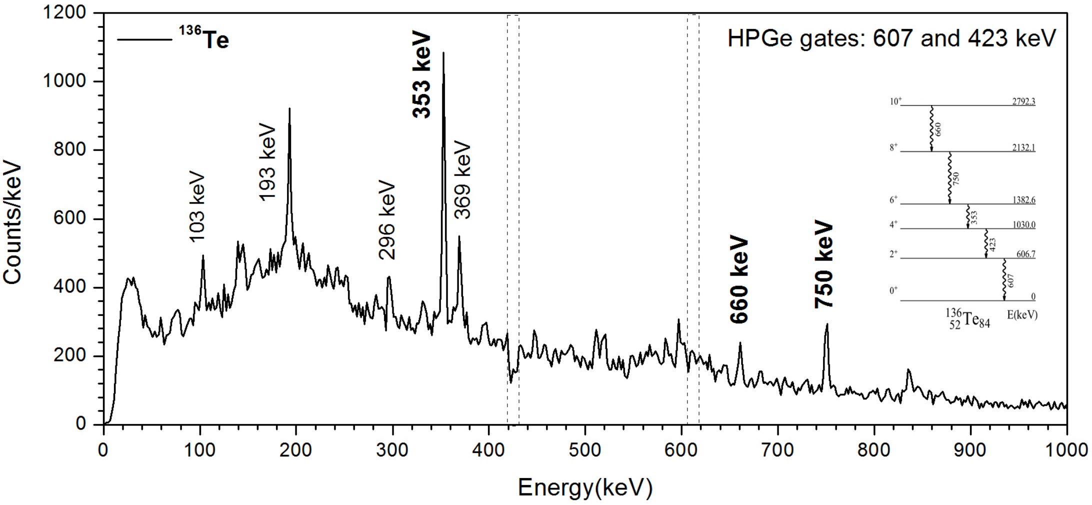

**Figure 5.14: Coincident HPGe-Clover spectrum gated by the 607 and 423-keV $\gamma$-ray.** - Coincident HPGe-Clovers spectrum gated by the 607- and 423-keV $\gamma$-rays. The width of the gates is indicated with dashed lines, and the prominent peaks are labeled. The $\gamma$-rays from $^{136}$Te are marked in bold font with their energy, and a partial scheme is embedded on the right hand side of the graph.

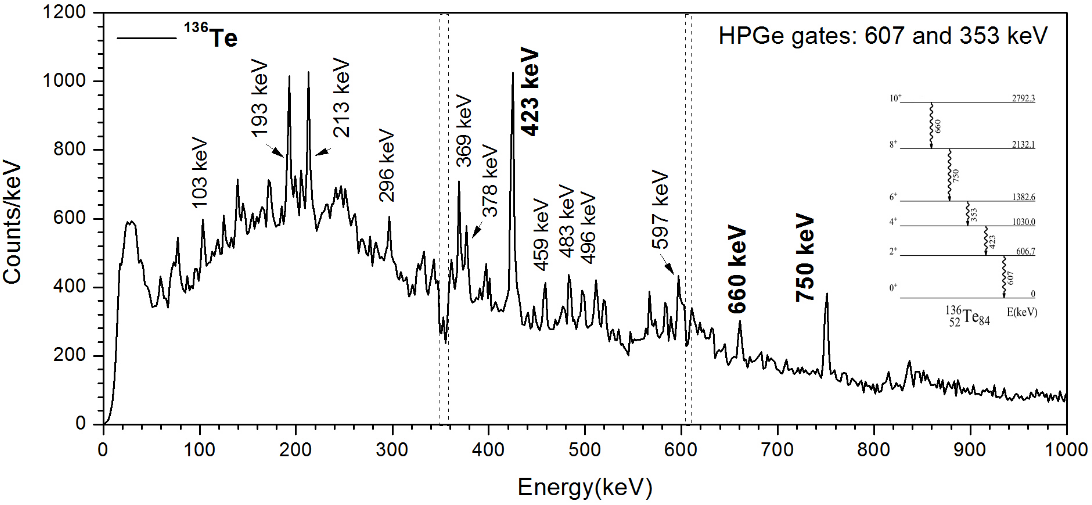

**Figure 5.15: Coincident HPGe spectrum gated in the 607- and 353-keV $\gamma$-transitions.** - Energy spectrum of the coincident HPGe-Clover detectors gated by 607- and 353-keV $\gamma$-rays. The width of the gates is indicated with dashed lines, and the prominent peaks are labeled. The $\gamma$-rays from $^{136}$Te are marked in bold font with their energy, and a partial scheme is embedded on the right hand side of the graph.

contain unresolved FEPs that may contribute to the total time distribution. However, from the inset of Figure 5.16 one can observe the presence of a second peak in addition to the 353-keV FEP, unresolved in the $\mathrm{LaBr_3(Ce)}$. Therefore, to avoid the potential contribution of the unresolved doublet, the width of the $\mathrm{LaBr_3(Ce)}$ gate is reduced as shown in the Figure with dashed blue lines.

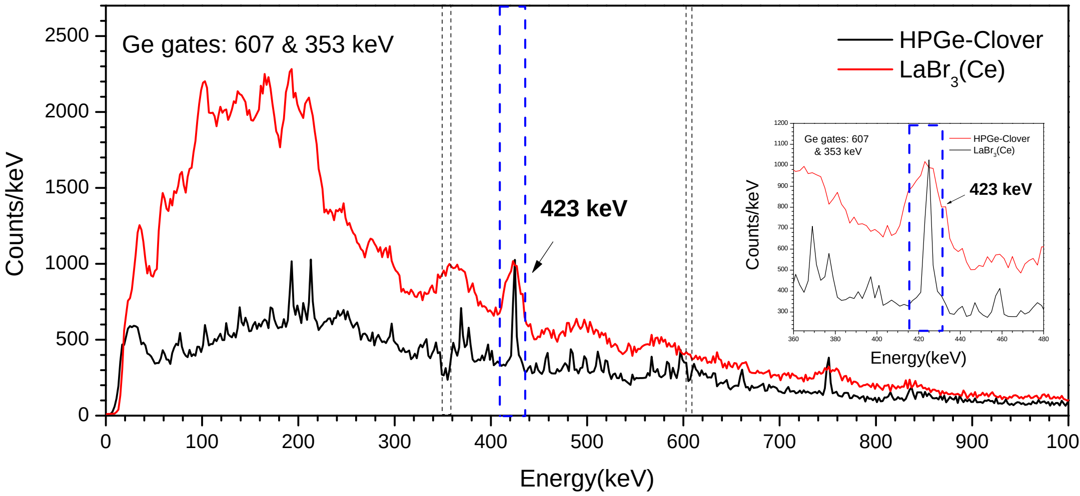

**Figure 5.16: Coincident HPGe and $\mathrm{LaBr_3(Ce)}$ spectra gated in the 607- and 353-keV $\gamma$-transitions.** - Energy spectrum of the HPGe-Clovers, in black and $\mathrm{LaBr_3(Ce)}$ detectors, in red, after applying energy gates at the 607- and 353-keV $\gamma$-transitions ($\gamma\gamma\gamma$). The selected area for the 423-keV peak is about 26 keV. The used target is $^{241}$Pu.

### C. Fast-timing matrices: Clover-$\mathrm{LaBr_3(Ce)}$-$\mathrm{LaBr_3(Ce)}$

Once the energy gates have been decided, the last step is to sort the two Ft-matrices, the Start and the Stop one, to calculate the delayed and anti-delayed time spectra by gating the matching $\mathrm{LaBr_3(Ce)}$ detectors in the corresponding energy. Figure 5.18 presents the delayed and the anti-delayed time distributions for deriving the lifetime of the $4^+$ state. From the experimental centroid difference of the time spectra, and applying the timing calibrations, the actual level lifetime is derived.

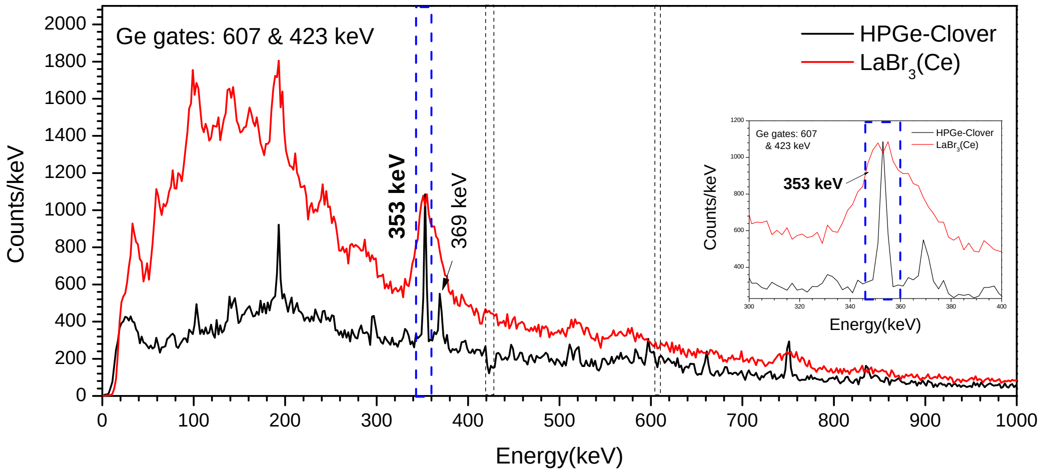

**Figure 5.17: Coincident HPGe and LaBr$_3$(Ce) spectra gated in the 607- and 423-keV $\gamma$-transitions.** - Energy spectrum of the HPGe-Clovers, in black and LaBr$_3$(Ce) detectors, in red, after applied energy gates at the 607 and 423 keV $\gamma$-transitions ($\gamma\gamma\gamma$). The gate width is indicated with black dashed lines for the Ge detectors and blue dashed lines for the coincident LaBr$_3$(Ce) spectrum. The 353 keV peak width is about 18 keV to avoid the 369 keV. The used target is $^{241}$Pu.

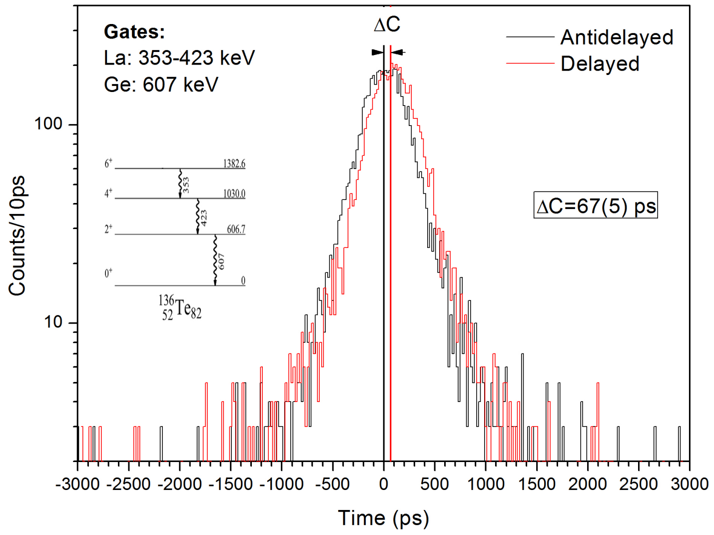

**Figure 5.18: Delayed and anti-delayed time distributions of the $4_1^+$ state in $^{136}$Te.** - Delayed (red) and anti-delayed (black) time distributions for the lifetime measurement of the first $4^+$ state in $^{136}$Te. The high-resolution energy gate of the HPGe-Clover detectors is set in 607 keV $\gamma$ray. The LaBr$_3$(Ce) gates were selected for the delayed distribution as: 353 keV for start and 423 keV for stop and for the anti-delayed spectrum as 423 keV for start and 353 keV for stop. A partial scheme of $^{136}$Te is provided in the left hand side, for clarity. The used target is $^{241}$Pu.

### 5.6.3 Quadruple events

In exotic nuclei studies such as those performed during the EXILL-FATIMA campaign, where the background level is large and the amount of $\gamma$-rays is high, it may be convenient to add a fourth coincident condition using a high-resolution HPGe-gate to exclude transitions that do not actually belong to the cascade. In spite of the higher quality of the coincident data, one should consider the sharp reduction in statistics. But in some cases the use of a fourth condition at the expense of the reduction in statistics is favourable: the FEP to background ratio (P/B) improves, most of the partners and contaminants are reduced, and some unresolved FEPs appear as stand-alone peaks. However, in some other examples, the (P/B) does not improve remaining almost constant and the lack of statistics considerably hinders the timing analysis, being therefore not worth to use quadruple events.

The analysis procedure regarding quadruple events $\gamma\gamma\gamma\gamma$ is equivalent to the one in triple events but just adding another high-resolution energy condition to another $\gamma$-ray from the decay. The first step consists in a detailed investigation of the possible contaminants or partners that could appear in coincidence with the three $\gamma$-transitions that have been selected (Clover-Clover-Clover-Clover). This part of the analysis is equivalent to the Clover-Clover-Clover procedure explained in Section 5.6.2.1 for triple events. The second step is devoted to a proper gate selection; to this aim, a Clover-Clover-$LaBr_3$(Ce)-Clover sorting is needed. The gate adjustment is carried out following the same procedure described in Section 5.6.2.2. The third one entails the construction of the fast timing matrices with the subsequent timing analysis. For this purpose, a Clover-Clover-$LaBr_3$(Ce)-$LaBr_3$(Ce) sorting is required. The timing analysis performed here is equivalent to the one explained in Section 5.6.2.3. Regarding the background contribution, even though the influence in quadruple events is not as significant as the one in triple events, the total time distributions may still appear shifted as a consequence of the background. Thus, it is also necessary to apply a timing correction, that can either be an external Compton curve constructed by calibration sources or an internal background curve that accounts for the background behaviour.

## 5.7 Timing Calibrations

Fast-timing methods, such as the Advanced-Time-Delayed technique (ATD) [MGM89, MM89] or the Generalized Centroid-shift Difference method (GCD) [RMS$^+$13] make it possible to measure lifetimes of excited nuclear states down to the few picoseconds range with an accuracy better than 5 ps, depending on the experimental conditions.

Half-lifes are obtained in the ATD method through the measurements of the time differences between the arrival of the $\beta$-particles from the decaying parent and the subsequent de-exciting $\gamma$-rays, as it was explained in detail in Section 2.1. In the GCD technique, lifetimes are given by the time differences between the $\gamma$-rays that populate and de-excite the level of interest, as was is explained in Section 2.2.

Independently of the selected method, the measured time distribution contains the intrinsic system resolution in addition to the lifetimes. That is to say, the delayed time spectrum is the convolution of the system response at the given energies and the level lifetime of interest. It can be expressed with equation 5.2, where the $P(t_j)$ characterizes the prompt time distribution or the system response, and $f(t) = e^{-\lambda t}$ for t $> 0$, where $\lambda$ is the decay constant of the level, $\lambda = \frac{ln(2)}{T_{1/2}}$ [MGM89, MM89]. Therefore, to extract the actual lifetime value it is necessary to deconvolute the prompt time distribution from the total delayed spectrum.

$$F(t_j) = \int_0^{+\infty} P(t_j - t) f(t) dt \tag{5.2}$$

The best way to obtain the system response is to measure the time distributions of levels de-excited by prompt transitions, which for our purpose are level lifetimes shorter than 1 ps. In this case, the centroid position of the quasi-Gaussian time distribution only depends on energy. If the selected level is long-lived, the centroid position of the time distribution is shifted by the lifetime of the level [MGM89, MM89].

To achieve good accuracy with the ATD or the GCD methods, it is necessary to perform time calibrations, taking into account that these techniques are highly sensitive to the time response of the setup as a function of energy. The two main time calibrations are the FEP-curve that accounts for the energy dependent system response and the Compton-distribution aimed at background corrections. Both corrections are explained in detail in the following Section 5.7.1 and Section 5.7.2.

### 5.7.1 Time calibration for FEPs: the PRD

The Full-Energy-Peak (FEP) curve accounts for the system response to the $\gamma$-rays that have fully deposited their energy in the $LaBr_3$(Ce) crystals. The idea is to use prompt $\gamma$-rays coming from a short-lived level whose lifetime is shorter than the technique sensibility in order to obtain the actual system response for half-life corrections. If the selected transition is not prompt, the centroid position of the measured time distribution is shifted by the lifetime of the level (See Section 2.1). The FEP-curve in the MSC and GCD methods [RPJR10, RMS$^+$13] is called PRD, Prompt Response Distribution, and provides the system response as a function of the energy. However, the PRD is not a direct walk curve but a difference of two other distributions, the delayed and the anti-delayed walk curves. That is to say, to build the PRD curve it is necessary to measure the difference of the centroid positions between the delayed and the anti-delayed time distributions. The delayed distribution corresponds to the time spectra measured when the $\gamma$-ray that de-excites the selected level works as the stop, and the anti-delayed distribution is the time spectra given (by the TACs) when the $\gamma$-ray that de-excites the selected level works as the start. Since it is not a constant, the PRD reflects the asymmetric time response of the system.

#### 5.7.1.1 Construction of the PRD

To construct the PRD curve for a fast-timing experiment, the first step is to set a fixed gate on a $\gamma$-ray populating or depopulating a given state, while the corresponding gating condition is set on coincident transitions of different energies. In the present analysis, the PRD was built by using an external $^{152}$Eu source in the energy range from 40-1408 keV, and the $^{48}$Ti(n,$\gamma$)$^{49}$Ti capture reaction from 137-6760 keV.

The $^{152}$Eu source is a standard $\gamma$-ray calibration source commonly used for fast-timing calibrations. It has two decaying branches: the electron capture to $^{152}$Sm and the $\beta$-decaying branch to $^{152}$Gd. In the $\beta$-decaying branch, the 344 keV state in $^{152}$Gd is populated by five transitions with a good intensity that are in coincidence with the de-exciting 344 keV $\gamma$-ray. This $\gamma$-ray is also in coincidence with two other $\gamma$-transitions of interest, the 368-keV and the 679-keV ones that populate a level above the 755-keV state. Therefore the 344-keV $\gamma$-ray is a good choice as a reference for the construction of the PRD, because it allows using the same $\gamma$-ray as a reference for seven different energies [NND], and avoids the need of shifting the points to match the same zero, thus preventing from sources of uncertainty. Although it would be better to use a calibration that contained short-lived levels de-excited by prompt $\gamma$-rays, which is not the case for the $^{152}$Eu decay, it is still advantageous to this calibration. The main caveat is that the measured centroids of the time distributions should be corrected by the lifetimes of the levels in the order of tens of picoseconds, which have been measured with good accuracy and available in the literature.

Figure 5.19 depicts a partial level scheme of $^{152}$Gd, with the most relevant $\gamma$-rays that are in coincidence with the 344-keV transition. The transitions marked in black directly populate the 344-keV state, while the $\gamma$-rays in blue populate a level above, the 755-keV state. The level lifetimes are also indicated.

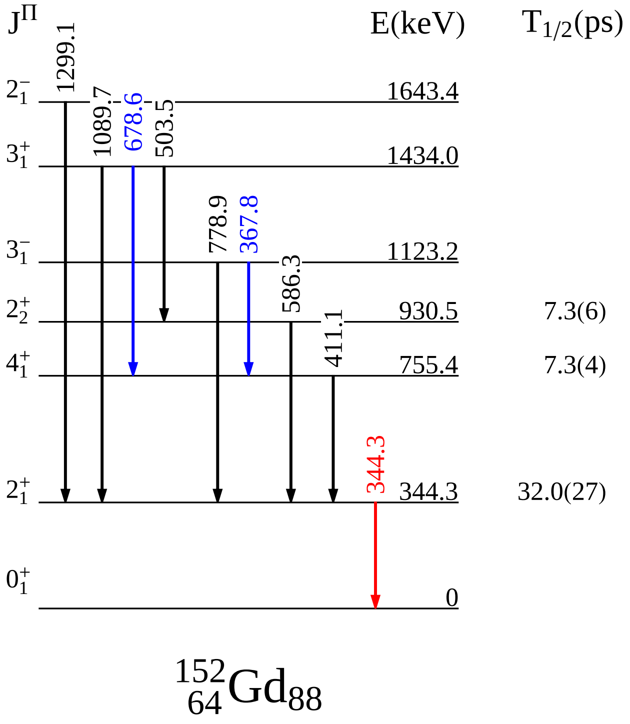

**Figure 5.19: Partial level scheme of $^{152}$Gd.** - Partial level scheme of the $\beta-$decay branch of $^{152}$Eu to $^{152}$Gd [NND]. The 344.3-keV $\gamma$-transition that is taken as the reference for the PRD construction is marked in red. The transitions that directly feed the 344-keV state are plotted in black to indicate that the centroid differences should be only corrected by the lifetime of this level ($\tau$=46.2(39) ps). Transitions that feed the 755-keV level are plotted in blue to indicate that the centroid differences should be corrected by the lifetimes of both levels, ($\tau$=46.2(39) and $\tau$=10.5(6) ps) respectively.

When calculating the PRD with the 344-keV $\gamma$ ray as the reference, the experimental centroids of the time distributions have to be corrected by (at least) the lifetime of the 344-keV state, which is $\tau$=46.2(2.5) ps. This is the case for transitions that directly populate the 344-keV level. However, for $\gamma$-rays that feed levels from above, the experimental centroids should be corrected by all the lifetimes of the levels that are involved. For example, if the 367- or 678-keV $\gamma$-transitions are selected the experimental centroids should be corrected by the lifetime $\tau$= 10.5(6) ps of the 755-keV level, in addition to $\tau$= 46.2(2.5) ps of the 344-keV level. When looking at the time spectra, one may appreciate that time distributions show asymmetries on the right or the left side of the quasi-Gaussian distribution, depending whether it is the delayed or the anti-delayed distribution, deviating from the Gaussian shape that a prompt transition would present. It is a consequence of the magnitude of the half-life $\tau$= 46.2(2.5) ps in some cases or $\tau$= 46.2(2.5)+10.5(6) ps in some other cases. Figure 5.20 shows the $\gamma$-transitions that are in coincidence with the 344-keV $\gamma$-ray.

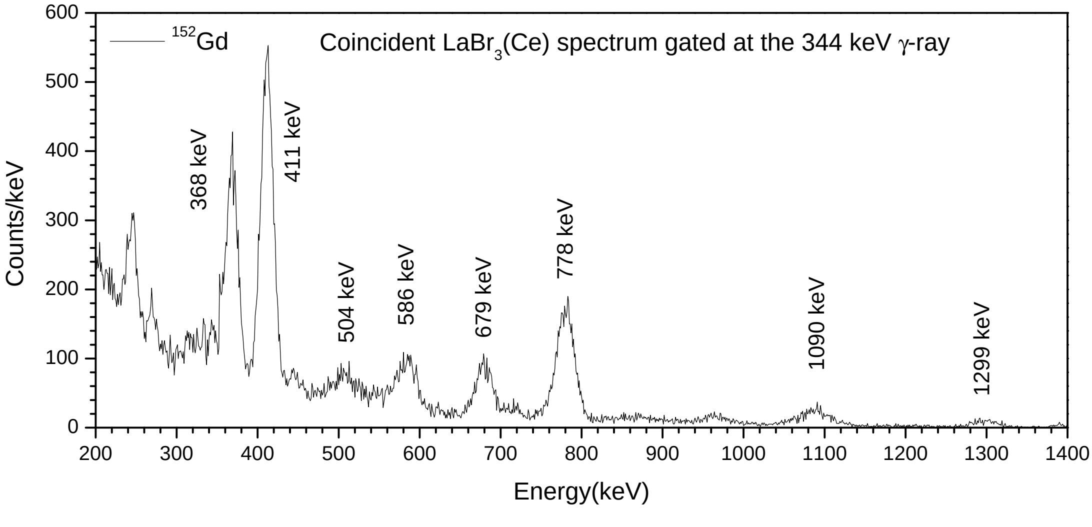

**Figure 5.20: Coincident LaBr$_3$(Ce) spectrum of $^{152}$Gd gated by the 344-keV transition.** - LaBr$_3$(Ce) spectrum of $^{152}$Gd in coincidence with the 344-keV $\gamma$-ray in the LaBr$_3$(Ce) detectors. The most relevant peaks that have been used for constructing the PRD are labeled with their energy.

In the electron capture branch, the 244.7-keV transition that de-excites the 367-keV level is a good a good candidate to be used as a reference for the construction of the PRD. Figure 5.21 depicts a partial level scheme of $^{152}$Sm, where the most relevant transitions for the construction of the PRD are shown. The 244-keV transition, which is selected as the reference, is plotted in red while the coincident $\gamma$-rays are in blue. The coincident transitions of 444 and 488 keV do not directly feed the 366 keV-state, but de-excite short-lived levels whose lifetimes are shorter than 1 ps, and hence their contribution to the time distribution is negligible. Consequently, the experimental centroid differences only need to be corrected by $\tau$= 83.2(9) ps. In this branch, one should take care because there is a long-lived state of $\tau$=2.02(2) ns at 121.8 keV. Figure 5.22 displays a LaBr$_3$(Ce) spectrum with the most relevant $\gamma$-transitions for the constructions of the PRD when there are two energy conditions applied: one in the 244 keV $\gamma$-ray in the LaBr$_3$(Ce) detectors and another one at 122 keV in the HPGe-Clovers.

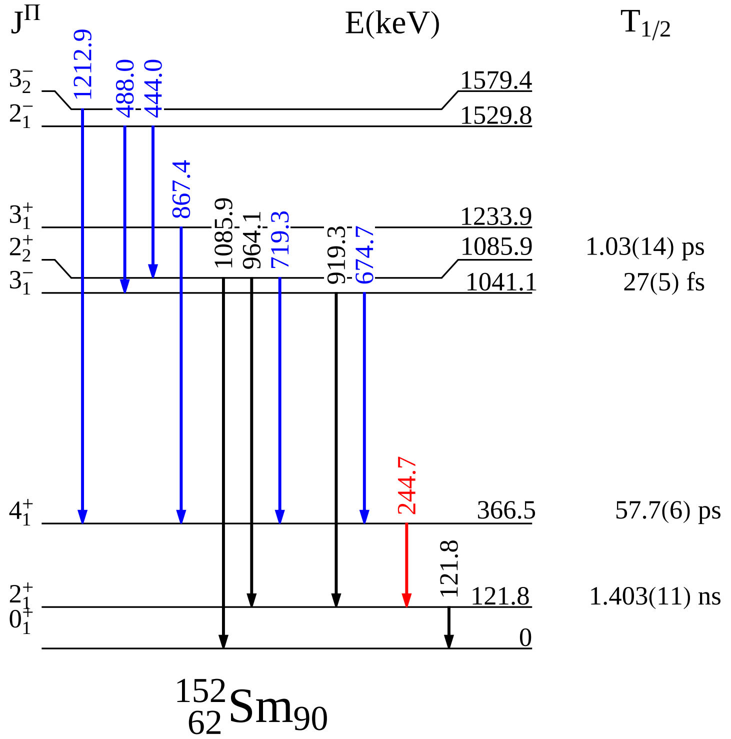

**Figure 5.21: Partial level scheme of $^{152}$Sm.** - Partial level scheme of the electron capture decay branch of $^{152}$Eu to $^{152}$Gd. The 244.3-keV $\gamma$ transition that is selected as the reference for the PRD construction is plotted in red, while the coincident $\gamma$-transitions are marked in blue. The experimental centroid differences should be corrected by the level lifetime of decay branch $\tau$= 83.2(9) ps.

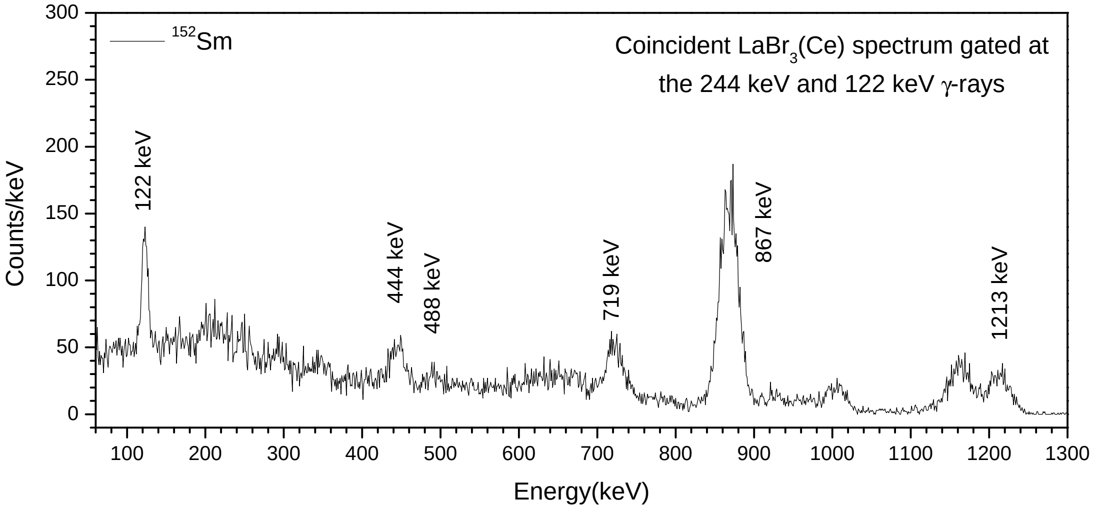

**Figure 5.22: LaBr$_3$(Ce) spectrum of $^{152}$Sm in coincidence with the 244- and 122-keV $\gamma$-transitions.** - LaBr$_3$(Ce) spectrum of $^{152}$Gd in coincidence with the 244-keV $\gamma$-ray in the LaBr$_3$(Ce) detectors and the 122-keV transition in the HPGe-clover detectors. The most relevant peaks for the construction of the PRD are labeled with their energy.

The other calibration source used in this work to extend the timing calibration to higher energies is the $^{49}$Ti isotope produced by the $^{48}$Ti(n,$\gamma$)$^{49}$Ti neutron capture reaction. The calibration procedure is similar to the one described above using a $^{152}$Eu source, but there is no need to correct by level lifetimes since the involved states are short-lived, being de-excited by prompt $\gamma$-rays. However, the level scheme of $^{49}$Ti is more complicated with the lack of a $\gamma$-ray that can be used as a common reference in the same way as those in $^{152}$Eu. Luckily, there is a strong $\gamma$-ray of 342 keV in $^{49}$Ti that was intentionally selected as a reference for the $^{49}$Ti source, with the aim of merging both PRD curves, those ones measured with $^{152}$Eu and $^{49}$Ti, because its energy is very close to the 344-keV transition in $^{152}$Eu that also issued as a reference.

The first step for constructing the PRD is to calculate the experimental centroid increment $\Delta C_{exp}$ for different energy differences ($\Delta E_{\gamma}$), where we arbitrarily define $\Delta E_{\gamma} = E_{Feeder} - E_{Decay}$, thus $\Delta E_{\gamma}$ can be positive or negative. It is performed by subtracting the centroid positions of the delayed and the anti-delayed distributions, using the same combination of $\gamma$-rays in the LaBr$_3$(Ce) but inverting the start and the stop in the TAC. This is expressed in equation 5.3.

$$\Delta C_{Exp}(\Delta E) = C_{Exp}^{Stop} - C_{Exp}^{Start} \tag{5.3}$$

Since both distributions are shifted by the lifetime $\tau$, one upwards and the other downwards, the centroid difference is given by the combined FEP prompt response for $\Delta E_\gamma$, the PRD, and twice the the known lifetime, equation 5.4.

$$\Delta C_{Exp}(\Delta E_\gamma) = PRD(\Delta E_\gamma) + 2\tau \tag{5.4}$$

In this procedure, it is assumed that the Compton contribution under full-energy peaks can be neglected, see below. From equation 5.4 the PRD curve can be obtained as expressed in Equation 5.5, that summarizes the MSC method [RPJR10].

$$PRD(\Delta E_\gamma) = \Delta C_{Exp}(\Delta E) - 2\tau \tag{5.5}$$

The experimental centroid differences depend on the energy of the $\gamma$-ray that works as a reference and on the energy of the matching $\gamma$-ray. The centroid differences after lifetime correction can be plotted as a function of the matching $\gamma$-energy. To achieve this, one needs to select reference energies, which in the present case were set to the 344-keV and 244-keV $\gamma$-rays. As a consequence of the two separate references, two curves with the same trend but shifted by an offset are obtained. The final distribution is obtained by just shifting one curve to the other. PRD curves presented in this analysis were calculated using a $^{152}Eu$ source using triple events, namely, two $\gamma$-rays detected in the LaBr$_3$(Ce) detectors and an another one in the HPGe-clover detectors. The high-resolution gate in the Ge allows skipping the background subtraction in this case when calculating the PRD, as the amount that is present underneath the FEPs is very low. However, in other cases background reduction is indispensable. Because of the lower statistics available in the neutron capture reaction, events were sorted with multiplicity two, $\gamma$-$\gamma$(t).

Once the PRD points are obtained, the PRD can be either obtained by linear interpolation or by a fit to a function. That is, to obtain the system response to an energy between them, or one can derive the centroid position by using the fitting function. In the current experiment, they are well fitted by a function of the form of the Equation 5.6 where a, b, c, d and e are the free parameters [ARJ$^+$17].

$$\Delta T(E) = \frac{a}{\sqrt{E_\gamma + b}} + cE_\gamma + dE_\gamma^2 + e \tag{5.6}$$

A common PRD curve for the analysis of the EXILL-FATIMA experiment was derived by J.-M. Régis [RSB$^+$14], which is shown in Figure 5.23. The combination of the $^{152}$Eu source with the neutron capture reaction resulted in a good cross-check as the two distinct distributions fitted well in the overlapping region. The overall PRD uncertainty given in [ARJ$^+$17] is 10 ps for the $3\sigma$ limit.

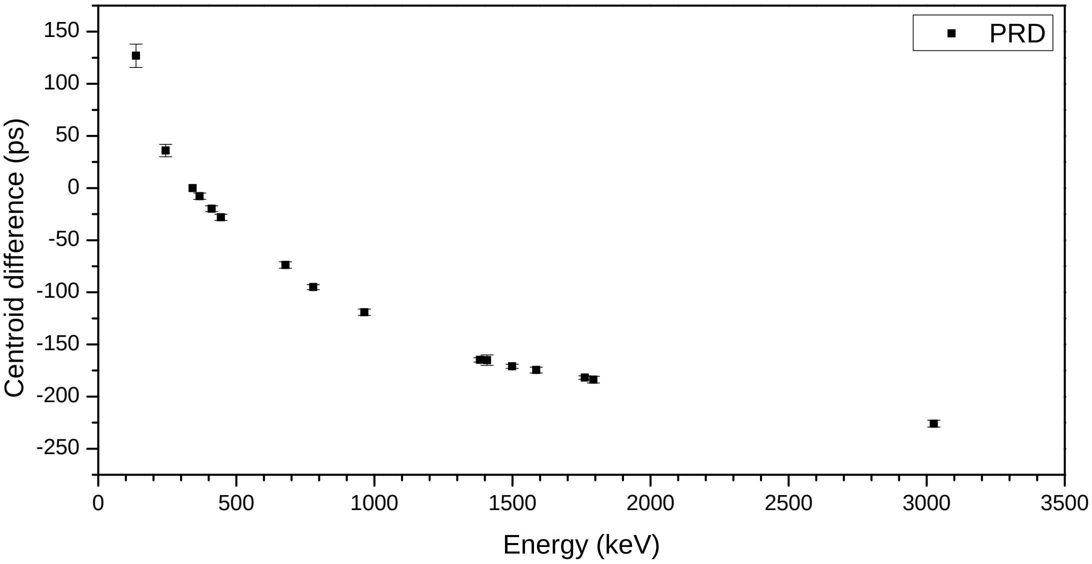

**Figure 5.23: PRD curve for the data analysis of the EXILL-FATIMA experiment.** - Energy dependent prompt response distribution, PRD, for the analysis of the EXILL-FATIMA experiment. The curve, which is taken from [RSB$^+$14], was derived using triple events, $\gamma\gamma\gamma$(t) from an $^{152}$Eu source and double events, $\gamma\gamma$(t) from the $^{48}$Ti(n,$\gamma$)$^{49}$Ti reaction. The Y-axis shows the centroid differences between the delayed and the anti-delayed distributions at a given energy. All points are shifted to the 342-keV $\gamma$-ray from the $^{48}$Ti(n,$\gamma$)$^{49}$Ti reaction, which is taken as the reference.

The general PRD curve (Figure 5.23) has been tested in this work by means of the $^{152}$Eu calibration source. The first approach consisted in measuring the level lifetimes of $^{152}$Sm and $^{152}$Gd, and the second test consisted in the construction of a partial PRD curve using the available energies from the $^{152}$Eu decay. In both cases, the measured values and those from the PRD curve in [RSB$^+$14] agree within a 10 ps uncertainty band. Hence, the distributed PRD curve was used in the present analysis, but using a 10 ps uncertainty for the interpolated values of PRD($\Delta E_\gamma$).

The experimental PRD has been also used to monitor the long-term stability of the set-up, along the five weeks of the experiment by checking possible drifts or variations among the three $^{152}$Eu data sets that were measured during the campaign.

### 5.7.2 Compton Response Time Distributions

In addition to the system response, the measured time spectra also contain the contribution of the Compton continua that lies underneath FEPs, being necessary to correct for this effect. Unfortunately, it is difficult to directly measure the Compton underneath the FEPs, but it can be derived by setting energy gates in the regions next to the FEP that only contain Compton events. In this way, it is possible to obtain the Compton time response at different energies, making it possible to construct Compton timing calibration curves. The idea of these curves is to use them to derive the Compton time response at the FEP energy by interpolating the value in the curve.

These curves provide the system response to the $\gamma$-rays that have only deposited part of their energy in the $\mathrm{LaBr_3(Ce)}$ crystals as a consequence of Compton scattering. In the past, the Compton-curve was only accessible through external calibration sources, nevertheless, thanks to the good energy resolution of the $\mathrm{LaBr_3(Ce)}$ crystals, it is possible nowadays to construct an internal curve for Compton corrections that accounts better for all the Compton continuum. The Compton curve should follow a very similar trend as the one displayed by the PRD curve, except for the low energies [MGM89].

In this work, we distinguish between two types of Compton-response distributions: the CRD (Compton Response Distribution) and the CCRD (Compton-Compton Response Distribution). In fact, both curves account for the time response of Compton events by changing the reference. The CRD curve gives the time response of the Compton continuum that is in coincidence with a peak composed of full-energy events and the related Compton underneath. The aim of deriving this curve is to correct by the contribution to the total time spectrum produced by the Compton that is in coincidence with total peaks (FEP+Compton). The other type of Compton-curve is the CCRD, which provides the time response of the pure Compton events that are in coincidence with pure Compton events. In this case, there is not any FEP involved. This distribution becomes very important when dealing with data sets that contain a high level of Compton events. For further information on both types of curves see Section 5.8.2.

The procedure to construct the CRDs and the CCRD is similar to the one of the PRD. The first step consists in calculating the centroids of the delayed and the anti-delayed time distributions for different energy increments $\Delta E_\gamma$, where the reference energy works as the start or the stop of the TAC. When calculating the CRD curves a peak containing full-energy events and the Compton underneath acts as the reference for deriving the delayed and the anti-delayed distributions, while a region containing only Compton events works as the reference when deriving the CCRD. The second step consists in calculating the experimental centroid differences of the delayed and the anti-delayed time spectra for different energy increments, as expressed in Equation 5.7. Then, the derived $\Delta C(\Delta E_\gamma)$ values will be plotted as a function of the energy to construct the Compton-curves. Examples of the CRD and CCRD curves are provided in the following sections 5.7.2.1 and 5.7.2.2.

$$\Delta C(\Delta E_\gamma) = C_{Exp}^{Delayed} - C_{Exp}^{anti-delayed} \tag{5.7}$$

#### 5.7.2.1 Compton Response using calibration sources

A good way to calculate the system response to Compton events is to use an external calibration source, such as $^{60}$Co. The latter is an excellent candidate since it only contains two $\gamma$-rays in coincidence with energies of 1173 and 1332 keV, and it allows to set the energy gates in the Compton continuum ensuring that there is no FEP contribution. This is the same procedure as the one used in Chapter 3, Section 3.6.5 to construct the Compton walk curves, but in this case, using the reference as either start or stop. The approach consists in defining an energy gate in 1332-keV $\gamma$-ray as the reference, while the delayed and anti-delayed time distributions of the coincident Compton continua from the 1173-keV $\gamma$-transition are obtained. The method to obtain the final CRD is similar to the one followed for the PRD explained in Section 5.7.1.1. Figure 5.24 shows the Compton time response through the delayed (black) and anti-delayed (red) distributions derived for the $^{60}$Co source. In this example, the reference is set in the 1332-keV $\gamma$-transition, therefore the Start curve corresponds to the delayed distribution and the Stop to the anti-delayed. One should note that the measured centroids have been shifted to the position of the 1173-keV FEP which is taken as the zero reference. The combined Compton Response Distribution (CRD) is plotted in Figure 5.25.

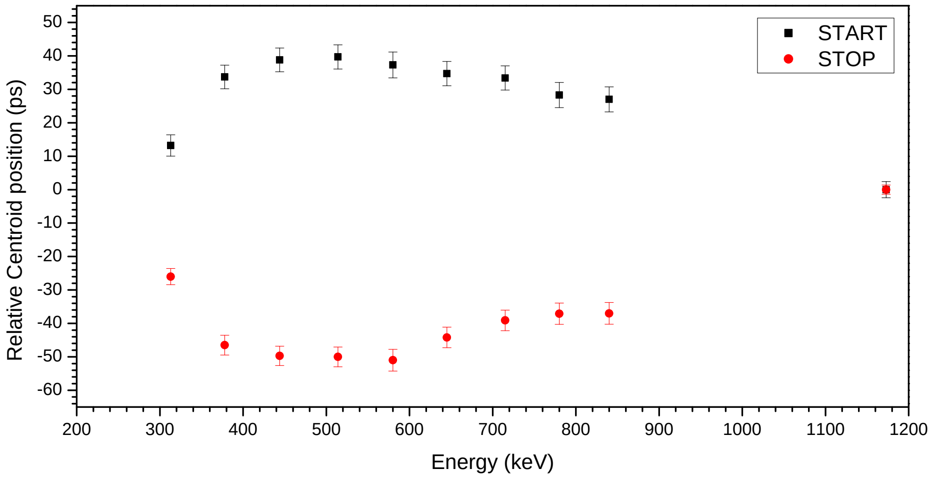

**Figure 5.24: Compton Response Distributions, Start and Stop, measured using an external $^{60}$Co source** - Compton time response calculated by using an external $^{60}$Co source. The plot shows the Start (black) and the Stop (red) distributions derived when the reference is set in the 1332-keV FEP. The measured centroids have been shifted to the position of the 1173-keV FEP, which is taken as zero.

The main advantage of using the $^{60}$Co source is that the selected Compton continua only comes from the coincident 1173 keV $\gamma$-transition, while the main drawback is the maximum energy, limited to the Compton edge of the 1173-keV $\gamma$-ray (963 keV). In the first approximation, an external Compton Response Distribution built with calibration sources reproduces well the system response to Compton events.

To calculate the Compton-Compton response distribution, the procedure is analogous to the one described above, but selecting for the energy reference a region that contains only Compton events, instead of the 1332 keV $\gamma$-ray. The delayed and anti-delayed time distributions are built with the coincident Compton continua.

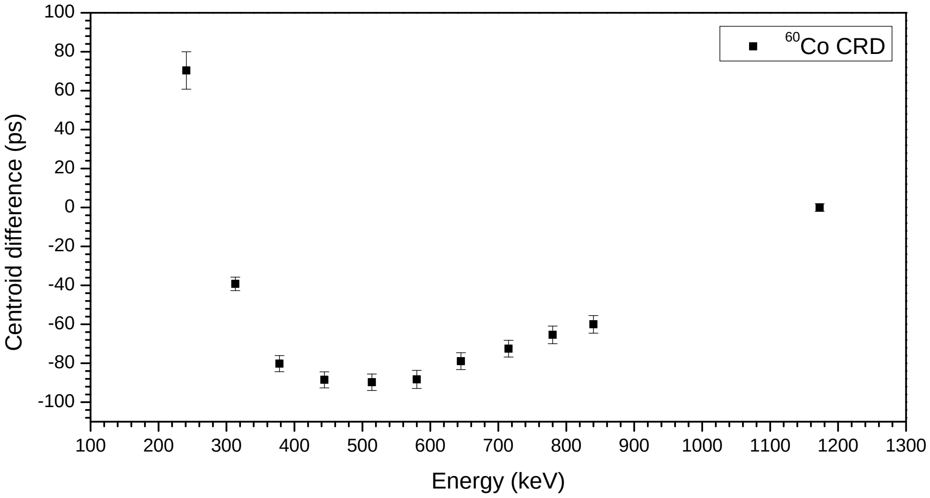

**Figure 5.25: Compton Response Distributions measured using an external $^{60}$Co source.** - Compton time response (CRD) obtained with an external $^{60}$Co source. The reference is set in the 1332-keV FEP. The measured centroids have been shifted to the position of the 1173-keV FEP, which is taken as the zero.

#### 5.7.2.2 Internal Compton Response distribution: CRD$_{feeder}$ and CRD$_{decay}$

In this thesis, we refer to peak-to-background-ratios (P/B), as the ratio between the full-energy events contained in the total peak and the background events $P/B = (A_T - A_{Bkg})/A_{Bkg}$. If no extra cleaning is applied, in this experiment the background under the FEPs is approximately 40% of the total statistics, reaching in some cases P/B = 1, which means that there is the same amount of background than full-energy events. Hence, it is absolutely necessary to correct for this effect. Considering that the underlying background is mostly composed by the Compton continua of several $\gamma$-rays of higher energy, and given the scattering conditions during the experiment, especially from $\gamma$-ray energies which are way different, it is preferred to use an internal Compton-response distribution.

The procedure to construct the internal CRD is equivalent to the one explained in Section 5.7.2.1, but the energy regions are now selected in the coincident LaBr$_3$(Ce) spectra after having applied one or two energy conditions on the Clover detectors (triple or quadruple events), and one in the LaBr$_3$(Ce) detectors. The first step consists in gating on the $\gamma$ that populates ($\gamma_{feeder}$) or de-excites the level ($\gamma_{decay}$), while the matching LaBr$_3$(Ce) detectors are gated in background regions at different energies around the FEP of interest ($\gamma_{feeder}$ or $\gamma_{decay}$).

Figure 5.26 illustrates the procedure of Compton background selection for building an internal CRD curve. The plot combines the coincident spectra of LaBr$_3$(Ce) detectors in red and of HPGe-Clovers in black, which is used to ensure that the selected regions do not include FEPs. The plot corresponds to the CRD$_{decay}$ construction to derive the $4^+$ lifetime in $^{136}$Te. The background regions are selected around the 423-keV FEP, which is the energy of interest in the present example. They are marked with gray shadowed areas in the plot.

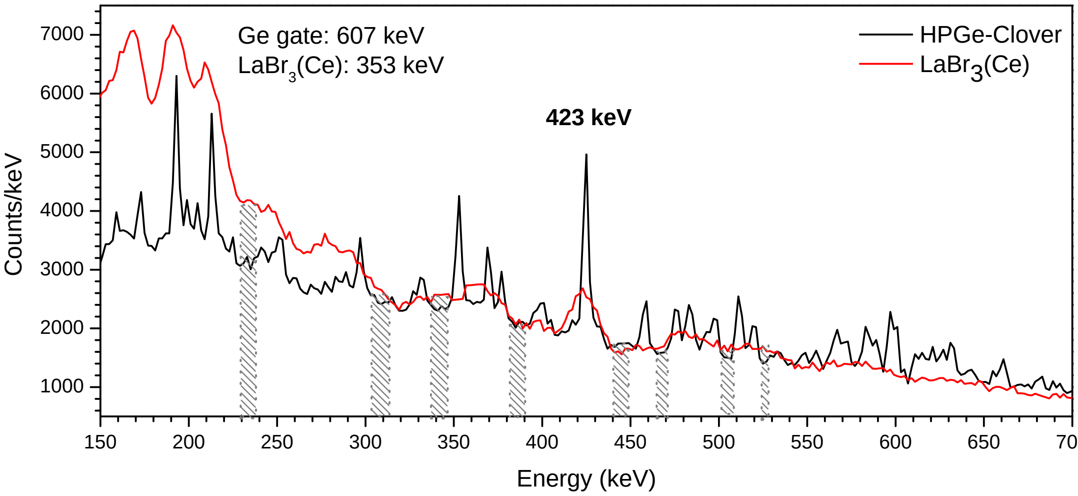

**Figure 5.26: Coincident HPGe and LaBr$_3$(Ce) spectra gated in the 607- and 353-keV $\gamma$-ray for the selection of the background regions.** - Energy spectra of the HPGe-Clovers (black) and the LaBr$_3$(Ce) detectors (red) in coincidence with the 607-keV $\gamma$-transition in the HPGe and 353-keV $\gamma$-ray in the LaBr$_3$(Ce) detectors. The plot provides an example of how the Compton regions are selected to derive the Compton time response at different energies and the related Compton-curve. The background regions which are selected around the 423-keV FEP, are marked with gray shadowed. The reference energy is set at 353 keV $\gamma$-ray. The example uses the $^{241}$Pu data set.

The second step, as already mentioned, consists in obtaining the centroid positions of the delayed and anti-delayed time distributions at the different energy increments ($\Delta E_\gamma$) and the corresponding centroid difference ($\Delta C_{exp}(\Delta E_\gamma)$). The last step is to represent the measured $\Delta C_{exp}(\Delta E_\gamma)$ as a function of the energy increment, constructing the CRD curves.

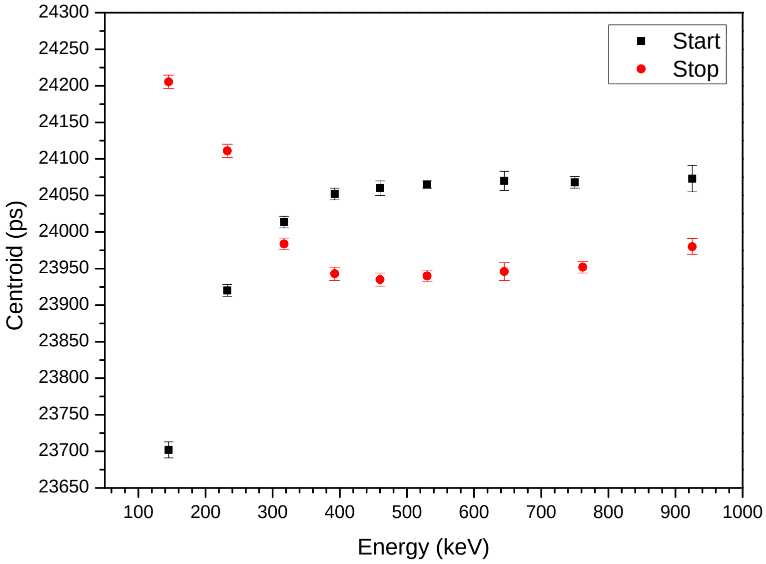

**Figure 5.27: Delayed and anti-delayed Compton Response Distribution measured with the 353-keV $\gamma$-ray taken as reference.** - Internal Compton Response Distributions, start and stop, derived for the lifetime measurement of the $4^+$ state in $^{136}$Te. In this case the Start curve (black) corresponds to the delayed distribution because the 353-keV $\gamma$-ray is set as reference. The Start curve provides the time differences between the Compton events, which act as the Start of the TAC and the 353-keV $\gamma$-transition that works as the Stop. The Stop curve (red) is, in this case, the anti-delayed distribution. It provides the time difference between Compton events that work as the Stop of the TAC and the 353-keV $\gamma$-ray that acts as the Start.

As there are two $\gamma$-rays involved in the calculation, the $\gamma_{feeder}$ and $\gamma_{decay}$, this procedure should be carried out twice to account for the Compton contribution of both transitions. Hence, there would be a CRD$_{decay}$ curve that provides the Compton response of the background underneath the $\gamma_{decay}$, and there would be a CRD$_{feeder}$ that gives the response of the Compton under the $\gamma_{decay}$. When constructing the CRD$_{feeder}$ or the CRD$_{decay}$ the energies that act as the reference is the $\gamma_{feeder}$ and the $\gamma_{decay}$ respectively. Figure 5.27 provides as an example the Start and the Stop curves that compose the CRD$_{feeder}$ distribution used to derive the lifetime of the $4^+$ state. In this case, the 353-keV $\gamma$-ray has been set as the reference, hence, the Start curve corresponds to the delayed distribution, and the Stop to the anti-delayed one. The CRD$_{feeder}$ distribution, which is the difference between the start and the stop curves, is shown in Figure 5.28. The HPGe-Clovers gate was selected in the 750-keV $\gamma$-ray.

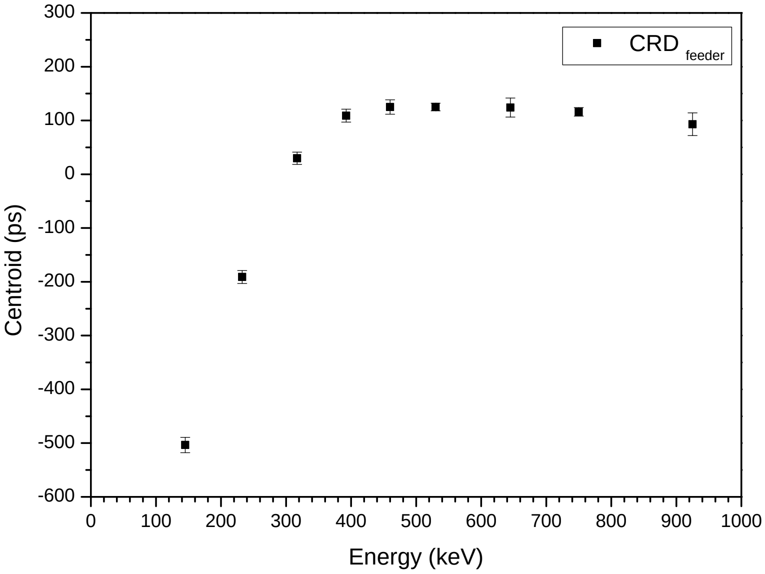

**Figure 5.28: Internal Compton Response Distribution, CRD$_{feeder}$, for the lifetime measurement of the 4$^+$ state.** - Example of the internal Compton Response CRD$_{feeder}$ derived for the lifetime measurement of the 4$^+$ state in $^{136}$Te. The 353-keV $\gamma$-ray was set as the reference and the Ge-gate on the 750-keV $\gamma$-ray. The curve shown here is the subtraction of the Start and Stop curves displayed in Figure 5.27.

### 5.7.2.3 Internal Compton Response distribution: CCRD

The Compton-Compton response (CCRD), accounts for the system response to the Compton events that are in coincidence with pure Compton events. The aim of this curve is to obtain the time response generated by the Compton continua that lie underneath both FEP peaks, $\gamma_{feeder}$ and $\gamma_{decay}$. As this quantity cannot be directly measured, it is derived by interpolating the CCRD curve at the corresponding energy difference. This curve is the Compton analogous to the PRD. The procedure to build it is identical to the one followed to construct the CRD$_{feeder}$ or CRD$_{decay}$ curves, but selecting as the reference a region that contains only Compton events. Once one or two gating conditions are chosen in the high-resolution HPGe-Clovers two energy gates are set in the LaBr$_3$(Ce) detectors, now on regions that only contain Compton events. The experimental centroids for the delayed and the anti-delayed distributions have been measured and can be plotted as a function of energy, as illustrated in Figure 5.29.

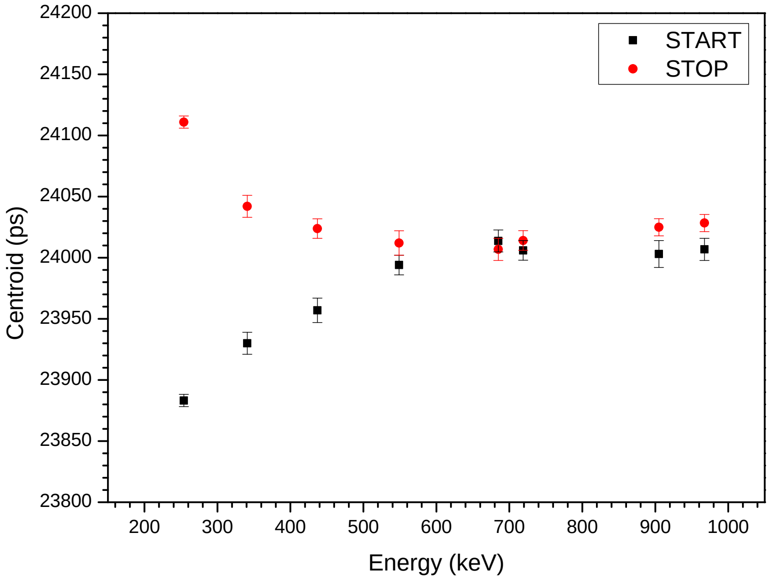

**Figure 5.29: Compton-Compton Start and Stop response distribution, for the data analysis of the EXILL-FATIMA experiment.** - Start and Stop distributions that provide the Compton-Compton time response. The reference in the $LaBr_3$(Ce) detectors has been set in 644 keV, while the Ge-gate in 750 keV. The Start curve, which is plotted in black, provides the time differences between the Compton events at different energies that act as the Start of the TAC and the Compton events at 644 keV that work as the Stop. The Stop distribution (red) provides the time differences between the Compton events at 644 keV (start) and the rest of the energies (stop). These curves have been derived by using the $^{241}$Pu data set.

The next step consists in calculating the corresponding differences at the energy increment, and plot them as a function of the energy, as shown in Figure 5.30, where the CCRD curve derived by using the $^{241}$Pu data set is plotted. The curve is aimed at correcting the Compton-Compton effect that is present in data sets sorted with multiplicity three, with only one high-resolution energy gate and two gates in $LaBr_3$(Ce) detectors. Since this curve has been derived for the current data analysis, there is no need for data points of energies above 1 MeV. The way in which the CCRD($\Delta E_\gamma$) is used for an energy increment $\Delta E_\gamma$ is equivalent to the usage of the PRD($\Delta E_\gamma$), that it to say:

$$CCRD(\Delta E_{feeder-decay}) = CCRD(E_{feeder}) - CCRD(E_{decay}). \tag{5.8}$$

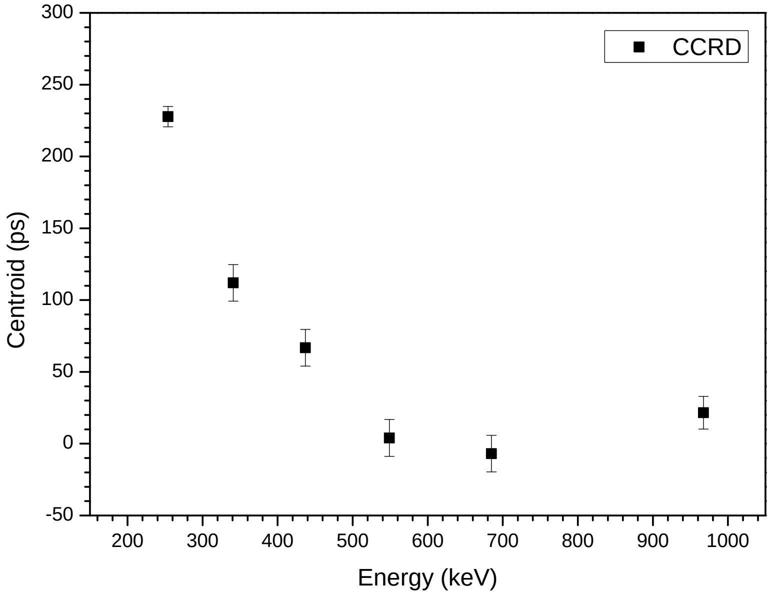

**Figure 5.30: Compton-Compton Response Distribution, CCRD.** - Internal Compton-Compton response distribution, CCRD, for the data analysis of the EXILL-FATIMA experiment. The reference energy in the $LaBr_3(Ce)$ detectors has been set in 644 keV, while the high-resolution energy gate in 750 keV.

## 5.8 Implementation of the background corrections

As already explained, the level of background in the fission experiments performed within the EXILL-FATIMA campaign is very high, mostly caused by Compton-scattered $\gamma$-rays. Especially at energies under 300 keV, there is a large superposition of Compton continua from $\gamma$-rays of higher energy with a substantial contribution of backscatter around 200 keV. The measured time spectrum arises from the superposition of the time distributions originated by full-energy events and Compton events. As a consequence of the different time response of Compton and full-energy events [MGM89, MWM$^+$91] it is necessary to correct for the time shift from Compton events. In general, because we are dealing with the time difference between two $\gamma$-rays, when gating at the $\gamma_{feeder}$ and the $\gamma_{decay}$ the measured time distribution can be described as the convolution of four time responses: the response derived from the full-energy events from the $\gamma_{feeder}$ in coincidence with the full-energy events of the $\gamma_{decay}$ (FEP-FEP), the response of the full-energy events of the $\gamma_{feeder}$ in coincidence with the Compton under the $\gamma_{decay}$ (FEP-Compton), the contribution of the Compton under the $\gamma_{feeder}$ and the full-energy events of the $\gamma_{decay}$ (Compton-FEP), and the response of the Compton under both $\gamma$-rays (Compton-Compton). Schematically it can be written as follows.

$$T_{exp} = \overbrace{T_{FEP-FEP}}^{1} \oplus \overbrace{T_{FEP-Compton}}^{2} \oplus \overbrace{T_{Compton-FEP}}^{3} \oplus \overbrace{T_{Compton-Compton}}^{4} \tag{5.9}$$

Every term includes the contribution of the centroid shift for each type of coincident event and the total number of counts for each type, i.e. if no background is present, the experimental time distribution will only be given by the first term.

### 5.8.1 First-order background corrections

If we consider the time spectrum originating by gating on one of the two $\gamma$-rays (which includes a FEP and a Compton component) and examine the projection onto the LaBr$_3$(Ce) energy, the experimental centroid shift $\Delta C_{exp}$ measured from the TAC spectra may be written in Equation 5.10 as

$$\Delta C_{exp} \cdot A_{Total} = \Delta C_{FEP} \cdot A_{FEP} + \Delta C_{Comp} \cdot A_{Comp}, \tag{5.10}$$

where $\Delta C_{Comp}$ is the centroid increment due to Compton events and $\Delta C_{FEP}$ is the centroid difference due to the full-energy events, which is the magnitude required to obtain $\tau$. The area relation is $A_T = A_{FEP} + A_{Comp}$. Equation 5.10 can be rewritten as Equation 5.11, where the centroid shift due to the full-energy events is expressed as a function of the experimental centroid increment ($\Delta C_{exp}$), the peak-to-background ratio (P/B)= ($A_{FEP}/A_{Comp}$) and the centroid shift due to Compton events ($\Delta C_{Comp}$).

$$\Delta C_{FEP} = \Delta C_{exp} + \frac{\Delta C_{exp} - \Delta C_{Comp}}{P/B} \tag{5.11}$$

The $\Delta C_{Comp}$ magnitude can be obtained using an external CRD curve such as the one explained in Subsection 5.7.2.1 or using internal CRD curves like those described in Subsection 5.7.2.2. But this procedure only takes into account one of the two combinations of $\gamma$-rays in the LaBr$_3$(Ce) detectors, so the background correction should be applied twice, one for the Compton underneath the $\gamma_{decay}$ and one for the Compton beneath the $\gamma_{feeder}$, given by Equation 5.12.

$$t_{cor.}(E_{feeder}) = \frac{\Delta C_{exp} - \Delta C_{Bkg}^{feeder}}{P/B_{feeder}} \qquad t_{cor.}(E_{decay}) = \frac{\Delta C_{exp}^{decay} - \Delta C_{Bkg}}{P/B_{decay}} \tag{5.12}$$

In the previous expression, $\Delta C_{Bkg}$ is the centroid shift due to the time response of the background and P/B is the peak to background ratio defined as $(P/B) = (A_{FEP}/A_{Bkg})$. The time response of the background $\Delta C_{Bkg}$ is obtained by interpolating the time response of the Compton events around the FEP at the corresponding energy by using the CRD$_{feeder}$ or CRD$_{decay}$ curves, respectively.

One should note that both CRD$_{feeder}$ and CRD$_{decay}$ curves provide the time response of the Compton events that are in coincidence with the reference peak, which contains both full-energy events and Compton events. That is to say, the derived $\Delta C_{Bkg}$ values are the superposition of both influences, the Compton-Compton and FEP-Compton. Therefore if both $t_{cor.}$ corrections were applied to obtain $\Delta C_{FEP}$ the effect of Compton-Compton events would be over-corrected. A way of taking this into account while conserving the total area of the coincidence is applying a first-order correction in the form of Equation 5.13, where the experimental centroid differences $\Delta C_{exp}$ is shifted by the average of the Compton corrections relative to the $\gamma_{feeder}$ and the $\gamma_{decay}$ [ARJ$^+$17].

$$\Delta C_{FEP} = \Delta C_{exp} + \frac{1}{2}[t_{cor.}(E_{feeder}) + t_{cor.}(E_{decay})] \tag{5.13}$$

The main advantage of this procedure is that it can be applied in most of the situations, even when the correction contributions from the feeder and the decay, $t_{cor}(E_{feeder})$ and $t_{cor}(E_{decay})$, are very different like in the case of $^{100}$Zr described in [ARJ$^+$17]. However, the main drawback is that it does not totally account for the Compton-Compton effect. It corrects by the mean value of the Compton-Compton contribution included in $\Delta C_{Bkg}$, which is derived from CRD$_{feeder}$ and CRD$_{decay}$. This procedure has been successfully used in several analyses by our collaboration [RJSS$^+$17, ARJ$^+$17].

Once the experimental centroid difference has been corrected, the $\Delta C_{FEP}$ value should be shifted by the PRD($\Delta E_\gamma$) curve at the corresponding energy increment. Afterwards, the general equation of the MSC method, Equation 2.6, can be applied to derive the lifetime of the level of interest.

The total uncertainty $\delta\tau$ in lifetime measurements when using the correction to first order is expressed by Equation 5.14. It accounts for the uncertainty in the experimental centroid difference $\delta\Delta C_{exp}$, the error derived from the Compton corrections on both $\gamma_{feeder}$ and the $\gamma_{decay}$, $\delta t_{corr}$, and the PRD uncertainty $\delta PRD$:

$$\delta\tau = \frac{1}{2}\sqrt{(\delta\Delta C_{exp})^2 + (\delta t_{corr})^2 + (\delta PRD)^2}. \tag{5.14}$$

In the present analysis, the PRD contribution $\delta PRD$ is 10 ps, the uncertainty $\delta\Delta C_{exp}$ derived from the experimental centroid shift depends on every case but typical values yield around 8 ps, and the error related to the Compton correction $\delta t_{corr}$ is given by Equation 5.16. Equation 5.15 expresses the individual contributions to the uncertainty, from the correction by the feeder and the decay transitions.

$$\delta t_{corr}(E_{feeder/decay}) = \sqrt{\left(\frac{\delta(\Delta C_{exp})}{P/B}\right)^2 + \left(\frac{\delta(-\Delta C_{Bkg}(}{P/B}\right)^2 + \left(\frac{-(\Delta C_{exp} - \Delta C_{Bkg})\cdot\delta(P/B)}{(P/B)^2}\right)^2} \tag{5.15}$$

$$\delta t_{corr}(\Delta E) = \frac{1}{2}\sqrt{(\delta t_{corr}(E_{feeder}))^2 + (\delta t_{corr}(E_{decay}))^2}. \tag{5.16}$$

### 5.8.2 Compton correction implemented in this thesis

When dealing with data sets that contain a high proportion of Compton events, the Compton-Compton contribution becomes relevant and in some cases dominant. To account for this problem, in the present work a Compton correction that accounts totally for the Compton contribution has been developed. For this purpose let us return to Equation 5.9, which illustrates the four contributions to the overall time response of a $\gamma$-$\gamma$(t) coincidence. The FEP-FEP contribution is labeled with 1, the FEP-Compton response is marked with 2, the Compton-FEP contribution is indicated with 3 and the Compton-Compton with 4. Using the simplified notation $F$=$FEP$, $C$=$Compton$ and $T$=Total, the relation between the measured centroid shift and the four contributions considering their areas can be expressed with Equation 5.17.

$$\begin{aligned} A_T \cdot \Delta C_{exp} = \overbrace{A_T \Delta C_{FC-FC}}^{T} = \\ = \overbrace{A_{F-F}\Delta C_{F-F}}^{1} + \overbrace{A_{F-C}\Delta C_{F-C}}^{2} + \overbrace{A_{C-F}\Delta C_{C-F}}^{3} + \overbrace{A_{C-C}\Delta C_{C-C}}^{4} \end{aligned} \tag{5.17}$$

The term labeled with $T$ represents the total time response of the $\gamma_{feeder}$ versus $\gamma_{decay}$, which comprises the four time responses already mentioned. The term marked with 1 is the actual quantity of interest for lifetime measurements, which is the time response derived from the full-energy events in both $\gamma_{feeder}$ and $\gamma_{decay}$. This response cannot be directly measured but it may be obtained from the rest of the components of Equation 5.17. The term marked with a 2 is the contribution derived from the Compton under the $\gamma_{decay}$ and the full-energy events from the $\gamma_{feeder}$; the term indicated with 3 reflects the time response of the full-energy events in the $\gamma_{decay}$ and the Compton under the $\gamma_{feeder}$; and the term labeled with 4 is the response of the Compton events that are in coincidence underneath both FEPs.

The terms marked with 2, 3 and 4 in Equation 5.17 cannot be directly measured. Nevertheless, terms 2 and 3 can be derived from the CRD$_{feeder}$ and CRD$_{decay}$ curves, since these curves provide the time response of the Compton events that are in coincidence with the $\gamma_{feeder}$ and the $\gamma_{decay}$ (FEP+Compton), and term 4 can be obtained from the CCRD curve. For this purpose Equation 5.17 is transformed into Equation 5.18 as follows:

$$\begin{aligned} A_T \cdot \Delta C_{exp} = A_T \Delta C_{FC-FC} = \\ = A_{F-F}\Delta C_{F-F} + (A_{FC-C}\Delta C_{FC-C} - A_{C-C}\Delta C_{C-C}) + \\ +(A_{C-FC}\Delta C_{C-FC} - A_{C-C}\Delta C_{C-C}) + A_{C-C}\Delta C_{C-C} \end{aligned} \tag{5.18}$$

Therefore, the centroid shift arising from FEPs, the one that provides the level lifetime is simply given by

$$\begin{aligned} \Delta C_{F-F} = \frac{1}{A_{F-F}}(A_{FC-FC} \cdot \Delta C_{FC-FC} + A_{C-C} \cdot \Delta C_{C-C} \\ -A_{FC-C} \cdot \Delta C_{FC-C} - A_{C-FC} \cdot \Delta C_{C-FC}). \end{aligned} \tag{5.19}$$

Equation 5.19 is the kingpin of the background corrections in the mirror symmetric centroid method.

Nonetheless, in the experiment the contribution arising from Compton background underneath FEP peaks cannot be directly measured; instead Compton gates around the FEP peaks can be defined in order to derive these contributions as shown in Figure 5.26, which we label as C′. Hence the three background contributions can be alternatively expressed as:

- $\Delta C_{FC-C'}$: Time response derived from the full-energy and Compton events in the $\gamma_{feeder}$ (FC) versus the related Compton events (C) in the $\gamma_{decay}$ selected on the right hand side of the FEP. This time response should be shifted to the energy of C by using the calibration curve.
- $\Delta C_{C'-FC}$: Compton on the right hand side of the $\gamma$-feeder versus Compton+FEP on the $\gamma$-decay.
- $\Delta C_{C'-C'}$: Compton versus Compton contribution obtained from gates on the side of both FEPs.

As a function of the new time shifts Equation 5.19 may be written as:

$$\begin{aligned} \Delta C_{F-F} = \frac{1}{A_{F-F}}(A_{FC-FC} \cdot \Delta C_{FC-FC} + A_{C'-C'} \cdot \Delta C_{C'-C'} \\ -A_{FC-C'} \cdot \Delta C_{FC-C'} - A_{C'-FC} \cdot \Delta C_{C'-FC}). \end{aligned} \tag{5.20}$$

The time distributions of $\Delta C_{FC-C'}$, $\Delta C_{C'-FC}$ and $\Delta C_{C'-C'}$ are experimentally measured and shifted to the corresponding energies of the FEP-FEP by using the $\mathrm{CRD}_{feeder}$ and $\mathrm{CRD}_{decay}$ curves (see section 5.7.2.2). In addition, the total area of the time distribution can be written as a function of the four components as expressed in Equation 5.21.

$$A_T = A_{F-F} + A_{F-C} + A_{C-F} + A_{C-C} \tag{5.21}$$

And considering that $A_{FC-C} = A_{F-C} + A_{C-C}$ and $A_{C-FC} = A_{C-F} + A_{C-C}$, the area of interest, $A_{F-F}$, can be derived from Equation 5.22 below.

$$A_{F-F} = A_T - A_{FC-C} - A_{CF-C} + A_{C-C} \tag{5.22}$$

The areas need to be extrapolated from the measured areas $A_{FC-C'}$, $A_{C'-FC}$ and $A_{C'-C'}$.

Once measured, the $\Delta C_{F-F}$ value derived from 5.19 should be shifted by the $\mathrm{PRD}(\Delta E_\gamma)$ curve for the corresponding energy increment. The uncertainty arises from error propagation in Equation 5.19.

### 5.8.3 Verification of the analysis procedure using $^{100}$Zr

Taking advantage of the fact that $^{100}$Zr comes as a contaminant with good production yield in our data set (See Chapter 6), the analysis procedure and the Compton correction implemented in this PhD Thesis have been tested and validated. The lifetime values in $^{100}$Zr were measured and published by S. Ansari and co-workers in [ARJ$^{+}$17] using the data recorded during the EXILL-FATIMA experiment, and by A.G. Smith *et.al.* in [SWP$^{+}$02] making use of a differential plunger and a $^{252}$Cf source. The lifetime of the $4^+$ state appears to be a good candidate to check the effectiveness of the analysis procedure and the Compton corrections implemented in this work. This is because Smith and co-workers report a value of 54(4) ps, while Ansari *et al.* quote 37(4) ps.

Moreover, in [ARJ+17], it is reported that the data set from $^{241}$Pu does not yield reliable results for this level lifetime as a consequence of the fission partners contributions, which can not be separated properly. A partial level scheme of $^{100}$Zr is provided in Figure 5.31.

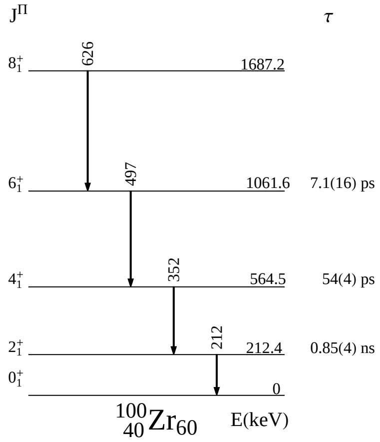

**Figure 5.31: Partial level scheme of $^{100}$Zr**

In order to investigate this issue and to cross-check the analysis procedure, the $4^+$ lifetime in $^{100}$Zr has been measured using the $^{241}$Pu target, via triple coincidences $\gamma\gamma\gamma$(t). In triple coincidences, the time information is derived from the difference in the centroid positions of the delayed and the anti-delayed TAC spectra, after being triple gated (HPGe-LaBr$_3$(Ce)-LaBr$_3$(Ce)). The $\gamma$-transitions that populate and de-excite the level of interest are selected in the LaBr$_3$(Ce) detectors, while an extra $\gamma$-ray from the cascade is chosen at the HPGe detectors to clean the coincidence events. Hence, the lifetime of the $4^+$ state in $^{100}$Zr is derived by the time differences between the arrival of the 497-keV transition that populates the level and the 352-keV $\gamma$-ray that de-excites it. In this case, the Ge-gate has been set in the 212-keV transition, but it could have been set in the 623-keV $\gamma$-ray.

The first step in the analysis is to check the coincident spectra in order to identify potential contaminants that may hamper the analysis and to set the width of the gates. Three coincident spectra LaBr$_3$(Ce)-gated in the 212-keV $\gamma$-ray are shown in Figure 5.32. The black one is Ge-gated by the 212-keV transition, the red plot is Ge-gated in the background on the right hand side of the 212-keV peak (C) and the blue spectrum is the difference of the black and the red ones. This figure is also aimed at confirming

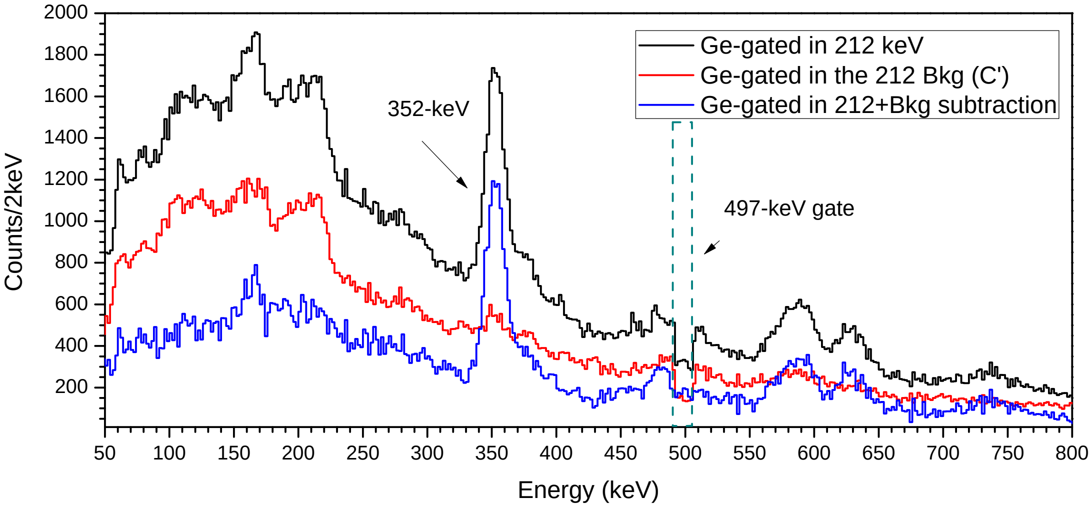

**Figure 5.32: Coincident LaBr$_3$(Ce) spectra Ge-gated by the 212-keV transition and LaBr$_3$(Ce)-gated by the 497-keV $\gamma$-ray** - Coincident LaBr$_3$(Ce) spectra Ge-gated by the 212-keV $\gamma$-ray (black) and in the background on the right hand side of 212 keV ($C'$) (red) for the $^{241}$Pu dataset. The blue plot is the difference between the black and the red and illustrates the effect of subtracting the events in coincidence with the background of the Ge-gated peaks. The width of LaBr$_3$(Ce) gate is indicated in the plot with green dashed lines, and the matching energy of 353 keV is labelled.

whether the Ge-background subtraction approach explained in Section 5.5.2.3 is worth to be applied here. Using this approach, the (P/B) ratio of the 352-keV transition is (P/B)=6.0(3) and (P/B)=2.8(2) for the 497-keV $\gamma$-ray, and consequently it is used. From Figure 5.32 there are no potential contaminant visible. The width of the gates displayed in the plot is the same as the one employed for building the delayed and the anti-delayed Ft-matrices. Next we check the Compton correction implemented in this PhD thesis. Detailed information about the intermediate steps of the analysis will be provided in Section 6.2.2 dealing with $^{136}$Te lifetimes.

Figure 5.33 presents the measured delayed (497-352-keV) and anti-delayed (352-497-keV) time distributions. The centroid difference for this case is $\Delta C_{exp}$=34(6) ps. The nest step after having obtaining the experimental centroid difference $\Delta C_{exp}(\Delta E_\gamma)$ is to obtain the system response at the energy difference $\Delta E_\gamma = E_{feeder} - E_{decay}$, where $E_{feeder}$ = 352 keV and $E_{decay}$ = 212 keV by interpolating in the PRD curve (Figure 5.23), PRD($E_{497}$-$E_{352}$)=−39(10) ps. Although both peak-to-background ratios (P/B) of $\gamma_{feeder}$ and $\gamma_{decay}$ are much higher than one, which means that the Compton

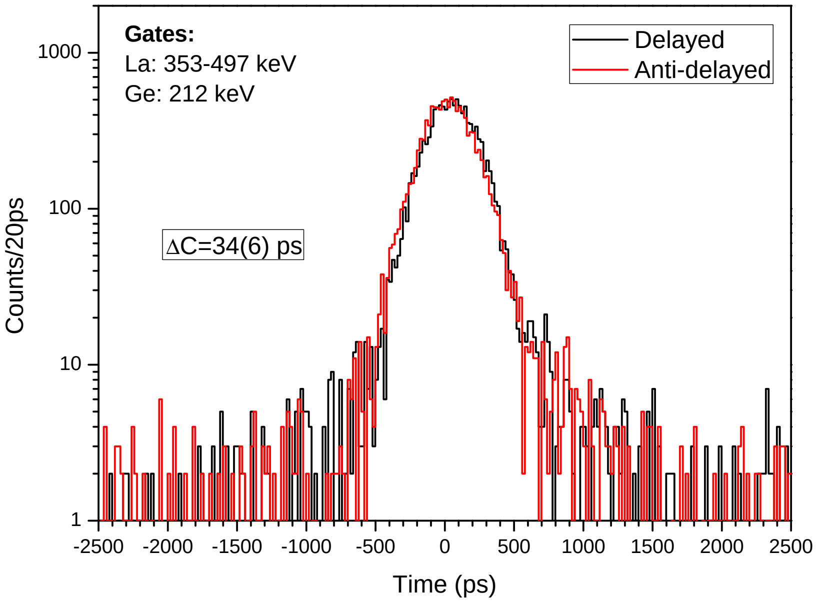

**Figure 5.33: Delayed and anti-delayed time distributions to measure the lifetime of the $4^+$ state in $^{100}$Zr.** - Delayed (red) and anti-delayed (black) time distributions for the lifetime measurement of the first $4^+$ state in $^{100}$Zr. The time spectra were Ge-gated by the 212-keV $\gamma$-ray and the LaBr$_3$(Ce)-gates in the 352- and 497-keV transitions. The delayed time spectrum is obtained when the 497-keV $\gamma$-ray acts as Start in the TAC and the 352-keV transition as the Stop. The anti-delayed distribution is measured when the Start and the Stop are reversed in the TAC. The target used is $^{241}$Pu with event multiplicity three ($\gamma\gamma\gamma$).

contribution to the total time peak is dominated by the FEP events, it still influence the centroid position. Hence, before deriving the lifetime using the general equation of the GCD method (Equation 2.6)), the experimental centroid difference $\Delta C_{exp}$=34(6) ps should be corrected by the Compton effect. The Compton correction procedures to first and to second order are explained in detail in Section 5.8 above.

The obtained values are summarized below:

**- Compton corrections at first order**

$$\tau = 37(7)\ ps$$

**- Compton corrections implemented in this work**

$$\tau = 31(8)\ ps$$

We report a lifetime of $\tau_{4^+}$=31(8) ps for the $4_1^+$ state, which is in agreement with the value of $\tau_{4^+}$=37(4) ps reported by S. Ansari et al. in [ARJ$^+$17] and at variance with $\tau_{4^+}$=54(4) ps published by A. G. Smith and coworkers in [SWP$^+$02]. For the present case, the correction to first order and to second order yield compatible values but not identical as it happens in other examples ($\tau_{4^+}$ lifetime in $^{136}$Te, for that see Chapter 6), this is a consequence of the Compton contribution under the FEPs. Despite the (P/B) ratios are much greater than one (P/B=6.0(3) for 352-keV transition and P/B=2.8(2) for 497-keV $\gamma$-ray), the effect of the Compton contribution is visible in the small difference of the two correcting procedures.

In addition to reduce Compton effect, the use of Ge-background subtraction approach in this case prevents from the contribution of long-lived contaminants that make the analysis impossible when using the $^{241}$Pu target as reported in [ARJ$^+$17]. When using the correction to first order, we obtain a lifetime of $\tau_{4^+}$=37(7) ps, which is identical to the value that S. Ansari *et al.* measured using the $^{235}$U target. We believe that the main problem regarding the $^{241}$Pu target was the background underneath the 212-keV transition. One should note that the total uncertainties provided here are about double than that provided by S. Ansari and coworkers. The reason for this is a combined effect of a reduction of statistics in the total time spectra as well as a consequence of the subtraction of the events in coincidences of the Ge-gated peaks and a re-examination of the total error in the distributed PRD (Prompt Response Distribution). The total uncertainty regarding the two correcting procedures when using the Ge-background subtraction approach is slightly larger for the correction at second order because of the extra terms that are included in order to totally account for the Compton effect.

We conclude that the Compton correction procedure developed in this PhD Thesis has been tested and validated.

## 5.9 Summary and conclusions of this chapter

This chapter explains in detail the procedure followed for the preparation and analysis of the data recorded in the EXILL-FATIMA experiment in neutron induced fission [JBdF+, RSB+14]. It also provides detailed information about the analysis software, SOCOv2, and the input files that it requires.

We have investigated in depth the most important analysis conditions, namely the target selection, the strategies for background reduction and the event multiplicity, and we have found the best suited ones for the analysis of $^{136}$Te.

The target selection is made in base of the fission yields, optimizing the $^{136}$Te production and preventing to some extent the presence of contaminants and fission partners. A comprehensive gating procedure is also explained in this chapter. Although both $^{235}$U and $^{241}$Pu targets abundantly produce $^{136}$Te in fission, most of the lifetimes derived in this thesis were measured using the $^{241}$Pu target because of the long-lived Zr isotopes that come as partners in the fission of $^{235}$U and hamper the analysis.

Regarding the event multiplicity, it is found that the use of triple $\gamma\gamma\gamma$(t) events once the right background reduction procedures are applied, is normally more favourable than the use of quadruple $\gamma\gamma\gamma\gamma$(t) events.

It was found that the approach of subtracting the events that are in coincidences with the background of the Ge-gated peak is the best performing strategy among all procedures to reduce the effect of the background on the time distributions. This approach improves the P/B ratio for all the cases a factor form 6 to 18.

In this chapter, we have also examined in detail the effect of full-energy and Compton events on the time distribution and we have developed a new method to correct the effect of Compton events under FEP on the time shifts taking care of the different contributions. We have cross-checked the Prompt Response Distribution (PRD), and constructed the Compton and Compton-Compton Response Distributions (CRD and CCRD).

At the end of the chapter a validation of the correction procedure developed in this thesis is provided, by making use of the $^{100}$Zr nucleus, which comes as a contaminant. The measured and Compton corrected lifetime value for the $4^+$ state in $^{100}$Zr is in good agreement with previous values [ARJ+17]. Therefore, the method will be used in the analysis of the $^{136}$Te nucleus (See Chapter 6).

# 6

# Lifetime measurements in $^{136}$Te

Nuclei with few valence particles outside of a doubly magic core provide valuable information about single-particle energies, nucleon-nucleon effective interactions and give an insight into the onset of collectivity. Nuclei in the vicinity of $^{132}$Sn isotope are of special interest because they exhibit unexpected modifications of the shell structure and sudden collective phenomena. This Chapter summarizes the investigation of the structure of $^{136}$Te, with a couple of protons and a couple of neutrons above the doubly magic $^{132}$Sn (Z=50 and N=82). The $^{136}$Te nucleus provides an excellent testing ground to probe the onset of collectivity and the nucleon-nucleon interaction in the region north-west of $^{132}$Sn.

Lifetime measurements of excited states provide direct access to the electromagnetic transition probabilities, which are key quantities in nuclear physics. Transition rates provide unique knowledge about nuclear structure and information about important aspects such as the ground state deformation, collective behaviour or shape coexistence.

Among the different experimental techniques to measure lifetime values, Fast-timing methods such as the Advanced Time Delayed (ATD) technique [MGM89, MWM$^{+}$91] or the Generalized Centroid Shift (GCD) method [RMS$^{+}$13], are the best suited experimental techniques to measure lifetimes from ten of picoseconds to few of nanoseconds, which is the time range where the relevant lifetimes values of the excited states in $^{136}$Te lie.

In this chapter, we investigate the exotic $^{136}$Te nucleus through the lifetime measurements of its excited levels focusing on the lifetime values of the rotational yrast band from the $2^{+}$ to the $8^{+}$ states. The lifetime values presented in this work were derived from the data taken during the EXILL-FATIMA campaign, using the GCD method [RMS+13] and the correction procedure developed and tested in Chapter 5. It is worth to mention that lifetime values of the $6^+$ and $8^+$ states from this work are measured for the first time. Prior to the experimental results, we provide a detailed summary of the available information on the $^{136}$Te collectivity and we present the puzzling situation of the unexpected low value of the B(E2) strength of the first $2^+$ state and the mismatch between different experimental values. The chapter also provides a compilation of the different theoretical calculations that are available nowadays in the literature together with the recent shell-model calculations performed by A. Gargano *et. al.* for comparison to the experimental results from this thesis.

## 6.1 Previous information on $^{136}$Te

The collectivity of the $^{136}$Te nucleus, with two protons and two neutrons coupled to the doubly-magic $^{132}$Sn core, was firstly investigated by means of Coulomb excitations measurements of radioactive ion beams in inverse kinematics by D. Radford and collaborators [RBB+02]. In their work, they presented the experimental measurement of the transition rates for $^{132,134,136}$Te where an unexpectedly low B(E2; $0^+ \rightarrow 2^+$) strength of 0.103(15) $e^2b^2$ was measured for $^{136}$Te, while the results for $^{132,134}$Te were in good agreement with the systematics of the lighter Te isotopes. The low value for $^{136}$Te was at variance with the transition rates of Xe and Ba isotopes and was not well reproduced by shell model calculations using realistic effective interactions.

The B(E2) strength values of Te isotopes were lately modified due to a re-examination of the experiment where the target thickness was corrected, yielding new values of B(E2; $0^+ \rightarrow 2^+$) for $^{132,134,136}$Te of 0.216(22), 0.114(13) and 0.122(18) $e^2b^2$ respectively [DRP+11]. Although the new B(E2) implies a modification of the lifetime values of the first $2^+$ states of Te isotopes, the main conclusion of a lower B(E2) value for $^{136}$Te is not affected by these corrections. Using the energies of the first $2^+$ states in the $^{132,134,136}$Te isotopes, the new values of the lifetimes correspond to 2.2(2), 1.05(12) and 41(6) ps, respectively. The low B(E2; $0^+ \rightarrow 2^+$) value in $^{136}$Te was partially justified in [DRP+11] by a decrease of the pairing force, however, this explanation is not completely satisfactory, because the smaller B(E2) transition rate in $^{136}$Te than in $^{132}$Te points to a crucial difference in the wave functions of the $2_1^+$ states in these two Te isotopes, only differing in 4 neutrons, and therefore neutron components should play a role in this difference.

An ensuing publication addressed again the unexplained low transition probability using the same technique, Coulomb excitation of a $^{136}$Te on a titanium target [ASB$^+$17]. In this case, several electromagnetic moments of the three lowest-lying states were measured, thus extending the knowledge to the $4_1^+$ state and also to the second $2_2^+$ state, which was earlier predicted as a mixed symmetry state by several theoretical calculations [SOMH04, TENS02].

The value for the B(E2; $0^+ \rightarrow 2^+$) transition drastically changed by 50% to 0.181(15) $e^2b^2$, 2 sigma away from the previous value of 0.122(18) $e^2b^2$ [DRP$^+$11], and even further than the original value of 0.103(15) $e^2b^2$ from [RBB$^+$02]. The derived lifetime from this recent value is $\tau_{2^+} = 27.5(23)$ ps. Additionally the B(E2; $4_1^+ \rightarrow 2_1^+$) was measured to be 0.060(9) $e^2b^2$, which corresponds to a long $\tau_{4^+} = 100(15)$ ps.

The lifetime of the $2_1^+$ state in $^{136}$Te has been measured also in $\beta$-decay experiments, using the Advanced Time Delayed $\beta$-$\gamma$-$\gamma$(t) method [F$^+$08]. This independent method yields a B(E2; $2^+ \rightarrow 0^+$) value of 245(50) $e^2fm^4$, corresponding to a B(E2; $0^+ \rightarrow 2^+$) of 0.125(25) $e^2b^2$, therefore in agreement with [DRP$^+$11], but not with the most recent CoulEx measurement [ASB$^+$17].

Table 6.1 summarizes the different experimental B(E2) strength values for the first $2^+$ state in $^{136}$Te. The related lifetime values are also given, and the corresponding experimental technique. The values of the upward transition rates are expressed in $e^2b^2$ and the units of the downward transition rates in $e^2fm^4$.

| **B(E2; $0^+ \rightarrow 2^+$) ($e^2b^2$)** | **B(E2; $2^+ \rightarrow 0^+$) ($e^2fm^4$)** | **Lifetime (ps)** | **Technique** | **Reference** |
|---|---|---|---|---|
| 0.103(15) | 208(29) | 48(5) | CoulEX | [RBB$^+$02] |
| 0.122(18) | 244(36) | 41(6) | CoulEX | [DRP$^+$11] |
| 0.181(15) | 362(30) | 27.5(23) | CoulEX | [ASB$^+$17] |
| 0.123(25) | 245(50) | 43(9) | $\beta$-Decay+ATD | [F$^+$08] |

**Table 6.1: Experimental B(E2) strength values for the first $2^+$ state in $^{136}$Te** - Summary table of the different experimental B(E2) strength values for the first $2^+$ state in $^{136}$Te. The table also provides the corresponding lifetime values.

Figure 6.1 shows the B(E2) systematics of exotic nuclei in the $^{132}$Sn region and summarizes the different experimental B(E2) values measured for $^{136}$Te. The black diamond in $^{136}$Te represents the B(E2) strength of 0.103(15) $e^2b^2$ measured by C. Radford and collaborators [RBB$^+$02], while the red diamond in $^{136}$Te corresponds to 0.122(18) $e^2b^2$, which is the value derived after the target thickness corrections [DRP$^+$11]. The diamond in blue is the B(E2) strength of 0.181(15) $e^2b^2$ obtained by J.M. Allmond and coworkers [ASB$^+$17]. The green squares in the Xe isotopes correspond to experimental values measured in CoulEx studies at REX-ISOLDE [KBK$^+$07]. In Figure 6.1 it is clear the discrepancy of the different experimental values for $^{136}$Te. The B(E2) strength derived from lifetime measurements in $\beta$-decay studies [F$^+$08] is not included in the plot, but the value of 0.123(25) $e^2b^2$ would overlap with the number obtained by M. Danchev and collaborators [DRP$^+$11].

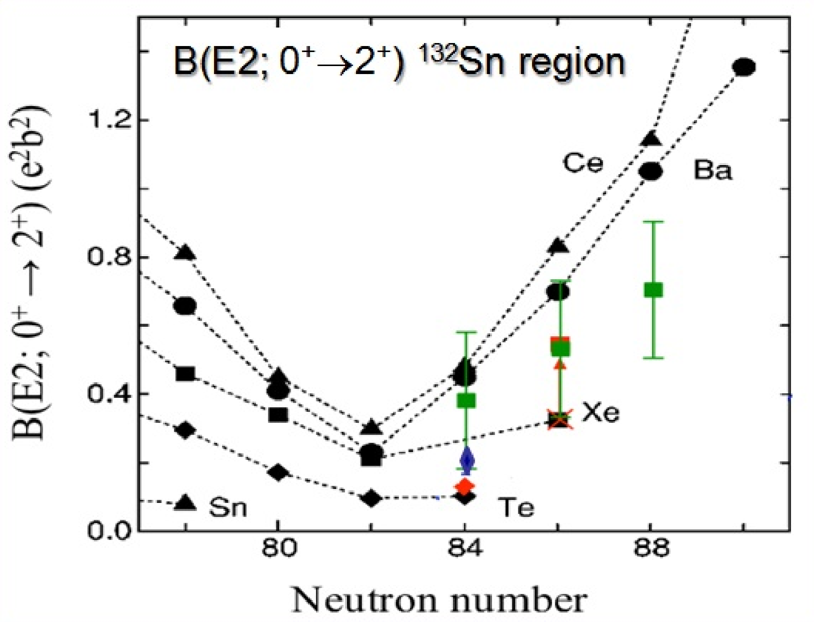

**Figure 6.1: B(E2; 0$^+$ →2$^+$) systematics in the $^{132}$Sn region** - B(E2;0$^+$ →2$^+$) systematics of the exotic nuclei in the vicinity of the doubly magic $^{132}$Sn. The black diamonds in $^{136}$Te represents the B(E2) strength of 0.103(15) $e^2b^2$ measured by C. Radford and collaborators [RBB$^+$02], while the red diamond in $^{136}$Te corresponds to 0.122(18) $e^2b^2$, that is the value derived after the target thickness corrections [DRP$^+$11]. The diamond in blue is the B(E2) strength of 0.181(15) $e^2b^2$ obtained by J.M. Allmond and coworkers [ASB$^+$17]. The green squares in the Xe isotopes are the experimental values measured in CoulEx studies from [KBK$^+$07]. This plot has been taken from [F$^+$08].

In conclusion, the existing experimental values of the B(E2; $0^+ \rightarrow 2^+$) reduced transition probability in $^{136}$Te available nowadays in the literature differ by almost a factor of two. This experimental inconsistency indicates the need for a new direct B(E2; $0^+ \rightarrow 2^+$) measurements. Regarding the B(E2; $4_1^+ \rightarrow 2_1^+$) rate, there is a single existing measurement that yields a pretty long lifetime for the $4_1^+$ state of 100 ps, and no measurement exists for the lifetimes of the higher-lying states in $^{136}$Te. The population in fission of $^{136}$Te and the lifetime measurements with the mixed EXILL-FATIMA array provides a unique opportunity to access these lifetimes.

## 6.2 Lifetime measurements of excited states in $^{136}$Te

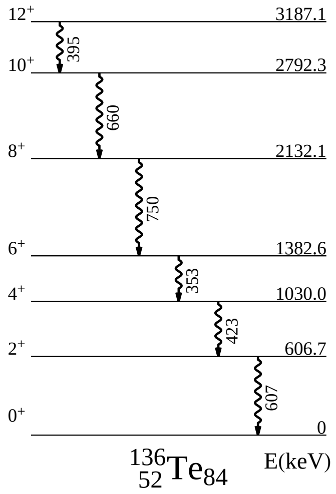

**Figure 6.2: Partial $^{136}$Te level scheme that show the g.s. yrast rotational band.**

Taking advantage of the good production rates achieved during the EXILL-FATIMA experiment and of the good performance of the hybrid spectrometer, it is possible to access the $2^+$ and $4^+$ lifetimes in $^{136}$Te and to extend the measured values higher in the band to the $6^+$ and $8^+$ states. Figure 6.2 provides a partial level scheme of $^{136}$Te, where the ground state yrast rotational band and the $\gamma$-rays involved in the lifetime measurements are shown.

### 6.2.1 Partners and contaminants

As mentioned before in Chapter 5, the most likely fission partners of $^{136}$Te when using the $^{241}$Pu target are: $^{103}$Mo, $^{104}$Mo and $^{105}$Mo isotopes. The $^{105}$Mo is less likely to be present when considering the mean number of neutrons evaporated in the reaction. However, its fission yield of 4.13 % is greater than any of the other two partners, $^{103}$Mo and $^{104}$Mo, and it is more than a factor of two larger than the production of $^{136}$Te. Hence, this nuclei should also be taken into account. Table 6.2 summarizes the fission yield of the $^{136}$Te partners and compares them with that of $^{136}$Te. The table also provides the fission yield of $^{100}$Zr, which comes as a contaminant because of its 352-keV $\gamma$-transition.

| **$^{241}$Pu** | **Te** | **Most likely** | | | **Less likely** | | **Contaminant** |
|---|---|---|---|---|---|---|---|
| **Isotope** | $^{136}$Te | $^{105}$Mo | $^{104}$Mo | $^{103}$Mo | $^{102}$Mo | $^{101}$Mo | $^{100}$Zr |
| **Yield (%)** | 1.68 | 4.13 | 3.61 | 1.72 | 0.54 | 0.11 | 4.29 |

| **$^{235}$U** | **Te** | **Most likely** | | **Less likely** | | **Contaminant** |
|---|---|---|---|---|---|---|
| **Isotope** | $^{136}$Te | $^{97}$Zr | $^{98}$Zr | $^{99}$Zr | $^{95}$Zr | $^{100}$Zr |
| **Yield (%)** | 1.32 | 1.09 | 2.57 | 3.58 | 0.13 | 4.98 |

**Table 6.2: Thermal neutron fission yields of the $^{241}$Pu and $^{235}$U targets for the $^{136}$Te nucleus and Te partners.** - Production rates of the $^{241}$Pu and $^{235}$U targets for $^{136}$Te and its partners. The table also includes the fission yield of $^{100}$Zr that appears in coincidences with $^{136}$Te as a consequence of the 352-keV $\gamma$-transition in $^{100}$Zr, which is of the same energy than the 353-keV $\gamma$-ray in $^{136}$Te. Values were taken from [LAdB$^{+}$10]

The best strategy to find out what appears in coincidence with $^{136}$Te $\gamma$-rays is to investigate the contents of the coincident HPGe-clover spectra after gating in two known $\gamma$-rays in $^{136}$Te. Figure 6.3 shows the Ge coincident spectrum when selecting energy conditions on the 423 and the 353-keV transitions. The transitions marked in bold belong to $^{136}$Te, while the other FEPs corresponds to fission partners and contaminants. In the plot, the $\gamma$-rays from the $^{103}$Mo and $^{104}$Mo partners can be identified [NND]. Although both molybdenum isotopes have long-lived states of the order of hundreds of picoseconds, the energies of the populating and de-exciting transitions are not close to those under study in the $^{136}$Te, therefore not posing big problems for the analysis. In fact, the presence of the molybdenum isotopes provides an excellent way to cross-check the internal timing calibrations, since there are lifetimes of excited states measured with good precision in both $^{103}$Mo and $^{104}$Mo.

Figure 6.4 presents the coincident HPGe spectrum Ge-gated by the 193- and 607-keV $\gamma$-rays. The 193-keV $\gamma$-transition is one of the most intense $\gamma$-rays in both $^{103}$Mo and $^{104}$Mo isotopes, while the 607-keV transition feeds the ground state of $^{136}$Te.

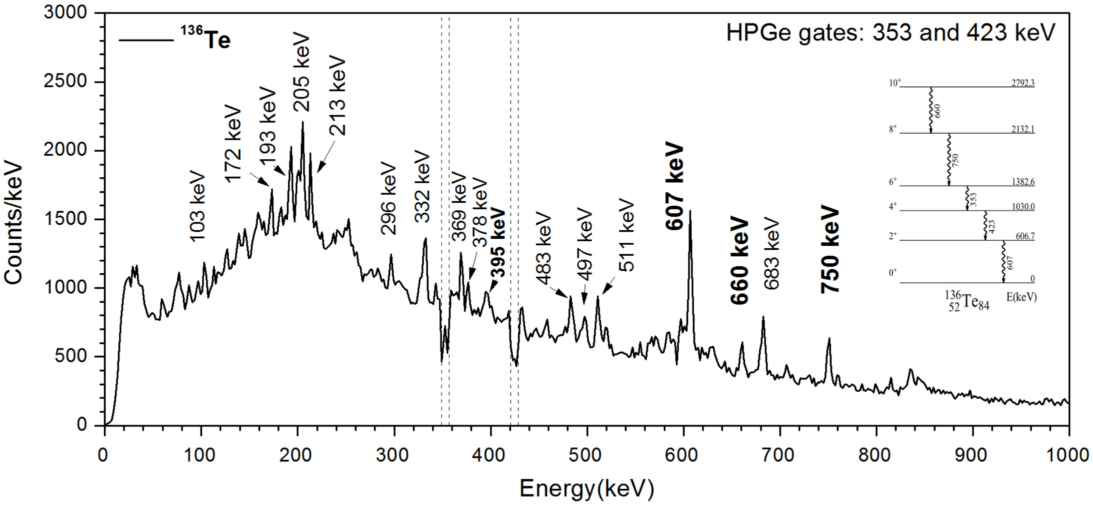

**Figure 6.3: Coincident HPGe spectrum HPGe-gated by the 423- and 352-keV $\gamma$-transitions.** - Coincident HPGe spectrum Ge-gated by the 423- and 352-keV $\gamma$-rays ($\gamma\gamma\gamma$). The width of the gates is indicated with dashed lines and the most prominent peaks are labelled. The $^{136}$Te $\gamma$-rays are marked in bold font, and a scheme of the band is included on the right hand side for a better understanding.

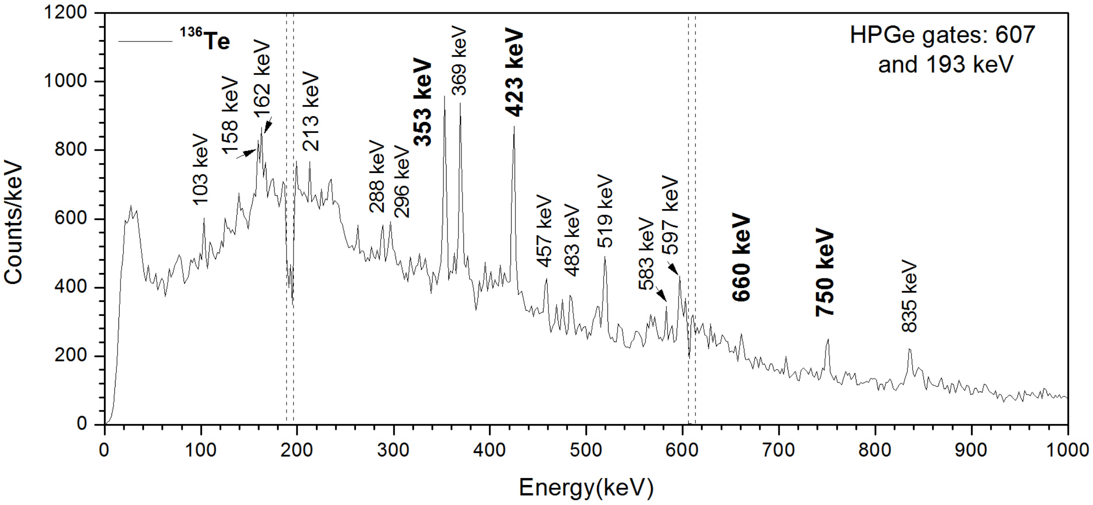

**Figure 6.4: Coincident HPGe spectrum Ge-gated by the 750- and 353-keV transitions.** - Coincident energy spectrum Ge-gated by the 750- and 353-keV $\gamma$-transitions ($\gamma\gamma\gamma$). The width of the gates is indicated with dashed lines and the most prominent peaks are labelled. The $\gamma$-rays from the $^{136}$Te are marked in bold font, and a scheme is provided on the right hand side. The dataset corresponds to the $^{241}$Pu target.

Besides the $^{103}$Mo and $^{104}$Mo partners, certain $\gamma$-rays from the $^{100}$Zr appear in coincidence with $^{136}$Te. This is a consequence of the 352-keV transition in $^{100}$Zr, whose energy overlaps with the 353-keV ray in $^{136}$Te. Special caution should be taken as there are several long-lived states in the nanosecond range in $^{100}$Zr and its fission yield of 4.29% is higher than the $^{136}$Te production of 1.68% ($^{241}$Pu target). The 231- and the 497-keV transitions of $^{100}$Zr, which are in coincidence with the 352-keV $\gamma$-ray, can be seen in Figure 6.3.

### 6.2.2 Lifetime values in $^{136}$Te measured in triple coincidences

In triple coincidences, the time information is derived from the centroid positions of the TAC spectra after being triple gated (HPGe-LaBr$_3$(Ce)-LaBr$_3$(Ce)). The $\gamma$-rays that populate and de-excite the level of interest are selected in the LaBr$_3$(Ce) detectors, while an extra $\gamma$-ray from the cascade is chosen at the HPGe detectors to clean the coincidence events. The amount of true coincident events in the time distributions after imposing three energy conditions is still larger than $3 \times 10^3$ counts. Despite the high-resolution energy condition set in the Ge detectors, the level of background that appears in coincidence in triple events is still high, attaining a similar order of magnitude than the full-energy events and consequently, yielding peak-to-background ratios that reach the value of one for most of the cases. Hence, a Compton correction is necessary.

#### 6.2.2.1 Lifetime of the first excited $2^+$ state

The lifetime of the $2^+$ state in $^{136}$Te is derived by the time difference between the 423-keV $\gamma$-transition that populates the level and the 607-keV $\gamma$-ray that de-excites it. Both $\gamma$-transitions are selected in the LaBr$_3$(Ce) detectors to construct the fast-timing matrix and the subsequent delayed (423-607 keV) and anti-delayed (607-423 keV) time distributions, where the lifetime is derived from the time differences of their centroid positions.

In this case, the HPGe-gate can be either set in the 353-keV or 750-keV $\gamma$-rays providing sufficient statistics at the coincident time spectrum. The option of setting the HPGe-gate in the 660 keV $\gamma$-ray is discarded due to the lack of statistics to resolve the coincident FEPs at the LaBr$_3$(Ce). Due to the possibility of setting two different HPGe-gates, the lifetime of the $2^+$ state can be firstly derived for every combination of gates, which are HPGe(353 keV)-LaBr$_3$(Ce)(423 keV)-LaBr$_3$(Ce)(607 keV) and HPGe(750 keV)-LaBr$_3$(Ce)(423 keV)-LaBr$_3$(Ce)(607 keV) and secondly the two values can be compared. One should note that the amount of available statistics is higher for the data set Ge-gated by the 353-keV $\gamma$-ray. In the following subsections, the $^{241}$Pu target has been used to derive the lifetime of the $2^+$ state.

**- Lifetime of the $2^+$ state: high-resolution energy gate set in the 353 keV**

Special care must be taken when using the set of gates that contains the 353-keV $\gamma$-transition since there is a very intense 352-keV $\gamma$-ray in the $^{100}$Zr isotope, which is also selected within this gate. It causes that certain $\gamma$-rays from the $^{100}$Zr that deexcite long-lived states may appear in coincidence and may contribute to the total time distribution. To avoid the contribution of the $^{100}$Zr isotope, the coincident spectra of the HPGe-clovers and LaBr$_3$(Ce) were carefully examined. The idea is to use the high-resolution capability of the HPGe detectors to investigate the presence of unresolved FEPs that may be inside the selected LaBr$_3$(Ce)-gate. Therefore, the set of gates for checking the spectra was the same as the one used for sorting the Ft-matrix. In this way, it is possible to find out the contributions to the total time spectrum.

Figures 6.5 shows the coincident spectra of the Clovers and the LaBr$_3$(Ce) detectors Ge-gated by the 353-keV transition and LaBr$_3$(Ce)-gated by the 607-keV $\gamma$-ray. The aim of this plot is to check the presence of potential contaminants in the 423-keV gate. Figure 6.5 shows that there is no unresolved FEP, and the only problem hindering the analysis is the Compton continuum underneath the 423-keV FEP.

To complete the investigation, the 607-keV transition should be examined as well. To this aim, the Ge-gate is kept in the 353-keV transition, while the LaBr$_3$(Ce)-gate is set at the 423-keV $\gamma$-ray. Figure 6.6 shows the coincident HPGe-clover and LaBr$_3$(Ce) spectra Ge-gated by 353 keV and LaBr$_3$(Ce)-gated by 423 keV. It is visible that next to the 607-keV transition, there are three FEPs whose energies are 573, 590 and 596 keV. The FEPs of 573 and 590 keV do not represent a problem since they can be totally excluded by setting a narrow gate, however, the 596 keV transition could still be contained in the energy window. Therefore, to avoid the potential contribution of the 596-keV FEP, a very narrow energy gate of 15 keV has been selected. The selected width for the 423-keV $\gamma$-ray is 32 keV. Besides the three FEPs that appear next to $\gamma$-decay, the high level of background underneath the 423-keV FEP should be considered as an important source of errors.

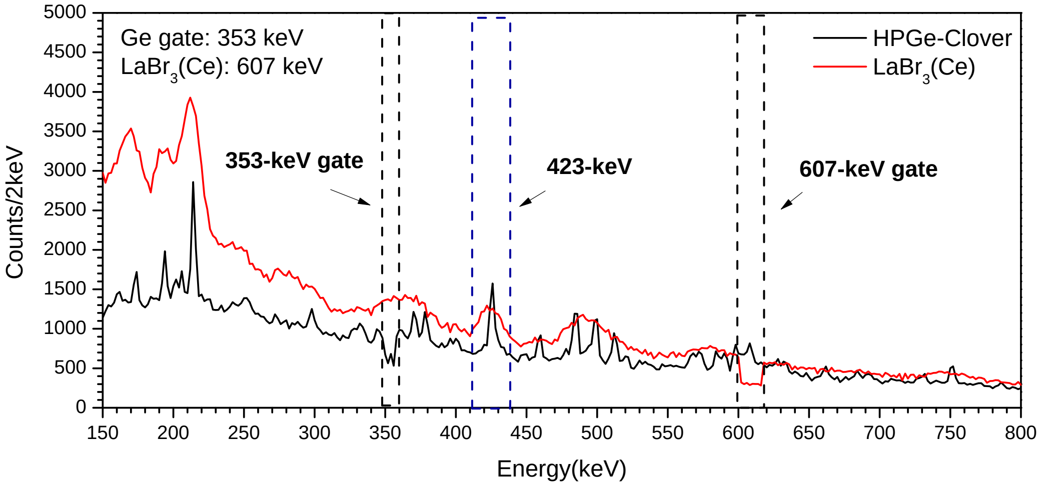

**Figure 6.5: Coincident HPGe-Clover and LaBr$_3$(Ce) spectra gated by the 353- and 607-keV transition.** - Energy spectra of HPGe-Clover detectors (black) and LaBr$_3$(Ce) crystals (red), in coincidence with the 353 keV $\gamma$-ray in the Ge detectors and the 607 keV in the LaBr$_3$(Ce) detectors. The width of the gates is indicated with black dashed lines, and the size of the second selected gate in the LaBr$_3$(Ce) is plotted in blue. The target used is $^{241}$Pu.

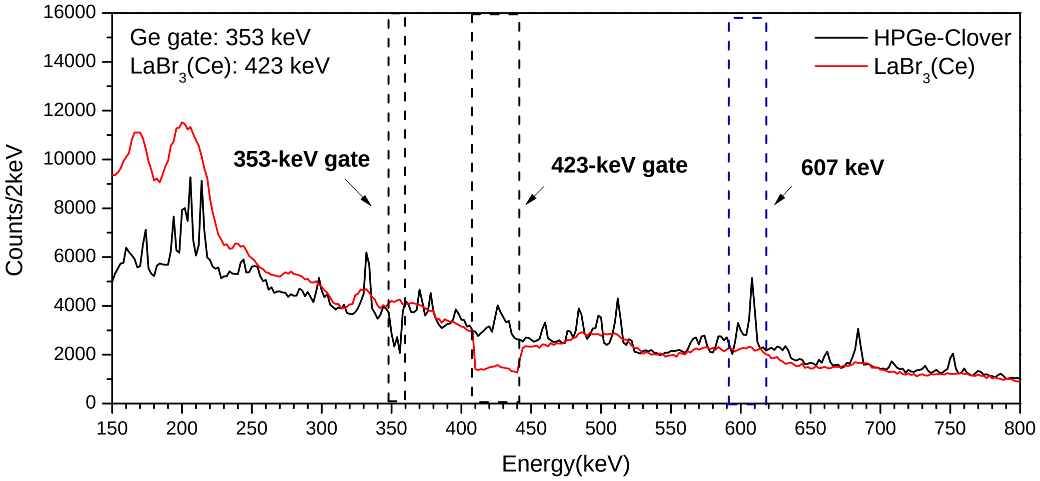

**Figure 6.6: Coincident HPGe-Clover and LaBr$_3$(Ce) spectra gated by the 353- and 423-keV transition.** - Energy spectra of HPGe-Clover detectors (black) and LaBr$_3$(Ce) crystals (red), in coincidence with the 353 keV $\gamma$-ray in the Ge detectors and the 423 keV in the LaBr$_3$(Ce) detectors. The width of the selected gates is indicated in the plot with black dashed lines, while the size of the second selected gate in the LaBr$_3$(Ce) is plotted in blue. The used target is $^{241}$Pu.

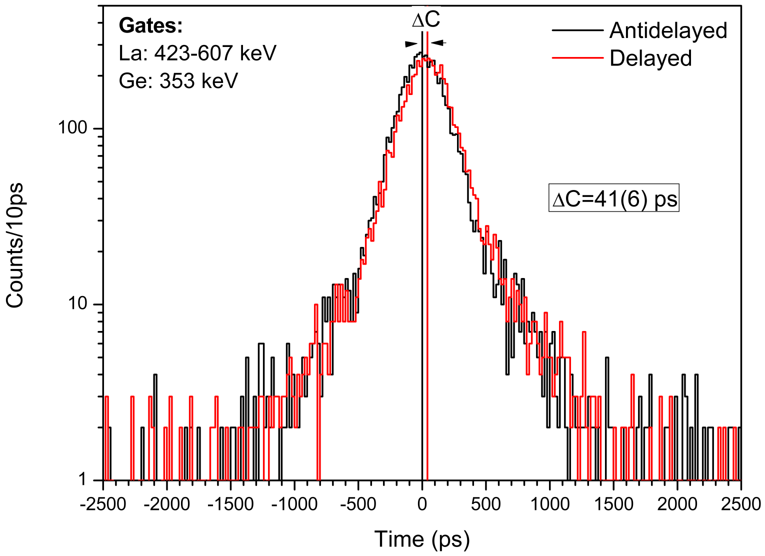

**Figure 6.7: Delayed and anti-delayed time distributions to derive the lifetime of the $2_1^+$ state in $^{136}$Te.** - Delayed (red) and anti-delayed (black) time distributions for the lifetime measurement of the first $2^+$ state in $^{136}$Te. The HPGe-gate was set in the 353-keV $\gamma$-ray and the LaBr$_3$(Ce)-gates in the 423- and 607-keV transitions. The delayed time spectrum is obtained when the 423-keV $\gamma$-ray acts as the Start in the TAC and the 607-keV transition as the Stop. The anti-delayed distribution is measured when the Start and the Stop are reversed in the TAC. The add-back reconstruction option was used in this case to sort the Ft-matrix, and the used target is $^{241}$Pu with event multiplicity three ($\gamma\gamma\gamma$).

As a consequence of the 596-keV peak that appears next to the 607-keV FEP and may contribute to the total time distribution, the lifetime derived for this combination of gates should be compared with a different combination of gates or with the values measured using quadruple events. One should also consider that when using narrow energy gates of 3-keV width in the HPGe-clovers detectors, the coincident Ge spectra do not show any significant 596-keV FEP contribution.

The next step after having set the optimal width of the LaBr$_3$(Ce)-gates is to calculate the experimental centroid differences between the delayed (423-607 keV) and the anti-delayed (607-423 keV) time distributions. The delayed time spectrum is obtained when the 423-keV $\gamma$-ray acts as the Start of the TAC and the 607-keV as the Stop. The anti-delayed distribution is measured for the reversed combination, 423 keV as the Stop and 607 keV as the Start.

When using the add-back reconstruction for building the Ft-matrix, the measured

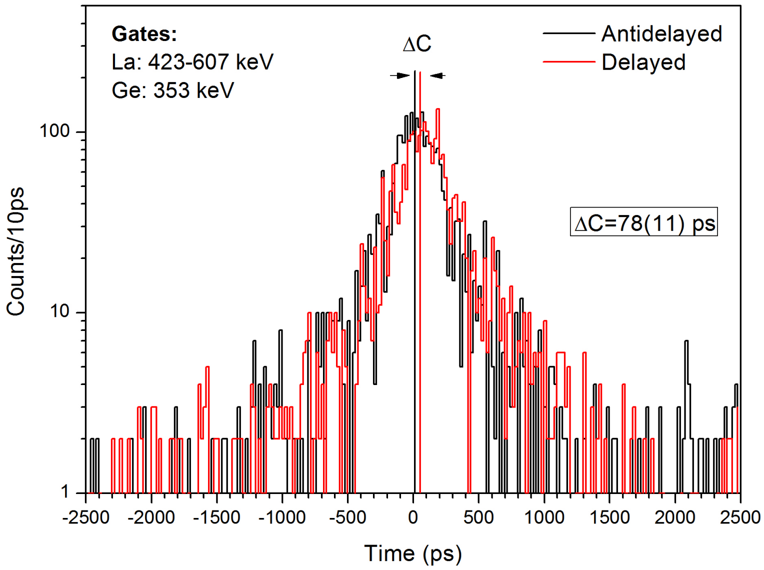

**Figure 6.8: Delayed and anti-delayed time distributions to derive the lifetime of the $2_1^+$ state in $^{136}$Te** - Delayed (red) and anti-delayed (black) time distributions for the lifetime measurement of the first $2^+$ state in $^{136}$Te. The high-resolution energy gate was set in the 353-keV $\gamma$-ray. The LaBr$_3$(Ce) gates were selected at 423 keV for start and 607 keV for stop for the delayed distribution, and reversed for the anti-delayed time spectrum. The events in coincidence with the background of the Ge-gated peaks were subtracted. The used target is $^{241}$Pu with multiplicity three ($\gamma\gamma\gamma$).

centroid shift is $\Delta C_{exp}$=41(6) ps. Figure 6.7 shows the delayed (red) and the anti-delayed (black) time distributions Ge-gated by the 353 keV $\gamma$-ray and including the add-back reconstruction. The plot also depicts the centroid difference of $\Delta C_{exp}$=41(6) ps and the gate combination. In this case (Ft-matrix using the add-back reconstruction), the peak-to-background ratio P/B of the 607-keV $\gamma$-transition is P/B=0.65 and P/B=0.60 for the 423-keV $\gamma$-ray. These ratios indicate that the amount of Compton-events of the total peak is much higher than the true FEP-events in both $\gamma_{feeder}$ and $\gamma_{decay}$. As a consequence, the Compton contribution to the total time distribution dominates over the FEP-FEP contribution. With these P/B ratios, despite the existence of Compton corrections, it is preferable not to derive the lifetime from this data set. The associated uncertainty would be very higher and the accuracy of the value low.

Nevertheless, if the events that are in coincidence with the background under the Ge-gated peaks are subtracted (Section 5.5.2.3) the P/B in both $\gamma_{feeder}$ and $\gamma_{decay}$ improves from P/B=0.65 to P/B=3.9 in the 607-keV $\gamma$-ray and from P/B=0.60 to

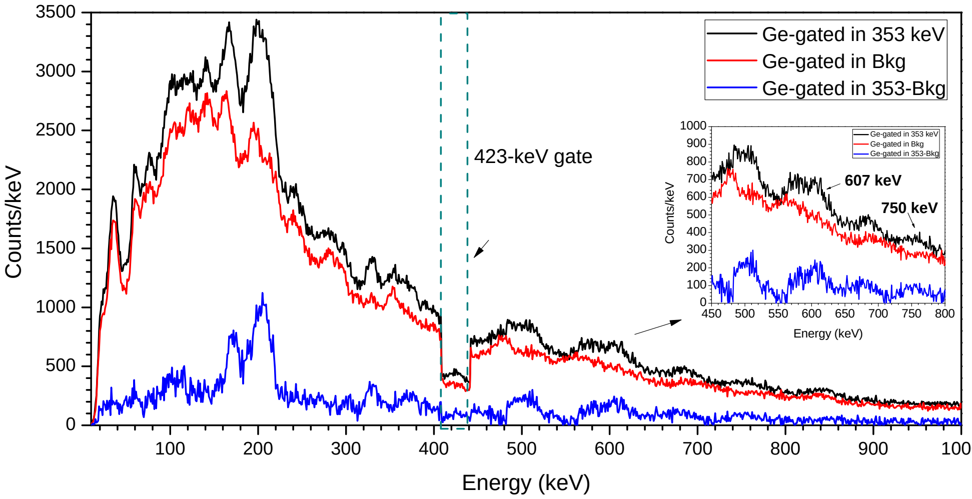

**Figure 6.9: Coincident LaBr$_3$(Ce) spectra to derive the lifetime of the $2_1^+$ state in $^{136}$Te.** - Coincident LaBr$_3$(Ce) spectra that show the effect of subtracting the events that are in coincidence with the background of the Ge-gated peaks in the Clovers. The three spectra are LaBr$_3$(Ce)-gated by the 423-keV transition, which is marked with dashed green lines. The black plot corresponds to the coincident LaBr$_3$(Ce) spectrum Ge-gated by the 353-keV $\gamma$-ray, while the one in red is Ge-gated on the right hand side background (C′) of the 353-keV peak. The blue plot is the difference between the black and the red one and illustrates the effect of subtracting the Ge background. The background level has been reduced considerably improving the P/B ratio. The inset provides a zoom into the region of the 607-keV FEP peak. The data set corresponds to the $^{241}$Pu target with multiplicity three ($\gamma\gamma\gamma$).

P/B=2.2 in the 423-keV $\gamma$-transition. Considering this major improvement in the P/B ratios the lifetime of the $2^+$ state is measured in the present analysis using the background subtraction of the Ge-gated peaks in the Clovers. Figure 6.8 presents the delayed (red) and the anti-delayed (black) time distributions obtained when the events that are in coincidence with the Ge-gated peaks are subtracted. The time spectra are Ge-gated by the 353-keV $\gamma$-ray and LaBr$_3$(Ce)-gated by the 423-keV and 607-keV $\gamma$-transitions. Figure 6.8 also provides the experimental centroid difference between the delayed and the anti-delayed distributions, which is $\Delta C_{exp}$=78(11) ps. The effect of subtracting the events that are in coincidence with the background of the Ge-gated peaks in the HPGe-Clovers becomes apparent. In addition to the large improvement of the P/B ratio, the experimental centroid difference $\Delta C_{exp}$ has incremented by almost 50% from $\Delta C_{exp}$=41(6) to $\Delta C_{exp}$=78(11) ps. Figure 6.9 shows the influence on the energy spectra of the matching LaBr$_3$(Ce) detector from the ft-matrices. The blue plot, which is the difference between the black (Ge-gated by the 353-keV $\gamma$-ray) and the red (Ge-gated by the 353-keV background C$'$) spectra, is basically composed by the $\gamma$-rays of $^{136}$Te, by its partners and by the $^{100}$Zr transitions that are in coincidence with 353-keV $\gamma$-ray (See Chapter 5.6). The level of background has significantly been reduced and the 607-keV peak is cleaner. In addition to checking the background of the Ge-gated peaks, this plot is also aimed at investigating the 353-423-coincident FEPs that may appear in the vicinity of 607-keV FEP.

After having calculated the experimental centroid difference $\Delta C_{exp}(\Delta E_\gamma)$, the next step for deriving the lifetime is to obtain the system response at the energy difference $\Delta E_\gamma = E_{feeder} - E_{decay}$, where $E_{feeder} = 423$ keV and $E_{decay} = 607$ keV. This is done by interpolating the corresponding energies in the PRD curve, which is shown in Figure 5.23. The interpolated value at $\Delta E_\gamma$ is PRD($E_{423}$-$E_{607}$)=42(10) ps. Figure 6.10 plots together the two interpolated values at 423 and 607 keV with the PRD points in the range of interest. The total uncertainty in the PRD curve is taken as 10 ps as explained in Section 5.7.1.1.

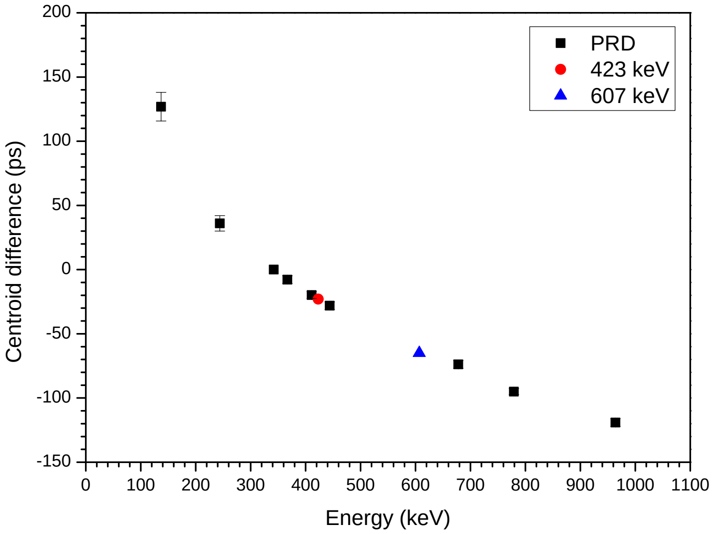

**Figure 6.10: Prompt Response Distribution PRD.** - Prompt response distribution of the EXILL-FATIMA experiment (black squares). The interpolated value at 423 keV is marked with a red circle and the system response at 607 keV with a blue triangle. From the difference between these two values one can obtain the quantity of PRD(423-607)=42(10) ps. Error bars are plotted for the data points.

Before deriving the lifetime using the general equation of the GCD method (Equation 2.6), the experimental centroid differences, $\Delta C_{exp}(\Delta E_\gamma)$ should be corrected by the contribution of the Compton continuum underneath the LaBr$_3$(Ce)-gated peaks. The corrections employed here are the Compton correction to first order (Section 5.8.1) and the corrections implemented in this thesis (Section 5.8.2). Both types of corrections rely on the use of the CRD curves. Figures 6.11 and 6.12 provide the measured CRD$_{feeder}$ and CRD$_{decay}$ respectively for the lifetime measurement of the $2^+$ state. In this case, the $CRD_{feeder}$ curve accounts for the time response of the Compton continuum underneath the 423-keV FEP, and the $CRD_{decay}$ distribution for the Compton events underneath the 607-keV peak. The procedure for deriving the CRD distributions was explained in Section 5.7.2. It is visible that the error bars from this distribution are larger than those from the PRD curve; this is caused by the amount of available statistics in the selected regions. The PRD was constructed using a $^{152}Eu$ source with a high amount of statistics, while the CRD curves were obtained directly from the $^{241}$Pu data set.

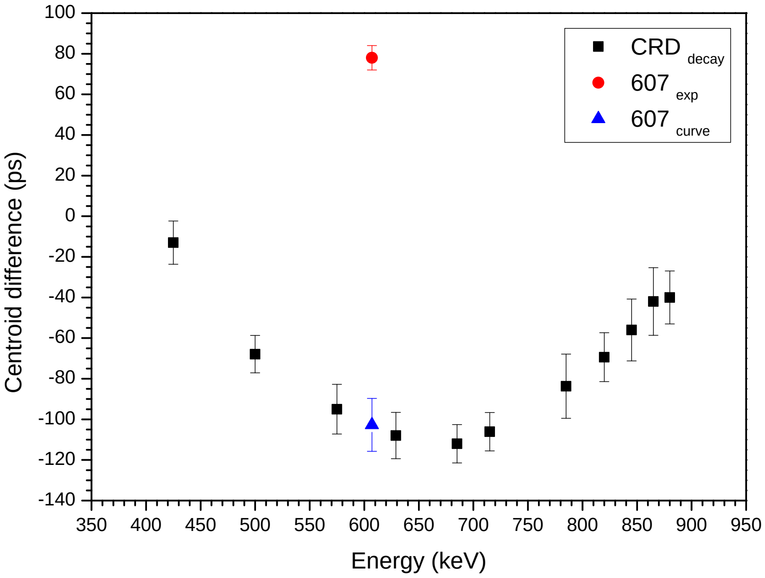

**Figure 6.11: Compton response distribution ($CRD_{decay}$).** - Compton response distribution $CRD_{decay}$ that provides the system response to Compton events underneath the 607-keV FEP. The reference has been set at the 423-keV FEP with a width of 32 keV. The plot provides the measured centroid difference $\Delta C_{exp}(\Delta E_\gamma)$=78(11) ps at $\Delta E$=423-607 keV by a red circle and the Compton response at 607 keV by a blue triangle, which is obtained by interpolating the data points from the curve.

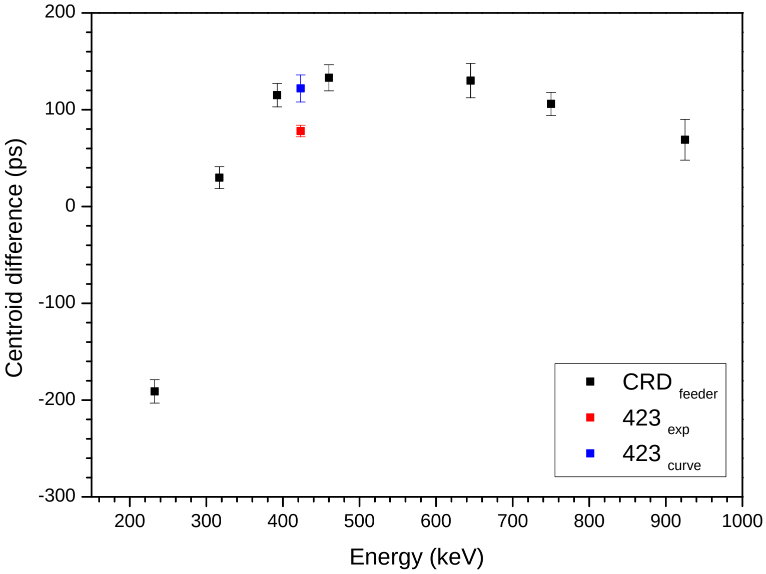

**Figure 6.12: Compton response distribution (CRD$_{feeder}$).** - Compton response distribution CRD$_{feeder}$ that provides the system response to Compton events underneath the 423-keV FEP. The reference has been set at the 607-keV FEP with a width of 15 keV. The plot also displays the experimental centroid difference $\Delta C_{exp}(\Delta E_{\gamma})$=78(11) ps at $\Delta E_{feeder-decay}$=423-607 keV by a red circle and the Compton response at 423 keV by a blue triangle, which is obtained by interpolating the curve.

### - Compton corrections to first order

The Compton correction to first order is taken as the mean average of the two corrections derived for the $\gamma$-feeder and $\gamma$-decay. This procedure is explained in detail in Section 5.8.1 and is summarized in Equations 6.1 and 6.2. Once the experimental centroid difference is corrected by the Compton contribution giving $\Delta C_{FEP}$, this quantity will be used to derive the lifetime by using the general equation of the GCD method, Equation 2.6.

$$\Delta C_{FEP} = \Delta C_{exp} + \frac{1}{2}[t_{cor.}(E_{feeder}) + t_{cor.}(E_{decay})] \tag{6.1}$$

$$t_{cor.}(E_{feeder}) = \frac{\Delta C_{exp} - \Delta C_{BG}^{feeder}}{P/B_{feeder}} \qquad t_{cor.}(E_{decay}) = \frac{\Delta C_{exp} - \Delta C_{BG}^{decay}}{P/B_{decay}} \tag{6.2}$$

In the present case the experimental centroid difference is $\Delta C_{exp}$=78(11) ps. The values of $\Delta C_{BG}$ for the $\gamma$-feeder and $\gamma$-decay are extracted from the $CRD_{feeder}$ and CRD$_{decay}$ curves that are shown in Figures 6.12 and 6.11. The interpolated values correspond to $\Delta C_{BG}^{feeder}$=122(9) ps and $\Delta C_{BG}^{decay}$=$-$103(10) ps. Considering the ratios of P/B$_{feeder}$ =2.2(2) and P/B$_{decay}$=3.9(4), the two corrections for the $\gamma$-feeder and $\gamma$-decay are $t_{cor}(E_{feeder})$=$-$20(6) ps and $t_{cor}(E_{decay})$=46(6) ps. The combined correction of $\gamma_{feeder}$ and $\gamma_{decay}$ is $t_{corr}$=13(6) ps, therefore using Equation 5.13, the corrected value is $\Delta C_{FEP}$=91(12) ps.

Using the general equation of the method (Equation 2.6) and the PRD value at ($\Delta E_{\gamma}$) of PRD(E$_{423}$-E$_{607}$)= 42(10) ps, together with the corrected centroid difference of $\Delta C_{FEP}$=91(12) ps, the value for the lifetime of the $2^+$ state using the correction to first order is:

$$\tau_{2^+} = 25(8)\ ps$$

**- Compton correction implemented in this work**

The Compton correction implemented in this thesis accounts for the three Compton terms that contribute to an experimental time spectrum, which are FEP$_{feeder}$-Compton$_{decay}$, $Compton_{feeder}$-FEP$_{decay}$ and Compton$_{feeder}$-Compton$_{decay}$. This correction is explained in detail in Section 5.8.2.

Therefore, in addition to the $CRD_{feeder}$ and $CRD_{decay}$, the Compton-Compton response distribution (CCRD) is also required. As mentioned in Section 5.8.2, the CCRD (Compton-Compton response distribution) accounts for the system response to the Compton events, being the CCRD the Compton analogous to the PRD (Prompt response distribution), which accounts for the system response to the prompt $\gamma$-rays.

An example of CCRD is displayed in Figure 6.13, where the reference energy has been set at 644 keV through the selection of a Compton-background region 18-keV wide. This curve has been derived from triple events $\gamma\gamma\gamma$(t) using the $^{241}$Pu data set. In addition to the CCRD curve, Figure 6.13 presents the interpolated values at 423 and 607 keV for the Compton-Compton correction.

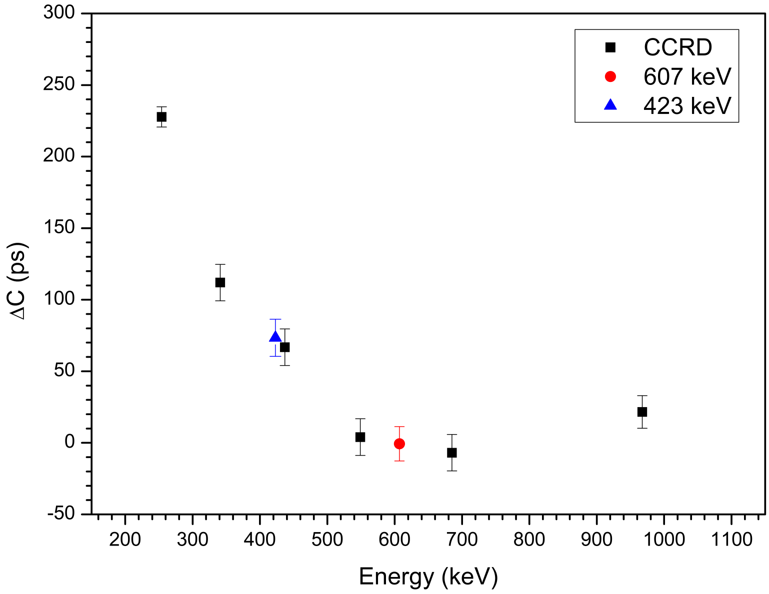

**Figure 6.13: Compton-Compton response distribution (CCRD).** - Compton-Compton response distribution (CCRD) derived from triple events $\gamma\gamma\gamma$ using the $^{241}$Pu data set. The reference has been set at the energy of 644 keV.

In the present case, where the feeder energy is 423 keV and the decay energy 607 keV, the corresponding values of PRD ($\Delta E_\gamma$) and CCRD ($\Delta E_\gamma$) are PRD ($E_{423}$-$E_{607}$)= 42(10) ps and CCRD ($E_{423}$-$E_{607}$)= 74(10) ps.

The experimental centroid difference of $\Delta C_{exp}(\Delta E_\gamma)$=78(11) ps, is here Compton corrected to second order following equation 5.20 in Section 5.8.2, yielding a value of $\Delta C_{FEP}(\Delta E_\gamma)$=108(18) ps. After the corrections, the general expression of the GCD method, Equation 2.6, is applied to obtain the lifetime of the first $2^+$ state in $^{136}$Te. The value is:

$$\tau_{2^+} = 33(10)\ ps$$

### - Lifetime of the $2^+$ state: high-resolution energy gate set in the 750 keV

Due to the peaks that appear in the vicinity of 607-keV FEP, the value of the $2^+$ lifetime has been also derived using a different Ge-gate. The aim is to cross-check the result and to investigate whether those extra peaks disappear. When setting the HPGe-gate in the 750-keV transition, the three peaks that appeared next to the 607 keV FEP do not show up, although there is a small presence of the 596-keV FEP that can be neglected. It is important to mention that the background level is also high for this case, the P/B ratios when using the add-back reconstruction are P/B=0.75 for the 607-keV transition and P/B=0.71 for the 423-keV $\gamma$-ray. Hence, it is worthwhile to subtract the events that are in coincidence with the background under the Ge-gated peaks. Figure 6.14 shows the effect: the black plot is the coincident $LaBr_3$(Ce) spectrum: Ge-gated by the 753-keV and $LaBr_3$(Ce)-gated by the 423-keV transitions, while the red plot is $LaBr_3$(Ce) spectrum gated by the same 423-keV transitions, but on the background on the right hand side of the 753-keV $\gamma$-ray. The blue plot is the difference between the black and the red ones and illustrates the effect of subtracting the background of the Ge-gated peaks. The inset of Figure 6.14 shows that in this case, the 596-keV peak has totally faded away. In addition to eliminating unwanted peaks, with this approach the peak-to-background ratio in the 607-keV $\gamma$-ray improves from P/B=0.75 to P/B=11, and from P/B=0.71 to P/B=4.2 in the 423-keV transition. Therefore, the lifetime of the $2^+$ state is derived using the background subtraction approach.

Figure 6.15 shows the corresponding Delayed (black) and Anti-delayed time distributions for the present set of gates, after having subtracted the events in coincidence with the background of the Ge-gated peaks. The experimental centroid increment is $\Delta C_{exp}$=100(19) ps. The procedure to measure the lifetime of the $2^+$ state here is the same as the one followed in the previous example; the PRD($\Delta E_\gamma$) value is PRD(423-607)=42(10) ps and the CCRD(423-607)=74(10) ps. The only differences are the values obtained from the internal Compton response distributions, $\mathrm{CRD}_{feeder}$ and $\mathrm{CRD}_{decay}$, which are slightly different from the former example, but follow a similar trend.

Values derived using the correction to first order and the correction implemented in this work are summarized below.

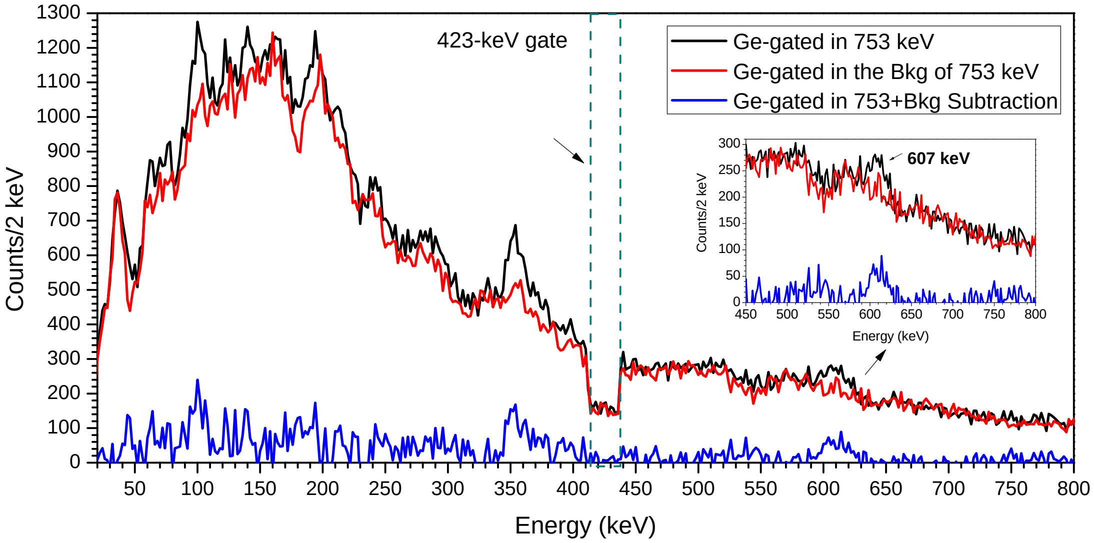

**Figure 6.14: Coincident LaBr$_3$(Ce) spectra to measure the lifetime of the $2_1^+$ state in $^{136}$Te.** - Coincident LaBr$_3$(Ce) spectra that determine the effect of subtracting the events that are in coincidence with the background of the Ge-gated peaks in the Clovers. The three spectra are LaBr$_3$(Ce)-gated by the 423-keV transition, which is marked with dashed green lines. The black plot corresponds to the coincident LaBr$_3$(Ce) spectrum Ge-gated by the 750-keV $\gamma$-ray, while the one in red is Ge-gated on the right hand side background of the 750-keV FEP. The blue plot is the difference between the black and the red ones and illustrates the effect of subtracting the Ge background. The background level has been reduced considerably improving the P/B) ratio from P/B=0.75 to P/B=11. The inset, which provides a zoom in the region around the 607-keV FEPs peak, shows the absence of satellite peaks and the 607-keV well resolved. The data set corresponds to the $^{241}$Pu target with multiplicity three ($\gamma\gamma\gamma$).

**- Compton corrections to first order**

$$\tau_{2^+} = 32(11)\ ps$$

**- Compton correction implemented in this work**

$$\tau_{2^+} = 34(13)\ ps$$

The good P/B ratios of this example indicate that the Compton contribution to the total time spectrum is low. As a consequence, the corrections to first and second order yield very similar values, almost identical. The uncertainties in this example (11

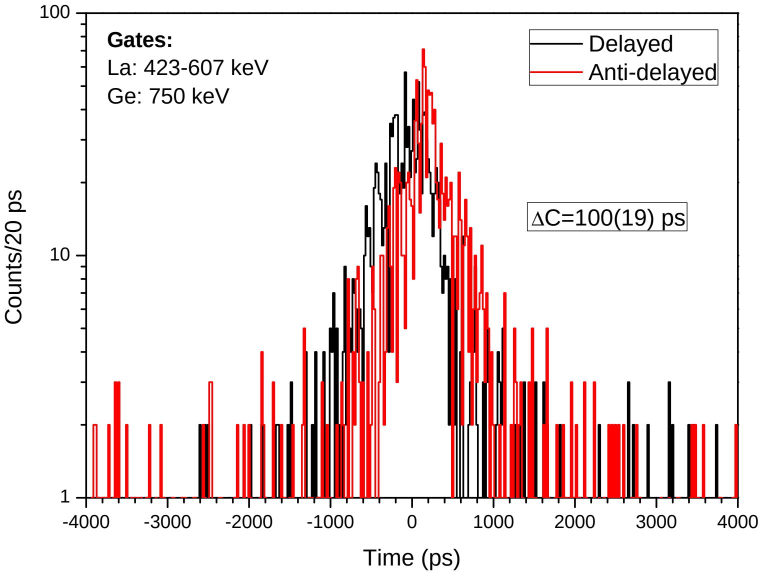

**Figure 6.15: Delayed and anti-delayed time distributions for deriving the lifetime of $2_1^+$ state in $^{136}$Te.** - Delayed (red) and anti-delayed (black) time spectra for the lifetime measurement of the first $2^+$ state in $^{136}$Te. The high-resolution energy gate was set in the 750 keV $\gamma$-ray and the LaBr$_3$(Ce)-gates in the 423-607 keV transitions. In the delayed time spectrum the 423-keV $\gamma$-ray acts as the start in the TAC and the 607 keV as the Stop. For the anti-delayed distribution, the LaBr$_3$(Ce)-gates are reversed 607-keV as Start and 423-keV as Stop. The used dataset comes from the $^{241}$Pu target sorted with multiplicity three ($\gamma\gamma\gamma$).

and 13 ps) are higher than those from the previous example (8 and 10 ps) due to the error coming from $\Delta C_{exp}(\Delta E_\gamma)$=100(19) ps as a consequence of the statistics, but one should keep in mind that the Compton effect in this example is much less significant.

Lifetime values derived for the $2^+$ state in $^{136}$Te using the $^{241}$Pu target data set and triple-coincident events are summarized in the following Table 6.3. The table provides the different values when setting the HPGe-gate either in the 353-keV or in the 750-keV transition for the two correcting procedures and the average value. This is possible because the values are assumed as independent.

The correction to second order yields identical values independently of the Compton contribution, which is much higher for the 353-keV-Ge-gated case than for the 750-keV-Ge-gated example. However, the correction to first order produces a value about 30% faster for the 353-keV-Ge-gated than the 750-keV-Ge-gated data set, which means that

| **Lifetime values of the first $2^+$ state in $^{136}$Te (ps)** | | |
|---|---|---|
| HPGe-gate | $1^{st}$ order correction | $2^{nd}$ order correction |
| 353 keV | 25(8) | 33(10) |
| 750 keV | 32(11) | 34(13) |
| Average value | 29(7) | 34(8) |

**Table 6.3: Lifetime values of the first $2^+$ state in $^{136}$Te measured from triple-coincidence events using the $^{241}$Pu target.**] - Lifetime values derived for the first $2^+$ state in $^{136}$Te using the $^{241}$Pu target and triple-coincident events. The HPGe-gate that was used in every case is indicated in the first column. The table compares the measured values when applying the first order correction (second column) and the correction implemented in this work (third column). The last row provides the mean average of the numbers obtained for each type of corrections.

it is not correcting totally the Compton effect. Nevertheless, the correction procedure to first order yields a very similar values to the one derived using the second order correction for the 750-keV-Ge-gated sorting, whose Compton contribution is lower.

We consider as the final value for the lifetime of the $2^+$ state the mean value of the numbers obtained using the second order correction.

$$\tau_{2^+} = 34(8)\ ps$$

#### 6.2.2.2 Lifetime of the first excited $4^+$ state

The lifetime of the $4^+$ state in $^{136}$Te is given by the time difference between the populating 353-keV $\gamma$-transition and the de-exciting 423-keV $\gamma$-ray. Both $\gamma$-transitions are selected in the LaBr$_3$(Ce) detectors to construct the fast-timing matrices and the related delayed (353-423 keV) and anti-delayed (423-353 keV) time distributions, where the lifetime is derived from the differences of their centroid positions. In this case, the HPGe-gate can be either set in the 607-keV or in the 750-keV $\gamma$-ray. In principle, both combinations are valid, nevertheless, the set of gates that contain the 607-keV $\gamma$-ray presents better statistics. And the time spectra Ge-gated with the 750-keV transition contain a long-lived contribution, which does not come from the $^{136}$Te isotope and results very difficult to separate from the one of interest. The long-lived contribution may be caused by the $^{100}$Zr isotope, which has a strong 353-keV $\gamma$-ray and maybe some unknown transition of energy close to 423 and 750 keV. Figure 6.16 provides a coincident HPGe spectrum Ge-gated by the 750 and 353-keV transitions. The aim of this plot is to investigate the presence of contaminants or fission partners that potentially may affect the analysis. In the plot, certain $\gamma$-lines from $^{100}$Zr at 213 and 497 keV are observed, as well as some $\gamma$-rays from $^{104}$Mo namely at 193, 369 and 520 keV. The 423-keV peak does not appear as an unresolved doublet.

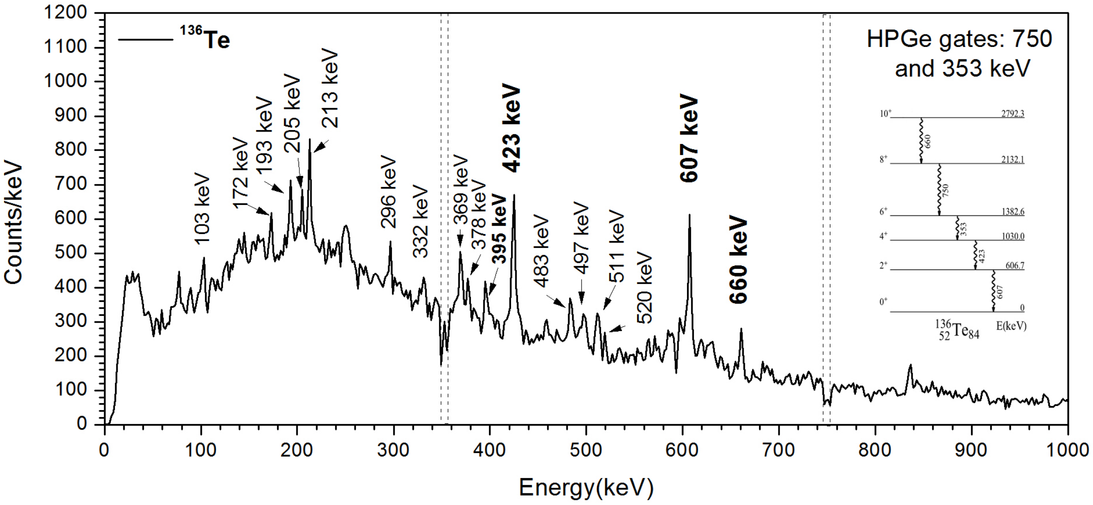

**Figure 6.16: Coincident HPGe spectrum Ge-gated by the 750- and 352-keV $\gamma$-rays.** - Coincident HPGe-Clover spectrum Ge-gated by 750- and 352-keV $\gamma$-transitions. The data set corresponds to the $^{241}$Pu target, the size of the gates is indicated with dashed lines and the most prominent peaks are labelled. The $\gamma$-rays coming from the $^{136}$Te are marked in bold font, and a scheme of the band is included on the right hand side for a better understanding.

The analysis procedure, in this case, is exactly the same as the one for the $2^+$ state, but in this case, the lifetime of $4^+$ state is obtained using the set of gates that contain the 607-keV $\gamma$-ray as high-resolution energy gate.

Like in the previous cases, the P/B ratios are much greater when using the background subtraction approach (Section 5.5.2.3) and the experimental centroid difference $\Delta C_{exp}$ increases by more than a 50%. Therefore, the lifetime is derived using the background subtraction approach. The P/B for the 423-keV $\gamma$-ray improves a factor of 11, it goes from P/B=0.39 to P/B=4.2, and the ratio of the 353-keV transition a factor of 18 from P/B=0.32 to P/B=5.8.

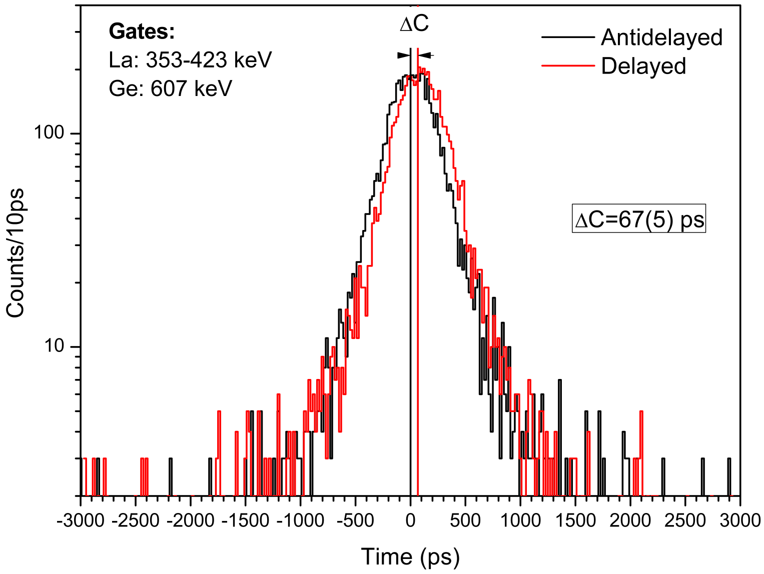

**Figure 6.17: Delayed and anti-delayed time distributions for the lifetime measurement of the $4_1^+$ state in $^{136}$Te using the add-back reconstruction.** - Delayed (red) and anti-delayed (black) time distributions for the lifetime measurement of the first $4^+$ state in $^{136}$Te using add-back reconstruction. The HPGe-gate was set in the 607-keV $\gamma$-ray. For the delayed time spectrum the 353-keV $\gamma$-ray performed as the start and the 423-keV transition as the stop. For the anti-delayed time spectrum, the gate selection was reversed. The used target is $^{241}$Pu.

Figure 6.17 depicts the delayed (353-423 keV) and the anti-delayed (423-353 keV) time distributions HPGe-gated by the 607-keV $\gamma$-ray when the add-back reconstruction is employed. It provides the experimental centroid difference, which is $\Delta C_{exp}$=67(5) ps. Figure 6.18 presents the delayed (353-423 keV) and the anti-delayed (423-353 keV) time distributions HPGe-gated by the 607-keV $\gamma$-ray, but obtained when the Ge-background approach is employed. The experimental centroid difference is $\Delta C_{exp}$=142(14) ps. Figure 6.19 shows the coincident LaBr$_3$(Ce) spectra Ge-gated by the 607-keV transition and the 353-keV $\gamma$-ray. The plot in blue is obtained when the events that are in coincidence with the background of Ge-gated peaks is subtracted.

To derive the lifetime it is required to obtain the PRD($\Delta E_\gamma$) and CCRD($\Delta E_\gamma$) values, which are PRD(E$_{353}$-E$_{423}$)= 20(10) ps and CCRD(E$_{353}$-E$_{423}$)=33(10) ps. Figure 6.20 presents the EXILL-FATIMA PRD together with the interpolated values at 353 and 423 keV. The internal Compton-Compton response CCRD is presented in Figure 6.21 including the interpolated values at $\Delta E(353-423)$.

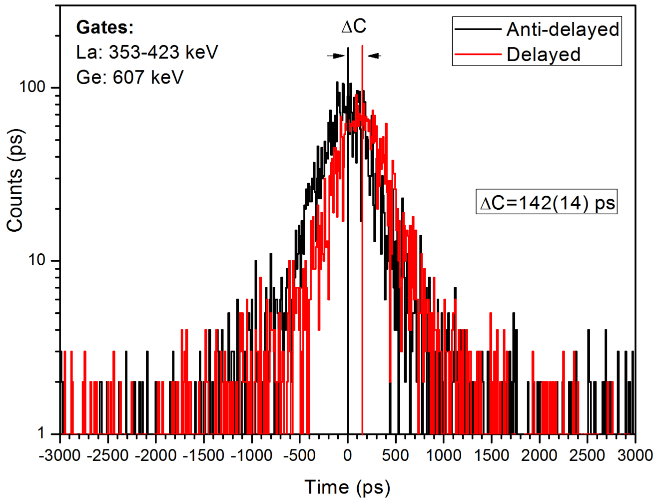

**Figure 6.18: Delayed and anti-delayed time distributions for the lifetime measurement of the first $4^+$ state in $^{136}$Te using the Ge-background subtraction approach.** - Delayed (red) and anti-delayed (black) time distributions for the lifetime measurement of the first $4^+$ state in $^{136}$Te. The HPGe-gate was set in the 607-keV. For the delayed spectrum the 353-keV $\gamma$-ray acts as the start and the 423-keV transition as the stop. For the anti-delayed spectrum, the selection was reversed. The target used is $^{241}$Pu.

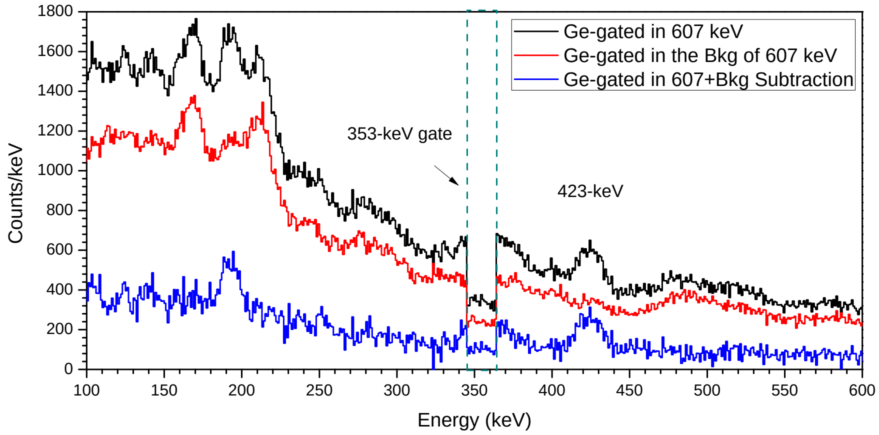

**Figure 6.19: Coincident LaBr$_3$(Ce) spectra to derive the lifetime of the $4_1^+$ state in $^{136}$Te.** - Coincident LaBr$_3$(Ce) spectra that show the effect of subtracting the events that are in coincidence with the background of the Ge-gated peaks in the Clovers. The three spectra are LaBr$_3$(Ce)-gated on the 353-keV transition, which is marked with dashed green lines. The black plot corresponds to the coincident LaBr$_3$(Ce) spectrum Ge-gated by the 607-keV $\gamma$-ray, while the one in red is Ge-gated on the right hand side background of the 607-keV FEP. The blue plot is the difference between the black and the red and illustrates the effect of subtracting the Ge background. The used target is $^{241}$Pu ($\gamma\gamma\gamma$).

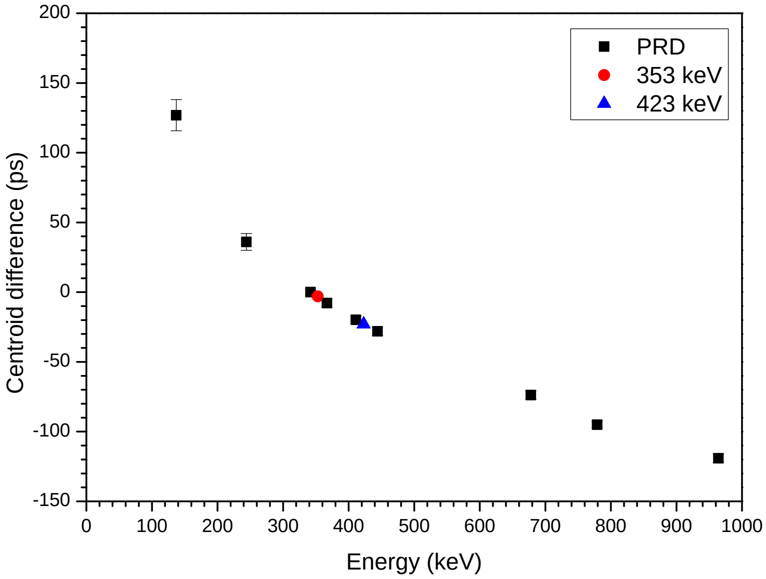

**Figure 6.20: Prompt Response Distribution PRD.** - Prompt response distribution of the EXILL-FATIMA experiment (black squares). The interpolated value at 423 keV is marked with a blue triangle and the system response at 607 keV with a red circle. From the difference between these two values one can obtain the quantity PRD(353-423)=20 ps.

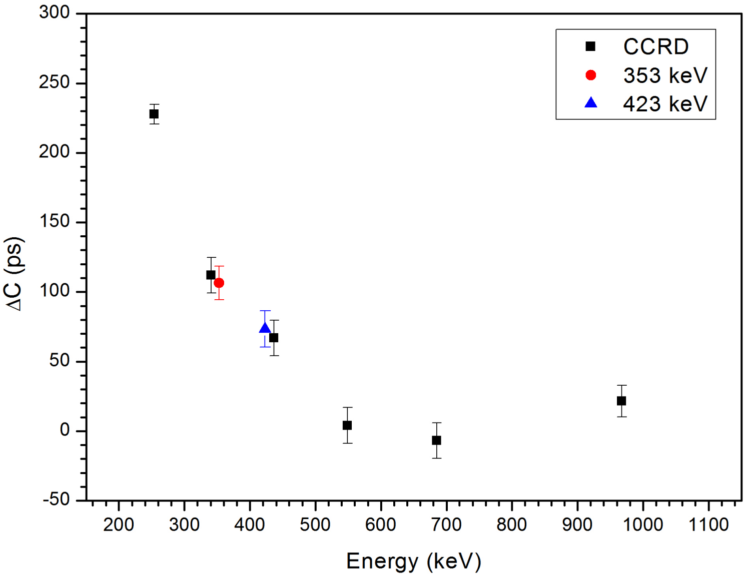

**Figure 6.21: Compton-Compton Response Distribution, CCRD.** - Compton-Compton response distribution (CCRD) derived using triple events $\gamma\gamma\gamma$ from the $^{241}$Pu target. The reference has been set at 644 keV through the selection of an energy region of 18 keV width. The plot also provides the interpolated values at 353 and 423 keV.

Lifetime values derived using the correction to first order and the correction implemented in this work are presented in the following:

**- Compton corrections to first order**

$$\tau = 85(7)\ ps$$

**- Compton correction implemented in this work**

$$\tau = 85(11)\ ps$$

For the present case, both correction procedures yield the same value. This is a consequence of the small Compton contribution underneath $\gamma_{feeder}$ (P/B=5.8) and $\gamma_{decay}$ (P/B=4.2).

#### 6.2.2.3 Lifetime of the first excited 6$^+$ state

The lifetime of the 6$^+$ state in $^{136}$Te is given by the time differences between the feeding 750-keV $\gamma$-transition and the de-exciting 353-keV $\gamma$-ray. For this level, the HPGe-gate can either be set in the 607 keV or in the 423 keV. The data set Ge-gated by the 423-keV $\gamma$-ray has better statistics and P/B, nevertheless, both options are valid. The followed strategy to derive the lifetime of the 6$^+$ state is to calculate separately the lifetime for every combination of gates and compare them afterwards.

In this case, the system response to the prompt $\gamma$-rays is PRD(750-353)=$-$88(10) ps and the response to the Compton-Compton events is CCRD(750-353)=$-$107(10) ps. Figure 6.22 shows the EXILL-FATIMA PRD and the interpolated values to 750 and 353 keV energies. The CCRD and the corresponding values are plotted in Figure 6.23.

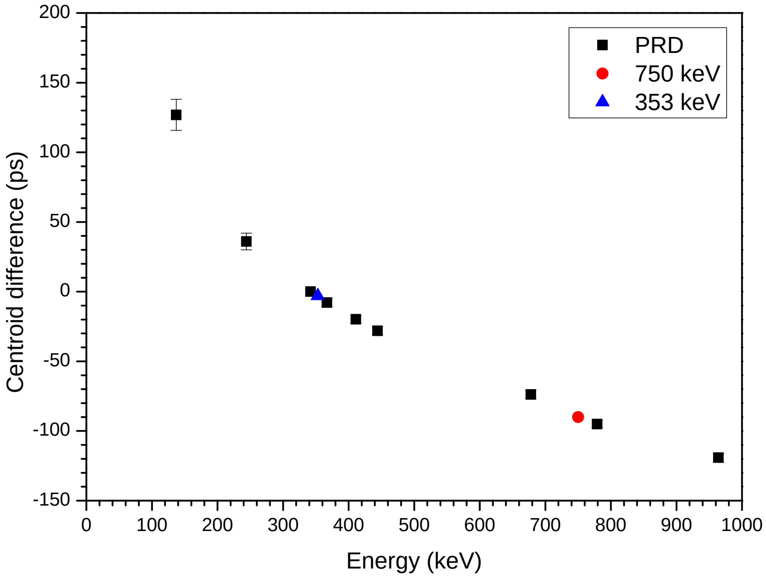

**Figure 6.22: Prompt Response Distribution PRD.** - Prompt response distribution of the EXILL-FATIMA experiment (black squares). The interpolated value to 750 keV is marked with a red circle, while the system response at 353 keV with a blue triangle. From the difference between these two values one can obtain the quantity PRD(750-353)$=-87$ ps.

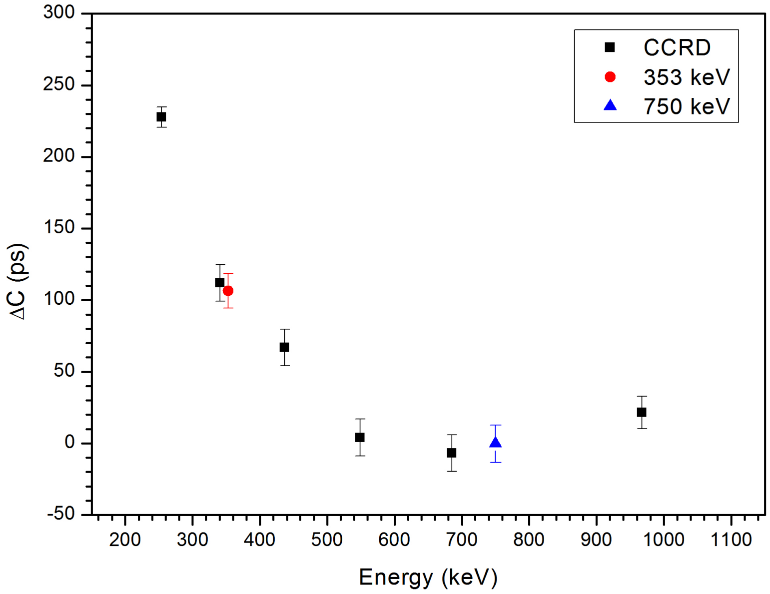

**Figure 6.23: Compton-Compton Response Distribution, CCRD.** - Compton-Compton response distribution (CCRD) derived using triple events $\gamma\gamma\gamma$ from the $^{241}$Pu target. The reference has been set at 644 keV through the selection of an energy region of 18 keV width. The plot also provides the interpolated values to 353 and 750 keV.

### - Lifetime of the $6^+$ state: high-resolution energy gate at 607 keV

Figure 6.24 presents the delayed (red) and the anti-delayed (black) time spectra for the lifetime measurement of the $6^+$ state in $^{136}$Te, when the add-back reconstruction is applied. The plot also provides the experimental centroid difference which is $\Delta C_{exp}$=178(10) ps for this case. The spectra have prominent tails on the right hand side (delayed) and on the left hand side (anti-delayed) respectively, which is a clear indication of a long-lived state. Like in the previous examples, the strategies of add-back reconstruction and background subtraction of the Ge-gated peaks have been checked, being more favourable to subtract the events in coincidence with the background of the Ge-gated peaks. In this case, the background subtraction ensures that the slopes at both sides are not caused by events in coincidence with the Ge-background. Figure 6.25 presents the delayed (red) and the anti-delayed (black) time distributions Ge-gated by the 607-keV transition and LaBr$_3$(Ce)-gated by the 750-353 keV combination, after having subtracted the background of the Ge-gated 607-keV $\gamma$-ray. The experimental centroid difference increases from $\Delta C_{exp}$=178(10) to $\Delta C_{exp}$=340(16) ps and the P/B has improved from P/B=0.66 to P/B=2.4 in the 353-keV FEP and from P/B=0.49 to P/B=1.1 for the 750-keV $\gamma$-peak.

### - Compton corrections to first order

$$\tau_{6^+} = 291(23)\ ps$$

### - Compton correction implemented in this work

$$\tau_{6^+} = 256(22)\ ps$$

The summary of the results for the present gate combination is :

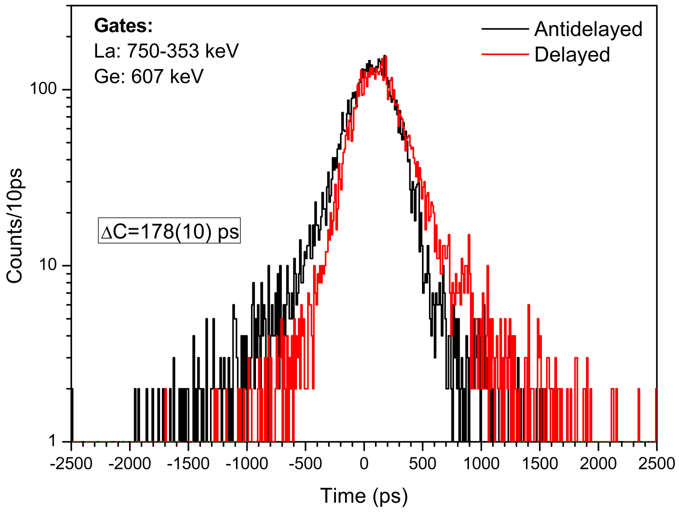

**Figure 6.24: Delayed and anti-delayed time distributions for the lifetime measurement of the $6_1^+$ state in $^{136}$Te.** - Delayed (red) and anti-delayed (black) time distributions for the lifetime measurement of the first $6^+$ state in $^{136}$Te. The HPGe-gate was set in the 607-keV $\gamma$-ray. For the delayed distribution the 750-keV $\gamma$-ray performed as the start and the 353-keV transition as the stop. For the anti-delayed time spectrum, the selection was reversed. The used target is $^{241}$Pu.

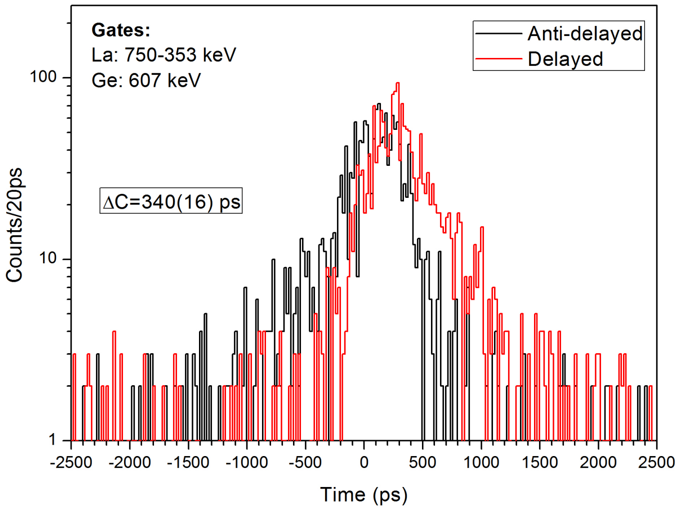

**Figure 6.25: Delayed and anti-delayed time distributions for the lifetime measurement of the $6_1^+$ state in $^{136}$Te.** - Delayed (red) and anti-delayed (black) time distributions for the lifetime measurement of the first $6^+$ state in $^{136}$Te. The HPGe-gate was set in the 607-keV $\gamma$-ray. For the delayed distribution the 750-keV $\gamma$-ray performed as the start and the 353-keV transition as the stop. For the anti-delayed time spectrum, the selection was reversed.The used target is $^{241}$Pu.

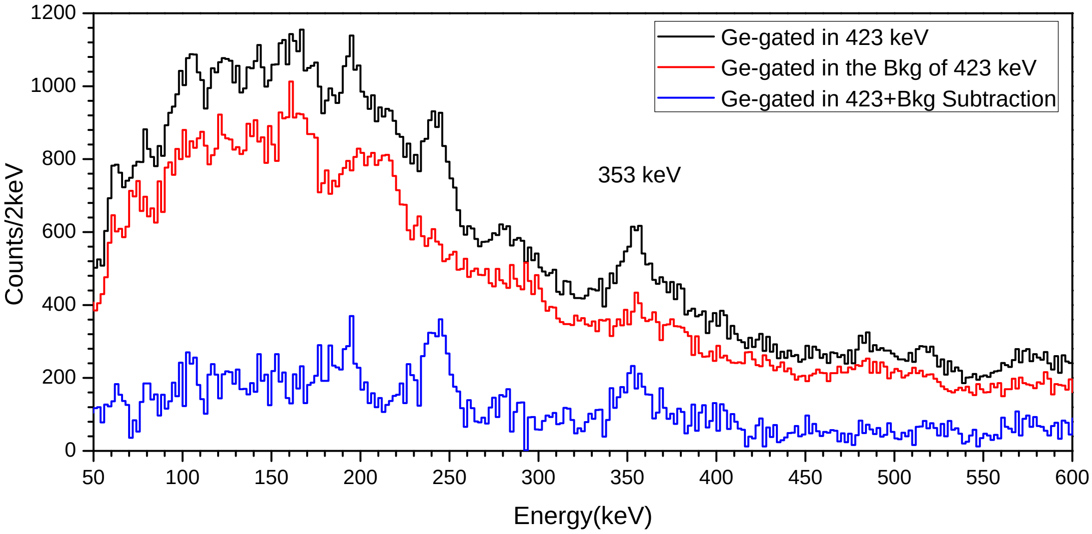

**Figure 6.26: Coincident LaBr$_3$(Ce) spectra to measure the lifetime of the $6_1^+$ state in $^{136}$Te.** - Coincident LaBr$_3$(Ce) spectra that shows the effect of subtracting the events that are in coincidence with the background of the Ge-gated peaks in the Clovers. The three spectra are LaBr$_3$(Ce)-gated by the 750-keV transition. The black plot is the coincident LaBr$_3$(Ce) spectrum Ge-gated by the 423-keV $\gamma$-ray, while the one in red is Ge-gated on the right hand side background (C) of the 423-keV FEP. The blue plot is the difference between the black and the red ones and illustrates the effect of subtracting the Ge background. The data set corresponds to the $^{241}$Pu target with multiplicity three ($\gamma\gamma\gamma$).

### - Lifetime of the $6^+$ state: high-resolution energy gate at the 423 keV

The same procedure is applied when the high-resolution energy gate is chosen at 423 keV, as illustrated in Figures 6.26 and 6.27. A summary of the measure lifetimes for the $6^+$ level is provided in the following:

### - Compton corrections to first order

$$\tau_{6^+} = 243(22)\ ps$$

### - Compton correction implemented in this work

$$\tau_{6^+} = 220(21)\ ps$$

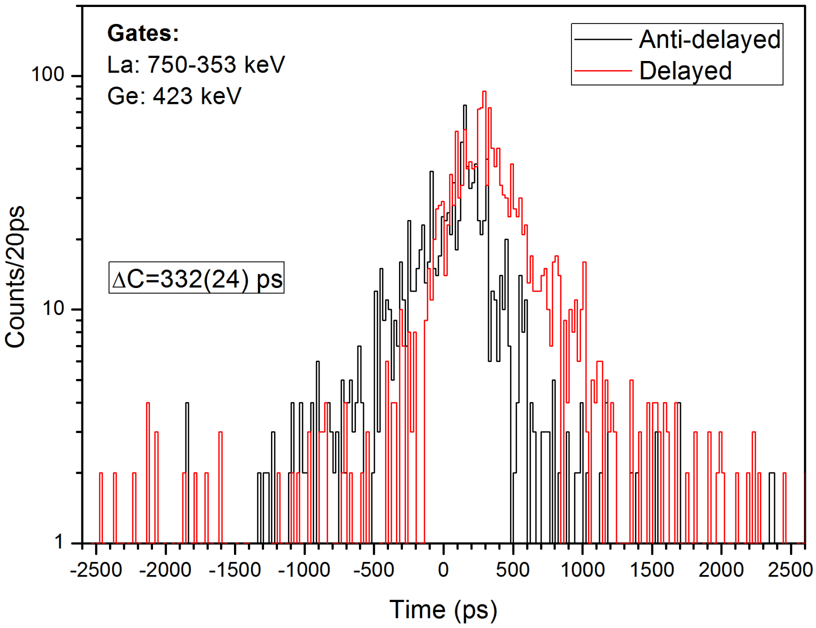

**Figure 6.27: Delayed and anti-delayed time distributions for the lifetime measurement of the $6_1^+$ state in $^{136}$Te.** - Delayed (red) and anti-delayed (black) time distributions for the lifetime measurement of the first $6^+$ state in $^{136}$Te. The HPGe-gate was set in the 423-keV $\gamma$-ray. For the delayed distribution the 750-keV $\gamma$-ray performed as the start and the 353-keV transition as the stop. For the anti-delayed time spectrum, the selection was reversed. The target used is $^{241}$Pu.

| Lifetime values of the first $6^+$ state in $^{136}$Te (ps) | | |
|---|---|---|
| HPGe-gate | $1^{st}$ order correction | $2^{nd}$ order correction |
| 607 keV | 291(23) | 256(22) |
| 423 keV | 243(22) | 220(21) |
| Average value | 267(23) | 238(22) |

**Table 6.4: Lifetime values of the first $6^+$ state in $^{136}$Te measured from triple-coincidence events using the $^{241}$Pu target.** - Lifetime values measured for the first $6^+$ state in $^{136}$Te using the $^{241}$Pu target and triple-coincident events. The HPGe-gate that was used in every case is indicated in the first column. The table compares the derived values when applying the first order correction (second column) and the correction implemented in this work (third column). The last row provides the mean average of the values obtained for each type of corrections.

We consider the value of 238(22) ps as the final result for the mean life of the $\tau(6^+)$. This lifetime has been also measured using the convolution technique (Section 2.1.1) yielding a range of values compatible with $\tau_{6^+}$ =238(22) ps. It has not been possible to obtain a precise value as a consequence of the FWHM of the time spectrum, which is of the order of 600 ps at this energies.

#### 6.2.2.4 Lifetime of the first excited $8^+$ state

The lifetime value of the $8^+$ state in $^{136}$Te is given by the time difference between the populating 660-keV $\gamma$-transition and the de-exciting 750-keV $\gamma$-ray. The HPGe-gate can be set in one of the 607 keV, 423 keV or 353 keV transitions. However, to prevent from potential contributions of the $^{100}$Zr isotope, the 353-keV transition is avoided, and 607 keV and 423 keV are the options of choice. The PRD($\Delta E_\gamma$) and CCRD($\Delta E_\gamma$) values for the present case are: PRD(660-750)=18 ps and CCRD(660-750)=−5 ps. Figures 6.28 and 6.29 show the corresponding curves and the interpolated values at 660 and 750 keV.

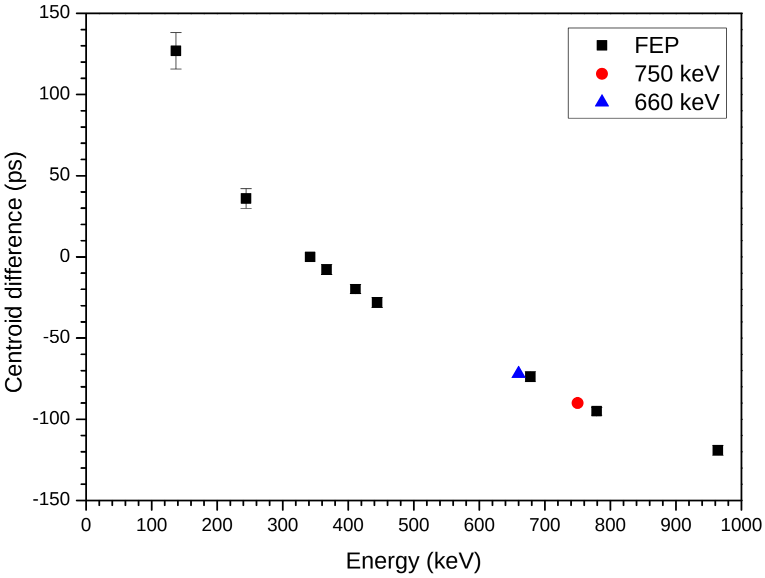

**Figure 6.28: Prompt Response Distribution PRD.** - Prompt response distribution of the EXILL-FATIMA experiment (black squares). The interpolated value at 750 keV is marked with a red circle, while the system response at 660 keV with a blue triangle. From the difference between these two values one can obtain the quantity PRD(660-750)=18 ps.

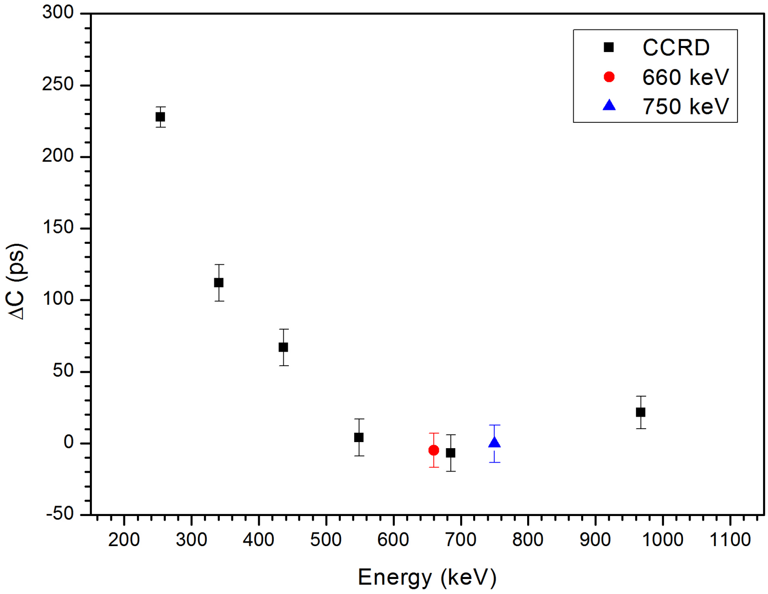

**Figure 6.29: Compton-Compton Response Distribution, CCRD.** - Compton-Compton response distribution (CCRD) derived using triple events $\gamma\gamma\gamma$ from the $^{241}$Pu target. The reference has been set at 644 keV through the selection of an energy region of 18 keV width. The plot also provides the interpolated values to 660 and 750 keV.

### - Lifetime of the $8^+$ state: high-resolution energy gate at 607 keV

Figure 6.30 shows the delayed (red) and the anti-delayed (black) time distributions Ge-gated by the 607 keV transition and LaBr$_3$(Ce)-gated by the 660 and 750-keV $\gamma$-rays. These spectra have been obtained using the add-back reconstruction procedure and present an experimental centroid difference of $\Delta C_{exp}$=8(7) ps. Like in the previous examples the P/B ratios improve when performing Ge-background subtraction. In this case, the P/B of the 660-keV transition improves from P/B=0.28 to P/B=1.0 and the P/B of the 750-keV $\gamma$-ray from P/B=0.30 to P/B=1.1. Therefore the lifetime values are obtained using data sets processed by the background subtraction approach. In this case, the experimental centroid position does not vary significantly, it changes from $\Delta C_{exp}$=8(7) ps to $\Delta C_{exp}$=10(24) ps. Figure 6.30 presents the delayed (red) and the anti-delayed (black) time spectra relative to the data sets corrected for the background underneath the Ge-gated peaks.

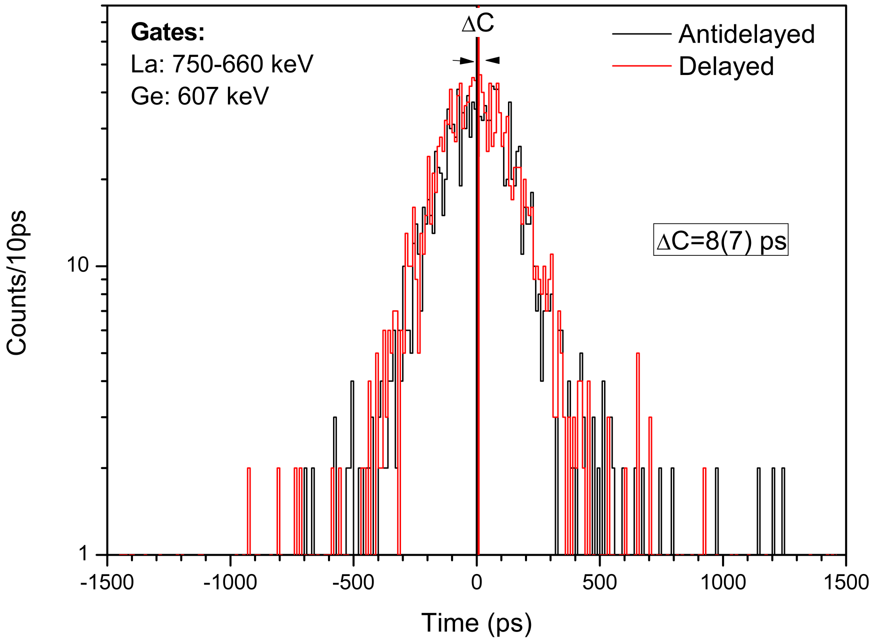

**Figure 6.30: Delayed and anti-delayed time distributions for the lifetime measurement of the $8_1^+$ state in $^{136}$Te using add-back reconstruction.** - Delayed (red) and anti-delayed (black) time distributions for the lifetime measurement of the first $8^+$ state in $^{136}$Te. The HPGe-gate was set in the 607-keV $\gamma$-ray. For the delayed distribution the 660-keV $\gamma$-ray was set as the start and the 750-keV as the stop. For the anti-delayed time spectrum the selection was reversed. The target used is $^{241}$Pu.

- **Compton correction to first order**

$$\tau_{8^+} = \leq 11\ ps$$

- **Compton correction implemented in this work**

$$\tau_{8^+} = \leq 16\ ps$$

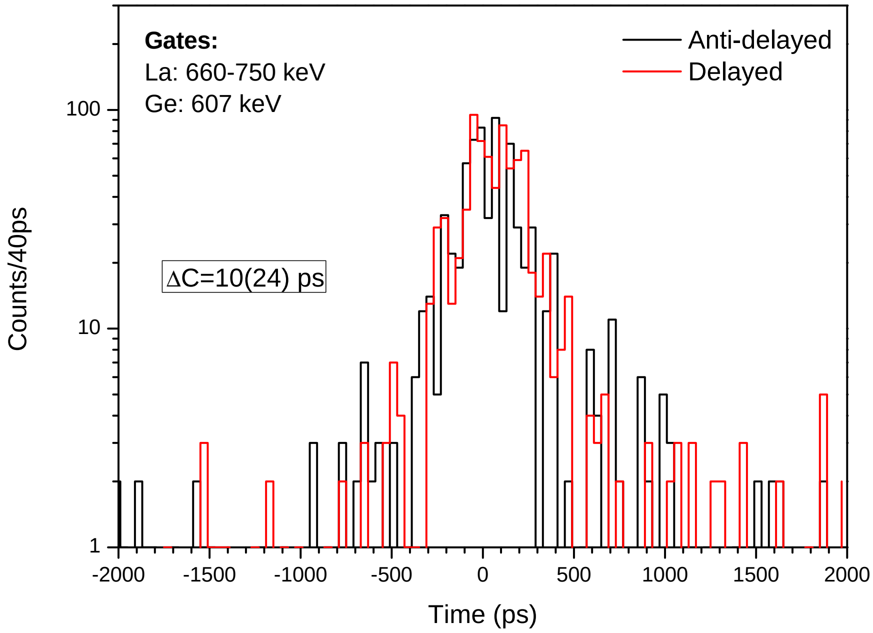

**Figure 6.31: Delayed and anti-delayed time distributions for the lifetime measurement of the $8_1^+$ state in $^{136}$Te subtracting the Ge background.** - Delayed (red) and anti-delayed (black) time distributions for the lifetime measurement of the first $8^+$ state in $^{136}$Te. The HPGe-gate was set in the 607-keV $\gamma$-ray. For the delayed distribution the 660-keV $\gamma$-ray was set as the start and the 750 keV as the stop. For the anti-delayed time spectrum the selection was reversed.The used target is $^{241}$Pu.

### - Lifetime of the $8^+$ state: high-resolution energy gate at 423 keV

The same procedure is applied for this combination of gates. A summary of the lifetime measurements of the $8^+$ state in $^{136}$Te is provided in the following:

**- Compton correction to first order**

$$\tau_{8^+} = \leq 19 \ ps$$

**- Compton correction implemented in this work**

$$\tau_{8^+} = \leq 20 \ ps$$

The values are summarized in the following Table 6.5

| **Lifetime values of the first $8^+$ state in $^{136}$Te (ps)** | | |
|---|---|---|
| HPGe-gate | $1^{st}$ order correction | $2^{nd}$ order correction |
| 607 keV | $\leq 11$ | $\leq 16$ |
| 423 keV | $\leq 19$ | $\leq 20$ |
| Average value | $\leq 12$ | $\leq 14$ |

**Table 6.5: Lifetime values of the first $8^+$ state in $^{136}$Te measured from triple-coincidence events using the $^{241}$Pu target.** - Lifetime values derived for the first $6^+$ state in $^{136}$Te using the $^{241}$Pu target and triple-coincident events. The HPGe-gate that was used in every case is indicated in the first column. The table compares the derived values when applying the first order correction (second column) and the correction implemented in this work (third column).

### 6.2.3 Lifetime values measured in quadruple coincidences

The main motivation to investigate quadruple events is to reduce the level of background present in triple events as well as the amount of certain nuclei with long-lived states, such as $^{104}$Mo or $^{100}$Zr (See Section 6.2). A second high-resolution gate set in the HPGe-clovers improves the peak to background ratio and eliminates most of the undesired contaminants; however, it causes a significant reduction of the statistics in the coincident spectra due to the lower efficiency. The drastic reduction of the statistics constitutes the main drawback for quadruple events because most of the time distributions have less than 1000 counts. With fewer counts, the centroid positions are very sensitive to the integration limits and have higher statistical uncertainty, which is up to 30 ps. As a direct consequence of the much lower statistics, the add-back reconstruction procedure when sorting the fast timing matrices is not beneficial for the analysis of quadruple events. When using the add-back reconstruction, the peak to background ratio improves, however the statistics of the time spectra decreases. As an example; the peak to background ratio of the 607 keV $\gamma$-ray in coincidence with the 750 and 353-keV $\gamma$-rays in the Ge detectors and with 423-keV transition in the LaBr$_3$(Ce) detectors, improves from 1.4 to 1.7 when performing the add-back. However, the statistics of the time distribution decreases from 610 to 330 counts. Therefore, for this part of the analysis, it is more convenient not to use the add-back reconstruction and correct the centroid position by the background contribution afterwards.

#### 6.2.3.1 Lifetime of the first excited $2^+$

As mentioned before the lifetime of the first $2^+$ state can be obtained by measuring the time difference between the arrival of the populating 423-keV $\gamma$-ray and the de-exciting 607-keV transition. In this case, there are two high-resolution energy gates set in the 750- and the 353-keV transitions. Figure 6.32 shows the coincident LaBr$_3$(Ce) spectrum triple gated, Ge-gated by the 750- and the 353-keV transitions and LaBr$_3$(Ce)-gated by the 607-keV $\gamma$-ray. Despite of being the spectrum much cleaner than those obtained using triple coincidences, the level of background is still high. Adding another Ge-gate has made it possible to eliminate most of the unwanted peaks that appeared; in Figure 6.32 the most prominent peaks are 423 and 192 keV, which correspond to $^{136}$Te and $^{104}$Mo respectively.

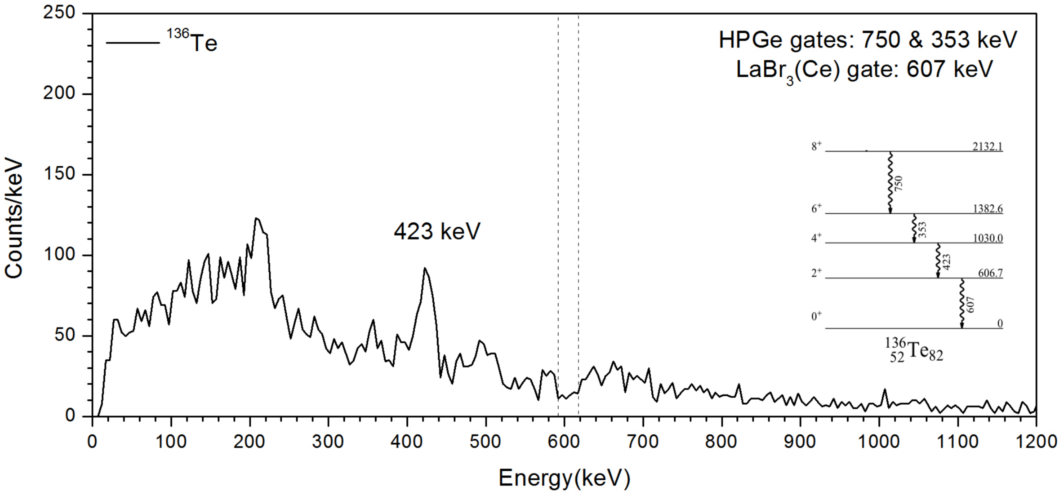

**Figure 6.32: Coincident LaBr$_3$(Ce) spectrum Ge-gated by 750- and 353-keV transitions and LaBr$_3$(Ce)-gated by 607-keV $\gamma$-ray.** - Coincident LaBr$_3$(Ce) Ge-gated by 750- and 353-keV transitions, and LaBr$_3$(Ce)-gated by 607 keV $\gamma$-ray. The LaBr$_3$(Ce) gate is marked with dashed lines and the matching energy for measuring the $2^+$ lifetime (423 keV) is labelled. For a better understanding the $^{136}$Te rotational band is provided on the right hand side of the plot. The data set corresponds to the $^{235}$U target.

Figure 6.33 is complementary to Figure 6.32, it shows the coincident LaBr$_3$(Ce) spectrum Ge-gated by 750- and the 353-keV transitions and LaBr$_3$(Ce)-gated by 423-keV the $\gamma$-ray. In both plots, the peaks that will be selected for building the fast-timing matrices appear clean, but the level of background is still significant. The P/B for the 607-keV transition is P/B=3.7 and for the 423-keV $\gamma$-ray P/B=1.4. The background

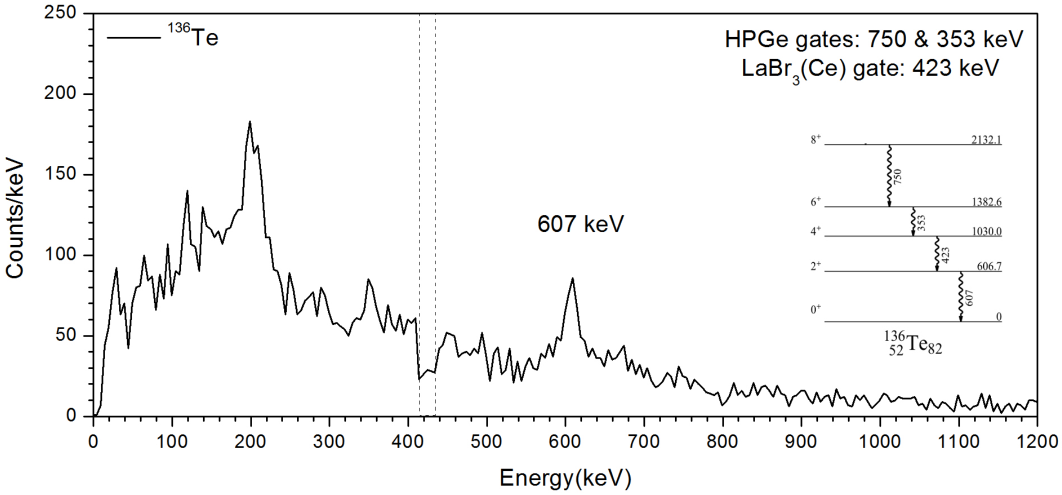

**Figure 6.33: Coincident LaBr$_3$(Ce) spectrum Ge-gated by the 750- and 353-keV transitions and LaBr$_3$(Ce)-gated by the 423-keV $\gamma$-ray.** - Coincident LaBr$_3$(Ce) spectrum Ge-gated by 750- and 353-keV transitions and LaBr$_3$(Ce)-gated by 423-keV $\gamma$-ray. The LaBr$_3$(Ce) gate is marked with dashed lines and the matching energy, 607 keV, is labelled. The $^{136}$Te rotational band is provided on the right hand side of the plot. The data set corresponds to the $^{235}$U target.

subtraction approach has not been applied here due to low statistics. Figure 6.34 presents the delayed (red) and the anti-delayed (black) time distributions Ge-gated by 750- and 353-keV transitions and LaBr$_3$(Ce)-gated by the 423 and 607-keV $\gamma$-rays. The experimental centroid difference for the present case is $\Delta C_{exp}$=5(21) ps. It can be seen that experimental uncertainty is much higher than in triple coincidences as a consequence of the much lower statistics.

The corresponding value of PRD($\Delta E$) is the same as the one used in Section 6.2.2.1, which is PRD(423-607)=42(10) ps. The curve and the interpolated values can be seen also in Section 6.2.2.1. The corresponding CRD$_{feeder}$ and CRD$_{decay}$ curves are shown in the following Figures 6.35 and 6.36 , and the CCRD in Figure 6.37. From the CCRD curve, it can be derived that CCRD(423-607) for the present case is CCRD(423-607)=54(24) ps.

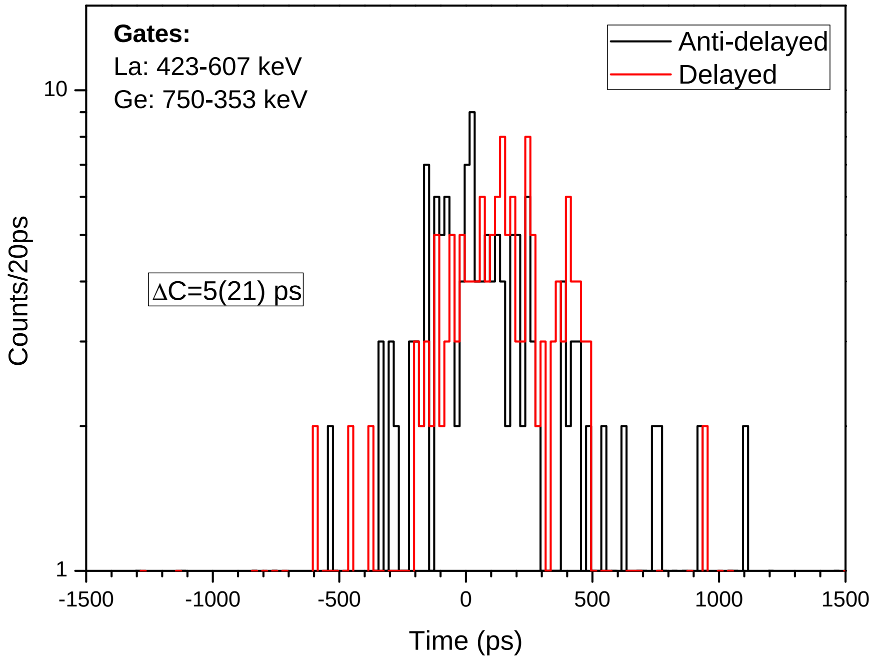

**Figure 6.34: Delayed and anti-delayed time distributions for the lifetime measurement of the $2_1^+$ state in $^{136}$Te.** - Delayed (red) and anti-delayed (black) time distributions for the lifetime measurement of the first $2^+$ state in $^{136}$Te. The time spectra were obtained using quadruple coincidences ($\gamma\gamma\gamma\gamma$), Ge-gated by the 607- and 353-keV $\gamma$-rays. For the delayed spectrum, the 423-keV $\gamma$-ray was set as the start and the 607 keV as the stop. For the anti-delayed time spectrum, the selection was reversed. The target used is $^{235}$U.

**- Compton correction to first order**

$$\tau_{2^+} = 10(26)\ ps$$

**- Compton correction implemented in this work**

$$\tau_{2^+} = 41(25)\ ps$$

The uncertainty of the value derived from quadruple coincidences is higher than the counterpart value from triple coincidences due to the lower statistics in the time peak.

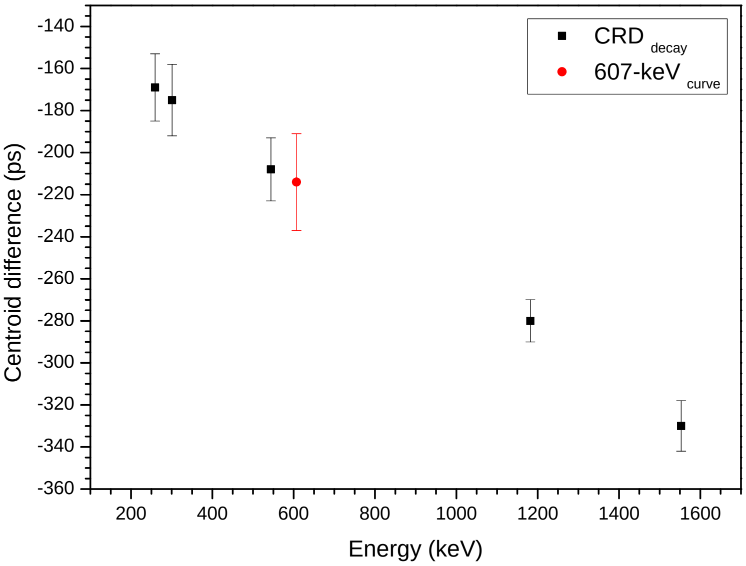

**Figure 6.35: Compton Response Distribution, CRD$_{decay}$.** - Compton response distribution (CRD) derived using quadruple events $\gamma\gamma\gamma\gamma$ from the $^{235}$U target.The reference has been set in the 423-keV peak. The plot also provides the interpolated value at 607 keV.

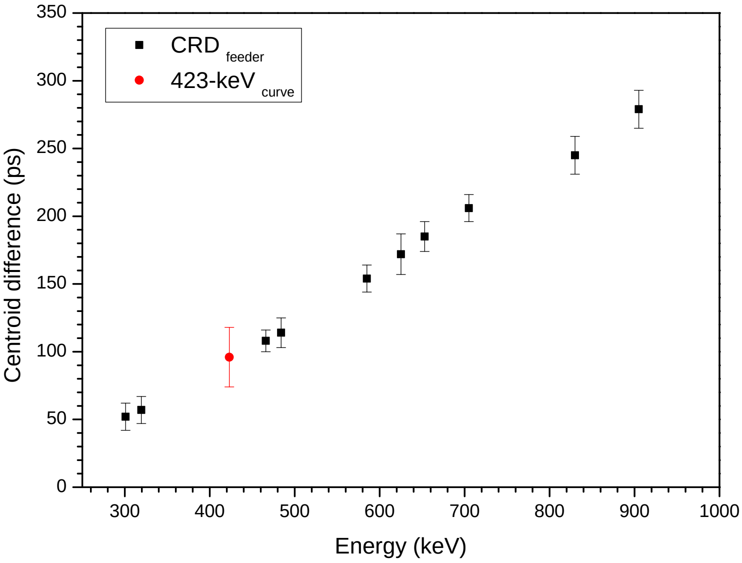

**Figure 6.36: Compton Response Distribution, CRD$_{decay}$.** - Compton response distribution (CRD) derived using quadruple events $\gamma\gamma\gamma\gamma$ from the $^{235}$U target.The reference has been set in the 423-keV peak. The plot also provides the interpolated value at 607 keV.

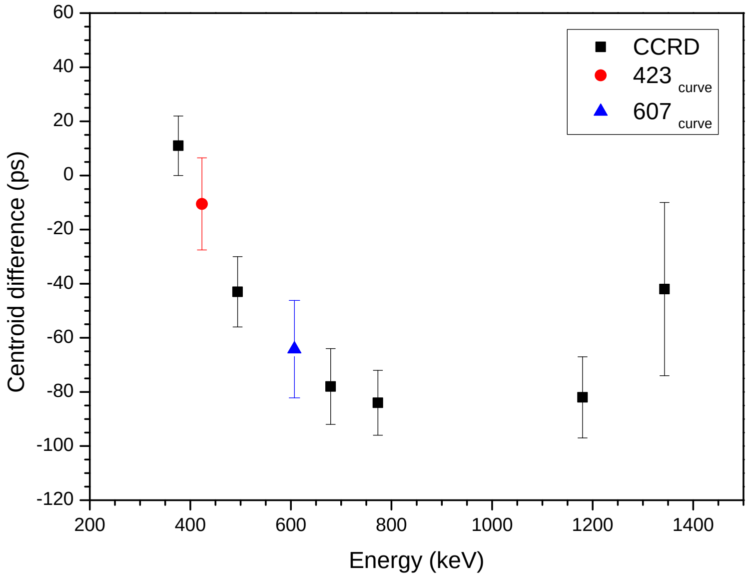

**Figure 6.37: Compton-Compton Response Distribution, CCRD.** - Compton-Compton response distribution (CCRD) derived using quadruple events ($\gamma\gamma\gamma\gamma$) from the $^{235}$U target. The reference has been set at 301 keV through the selection of an energy region of 18 keV with. The plot also provides the interpolated values at 423 and 607 keV.

## 6.3 Theoretical calculations for $^{136}$Te

As a consequence of the unexpected low value of the B(E2) strength measured for the first $2^+$ state in $^{136}$Te, there is available in the literature a good number of theoretical calculations that use different interactions and theoretical models such as shell model calculations, quasiparticle random phase approximation or $\alpha$-cluster.

A. Covello and co-workers performed in 2002 shell-model calculations taking $^{132}$Sn as a close core and using a realistic effective interaction, that was derived from the CD-Bonn nucleon-nucleon interaction renormalized by means of the $V_k$ approach, in a perturbative expansion [CCGI03]. The valence protons and neutron holes occupied the five single-particle levels $0g_{7/2}$, $ld_{5/2}$, $ld_{3/2}$, $2s_{1/2}$, and $0h_{11/2}$ of the 50-82 shell, and for the valence neutrons the model included all the six single-particle levels $0h_{9/2}$, $1f_{7/2}$, $1f_{5/2}$, 2p3/2, 2p1/2 and 0i13/2 of the 82-126 shell. For calculating the single particle and hole energies, the experimental energies from the one-neutron or one-proton nuclei around $^{132}$Sn were used when available, obtaining a remarkable agreement with the experimental energies for $^{134,135,136}$Te. In the calculation of the E2 transition probabilities, the effective charges of 1.55 e for protons and 0.7 e for neutrons were used in order to properly reproduce the transition rates in $^{134}$Sn. In spite of the very good agreement of the transition rates in $^{134}$Te and $^{135}$Te, the B(E2; $2^+ \rightarrow 0^+$) value in $^{136}$Te was more than a factor of 2 away from the experimental measurement available at that time, pointing towards a unsuitable model or effective charges. These theoretical calculations were published in [RBB$^+$02].

In the most recent version of these calculations by A. Gargano et al., described in [ASB$^+$17], the effective charge for protons is modified to 1.7 e and the single-particle matrix elements of the effective M1 operator are calculated by perturbation theory also, consistent with the derivation of the effective two-body interaction.

The B(E2; $2^+ \rightarrow 0^+$)= 410 e$^2$fm$^4$ is in excellent agreement with the newly measured 362(31) e$^2$fm$^4$ value [ASB$^+$17], in addition, other electromagnetic moments are very well reproduced, with the exception of the g-factor for the $2^+$ state. These calculations have been extended by A. Gargano and co-workers [Gar] to include the B(E2; $6^+ \rightarrow 4^+$) and B(E2; $8^+ \rightarrow 6^+$) values measured experimentally in this thesis. The calculations are summarized in Table 6.6.

| $J_i^\pi$ | $J_f^\pi$ | **B(E2; $J_i \rightarrow J_f$) ($e^2fm^4$)** | **$J_i^\pi$ Excitation energy (keV)** | |
|---|---|---|---|---|
| | | | Calculated | Experimental |
| $2_1^+$ | $0_1^+$ | 410 | 686 | 607 |
| $4_1^+$ | $2_1^+$ | 520 | 1098 | 1030 |
| $6_1^+$ | $4_1^+$ | 360 | 1361 | 1382 |
| $2_2^+$ | $4_1^+$ | 50 | 1573 | 1568 |
| $2_2^+$ | $2_1^+$ | 400 | 1573 | 962 |
| $2_2^+$ | $0_1^+$ | 30 | 1573 | 1568 |
| $8_1^+$ | $6_1^+$ | 300 | 2281 | 2132 |

**Table 6.6: Theoretical B(E2) transition rates in $^{136}$Te by A. Gargano *et al.*. -** Theoretical B(E2) reduced transition probabilities for $^{136}$Te calculated by A. Gargano and collaborators.

Another flavour of shell model calculations is also discussed in [ASB+17]. In this case B. Brown et al. use the same model space, but a different mixed interaction, where the proton-proton piece is based on the CD-Bonn potential, but the proton-neutron and neutron-neutron jj56pnb interaction is derived from the next-to-next-to-next-to-leading-order ($N^3LO$) potential. The effective charges were tuned in [ASB+17] to the E2 transitions rates in $^{134}$Te and $^{134}$Sn resulting $e_p$=1.56 e and $e_n$=0.66 e, but they were fixed to $e_p$=1.55 e and $e_n$=0.5 e. This results in a B(E2; $2^+ \rightarrow 0^+$) calculated value of 340 $e^2fm^4$. It is worth noting that in both shell model calculations discussed above the $2_1^+$ a $4_1^+$ wave functions are dominated by neutron configurations, which clearly overshadow proton configuration components.

Shimizu and co-workers also performed calculations in the framework of the nuclear shell model [SOMH04]. They used a Hamiltonian that had already been successfully employed for nearby Barium isotopes trying to explain the $^{136}$Te anomaly, in a parametrization that separates the two-body proton Hamiltonian, the neutron Hamiltonian (with monopole and quadrupole pairing interactions) and the proton-neutron interaction that is assumed to be of the quadrupole-quadrupole type. In this case, the effective charges are 1.6 e for protons and 0.6 e for neutrons. The result was much closer to the experimental one for the B(E2) transition rate.

In a very similar approach, Bianco et al. [BLIA+13] employ the same model space and two-body potential, but with fine-tuned single particle energies and pairing terms, and a different diagonalization algorithm. But their calculations overestimate the value of B(E2; $2^+ \rightarrow 0^+$) in $^{136}$Te, since they obtain 479 e$^2$fm$^4$. Interestingly enough, they provide calculations for the E2 transitions within the yrast band, from which the lifetimes can be derived. Similar B(E2) values are expected in the rotational band. They are summarized in Table 6.7.

| $\mathbf{J}_i$ | **B(E2; $\mathbf{J}_i \rightarrow J_{i-2}$) e$^2$fm$^4$** | **E$_\gamma$ (keV)** | **Lifetime (ps)** |
|---|---|---|---|
| $2^+$ | 479.4 | 606.5 | 21 |
| $4^+$ | 683.0 | 423.5 | 88 |
| $6^+$ | 612.8 | 352.6 | 244 |
| $8^+$ | 535.1 | 749.5 | 6 |
| $10^+$ | 517.6 | 660.2 | 13 |

**Table 6.7: Theoretical B(E2) transition rates in $^{136}$Te and derived level lifetimes by S. D. Bianco *et al.*.** - Theoretical B(E2) transition rates calculated by S. D. Bianco *et al.* [BLIA$^+$13], the corresponding level lifetimes are also provided.

Apart from the shell model, there are other descriptions of the properties of the first-excited $2^+$ state in $^{136}$Te. In the framework of the quasiparticle random phase approximation, Terasaki et al. [TENS02] used a phenomenological interaction for nuclei both below and above $^{132}$Sn to derive energies and transition rates. They obtain a low B(E2; $2^+ \rightarrow 0^+$) of 180 e$^2$fm$^4$, with they attribute to a diminished neutron pairing gap as N increases. This value is a factor of 2 lower than calculations using the shell model. More recent but similar QRPA calculations performed in [SAPW14] obtain a closely low B(E2) value and dominant neutron configurations in the wave function of the $2^+_1$ state of $^{136}$Te, while the $2^+_2$ state is proposed as a mixed symmetry state with substantial proton configuration contributions.

Bertsch et al. [BGH$^+$07] use the generator coordinate method with a Gaussian overlap approximation and density-dependent Gogny D1S interaction to globally describe the properties of the low-lying $2^+$ states in even-even nuclei. The B(E2) transition rate for $^{136}$Te is quoted in [ASB$^+$17] as 460 e$^2$fm$^4$.

There has also been a theoretical approach based on alpha clustering above double shell closures [WPX13], where the spectroscopic properties including the electromagnetic transition probabilities of $\alpha$-cluster nuclei above double shell closures across the table of isotopes are investigated using a cluster potential. The unexpectedly small B(E2; $2^+ \rightarrow 0^+$) in $^{136}$Te is explained as caused by the cluster structure of the 2 protons and 2 neutrons above $^{132}$Sn, being the calculated value 290 e$^2$fm$^4$. Predictions are proposed for the transitions from excited states, see Table 6.8.

| **J$_i$** | **B(E2; J$_i \rightarrow J_{i-2}$)** **e$^2$fm$^4$** | **E$_\gamma$** **(keV)** | **Lifetime** **(ps)** |
|---|---|---|---|
| $2^+$ | 286.6 | 606.5 | 35 |
| $4^+$ | 399.4 | 423.5 | 150 |
| $6^+$ | 416.1 | 352.6 | 360 |
| $8^+$ | 396.9 | 749.5 | 9 |
| $10^+$ | 355.5 | 660.2 | 18 |
| $12^+$ | 298.8 | 394.8 | 285 |
| $14^+$ | 232.2 | 533.4 | 81 |

**Table 6.8: Theoretical B(E2) transition rates in $^{136}$Te calculated using the $\alpha$-cluster model and related level lifetimes.** - Theoretical B(E2) transition rates in $^{136}$Te calculated by S.M. Wang *et al.* using the $\alpha$-cluster model [WPX13], the corresponding level lifetimes are also provided.

Finally, it is worth mentioning that collective $2^+$ states can be successfully described using the N$_p$ x N$_n$ scheme used by Casten *et al.* [Cas00], where N$_p$ denotes the number of valence proton particles or holes, and N$_n$ the same number for neutrons. As a function of this product, the behaviour of both excitation $2^+$ energies and B(E2) transition rates are smooth.

The collected values of the aforementioned B(E2) transitions rates calculated for the first $2^+$ state in $^{136}$Te following different approaches are compiled in Table 6.9. The available theoretical calculations for the first excited $4^+$ state to $2^+$ state are summarized in Table 6.10.

| **B(E2; $2^+ \rightarrow 0^+$) $e^2fm^4$** | **Model** | **Reference** |
|---|---|---|
| 500 | SM | A. Covello in [RBB+02] |
| 320 | SM | A. Covello in [CCGI03] |
| 300 | SM | N. Shimizu *et al.* [SOMH04] |
| 479 | SM | S. D. Bianco *et al.* in [BLIA+13] |
| 340 | SM | B. Brown *et al.* in [ASB+17] |
| 410 | SM | A. Gargano *et al.* in [ASB+17] |
| 452 | SM | B. Brown *et al.* in [BSS+05] |
| 412 | SM | H. Naïdja *et al.* in [NNB17] |
| 180 | QRPA | J. Terasaki *et al.* [TENS02] |
| 220 | QRPA | A. P. Severyukhin *et al.* in [SAPW14] |
| 460 | GCM-GOA | G.F. Bertsch *et al.* in [BGH+07] |
| 287 | $\alpha$-Cluster | S. M. Wang *et al.* in [WPX13] |

**Table 6.9: Theoretical B(E2) strength values of B(E2; $2^+ \rightarrow 0^+_{g.s}$) in $^{136}$Te.** - Summary table of the theoretical calculations of the B(E2) strength from the first $2^+$ to the state $0^+$ in $^{136}$Te.

| **B(E2; $4^+ \rightarrow 2^+$) $e^2fm^4$** | **Value Type** | **Reference** |
|---|---|---|
| 683.0 | SM | S. D. Bianco *et al.* in [BLIA+13] |
| 399.4 | $\alpha$-cluster | S. M. Wang *et al.* in [WPX13] |
| 520.0 | SM | A. Gargano *et al.* in [ASB+17] |
| 480.0 | SM | B. Brown *et al.* in [ASB+17] |
| 330.0 | SM | N. Shimizu *et al.* in [SOMH04] |

**Table 6.10: Theoretical B(E2) strength of B(E2; $4^+ \rightarrow 2^+$) in $^{136}$Te.**] - Summary table of the theoretical B(E2) values from the first $4^+$ to the first $2^+$ state in $^{136}$Te, B(E2; $4^+ \rightarrow 2^+$).

## 6.4 Discussion of lifetime values

The lifetimes of excited states in $^{136}$Te were measured in this work using the $^{241}$Pu target to avoid the presence of long-lived partners that may shadow the result. The lifetime values derived provide information about the origin of collectivity in $^{136}$Te, especially the values for the first $2^+$ and $4^+$ states. In addition, the $2^+$ state was of special interest because of the unexpected low value of the measured B(E2) strength, a sign of an anomalous behaviour, although discrepant values exist in the literature. Table 6.11 summarizes the B(E2) strengths derived in this PhD thesis from the lifetimes of the first $2^+$, $4^+$, $6^+$ and $8^+$ states in $^{136}$Te.

| **J$_i$** | **J$_f$** | **B(E2; J$_i$ →J$_f$)** (e$^2$fm$^4$) | **B(E2; J$_i$ →J$_f$)** (W.u) | $\tau$ (ps) |
|---|---|---|---|---|
| $2_1^+$ | $0_{g.s}^+$ | 290(70) | 7.0(16) | 34(8) |
| $4_1^+$ | $2_1^+$ | 715(90) | 17.2(22) | 85(11) |
| $6_1^+$ | $4_1^+$ | 628(60) | 15.1(14) | 238(22) |
| $8_1^+$ | $6_1^+$ | >255 | ≥6.1 | ≤14 |

**Table 6.11: Summary table of the B(E2) strengths derived from the lifetimes of the $2^+$, $4^+$, $6^+$ and $8^+$ states in $^{136}$Te.** - Summary table of the B(E2) strength of $^{136}$Te derived from the measured lifetimes in the present work. The table provides the values of the yrast band from the first $2^+$ to the $8^+$ state.

Concerning the $2_1^+$ state in $^{136}$Te, a lifetime of $\tau_{2+}$=34(8) ps has been measured in this PhD thesis with a direct electronic method, with a of B(E2;$2^+ \rightarrow 0^+$)=290(70) e$^2 fm^4$. This new experimental value points towards shorter lifetimes, in line with recent measurements of Allmond et al. [ASB$^+$17]. Table 6.12 summarises the existing experimental values of $2_1^+$ state lifetime and compares them with certain theoretical values. Despite the existence of several theoretical values for the $2_1^+$ state, the table only gathers the calculations that provide transition rates up to the $8_1^+$ state.

which are available till the $8^+$ state. The table also includes the lifetime measured in this work.

| **Value type** | **B(E2; $2^+ \rightarrow 0^+$) $e^2fm^4$** | $\tau_{2^+}$ **(ps)** | **Reference** |
|---|---|---|---|
| Shell-model (TH) | 410 | 24 | A. Gargano *et al.* [ASB+17] |
| Shell-model (TH) | 479 | 21 | S. D. Bianco *et al.* [BLIA+13] |
| $\alpha$-Cluster (TH) | 287 | 35 | S.M. Wang *et al.* [WPX13] |
| CoulEX (Exp) | 208(29) | 48(5) | D. Radford *et al.* [RBB+02] |
| CoulEX (Exp) | 244(36) | 41(6) | M. Danchev *et al.* [DRP+11] |
| CoulEX (Exp) | 362(30) | 27.5(23) | J. Allmond *et al.* [ASB+17] |
| $\beta\gamma\gamma$(t) (Exp) | 245(50) | 43(9) | H.Mach & L.M. Fraile [F+08] |
| $\gamma\gamma\gamma$(t) (Exp) | **290(70)** | **34(8)** | Present work |

**Table 6.12: Lifetime values of the $2_1^+$ state in $^{136}$Te and related B(E2; $2^+ \rightarrow 0^+$) strength.** - Theoretical and experimental values of the $2_1^+$ lifetimes and the corresponding B(E2; $2^+ \rightarrow 0^+$) strength. The experimental lifetime presented here was obtained using the Compton correction implemented in this work. The table compares the experimental numbers with the Shell-model calculations from A. Gargano *et al.* [ASB+17] and S. D. Bianco *et al.* [BLIA+13] and the $\alpha$-cluster calculations from [WPX13].

The experimental values of B(E2)=290(70) $e^2fm^4$ from this work and B(E2)=362(30) $e^2fm^4$ from [ASB+17] fit better the systematic of the region and are at variance with the extremely low value of B(E2)=208(29) $e^2fm^4$ from [RBB+02]. However, they still indicate a certain anomaly, as they deviate from the systematics. The B(E2;$2^+ \rightarrow 0^+$) provided by the empirical Grodzins relation for $^{136}$Te is 865(152)$e^2fm^4$, which is far from the experimental values, a factor of 3 larger than 290(70) $e^2fm^4$ and a factor of 2.4 bigger than 362(30) $e^2fm^4$. Figure 6.38 presents the relation between the B(E2;$0^+ \rightarrow 2^+$)·E($2^+$) product and the atomic number (A) for the Sn, Te, Xe and Ba isotopes. The deformed Xe and Ba isotopes perfectly follow the Grodzins product rule, while the Te nuclei deviate as the number of neutrons increases.

The B(E2) systematic of the $^{132}$Sn region is presented in Figure 6.39. The plot includes the value derived in this work with a pink circle in the Te data set at N=84. It is visible that Te isotopes follow a similar trend than the Xe or Ba isotopes and the derived value of B(E2;$2^+ \rightarrow 0^+$)=290(70) $e^2fm^4$ fits better in the systematic.

Despite the fact that the results are limited by the precision of the measurements, the value presented here is in better agreement with the measurement from Allmond

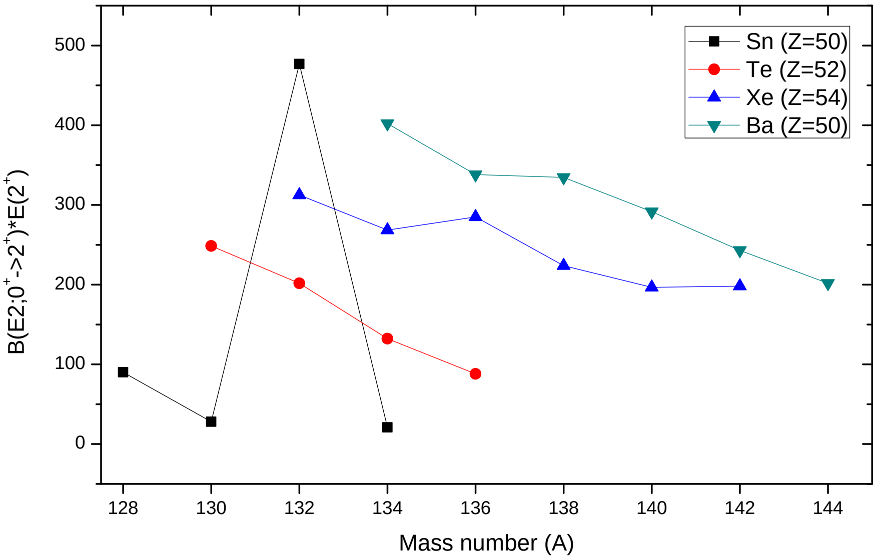

**Figure 6.38: Experimental product of B(E2; $0^+ \rightarrow 2^+$)·E($2^+$) as a function of the atomic mass (A).** - Experimental B(E2; $0^+ \rightarrow 2^+$)E($2^+$) product as a function of the atomic mass (A) for the Sn, Te, Xe and Ba isotopes. The plot gives a measure of the Grodzins product rule. All data points were obtained from [NND], apart from the last red circle at N=84 for the Te data set, which is the one derived in this P.h.D thesis.

and coworkers than previous CoulEx experiments [RBB$^+$02, DRP$^+$11] or former preliminary fast-timing results [F$^+$08], therefore, this measurement contributes to solve the experimental inconsistency.

Regarding the $^{136}$Te collectivity, the B(E2; $2^+ \rightarrow 0^+$) strength of 7.0(16) W.u in comparison with the B(E2) of 5.9(13) W.u from $^{132}$Sn indicates a low collective behaviour as expected, however the ratio of B(E2)$_{4^+ \rightarrow 2^+}$/B(E2)$_{2^+ \rightarrow 0^+}$=2.5 points to certain abnormality. The ratio for a pure rotational deformation would correspond to (10/7)=1.42, while for vibrational deformations it would be 2. The 5.9(13) W.u has been taken from [NND].

Figure 6.40 plots together all theoretical values available in the literature for the B(E2; $2^+ \rightarrow 0^+$) transition rate in $^{136}$Te. The plot represents the experimental value derived in this PhD thesis by a purple star including the error bars. The result of 290(70) $e^2fm^4$ is in relative good accord with most of the theoretical calculations as can be seen from Figure 6.40. Nevertheless, the values that are in the best agreement are those ones obtained with the $\alpha$-cluster model by Wang *et al.* [WPX13] and the Shell model calculations from B. Brown in [ASB$^+$17], A. Covello in [CCGI03] and

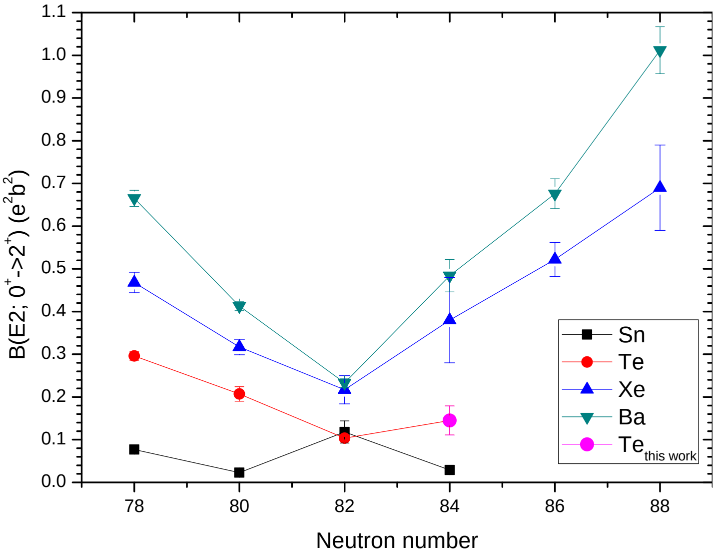

**Figure 6.39: B(E2; $0^+ \rightarrow 2^+$) systematics of exotic nuclei in the $^{132}$Sn region** - B(E2;$0^+ \rightarrow 2^+$) systematics of the exotic nuclei in the vicinity of the doubly magic $^{132}$Sn. The plot presents the Sn, Te, Xe and Ba isotopes as a function of the neutron number (N). The data points were obtained from [NND], while circle in pink at N=84 corresponds to the value derived in this work, and the rest of the points were

N. Shimizu [SOMH04]. One should note that the most recent version of the Shell model calculations of A. Covello corresponds to the calculation from A.Gargano et al. in [ASB+17], which yield 410 $e^2fm^4$. The quasiparticle random phase approximation (QRPA) from J. Terasaki et al. [TENS02] underestimates the value, while the QRPA calculations from A. P. Severyukhin et al. [SAPW14] are in better agreement. Looking at the new experimental value, it points towards a proton content on the wave function larger than previously thought.

From the wave functions decomposition in the SM calculations of B. Brown et al. [ASB+17], it can be learnt that the $2^+$ wavefunction is dominated by excited valence neutron configurations following $J_n$=2, $J_p$ =0 as the leading component with 60%, $J_n$=0, $J_p$=2 as the next leading term with 16% and the rest of the terms less than 10% [ASB+17]. A similar statement is made by the Montecarlo Shell model calculations (MCSM) in [SOMH04], which discusses that the probability of the $J_n$=2, $J_p$=0 component in the $2^+$ wavefunction is a factor of 4 larger than the probability of $J_n$=0, $J_p$=2. This proton-neutron asymmetry in the composition of the $2^+$ wavefunction decreases the coherence between protons and neutrons in the E2 transition yielding a

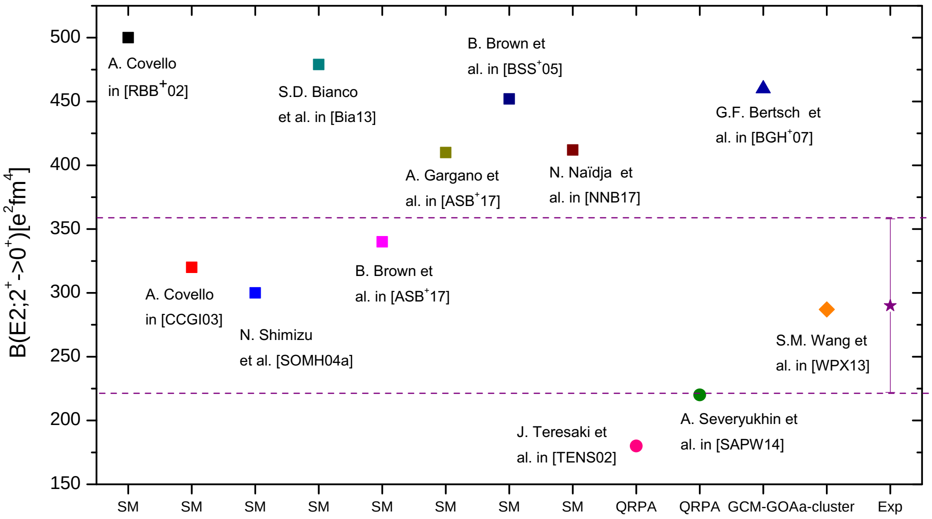

**Figure 6.40: Theoretical B(E2; $2^+ \rightarrow 0^+$) strengths of $^{136}$Te** - Theoretical B(E2;$2^+ \rightarrow 0^+$) strengths of the $^{136}$Te calculated using different models and interactions. The X axis indicates the type of calculation (SM, QRPA, $\alpha$-Cluster, etc) and the Y axis the calculated B(E2; $2^+ \rightarrow 0^+$) in e$^2$fm$^4$. Every data point is labelled with the related reference. The purple star that includes error bars, is the experimental value of 290(70) e$^2$fm$^4$ measured in this thesis.

weaker B(E2). Moreover, the neutron domination makes the B(E2) strength smaller because of the small neutron effective charge (0.6e). This asymmetry in the composition may be explained as a result of a reduction in the proton-neutron interaction. The fact that the experimental B(E2; $2^+ \rightarrow 0^+$) value is larger than earlier reported values points to a larger contribution of proton configuration to the $2^+$ state wave function.

Concerning the lifetime of the $4^+$ state, this PhD thesis reports a lifetime of $\tau_{4^+}$=85(11) ps and a related B(E2) strength of B(E2; $4^+ \rightarrow 2^+$)=715(90) e$^2 fm^4$. Table 6.13 gathers the corresponding experimental values of $4^+$ state lifetime and compares them with theoretical values available in the literature. The reported lifetime is consistent with the only former experimental value of $\tau_{4^+}$=100(15) ps derived from B(E2) measurements [ASB$^+$17]. Our new measurement seems to be rather well reproduced by the available shell-model calculations from S.D. Bianco [BLIA$^+$13] and A. Gargano [ASB$^+$17]. In this case, the $\alpha$-cluster model overestimates the lifetime by a factor of 2, which is difficult to reconcile with the good agreement obtained for the $2^+$ level lifetime. Similar situation happens with the MCSM model from [SOMH04].

From the wave function decomposition of the $4^+$ wavefunction in the SM calculations of A. Gargano et al. [ASB$^+$17], it can be understood that the leading component is 32% of $J_n$=4, $J_p$=0 and 42% of $J_n$=2, $J_p$=0. Therefore, the role of neutron pairs is enhanced with respect to the $2^+$ state.

| **Value type** | **B(E2; $4^+ \rightarrow 2^+$) $e^2fm^4$** | $\tau_{4^+}$ **(ps)** | **Reference** |
|---|---|---|---|
| SM (TH) | 520 | 116 | A. Gargano *et al.* [ASB$^+$17] |
| SM (TH) | 683 | 89 | S. D. Bianco *et al.* [BLIA$^+$13] |
| SM (TH) | 480 | 126 | B. Brown *et al.* [ASB$^+$17] |
| MCSM (TH) | 330 | 183 | N. Shimizu *et al.* [SOMH04] |
| $\alpha$-Cluster (TH) | 399 | 152 | S.M. Wang *et al.* [WPX13] |
| CoulEX (Exp) | 600(90) | 100(15) | J. Allmond *et al.* [ASB$^+$17] |
| $\gamma\gamma\gamma$ (Exp) | 715(90) | **85(11)** | **Present work** |

**Table 6.13: Lifetime values of the $4_1^+$ state in $^{136}$Te and related B(E2; $4^+ \rightarrow 2^+$) strength.** - Theoretical and experimental values of the $4_1^+$ state lifetimes and the related B(E2; $4^+ \rightarrow 2^+$) strength. The experimental value was obtained by using the Compton correction implemented in this work. The table compares the experimental number with Shell-model calculations from A. Gargano *et al.* [ASB$^+$17] and S. D. Bianco *et al.* [BLIA$^+$13], the $\alpha$-Cluster calculations from [WPX13] and Monte Carlo SM by N. Shimizu and coworkers [SOMH04].

| **Value type** | **B(E2; $6^+ \rightarrow 4^+$) $e^2fm^4$** | $\tau_{6^+}$ **(ps)** | **Reference** |
|---|---|---|---|
| Shell-model (TH) | 360 | 416 | A. Gargano *et al.* [ASB$^+$17] |
| Shell-model (TH) | 613 | 244 | S. D. Bianco *et al.* [BLIA$^+$13] |
| $\alpha$-Cluster (TH) | 416 | 360 | S.M. Wang *et al.* [WPX13] |
| Fast-timing (Exp) | 628(60) | 238(22) | Present work |

**Table 6.14: Lifetime values of the $6_1^+$ state in $^{136}$Te and related B(E2; $6^+ \rightarrow 4^+$) strength** - Theoretical and experimental values of the $6_1^+$ state lifetimes and the related B(E2; $6^+ \rightarrow 4^+$) strength. The table compares the experimental number from the present work with the Shell-model calculations from A. Gargano *et al.* [ASB$^+$17] and S. D. Bianco *et al.* [BLIA$^+$13] and the $\alpha$-Cluster calculations from [WPX13].

Regarding the new measurement for the $6^+$ state, a long lifetime of $\tau_{6^+}$=238(22) ps is measured by centroid shift in this work. This can be expected from a similar configuration of the wave function than the $4^+$ state, and the lower energy of the 353-keV de-exciting transition, which for a similar B(E2) transition rate would yield a meanlife of ∼190 ps. Shell model calculations (Table 6.14) are consistent with this description, although Gargano *et al.* predict a lower B(E2; $6^+ \rightarrow 4^+$) rate compared to the number for B(E2; $4^+ \rightarrow 2^+$), which does seem to be consistent with our results.

Finally, the $8^+$ lifetime is also measured here for the first time. It has a very short lifetime, at the limit of our technique, and it is rather successfully reproduced by theory.

| **Value type** | **B(E2; $8^+ \rightarrow 6^+$) $e^2fm^4$** | $\tau_{8^+}$ **(ps)** | **Reference** |
|---|---|---|---|
| Shell-model (TH) | 300 | 12 | A. Gargano *et al.* [ASB$^+$17] |
| Shell-model (TH) | 535 | 6 | S. D. Bianco *et al.* [BLIA$^+$13] |
| $\alpha$-Cluster (TH) | 397 | 9 | S.M. Wang *et al.* [WPX13] |
| **Fast-timing (Exp)** | **≥255** | **≤14** | **Present work** |

**Table 6.15: Lifetime values of the $8_1^+$ state in $^{136}$Te and related B(E2; $8^+ \rightarrow 6^+$) strength** - Theoretical and experimental values of the $8_1^+$ state lifetimes and the related B(E2; $8^+ \rightarrow 6^+$) strength. The table compares the experimental values from the present work with the Shell-model calculations from A. Gargano *et al.* [ASB$^+$17] and S. D. Bianco *et al.* [BLIA$^+$13] and the $\alpha$-Cluster calculations from [WPX13].

In summary, we have produced a complete set of B(E2) transition rates in the $^{136}$Te ground state band by direct measurements of the levels lifetimes. The new $2^+$ lifetime value points towards long proton content in the wave function, while the lifetime of higher states are compatible with contributions by larger number of neutron pairs.

# Conclusions and Outlook

Lifetime measurements of excited states are a powerful tool to study the atomic nucleus because they provide direct and model independent access to the reduced transition probabilities. Transition rates provide interesting information for the study of single-particle configurations, nuclear collectivity and allow to test theoretical models. Among the different regions in the Segré chart, exotic nuclei around the $^{132}$Sn draw particular attention because of the sudden modifications of the shell structure and the collective behaviour that arises. The $^{136}$Te with two protons and two neutrons coupled to the doubly-magic $^{132}$Sn (Z=50 and N=82) is a good candidate to study this region, and so it is investigated in this PhD thesis through the lifetime measurements of its excited states.

Among the different experimental techniques for lifetime measurements, fast-timing methods are the best suited for lifetimes of few nanoseconds down to tens of picoseconds, which is the range of interest in this PhD thesis. Fast-timing methods make use of fast coincidences between the radiation populating a nuclear level and de-exciting it. They are based on coincidences between fast scintillators such as $\mathrm{LaBr_3(Ce)}$, gated by HPGe detectors. Their sensitivity is directly determined by the time resolution of the setup in use, where the main contribution comes from the $\mathrm{LaBr_3(Ce)}$ detector. Therefore, to obtain the maximum sensibility, it is of key relevance to optimize the time resolution of the setup. For this reason, this PhD thesis presents an in-depth characterization of a standard fast-timing setup and explains in detail the optimization procedure for several $\mathrm{LaBr_3(Ce)}$ crystals of different shapes and sizes. Excellent time resolution has been obtained using a fast photomultiplier (Hamamatsu R9779) and analog electronics for signal processing. The crystal characterization work was partially motivated by the design and construction of a large $\mathrm{LaBr_3(Ce)}$ arrays, which are the evolution of the standard fast-timing setups.

# CONCLUSIONS AND OUTLOOK

The most important requirements of a highly performing $LaBr_3$(Ce) array are good time and energy resolution in addition to modular and flexible geometry. To this aim two innovative geometries of $LaBr_3$(Ce) crystals were designed and characterized.

The excited structure of $^{136}$Te has been investigated via fast-timing methods. The data on $^{136}$Te were obtained from the EXILL-FATIMA campaign at ILL, populating this nucleus in neutron induced fission. It was the first time that a hybrid spectrometer composed of a large $LaBr_3$(Ce) array was coupled to a highly-efficient HPGe array to measure picosecond to nanosecond lifetimes.

The main conclusions of the PhD thesis can be divided in two blocks. The first block is related to the characterisation and optimization of the time response of fast $LaBr_3$(Ce)-based scintillator detectors and they are listed below:

- We have characterized standard cylindrical $LaBr_3$(Ce) crystals of 1 inch in height and 1 inch in diameter, and two newly designed $LaBr_3$(Ce) crystals with the shape of a truncated cone and of a hybrid conical and cylindrical shape, respectively. The crystals were coupled to a fast photomultiplier tube, model R9779 from Hamamatsu and signals were acquired with the help of analogue electronic modules. An iterative procedure was designed to optimize the PMT bias voltage and the CFD external delay and zero crossing (Z), in order to achieve the best possible time resolution.

- We have found the optimal parameters for cylindrical $LaBr_3$(Ce) crystals 1 inch in height and 1 inch in diameter. The time resolution given as the FWHM for the time distribution for a single crystal reaches 98±2 ps at $^{60}$Co energies, the best value to date for this type of crystal.

- We have investigated the dependence of the time resolution with respect to the Ce doping for cylindrical $LaBr_3$(Ce) crystals 1 inch in height and 1 inch in diameter with 5%, 8% and 10% doping concentration. Unexpectedly the best time resolution is achieved for the crystal with 8% of Ce, which could be attributed to inhomogeneities in the Ce distribution of 10% doping crystal at the time it was manufactured.

- We have assessed other spectroscopic features, such as time walk, energy resolution, linearity and efficiency, and ensured that they are suitable for using these crystals for fast timing measurements.
- We have optimized the electronics parameters for the conical and hybrid detectors, and obtained the best time resolutions reported for these crystals at $^{60}$Co and $^{22}$Na energies, namely 110±3 ps and 111±3 ps, and 158±3 and 160±3 ps, respectively.
- In spite of the good time resolution of the hybrid $\mathrm{LaBr_3(Ce)}$ crystal it is found that this detector is not suitable for fast-timing measurements since it shows a strong deterioration of the time resolution and walk as a function of the external delay and double peaks in the energy spectrum. This effect may arise from optical photon reflections in the inner cylindrical and conical surfaces.
- Instead, the truncated cone $\mathrm{LaBr_3(Ce)}$ crystal is very well suited for fast-timing applications since it has excellent time response while maintaining good energy resolution. Its geometrical design makes it possible to densely pack several detectors in rings or other arrangements with sufficient efficiency to construct high sensitivity $\mathrm{LaBr_3(Ce)}$ fast-timing arrays.

The second block deals with the experimental analysis of the $^{136}$Te data. Successful experiments have been performed at ILL to investigate exotic nuclei populated in neutron-induced fission by using EXILL-FATIMA, a hybrid array combining the strengths of the fast-timing array FATIMA and the high resolution HPGe-clovers array EXOGAM. As a consequence of the large amount of $\gamma$-emitting nuclei produced in the fission process, a high level of Compton background is present unearth the full-energy peaks (FEPs) in the energy spectra, and consequently it is selected when setting energy gates contributing to the total time spectra.The main conclusions of this block are listed below:

- To reduced the background contribution we have explored different strategies for data analysis and selected the best one. We have found that subtracting to the fast-timing matrices the events that are in coincidences with the background underneath the Ge-gated peaks results crucial for reducing the Compton contribution. The peak-to-background ratios defined here as (P/B)=$A_{FEP}/A_{Bkg}$

improves by more than a factor 6 and in some cases up to a factor of 18. This background-reduction approach prevents from the contribution of contaminants or fission partners whose Compton edge sits underneath the Ge-gated peaks, and hence, appear in coincidences.

- We have defined and implemented a new method of timing corrections that fully takes into account the effect of Compton background continuum under full-energy peaks, and explored its impact in timing measurements within the EXILL-FATIMA campaign. We have found that the previous-existing procedure, coined here as Compton correction at first order does not totally correct the Compton contribution, very frequently it yields shorter lifetimes than applying the full correction.
- Taking advantage of the $^{100}$Zr nucleus, which comes as a contaminant, the Compton correction procedure developed in this work was tested and validated by measuring its lifetimes, which had already been measured and published. We report a lifetime of $\tau_{4^+}$=31(8) ps for the $4_1^+$ state, which is in agreement with the published value $\tau_{4^+}$=37(4) ps by S. Ansari et al. in [ARJ$^+$17] and at variance with $\tau_{4^+}$=54(4) ps published by A. G. Smith and coworkers in [SWP$^+$02].
- We have applied these methods to the investigation of the lifetimes of the $^{136}$Te yrast rotational band.
- The direct measurement of $\tau_{2^+}$=34(8) ps and the B(E2; $2^+ \rightarrow 0^+$)=290(70) e$^2$fm$^4$ contributes to solve the existing experimental inconsistency. It points towards shorter lifetimes values, being in better agreement with $\tau_{2^+}$=27.5(23) ps from J. M. Allmond et al. in [ASB$^+$17] than previous measurements from CoulEX experiments [RBB$^+$02, DRP$^+$11] or preliminary fast-timing studies [F$^+$08]. The B(E2; $2^+ \rightarrow 0^+$)=290(70) e$^2$fm$^4$ strengh is at variance with the low value of B(E2; $2^+ \rightarrow 0^+$)=208(29) e$^2$fm$^4$ reported by Radford and coworkers in [RBB$^+$02], and fits better the systematic of the region. However, the new value still points to certain abnormality as it does not follow the Grodzins product rule. We compared our experimental results with state-of-the-art shell model calculations, which helps the interpretation of the structure of $^{136}$Te. Among the multiple theoretical values that exist for the lifetime of the $2^+$ state. Our experimental

value of $\tau_{2^+}$=34(8) ps is in best agreement with the Shell-model values from by S. D. Bianco and coworkers in [BLIA$^+$13] and N. Shimizu et al. in [SOMH04] and with the $\alpha$-cluster model from [WPX13]. The higher B(E2) points towards a higher proton contribution of the first $2^+$ in $^{136}$Te with respect to previous assessment.

- We have measured the lifetime of the $4^+$ state, $\tau_{4^+}$=85(11) ps, and found it is in agreement with the previously reported value $\tau_{4^+}$=100(15) ps from J. M. Allmond and coworkers [ASB$^+$17].
- The lifetimes of the $6^+$ and $8^+$ states were measured here for the first time yielding $\tau_{6^+}$=238(22) ps and $\tau_{8^+}$ =≤14 ps respectively.
- Most of the theoretical calculations have difficulties in simultaneously explaining the depleted B(E2; $2^+_1 \rightarrow 0^+_{g.s}$) value and the measured B(E2) rates for the other states.

New designs of LaBr$_3$(Ce) crystals and the optimization of signal processing are able to take fast-timing detectors to new levels of sensitivity and time resolution. These detectors can be used in large detector arrays, such as FATIMA at the ILL, where fast-timing experiments on nuclei produced by neutron-induced fission were performed for the first time. The quality of the data and the spectroscopic capabilities of the hybrid EXILL-FATIMA apparatus has made it possible to analyze a complex set of data and measure level lifetimes of exotic nuclei such as $^{136}$Te. This work can be extended by the study of neighbouring $^{137}$Te and possibly $^{138}$Te, where the B(E2; $2^+ \rightarrow 0^+$) transition rate would provide key information for the understanding of the Te anomaly. Lifetime limits could be assessed in the decay of the predicted $2^+_{ms}$ mixed symmetry state in $^{136}$Te. In the future it is expected that this type of measurements will be performed at many large-scale facilities worldwide and that they will contribute to our understanding of nuclear structure far from the stability line.

# List of Figures

1.1 Empirical Grodzins rule for even-even nuclei. . . . . . . . . . . . . . . . . 16

1.2 Excitation energy of the first $2^+$ states in the $^{132}$Sn region. . . . . . . . 18

1.3 Structural evolution in regard to the $R_{4/2}$ ratio. . . . . . . . . . . . . . . . 19

2.1 Time distributions of long-lived and a short-lived states. . . . . . . . . . 24

2.2 Examples of delayed and anti-delayed time spectra. . . . . . . . . . . . . 27

3.1 Simplified block diagram of the ORTEC 935 CFD operation. . . . . . . 41

3.2 Working principle of the Constant Fraction Discriminator. . . . . . . . . 42

3.3 Test bench for crystal characterization. . . . . . . . . . . . . . . . . . . . . 45

3.4 Anode pulse of Crystal *A* coupled to Hamamatsu R9779 PMT. . . . . . 48

3.5 Truncated cone $LaBr_3$(Ce) crystal. . . . . . . . . . . . . . . . . . . . . . . 49

3.6 Hybrid $LaBr_3$(Ce) crystal. . . . . . . . . . . . . . . . . . . . . . . . . . . . 50

3.7 Relative energy resolution of Crystal *B* as a function of the energy. . . . 51

3.8 Functional relation between the peak position and the $\gamma$-ray energy that illustrates the detector linearity. . . . . . . . . . . . . . . . . . . . . . . . 53

3.9 Full-energy peak detection efficiency of a 1-in cylindrical crystal. . . . . 54

3.10 Time resolution of 1-in. $LaBr_3$(Ce) detector at 511 keV. . . . . . . . . . 56

3.11 Time resolution of 1-in $LaBr_3$(Ce) detector at $^{60}$Co energies. . . . . . . . 56

3.12 Time resolution of Crystals *A*, *B* and *C* as a function of the CFD external delay at $^{60}$Co energies. . . . . . . . . . . . . . . . . . . . . . . . . . . 57

3.13 Time resolution of Crystal *B* as a function of the CFD external delay at $^{60}$Co energies. . . . . . . . . . . . . . . . . . . . . . . . . . . . . . . . . . 58

3.14 Compton time walk of Crystal *A*. . . . . . . . . . . . . . . . . . . . . . . . 60

3.15 Compton time walk of Crystal *B*. . . . . . . . . . . . . . . . . . . . . . . . 61

3.16 Energy spectra of $^{137}$Cs measured with the truncated cone, the hybrid-tapered and the standard LaBr$_3$(Ce) detectors. . . . . . . . . . . . . . . 63
3.17 Absolute photopeak efficiencies of the truncated cone and hybrid-tapered LaBr$_3$(Ce) detectors. . . . . . . . . . . . . . . . . . . . . . . . . . . . . . 64
3.18 Time resolution of the truncated cone crystal as a function of the CFD external delay for $^{60}$Co and 511 keV energies. . . . . . . . . . . . . . . . 65
3.19 Time spectrum of the conical crystal vs. the reference detector at $^{60}$Co energies. . . . . . . . . . . . . . . . . . . . . . . . . . . . . . . . . . . . . 66
3.20 Time spectrum of the conical crystal vs. the reference detector at 511 keV ($^{22}$Na). . . . . . . . . . . . . . . . . . . . . . . . . . . . . . . . . . . . . 66
3.21 Time resolution of the hybrid-tapered crystal as a function of the CFD external delay for $^{60}$Co and 511 keV energies. . . . . . . . . . . . . . . . 68
3.22 Time spectra of the hybrid LaBr$_3$(Ce) at $^{60}$Co energies for different CFD delays. . . . . . . . . . . . . . . . . . . . . . . . . . . . . . . . . . . . . 69
3.23 FWHM time resolution as a function of the CFD external delay at $^{60}$Co energies. . . . . . . . . . . . . . . . . . . . . . . . . . . . . . . . . . . . . 70
3.24 FWHM time resolution as a function of the CFD external delay at 511 keV ($^{22}$Na) . . . . . . . . . . . . . . . . . . . . . . . . . . . . . . . . . 71
3.25 Compton time walk of conical and tapered crystals coupled to the Hamamatsu R9779 PMT. . . . . . . . . . . . . . . . . . . . . . . . . . . . . 73
3.26 Compton time walk of the conical crystal for different Z values. . . . . . 74

4.1 Nuclear reactor of the institute Laue-Langevin (ILL). . . . . . . . . . . . 80
4.2 Schematics of the nuclear reactor of ILL. . . . . . . . . . . . . . . . . . . . 81
4.3 Schematic layout of the collimation system placed at the H113 neutron guide. . . . . . . . . . . . . . . . . . . . . . . . . . . . . . . . . . . . . . . 82
4.4 Schematic layout of the target chamber. . . . . . . . . . . . . . . . . . . 83
4.5 Schematic view of the target chamber structure showing the two operating configurations. . . . . . . . . . . . . . . . . . . . . . . . . . . . . . . . 84
4.6 Hybrid spectrometer developed for the EXILL-FATIMA experiment. . . 85
4.7 Setup picture of the target area. . . . . . . . . . . . . . . . . . . . . . . 86
4.8 Schematic view of the different Ge detectors employed during the EXILL-FATIMA campaign and their placement. . . . . . . . . . . . . . . . . . . 87

4.9 Schematic layout of the EXILL-FATIMA spectrometer and the employed detectors. . . . . . . . . . . . . . . . . . . . . . . . . . . . . . . . . . 89
4.10 Electronics scheme of the FATIMA branch of the hybrid spectrometer. . 91
4.11 Simplified electronics scheme of the FATIMA branch. . . . . . . . . . . . 92

5.1 Time-stamps offsets. . . . . . . . . . . . . . . . . . . . . . . . . . . . 95
5.2 Multiplicity Matrix. . . . . . . . . . . . . . . . . . . . . . . . . . . . 96
5.3 Detectors drifts. . . . . . . . . . . . . . . . . . . . . . . . . . . . . . 97
5.4 Coincident HPGe-Clover spectra that illustrate the add-back reconstruction. . . . . . . . . . . . . . . . . . . . . . . . . . . . . . . . . . . 111
5.5 Coincident $LaBr_3$(Ce) spectra illustrating the add-back reconstruction procedure. . . . . . . . . . . . . . . . . . . . . . . . . . . . . . . . 111
5.6 Partial level scheme of $^{136}$Te. . . . . . . . . . . . . . . . . . . . . . . 112
5.7 HPGe-Clover spectrum non-gated. . . . . . . . . . . . . . . . . . . . . . 113
5.8 Coincident HPGe spectra that illustrate the effect of background subtraction under the FEP peaks in the HPGe-clovers. . . . . . . . . . . . . 114
5.9 Coincident $LaBr_3$(Ce) spectra that show the effect of the background subtraction under the gated peaks on the HPGe-clovers. . . . . . . . . . 115
5.10 Coincident $LaBr_3$(Ce) spectra that display the effect of the background subtraction under the gated peaks on the HPGe-clovers. . . . . . . . . . 116
5.11 Coincident HPGe energy spectrum gated in the 750- and 353-keV $\gamma$-transitions. . . . . . . . . . . . . . . . . . . . . . . . . . . . . . . . . 120
5.12 Coincident HPGe-Clover and $LaBr_3$(Ce) spectra gated in the 607- and 353-keV transitions. . . . . . . . . . . . . . . . . . . . . . . . . . . 121
5.13 Delayed and anti-delayed time distributions of the $4^+$ state in $^{136}$Te. . . 123
5.14 Coincident HPGe-Clover spectrum gated by the 607 and 423-keV $\gamma$-ray 125
5.15 Coincident HPGe spectrum gated in the 607- and 353-keV $\gamma$-rays. . . . 125
5.16 Coincident HPGe and $LaBr_3$(Ce) spectra gated in the 607- and 353-keV $\gamma$-transitions. . . . . . . . . . . . . . . . . . . . . . . . . . . . . . . . 126
5.17 Coincident HPGe and $LaBr_3$(Ce) spectra gated in the 607- and 423-keV $\gamma$-transitions. . . . . . . . . . . . . . . . . . . . . . . . . . . . . . . . 127
5.18 Delayed and anti-delayed time distributions of the $4_1^+$ state in $^{136}$Te. . . 127
5.19 Partial level scheme of $^{152}$Gd. . . . . . . . . . . . . . . . . . . . . . . 131

5.20 Coincident $LaBr_3(Ce)$ spectrum of $^{152}$Gd gated by the 344-keV transition. 132
5.21 Partial level scheme of $^{152}$Sm. . . . . . . . . . . . . . . . . . . . . . . . 133
5.22 $LaBr_3(Ce)$ spectrum of $^{152}$Sm in coincidence with the 244- and 122-keV $\gamma$-transitions. . . . . . . . . . . . . . . . . . . . . . . . . . . . . . . . . . . 134
5.23 PRD curve for the analysis of the EXILL-FATIMA experiment. . . . . . 136
5.24 Compton Response Distributions, Start and Stop, measured using an external $^{60}$Co source . . . . . . . . . . . . . . . . . . . . . . . . . . . . 139
5.25 Compton Response Distributions measured using an external $^{60}$Co source. 140
5.26 Coincident HPGe and $LaBr_3(Ce)$ spectra gated in the 607- and 353-keV $\gamma$-ray for the selection of the background regions. . . . . . . . . . . . . . 141
5.27 Delayed and anti-delayed Compton Response Distribution measured with the 353-keV $\gamma$-ray taken as reference. . . . . . . . . . . . . . . . . . . . . . 142
5.28 Internal Compton Response Distribution, $CRD_{feeder}$, for the lifetime measurement of the $4^+$ state. . . . . . . . . . . . . . . . . . . . . . . . . . 143
5.29 Compton-Compton Start and Stop response distribution, for the data analysis of the EXILL-FATIMA experiment. . . . . . . . . . . . . . . . . . 144
5.30 Compton-Compton Response Distribution, CCRD. . . . . . . . . . . . . 145
5.31 Partial level scheme of $^{100}$Zr . . . . . . . . . . . . . . . . . . . . . . . . 152
5.32 Coincident $LaBr_3(Ce)$ spectra Ge-gated by the 212-keV transition and $LaBr_3(Ce)$-gated by the 497-keV $\gamma$-ray . . . . . . . . . . . . . . . . . . . . 153
5.33 Delayed and anti-delayed time distributions to measure the lifetime of the $4^+$ state in $^{100}$Zr. . . . . . . . . . . . . . . . . . . . . . . . . . . . . . 154

6.1 B(E2; $0^+ \rightarrow 2^+$) systematics of exotic nuclei in the $^{132}$Sn region . . . . . 160
6.2 Partial $^{136}$Te level scheme that show the g.s. yrast rotational band. . . . 161
6.3 Coincident HPGe spectrum Ge-gated by the 423- and 352-keV $\gamma$-transitions. 163
6.4 Coincident HPGe spectrum Ge-gated by the 750- and 353-keV $\gamma$-transitions. 163
6.5 Coincident HPGe-Clover and $LaBr_3(Ce)$ spectra gated by the 353- and 607-keV transition. . . . . . . . . . . . . . . . . . . . . . . . . . . . . . . . 166
6.6 Coincident HPGe-Clover and $LaBr_3(Ce)$ spectra gated by the 353- and 423-keV transition. . . . . . . . . . . . . . . . . . . . . . . . . . . . . . . . 166
6.7 Delayed and anti-delayed time distributions to derive the lifetime of the $2_1^+$ state in $^{136}$Te. . . . . . . . . . . . . . . . . . . . . . . . . . . . . . . 167

6.8 Delayed and anti-delayed time distributions to derive the lifetime of the $2_1^+$ state in $^{136}$Te . . . . . . . . . . . . . . . . . . . . . . . . . . . . . . 168
6.9 Coincident LaBr$_3$(Ce) spectra to derive the lifetime of the $2_1^+$ state in $^{136}$Te. . . . . . . . . . . . . . . . . . . . . . . . . . . . . . . . . . . . 169
6.10 Prompt Response Distribution PRD. . . . . . . . . . . . . . . . . . . . . . 170
6.11 Compton response distribution ($CRD_{decay}$). . . . . . . . . . . . . . . . 171
6.12 Compton response distribution (CRD$_{feeder}$). . . . . . . . . . . . . . . . 172
6.13 Compton-Compton response distribution (CCRD). . . . . . . . . . . . 174
6.14 Coincident LaBr$_3$(Ce) spectra to measure the lifetime of the $2_1^+$ state in $^{136}$Te. . . . . . . . . . . . . . . . . . . . . . . . . . . . . . . . . . . . 176
6.15 Delayed and anti-delayed time distributions for deriving the lifetime of $2_1^+$ state in $^{136}$Te. . . . . . . . . . . . . . . . . . . . . . . . . . . . . . 177
6.16 Coincident HPGe spectrum Ge-gated by the 750- and 352-keV $\gamma$-rays. . 179
6.17 Delayed and anti-delayed time distributions for the lifetime measurement of the $4_1^+$ state in $^{136}$Te using the add-back reconstruction procedure. . . 180
6.18 Delayed and anti-delayed time distributions for the lifetime measurement of the $4_1^+$ state in $^{136}$Te using the Ge-background subtraction approach. 181
6.19 Coincident LaBr$_3$(Ce) spectra to derive the lifetime of the $4_1^+$ state in $^{136}$Te. . . . . . . . . . . . . . . . . . . . . . . . . . . . . . . . . . . . 181
6.20 Prompt Response Distribution PRD. . . . . . . . . . . . . . . . . . . . . . 182
6.21 Compton-Compton Response Distribution, CCRD. . . . . . . . . . . . . 182
6.22 Prompt Response Distribution PRD. . . . . . . . . . . . . . . . . . . . . . 184
6.23 Compton-Compton Response Distribution, CCRD. . . . . . . . . . . . . 184
6.24 Delayed and anti-delayed time distributions for the lifetime measurement of the $6_1^+$ state in $^{136}$Te. . . . . . . . . . . . . . . . . . . . . . . . . . 186
6.25 Delayed and anti-delayed time distributions for the lifetime measurement of the $6_1^+$ state in $^{136}$Te. . . . . . . . . . . . . . . . . . . . . . . . . . 186
6.26 Coincident LaBr$_3$(Ce) spectra to measure the lifetime of the $6_1^+$ state in $^{136}$Te. . . . . . . . . . . . . . . . . . . . . . . . . . . . . . . . . . . . 187
6.27 Delayed and anti-delayed time distributions for the lifetime measurement of the $6_1^+$ state in $^{136}$Te. . . . . . . . . . . . . . . . . . . . . . . . . . 188
6.28 Prompt Response Distribution PRD. . . . . . . . . . . . . . . . . . . . . . 189
6.29 Compton-Compton Response Distribution, CCRD. . . . . . . . . . . . . 190

6.30 Delayed and anti-delayed time distributions for the lifetime measurement of the $8_1^+$ state in $^{136}$Te using add-back reconstruction. . . . . . . . . . . 191
6.31 Delayed and anti-delayed time distributions for the lifetime measurement of the $8_1^+$ state in $^{136}$Te subtracting the Ge background. . . . . . . . . . 192
6.32 Coincident $LaBr_3$(Ce) spectrum Ge-gated by 750- and 353-keV transitions and $LaBr_3$(Ce)-gated by 607-keV $\gamma$-ray. . . . . . . . . . . . . . . . 194
6.33 Coincident $LaBr_3$(Ce) spectrum Ge-gated by 750- and 353-keV transitions and $LaBr_3$(Ce)-gated by 423-keV $\gamma$-ray. . . . . . . . . . . . . . . . 195
6.34 Delayed and anti-delayed time distributions for the lifetime measurement of the $2_1^+$ state in $^{136}$Te. . . . . . . . . . . . . . . . . . . . . . . . . . 196
6.35 Compton Response Distribution, $\mathrm{CRD}_{decay}$. . . . . . . . . . . . . . . . . 197
6.36 Compton Response Distribution, $\mathrm{CRD}_{decay}$. . . . . . . . . . . . . . . . . 197
6.37 Compton-Compton Response Distribution, CCRD. . . . . . . . . . . . . 198
6.38 Experimental product of B(E2; $0^+ \rightarrow 2^+$)·E($2^+$) as a function of the atomic mass (A) . . . . . . . . . . . . . . . . . . . . . . . . . . . . . 206
6.39 B(E2; $0^+ \rightarrow 2^+$) systematics of exotic nuclei in the $^{132}$Sn region . . . . . 207
6.40 Theoretical B(E2; $2^+ \rightarrow 0^+$) strengths of $^{136}$Te . . . . . . . . . . . . . . . 208

# List of Tables

3.1 Relative energy resolution of cylindrical crystals at 662 keV. . . . . . . . 52

3.2 Best time resolution values (FWHM) of Crystals A, B and C at $^{60}$Co and $^{22}$Na (511 keV) energies . . . . . . . . . . . . . . . . . . . . . . . . . . 55

3.3 Relative energy resolution (Er) of the conical and tapered detectors measured with the Hamamatsu R9779 and R6231 PMT models. . . . . . . . 62

3.4 Best time resolution values (FWHM) of the truncated cone and hybrid-tapered crystal at $^{60}$Co and $^{22}$Na (511 keV) energies. . . . . . . . . . . . 72

5.1 Double events. . . . . . . . . . . . . . . . . . . . . . . . . . . . . . . . . . 98

5.2 Triple events. . . . . . . . . . . . . . . . . . . . . . . . . . . . . . . . . . . 99

5.3 Quadruple events. . . . . . . . . . . . . . . . . . . . . . . . . . . . . . . 99

5.4 ID type Gate-configure file. . . . . . . . . . . . . . . . . . . . . . . . . 100

5.5 Detector type Gate-configure file. . . . . . . . . . . . . . . . . . . . . . 100

5.6 Add-back type Gate-configure file. . . . . . . . . . . . . . . . . . . . . . 101

5.7 Thermal neutron fission yields of the $^{241}$Pu target for Te. . . . . . . . . 106

5.8 Thermal neutron fission yields of the $^{235}$U target for Te. . . . . . . . . . 106

5.9 Fission partners of $^{136}$Te and $^{137}$Te. . . . . . . . . . . . . . . . . . . . . 107

5.10 Fission yields of the $^{136}$Te partners when using $^{241}$Pu and $^{235}$U targets. . 108

5.11 Excluded LaBr$_3$(Ce) combination. . . . . . . . . . . . . . . . . . . . . . 110

6.1 Experimental B(E2) strength values for the $2_1^+$ state in $^{136}$Te . . . . . . 159

6.2 Thermal neutron fission yields of the $^{241}$Pu and $^{235}$U targets for the $^{136}$Te nucleus and Te partners. . . . . . . . . . . . . . . . . . . . . . . . . . 162

6.3 Lifetime values of the first $2^+$ state in $^{136}$Te measured from triple-coincidence events using the $^{241}$Pu target. . . . . . . . . . . . . . . . . . 178

6.4 Lifetime values of the first $6^+$ state in $^{136}$Te measured from triple-coincidence events using the $^{241}$Pu target. . . . . . . . . . . . . . . . . . . 188
6.5 Lifetime values of the first $8^+$ state in $^{136}$Te measured from triple-coincidence events using the $^{241}$Pu target. . . . . . . . . . . . . . . . . . . 193
6.6 Theoretical B(E2) transition rates in $^{136}$Te by A. Gargano *et al.*. . . . . 200
6.7 Theoretical B(E2) transition rates in $^{136}$Te and derived level lifetimes by S. D. Bianco *et al.*. . . . . . . . . . . . . . . . . . . . . . . . . . . . . . 201
6.8 Theoretical B(E2) transition rates in $^{136}$Te calculated using the $\alpha$-cluster model and related level lifetimes. . . . . . . . . . . . . . . . . . . . . . . . 202
6.9 Theoretical B(E2) strength of B(E2; $2^+ \rightarrow 0^+$) in $^{136}$Te. . . . . . . . . . 203
6.10 Theoretical B(E2) strength of B(E2; $4^+ \rightarrow 2^+$) in $^{136}$Te. . . . . . . . . . 203
6.11 Summary table of the B(E2) strengths derived from the lifetimes of the $2^+$, $4^+$, $6^+$ and $8^+$ states in $^{136}$Te. . . . . . . . . . . . . . . . . . . . . . 204
6.12 Lifetime values of the $2_1^+$ state in $^{136}$Te and related B(E2; $2^+ \rightarrow 0^+$) strength. . . . . . . . . . . . . . . . . . . . . . . . . . . . . . . . . . . 205
6.13 Lifetime values of the $4_1^+$ state in $^{136}$Te and corresponding B(E2; $4^+ \rightarrow 2^+$) strength. . . . . . . . . . . . . . . . . . . . . . . . . . . . . . . . . . . 209
6.14 Lifetime values of the $6_1^+$ state in $^{136}$Te and corresponding B(E2; $6^+ \rightarrow 4^+$) strength . . . . . . . . . . . . . . . . . . . . . . . . . . . . . . . . . . 209
6.15 Lifetime values of the $8_1^+$ state in $^{136}$Te and related B(E2; $8^+ \rightarrow 6^+$) strength . . . . . . . . . . . . . . . . . . . . . . . . . . . . . . . . . . 210

# References

[ADH$^+$06] H. Abele, D. Dubbers, H. Häse, M. Klein, A. Knöpfler, M. Kreuz, T. Lauer, B. Markisch, D. Mund, V. Nesvizhevsky, A. Petoukhov, C. Schmidt, M. Schumann, and T. Soldner. Characterization of a ballistic supermirror neutron guide. *Nuclear Instruments and Methods in Physics Research Section A: Accelerators, Spectrometers, Detectors and Associated Equipment*, 562(1):407 – 417, 2006. 81

[ARJ$^+$17] S. Ansari, J.-M. Régis, J. Jolie, N. Saed-Samii, N. Warr, W. Korten, M. Zielińska, M.-D. Salsac, A. Blanc, M. Jentschel, U. Köster, P. Mutti, T. Soldner, G. S. Simpson, F. Drouet, A. Vancraeyenest, G. de France, E. Clément, O. Stezowski, C. A. Ur, W. Urban, P. H. Regan, Zs. Podolyák, C. Larijani, C. Townsley, R. Carroll, E. Wilson, H. Mach, L. M. Fraile, V. Paziy, B. Olaizola, V. Vedia, A. M. Bruce, O. J. Roberts, J. F. Smith, M. Scheck, T. Kröll, A.-L. Hartig, A. Ignatov, S. Ilieva, S. Lalkovski, N. Mărginean, T. Otsuka, N. Shimizu, T. Togashi, and Y. Tsunoda. Experimental study of the lifetime and phase transition in neutron-rich $^{98,100,102}$Zr. *Phys. Rev. C*, 96:054323, 2017. 135, 136, 147, 151, 152, 155, 156, 214

[ARM$^+$13] T. Alharbi, P. H. Regan, P. J. R. Mason, N. Mărginean, Zs. Podolyák, A. M. Bruce, E. C. Simpson, A. Algora, N. Alazemi, R. Britton, M. R. Bunce, D. Bucurescu, N. Cooper, D. Deleanu, D. Filipescu, W. Gelletly, D. Ghiţă, T. Glodariu, G. Ilie, S. Kisyov, J. Lintott, S. Lalkovski, S. Liddick, C. Mihai, K. Mulholland, R. Mărginean, A. Negret, M. Nakhostin, C. R. Nita, O. J. Roberts, S. Rice, J. F. Smith, L. Stroe, T. Sava, C. Townsley, E. Wilson, V. Werner, M. Zhekova, and N. V. Zamfir. Electromagnetic transition rates in the $N = 80$ nucleus $^{138}_{58}$Ce. *Phys. Rev. C*, 87:014323, 2013. 28, 33

[ASB$^+$17] J. M. Allmond, A. E. Stuchbery, C. Baktash, A. Gargano, A. Galindo-Uribarri, D. C. Radford, C. R. Bingham, B. A. Brown, L. Coraggio, A. Covello, M. Danchev, C. J. Gross, P. A. Hausladen, N. Itaco, K. Lagergren, E. Padilla-Rodal, J. Pavan, M. A. Riley, N. J. Stone, D. W. Stracener, R. L. Varner, and C.-H. Yu. Electromagnetic moments of radioactive $^{136}$Te and the emergence of collectivity 2p$\bigoplus$2n outside of double-magic $^{132}$Sn. *Phys. Rev. Lett.*, 118:092503, 2017. 159, 160, 199, 200, 201, 203, 204, 205, 206, 207, 208, 209, 210, 214, 215

[Aza99] F. Azaiez. EXOGAM: a $\gamma$-ray spectrometer for radioactive beams. *Nuclear Physics A*, 654(1):1003c – 1008c, 1999. 86, 102

[BCDC$^+$16] D. Bucurescu, I. Căta-Danil, G. Ciocan, C. Costache, D. Deleanu, R. Dima, D. Filipescu, N. Florea, D. G. Ghiţă, T. Glodariu, et al. The *ROSPHERE* $\gamma$-ray spectroscopy array. *Nuclear Instruments and Methods in Physics Research Section A: Accelerators, Spectrometers, Detectors and Associated Equipment*, 837:1–10, 2016. 30

[BdFD$^+$13] A. Blanc, G. de France, F. Drouet, M. Jentschel, U. Köster, C. Mancuso, P. Mutti, J.M. Régis, G. Simpson, T. Soldner, C.A. Ur, W. Urban, and A. Vancraeyenest. Spectroscopy of neutron rich nuclei using cold neutron induced fission of actinide targets at the ILL: The EXILL campaign. *EPJ Web of Conferences*, 62:01001, 2013. 87

[BGH$^+$07] G.F. Bertsch, M. Girod, S. Hilaire, J-P. Delaroche, H. Goutte, and S. Péru. Systematics of the first $2^+$ excitation with the Gogny interaction. *Phys. Rev. Lett*, 99(3):032502, 2007. 201, 203

[BLIA$^+$13] D. Bianco, N. Lo Iudice, F. Andreozzi, A. Porrino, and F. Knapp. Spectroscopy of neutron-rich Te and Xe isotopes within a new shell model context. *Phys. Rev. C*, 88:024303, 2013. 200, 201, 203, 205, 208, 209, 210, 215

[BSS$^+$05] B. A. Brown, N. J. Stone, J. R. Stone, I. S. Towner, and M. Hjorth-Jensen. Magnetic moments of the $2_1^+$ states around $^{132}$Sn. *Phys. Rev. C*, 71:044317, 2005. 203

[C93] Rossi-Alvarez. C. The GASP array. *Nuclear Physics News*, 3(3):10–13, 1993. 86

[CAE] CAEN V1724. Technical information manual mod.V1724, 8 channel, 14 bit 100 MS/s digitiser, Italy (2010). https://www.caen.it. 89, 90

[Cas00] R. F. Casten. *Nuclear structure from a simple perspective*, volume 23. Oxford University Press on Demand, 2000. 18, 19, 202

[CCGI03] A. Covello, L. Coraggio, A. Gargano, and N. Itaco. Structure of neutron-rich nuclei in the $^{132}$Sn region. In *Fission And Properties Of Neutron-Rich Nuclei*, pages 14–21. World Scientific, 2003. 199, 203, 206

[CCGI13] L. Coraggio, A. Covello, A. Gargano, and N. Itaco. Evolution of single-particle states beyond $^{132}$Sn. *Phys. Rev. C*, 87(3):034309, 2013. 6

[DBT$^+$99] G. Duchêne, F.A. Beck, P.J. Twin, G. de France, D. Curien, L. Han, C.W. Beausang, M.A. Bentley, P.J. Nolan, and J. Simpson. The Clover: a new generation of composite Ge detectors. *Nuclear Instruments and Methods in Physics Research Section A: Accelerators, Spectrometers, Detectors and Associated Equipment*, 432(1):90 – 110, 1999. 86

[DDB$^+$08] W. Drozdowski, P. Dorenbos, A. J. J. Bos, G. Bizarri, A. Owens, and F. G. A. Quarati. $CeBr_3$ Scintillator Development for Possible Use in Space Missions. *IEEE Transactions on Nuclear Science*, 55(3):1391–1396, 2008. 35

[DdHvE95] P. Dorenbos, J.T.M. de Haas, and C.W.E. van Eijk. Non-proportionality in the scintillation response and the energy resolution obtainable with scintillation crystals. *IEEE Transactions on Nuclear Science*, 42(6):2190–2202, 1995. 52

[DH] DESPEC-HISPEC. HIgh-Resolution In-flight SPECtroscopy/DEcay SPECtroscopy, FAIR, Facility for Antiproton and Ion Research, https://fair-center.eu/for-users/experiments/nustar/experiments/hispecdespec.html. iv, viii, 30, 31

[Dor02] P. Dorenbos. Light output and energy resolution of $Ce^{3+}$-doped scintillators. *Nuclear Instruments and Methods in Physics Research Section A*, 486:208–213, 2002. 28

[DRP$^+$11] M. Danchev, G. Rainovski, N. Pietralla, A. Gargano, A. Covello, C. Baktash, J. R. Beene, C. R. Bingham, A. Galindo-Uribarri, K. A. Gladnishki, C. J. Gross, V. Yu. Ponomarev, D. C. Radford, L. L. Riedinger, M. Scheck, A. E. Stuchbery, J. Wambach, C.-H. Yu, and N. V. Zamfir. One-phonon isovector $2^+_{1,\mathrm{MS}}$ state in the neutron-rich nucleus $^{132}$Te. *Phys. Rev. C*, 84:061306, 2011. 158, 159, 160, 205, 206, 214

[DWSP$^+$10] M. E. Daube-Witherspoon, S. Surti, A. Perkins, C. C. M. Kyba, R. Wiener, M. E. Werner, R. Kulp, and J. S. Karp. Imaging performance of a $LaBr_3$(Ce)-based PET scanner. *Physics in Medicine and Biology*, 55:45–64, 2010. 33

[Els33] W. M Elsasser. Sur le principe de pauli dans les noyaux. *J. Phys. Radium*, 4(10):549–556, 1933. 5

[Els34] W. M. Elsasser. Sur le principe de pauli dans les noyaux-II. *J. Phys. Radium*, 5(8):389–397, 1934. 5

[EXI] EXILL. Proposal 57635 of EXILL-FATIMA campaign: Single particle states and collectivity in neutron-rich $^{136-139}$Te isotopes. 105

[EXO] EXOGAMM. https://pro.ganil-spiral2.eu/laboratory. v, ix, 86, 102

[F$^+$] L. M. Fraile et al. Technical Design Report for the DESPEC Fast-timing Array, https://fair-center.eu/fileadmin/fair/publications_exp/TDR_HISPEC_DESPEC._FATIMA_public.pdf, 2015. 31, 33, 34, 39, 77

[F$^+$08] L. M. Fraile et al. INPC 2007 proceedings. *Nucl. Phys. A*, 805:218, 2008. 159, 160, 205, 206, 214

[FAI] FAIR. Facility for Antiproton and Ion Research, http:/www.gsi.de/fair/. iv, viii, 30, 31, 77

[Fit] A. Fitzler. Manual of Tv-Software. Institute for Nuclear Physics University of Cologne (IKP), Germany. https://www.ikp.uni-koeln.de/fitz/viewspectra/Tv_user-manual/Tv_user-manual.html. 104

[FMO$^+$11] L. M. Fraile, H. Mach, B. Olaizola, V. Paziy, E. Picado, J. J. Sánchez, J. M. Udías, J. J. Vaquero, and V. Vedia. Assessment of new photosensors for fast-timing applications with large scintillator detectors. In *Nuclear Science Symposium and Medical Imaging Conference (NSS/MIC), 2011 IEEE*, pages 72 –74, 2011. iv, viii, 29, 37

[FMP$^+$13] L M. Fraile, H. Mach, E. Picado, V. Vedia, and J.M. Udías. Study of the time response of a LuAG(Pr) crystal for fast-timing applications. *Nuclear Instruments and Methods in Physics Research Section A: Accelerators, Spectrometers, Detectors and Associated Equipment*, 713(0):27 – 32, 2013. iv, viii, 29, 34

[FMV$^+$13] L. M. Fraile, H. Mach, V. Vedia, B. Olaizola, V. Paziy, E. Picado, and J.M. Udías. Fast timing study of a $CeBr_3$ crystal: Time resolution below 120 ps at $^{60}Co$ energies. *Nuclear Instruments and Methods in Physics Research Section A: Accelerators, Spectrometers, Detectors and Associated Equipment*, 701(0):235 – 242, 2013. iv, viii, 28, 29, 34, 37, 88

[Gar] A. Gargano. Private communication, 2018. 199

[GAS] GASP. https://npgroup.pd.infn.it/GASP. 86

[GMH$^+$05] J. Glodo, W. W. Moses, W. M. Higgins, E. V. D. Van Loef, P. Wong, S. E. Derenzo, M. J. Weber, and K. S. Shah. Effects of Ce Concentration on Scintillation Properties of $LaBr_3$(Ce). *IEEE Transactions on Nuclear Science*, 52(5):1805–1808, 2005. 35, 47, 52, 59, 75

[Gob] Saint Gobain. Brillance 380 Brochure, https://www.crystals.saint-gobain.com/products/standard-and-enhanced-lanthanum-bromide. 28, 88, 120

[Gro62] L. Grodzins. The uniform behaviour of electric quadrupole transition probabilities from first $2^+$ states in even-even nuclei. *Physics Letters*, 2(2):88 – 91, 1962. 15, 16

[GSI84] R. Gwin, R. R. Spencer, and R. W. Ingle. Measurements of the Energy Dependence of Prompt Neutron Emission from $^{233}$U, $^{235}$U, $^{239}$Pu, and $^{241}$Pu for $E_n$=0.005 to 10 eV Relative to Emission from Spontaneous Fission of $^{252}$Cf. *Nuclear Science and Engineering*, 87(4):381–404, 1984. 107

[Ham09] Hamamatsu Photonics. Photomultiplier Tube R9779 Specifications, 2009. 37, 88

[HKF$^+$02] H. Häse, A. Knöpfler, K. Fiederer, U. Schmidt, D. Dubbers, and W. Kaiser. A long ballistic supermirror guide for cold neutrons at ILL. *Nuclear Instruments and Methods in Physics Research Section A: Accelerators, Spectrometers, Detectors and Associated Equipment*, 485(3):453 – 457, 2002. 81

[HRZ$^+$95] J.H. Hamilton, A.V. Ramayya, S.J. Zhu, G.M. Ter-Akopian, Yu.Ts. Oganessian, J.D. Cole, J.O. Rasmussen, and M.A. Stoyer. New insights from studies of spontaneous fission with large detector arrays. *Progress in Particle and Nuclear Physics*, 35:635 – 704, 1995. 79

[ILL] ILL. https://www.ill.eu/. 79, 81

[JBdF$^+$] M. Jentschel, A. Blanc, G. de France, U. Köster, S. Leoni, P. Mutti, G. Simpson, T. Soldner, C. Ur, W. Urban, S. Ahmed, A. Astier, L. Augey, T. Back, P. Baczyk, A. Bajoga, D. Balabanski, T. Belgya, G. Benzoni, C. Bernards, D.C. Biswas, G. Bocchi, S. Bottoni, R. Britton, B. Bruyneel, J. Burnett, R.B. Cakirli, R. Carroll, W. Catford, B. Cederwall, I. Celikovic, N. Cieplicka-Oryczak, E. Clement, N. Cooper, F. Crespi, M. Csatlos, D. Curien, M. Czerwiski, L.S. Danu, A. Davies, F. Didierjean, F. Drouet, G. Duchêne, C. Ducoin, K. Eberhardt, S. Erturk, L.M. Fraile, A. Gottardo, L. Grente, L. Grocutt, C. Guerrero, D. Guinet, A.-L. Hartig, C. Henrich, A. Ignatov, S. Ilieva, D. Ivanova, B.V. John, R. John, J. Jolie, S. Kisyov, M. Krticka, T. Konstantinopoulos, A. Korgul, A. Krasznahorkay, T. Kröll, J. Kurpeta, I. Kuti, S. Lalkovski, C. Larijani, R. Leguillon, R. Licą, O. Litaize, R. Lozeva, C. Magron, C. Mancuso, E. Ruiz Martinez, R. Massarczyk, C. Mazzocchi, B. Melon, D. Mengoni, C. Michelagnoli, B. Million, C. Mokry, S. Mukhopadhyay, K. Mulholland, A. Nannini, D.R. Napoli, B. Olaizola, R. Orlandi, Z. Patel, V. Paziy, C. Petrache, M. Pfeiffer, N. Pietralla, Zs. Podolyak, M. Ramdhane, N. Redon, P. Regan, J.M. Régis, D. Regnier, R. J. Oliver, M. Rudigier, J. Runke, T. Rzaca-Urban, N. Saed-Samii, M.D. Salsac, M. Scheck, R. Schwengner, L. Sengele, P. Singh, J. Smith, O. Stezowski, B. Szpak, T. Thomas, M. Thürauf, J. Timar, A. Tom, I. Tomandl, T. Tornyi, C. Townsley, A. Tuerler, S. Valenta, A. Vancraeyenest, V. Vandone, J. Vanhoy, V. Vedia, N. Warr, V. Werner, D. Wilmsen, E. Wilson, T. Zerrouki, and M. Zielinska. EXILL a high-efficiency, high-resolution setup for $\gamma$-spectroscopy at an intense cold neutron beam facility. *Journal of Instrumentation.* v, ix, 31, 79, 81, 82, 83, 84, 86, 87, 88, 105, 156

[KBK+07] T. Kröll, T. Behrens, R. Krücken, V. Bildstein, R. Gernhäuser, P. Maierbeck, I. Stefanescu, O. Ivanov, J. Van de Walle, N. Warr, et al. Coulomb excitation of neutron-rich $^{138,140,142}$ Xe at REX-ISOLDE. *The European Physical Journal Special Topics*, 150(1):127–129, 2007. 160

[KBU+15] A. Korgul, P. Baczyk, W. Urban, T. Rzaca-Urban, A. G. Smith, and I. Ahmad. Investigation of the $i_{13/2}$ neutron orbital in the $^{132}$Sn region: New excited levels in $^{135}$Sb. *Phys. Rev. C*, 91(2):027303, 2015. 6

[KEHJO07] M. P. Kartamyshev, T. Engeland, M. Hjorth-Jensen, and E. Osnes. Effective interactions and shell model studies of heavy tin isotopes. *Phys. Rev. C*, 76(2):024313, 2007. 6

[KLM+11] S. Kisyov, S. Lalkovski, N. Mărginean, D. Bucurescu, L. Atanasova, D. L. Balabanski, G. H. Căta-Danil, I. Căta-Danil, J-M. Daugas, D. Deleanu, et al. In-beam fast-timing measurements in $^{103,105,107}$Cd. *Phy. Rev. C*, 84(1):014324, 2011. 30

[LAdB+10] J. Laurec, A. Adam, T. de Bruyne, E. Bauge, T. Granier, J. Aupiais, O. Bersillon, G. Le Petit, N. Authier, and P. Casoli. Fission Product Yields of $^{233}$U, $^{235}$U, $^{238}$U and $^{239}$Pu in Fields of Thermal Neutrons, Fission Neutrons and 14.7-MeV Neutrons. *Nuclear Data Sheets*, 111(12):2965 – 2980, 2010. Nuclear Reaction Data. 106, 107, 108, 162

[LBB+15] S. Lalkovski, A. M. Bruce, I. Burrows, D. M. Cullen, A. Grant, I. H. Lazarus, Zs. Podolyák, V. F. E. Pucknell, P. H. Regan, M. Rudigier, et al. Construction of the UK DESPEC array for fast-timing measurements. *Bulg. J. Phys*, 42:593–601, 2015. v, ix

[LDvE+02] E. V. van Loef, P. Dorenbos, C. W. E. van Ejik, K. Krämer, and H. U. Güdel. Scintillation properties of $LaBr_3$:$Ce_3^+$ crystals: Fast, efficient and high-energy-resolution scintillators. *Nuclear Instruments and Methods in Physics Research A*, 486:254–258, 2002. 28

[Lee97] I.Y. Lee. Physics with GAMMASPHERE and beyond. *Progress in Particle and Nuclear Physics*, 38:65 – 78, 1997. $4\pi$ High Resolution Gamma Ray Spectroscopy and Nuclear Structure. 79

[LN99] K. Lefmann and K. Nielsen. McStas, a general software package for neutron ray-tracing simulations. *Neutron News*, 10(3):20–23, 1999. 81

[Mac12] H. Mach. *Instructions for the program SORTM.* Internal Report. Universidad Complutense, 2012. 45

[MAR+12] P. J. R. Mason, T. Alharbi, P. H. Regan, N. Mărginean, Zs Podolyak, E. C. Simpson, N. Alkhomashi, P. C. Bender, M. Bowry, M. Bostan, et al. Half-life of the Iπ= $4^-$ intruder state in $^{34}$P: M2 transition strengths approaching the island of inversion. *Phys. Rev. C*, 85(6):064303, 2012. 30

[May49] M. Goeppert Mayer. On closed shells in nuclei. ii. *Physical Review*, 75(12):1969, 1949. 5

[MF14] H. Mach and L M. Fraile. Fast lifetime measurements on fission products. *Hyperfine Interactions*, pages 1–10, 2014. 49

[MGM89] H. Mach, R. L. Gill, and M. Moszyński. A method for picosecond lifetime measurements for neutron-rich nuclei (1) Outline of the method. *Nuclear Instruments and Methods in Physics Research A*, 280:49–72, 1989. v, ix, 22, 25, 28, 120, 129, 137, 145, 157

[MKG$^+$17] H. Mach, A. Korgul, M. Górska, H. Grawe, I. Matea, M. Stănoiu, L. M. Fraile, Yu. E. Penionzkevich, F. De Oliviera Santos, D. Verney, S. Lukyanov, B. Cederwall, A. Covello, Z. Dlouhý, B. Fogelberg, G. De France, A. Gargano, G. Georgiev, R. Grzywacz, A. F. Lisetskiy, J. Mrazek, F. Nowacki, W. A. Płóciennik, Zs. Podolyák, S. Ray, E. Ruchowska, M.-G. Saint-Laurent, M. Sawicka, Ch. Stodel, and O. Tarasov. Ultrafast-timing lifetime measurements in $^{94}$Ru and $^{96}$Pd: Breakdown of the seniority scheme in $N = 50$ isotones. *Phys. Rev. C*, 95:014313, 2017. 25

[MM89] M. Moszyński and H. Mach. A method for picosecond lifetime measurements for neutron-rich nuclei (2) Timing study with scintillation counters. *Nuclear Instruments and Methods in Physics Research A*, 277:407–417, 1989. v, ix, 22, 129

[Mos06] Moszyński, M. and Gierlik, M. and Kapusta, M. and Nassalski, A. and Szczięśniak, T. and Fontaine, C. and Lavoute, P. New Photonis XP20D0 photomultiplier for fast timing in nuclear medicine. *Nuclear Instruments and Methods in Physics Research Section A: Accelerators, Spectrometers, Detectors and Associated Equipment*, 567(1):31–35, 2006. Proceedings of the 4th International Conference on New Developments in Photodetection BEAUNE 2005 Fourth International Conference on New Developments in Photodetection. 36, 39, 59, 75

[MPM$^+$13] P. J. R. Mason, Zs. Podolyák, N. Mărginean, P. H. Regan, P. D. Stevenson, V. Werner, T. Alexander, A. Algora, T. Alharbi, M. Bowry, et al. Half-life of the yrast $2^+$ state in $^{188}$W: Evolution of deformation and collectivity in neutron-rich tungsten isotopes. *Phys. Rev. C*, 88(4):044301, 2013. 30

[MuuBB$^+$10] N. Mărginean, D.L. Balabanski, D. Bucurescu, S. Lalkovski, L. Atanasova, G. Căta-Danil, I. Căta-Danil, J.M. Daugas, D. Deleanu, P. Detistov, G. Deyanova, D. Filipescu, G. Georgiev, D. Ghiţă, K.A. Gladnishki, R. Lozeva,

T. Glodariu, M. Ivaşcu, S. Kisyov, C. Mihai, R. Mărginean, A. Negret, S. Pascu, D. Radulov, T. Sava, L. Stroe, G. Suliman, and N.V. Zamfir. In-beam measurements of sub-nanosecond nuclear lifetimes with a mixed array of HPGe and $LaBr_3$(Ce) detectors. *The European Physical Journal A*, 46(3):329–336, 2010. 28, 30, 33

[MWM+91] H. Mach, F. K. Wohn, G. Molnr, K. Sistemich, J. C. Hill, M. Moszyski, R. L. Gill, W. Krips, and D. S. Brenner. Retardation of B(E2; $0_1^+ \rightarrow 2_1^+$) rates in $^{90-96}$Sr and strong subshell closure effects in the A$\sim$100 region. *Nuclear Physics A*, 523(2):197 – 227, 1991. 22, 60, 145, 157

[NBM+14] C. R. Nita, D. Bucurescu, N. Marginean, M. Avrigeanu, G. Bocchi, S. Bottoni, A. Bracco, A. M. Bruce, G. Cata-Danil, G. Colo, et al. Fast-timing lifetime measurements of excited states in $^{67}$Cu. *Phys. Rev. C*, 89:064314, 2014. 30

[NNB17] H. Naïdja, F. Nowacki, and B. Bounthong. Shell-model investigation of spectroscopic properties and collectivity in the nuclei beyond $^{132}$sn. *Phys. Rev. C*, 96(3):034312, 2017. 6, 203

[NND] NNDC. National Nuclear Data Center. https://www.nndc.bnl.gov/. 107, 131, 162, 206, 207

[OFM+13] B. Olaizola, L M. Fraile, H. Mach, A. Aprahamian, J.A. Briz, J. Cal-González, D. Ghiţă, U. Köster, W. Kurcewicz, S.R. Lesher, D. Pauwels, E. Picado, A. Poves, D. Radulov, G.S. Simpson, and J. M. Udías. $\beta^-$decay of $^{65}$Mn to $^{65}$Fe. *Phys. Rev. C*, 88:044306, 2013. 28, 33

[OFU+01] T. Otsuka, R. Fujimoto, Y. Utsuno, B. A. Brown, M. Honma, and T. Mizusaki. Magic numbers in exotic nuclei and spin-isospin properties of the NN interaction. *Phys. Rev. Lett.*, 87(8):082502, 2001. 10

[OKK+10] T. Ohnishi, T. Kubo, K. Kusaka, et al. Identification of 45 New Neutron-Rich Isotopes Produced by In-Flight Fission of a $^{238}$U Beam at 345 MeV/nucleon. *Journal of the Physical Society of Japan*, 79(7):073201, 2010. 6

[Ola13] Bruno Olaizola. *Ultra-fast timing study of exotic neutron-rich Fe isotopes.* PhD thesis, UCM, Madrid, Dept. Phys., 2013. 24

[ORT] ORTEC 935 Quad Constant-Fraction 200-MHz Discriminator Operating and Service Manual. 40, 41, 90

[OSF+05] T. Otsuka, T. Suzuki, R. Fujimoto, H. Grawe, and Y. Akaishi. Evolution of nuclear shells due to the tensor force. *Phys. Rev. Lett.*, 95(23):232502, 2005. 10

[OSH+10] T. Otsuka, T. Suzuki, J. D Holt, A. Schwenk, and Y. Akaishi. Three-body forces and the limit of oxygen isotopes. *Phys. Rev. Lett.*, 105(3):032501, 2010. 6, 10

[Paz] V. Paziy. Internal communication. 85, 89, 91, 92

[Pod08] Podolyák, Zs. From RISING to HISPEC-DESPEC. *Nuclear Instruments and Methods in Physics Research Section B: Beam Interactions with Materials and Atoms*, 266(19-20):4589–4594, 2008. Proceedings of the XVth International Conference on Electromagnetic Isotope Separators and Techniques Related to their Applications. 34

[RBB$^+$02] D. C. Radford, C. Baktash, J. R. Beene, B. Fuentes, A. Galindo-Uribarri, C. J. Gross, P. A. Hausladen, T. A. Lewis, P. E. Mueller, E. Padilla, D. Shapira, D. W. Stracener, C.-H. Yu, C. J. Barton, M. A. Caprio, L. Coraggio, A. Covello, A. Gargano, D. J. Hartley, and N. V. Zamfir. Coulomb excitation of radioactive $^{132,134,136}$Te beams and the low $B(E2)$ of $^{136}$Te. *Phys. Rev. Lett.*, 88:222501, 2002. 158, 159, 160, 199, 203, 205, 206, 214

[RBR$^+$14] O. J. Roberts, A. M. Bruce, P. H. Regan, Zs. Podolyak, C. M. Townsley, J. F. Smith, K. F. Mulholland, and A. Smith. A LaBr$_3$(Ce) fast-timing array for DESPEC at FAIR. *Nuclear Instruments and Methods in Physics Research Section A: Accelerators, Spectrometers, Detectors and Associated Equipment*, 748:91 – 95, 2014. 39

[Rég] J.-M. Régis. Set of configuration input files for the data analysis of the EXILL-FATIMA campaign with SOCOv2. Internally distributed. 94, 95, 101, 109

[RJSS$^+$17] J.-M. Régis, J. Jolie, N. Saed-Samii, N. Warr, M. Pfeiffer, A. Blanc, M. Jentschel, U. Köster, P. Mutti, T. Soldner, G. S. Simpson, F. Drouet, A. Vancraeyenest, G. de France, E. Clément, O. Stezowski, C. A. Ur, W. Urban, P. H. Regan, Zs. Podolyák, C. Larijani, C. Townsley, R. Carroll, E. Wilson, L. M. Fraile, H. Mach, V. Paziy, B. Olaizola, V. Vedia, A. M. Bruce, O. J. Roberts, J. F. Smith, M. Scheck, T. Kröll, A.-L. Hartig, A. Ignatov, S. Ilieva, S. Lalkovski, W. Korten, N. Mărginean, T. Otsuka, N. Shimizu, T. Togashi, and Y. Tsunoda. Abrupt shape transition at neutron number $N = 60$: $B(E2)$ values in $^{94,96,98}\mathbf{Sr}$ from fast $\gamma - \gamma$ timing. *Phys. Rev. C*, 95:054319, 2017. 147

[RMS$^+$13] J.-M. Régis, H. Mach, G.S. Simpson, J. Jolie, G. Pascovici, N. Saed-Samii, N. Warr, A. Bruce, J. Degenkolb, L.M. Fraile, C. Fransen, D.G. Ghita, S. Kisyov, U. Köster, A. Korgul, S. Lalkovski, N. Mărginean, P. Mutti, B. Olaizola, Zs. Podolyak, P.H. Regan, O.J. Roberts, M. Rudigier, L. Stroe, W. Urban, and D. Wilmsen. The generalized centroid difference method for picosecond sensitive determination of lifetimes of nuclear excited states using large fast-timing arrays. *Nuclear Instruments and Methods in Physics Research Section A: Accelerators, Spectrometers, Detectors and Associated Equipment*, 726:191 – 202, 2013. v, ix, 118, 122, 129, 130, 157, 158

[RNT01] S. Raman, C.W. Nestor, and P. Tikkanen. Transition probability from the ground to the first-excited $2^+$ state of even-even nuclides. *Atomic Data and Nuclear Data Tables*, 78(1):1 – 128, 2001. 15

[RPG$^+$] B. Rubio, Zs Podolyák, M. Górska, J Gerl, and W. Korten. FAIR-EXPERIMENTS-26 DEcay SPECtroscopy DESPEC at the new FAIR-NUSTAR facility. iv, viii, 30

[RPJR10] J.-M. Régis, G. Pascovici, J. Jolie, and M. Rudigier. The mirror symmetric centroid difference method for picosecond lifetime measurements via $\gamma$-$\gamma$ coincidences using very fast $LaBr_3$(Ce) scintillator detectors. *Nuclear Instruments and Methods in Physics Research Section A: Accelerators, Spectrometers, Detectors and Associated Equipment*, 622(1):83 – 92, 2010. 26, 130, 135

[RSB$^+$14] J.-M. Régis, G. S. Simpson, A. Blanc, G. de France, M. Jentschel, U. Koster, P. Mutti, V. Paziy, N. Saed-Samii, T. Soldner, C.A. Ur, W. Urban, A. M. Bruce, F. Drouet, L .M. Fraile, S. Ilieva, J. Jolie, W. Korten, T. Kröll, S. Lalkovski, H. Mach, N. Marginean, G. Pascovici, Zs. Podolyak, P. H. Regan, O. J. Roberts, J.F. Smith, C. Townsley, A. Vancraeyenest, and N. Warr. Germanium-gated fast timing of excited states in fission fragments using the EXILl and FATIMA spectrometer. *Nuclear Instruments and Methods in Physics Research Section A: Accelerators, Spectrometers, Detectors and Associated Equipment*, 763:210 – 220, 2014. v, ix, 28, 31, 33, 79, 80, 88, 105, 136, 156

[SAF$^+$00] J. Simpson, F. Azaiez, G. De France, J. Fouan, J. Gerl, R. Julin, W. Korten, P. J. Nolan, B. M. Nyakö, G. Sletten, and P. M. Walker. The EXOGAM array: A radioactive beam gamma-ray spectrometer. *Acta Physica Hungarica, Series A: Heavy Ion Physics*, 11(1-2):159–188, 2000. 86, 102

[SAPW14] A. P. Severyukhin, N. N. Arsenyev, N. Pietralla, and V. Werner. Impact of variational space on M1 transitions between first and second quadrupole excitations in $^{132,134,136}$Te. *Physical Review C*, 90(1):011306, 2014. 201, 203, 207

[SGJ$^+$14] G. S. Simpson, G. Gey, A. Jungclaus, J. Taprogge, S. Nishimura, K. Sieja, P. Doornenbal, G. Lorusso, P.-A. Söderström, T. Sumikama, et al. Yrast $6^+$ Seniority Isomers of $^{136,138}$Sn. *Phys. Rev. Lett.*, 113(13):132502, 2014. 6

[SGK$^+$03] K. S. Shah, J. Glodo, M. Klugerman, W. W. Moses, S.E. Derenzo, and M.J. Weber. $LaBr_3$:Ce scintillators for Gamma-Ray spectroscopy. *Nuclear Science, IEEE Transactions*, 50(6):2410–2413, 2003. 28, 52

[SOMH04] N. Shimizu, T. Otsuka, T. Mizusaki, and M. Honma. Anomalous properties of quadrupole collective states in $^{136}$Te and beyond. *Phys. Rev. C*, 70:054313, 2004. 159, 200, 203, 207, 208, 209, 215

[SP08] O. Sorlin and M.-G. Porquet. Nuclear magic numbers: New features far from stability. *Progress in Particle and Nuclear Physics*, 61(2):602–673, 2008. 6

[SSa] N. Saed-Samii. Set of configuration input files for the data analysis of the EXILL-FATIMA campaign with SOCOv2. Internally distributed. 104

[SSb] N. Saed-Samii. SOCOv2 user manual. Institute for Nuclear Physics University of Cologne (IKP). https://gitlab.ikp.uni-koeln.de/nima/soco-v2/tree/master/manual. 93, 94, 95, 99, 104

[SS10] S. Sarkar and M. Saha Sarkar. New shell closure for neutron-rich sn isotopes. *Phys. Rev. C*, 81(6):064328, 2010. 6

[STVC+16] V. Sánchez-Tembleque, V. Vedia, M. Carmona, L. M. Fraile, S. Ritt, and J. M. Udías. Digital strategies for time and energy measurement for ultra fast scintillators. In *IEEE Nuclear Science Symposium, Medical Imaging Conference and Room-Temperature Semiconductor Detector Workshop (NSS/MIC/RTSD)*, pages 1–2, 2016. 40

[SWP+02] A. G. Smith, R. M. Wall, D. Patel, G. S. Simpson, D. M. Cullen, J. L. Durell, S. J. Freeman, J. C. Lisle, J. F. Smith, B. J. Varley, et al. Lifetimes of yrast rotational states of the fission fragments $^{100}$Zr and $^{104}$Mo measured using a differential plunger. *Journal of Physics G: Nuclear and Particle Physics*, 28(8):2307, 2002. 151, 155, 214

[TENS02] J. Terasaki, J. Engel, W. Nazarewicz, and M. Stoitsov. Anomalous behavior of $2^+$ excitations around $^{132}$Sn. *Phys. Rev. C*, 66:054313, 2002. 159, 201, 203, 207

[VCGF+17] V. Vedia, M. Carmona-Gallardo, L. M Fraile, H. Mach, and J. M. Udías. Performance evaluation of novel $LaBr_3$(Ce) scintillator geometries for fast-timing applications. *Nuclear Instruments and Methods in Physics Research Section A: Accelerators, Spectrometers, Detectors and Associated Equipment*, 857:98–105, 2017. 34, 64

[VMF+15] V. Vedia, H. Mach, L M. Fraile, J.M. Udías, and S. Lalkovski. Enhanced time response of 1-inch $LaBr_3$(Ce) crystals by leading edge and constant fraction techniques. *Nuclear Instruments and Methods in Physics Research Section A: Accelerators, Spectrometers, Detectors and Associated Equipment*, 795:144 – 150, 2015. 34, 38, 41, 88, 120

[WFL04] P. Willendrup, E. Farhi, and K. Lefmann. McStas 1.7 - a new version of the flexible Monte Carlo neutron scattering package. *Physica B: Condensed Matter*, 350(1, Supplement):E735 – E737, 2004. Proceedings of the Third European Conference on Neutron Scattering. 81

[WMF+07] E. R. White, H. Mach, L. M. Fraile, U. Köster, O. Arndt, A. Blazhev, N. Boelaert, M. J. G. Borge, R. Boutami, H. Bradley, N. Braun, Z. Dlouhy, C. Fransen, H. O. U. Fynbo, Ch. Hinke, P. Hoff, A. Joinet, A. Jokinen, J. Jolie, A. Korgul, K.-L. Kratz, T. Kröll, W. Kurcewicz, J. Nyberg, E.-M. Reillo, E. Ruchowska, W. Schwerdtfeger, G. S. Simpson, M. Stanoiu, O. Tengblad, P. G. Thirolf, V. Ugryumov, and W. B. Walters. Lifetime measurement of the 167-kev state in $^{41}$Ar. *Phys. Rev. C*, 76:057303, 2007. 28, 33

[WPX13] S. M. Wang, J. C. Pei, and F. R. Xu. Spectroscopic calculations of cluster nuclei above double shell closures with a new local potential. *Phys. Rev. C*, 87(1):014311, 2013. 201, 202, 203, 205, 206, 209, 210, 215

[Zuk03] A. P. Zuker. Three-body monopole corrections to realistic interactions. *Phys. Rev. Lett.*, 90(4):042502, 2003. 6, 9

# Scientific publications and conferences contributions

During this PhD. Thesis the following investigations were published in international journals relevant in the field or presented in international conferences.

## Scientific publications in indexed international journals

1. **V. Vedia**, H. Mach, L .M. Fraile, J. M. Udías. Optimization of the Time Response of LaBr$_3$(Ce) crystals, and its dependence on the Ce Concentration. *Journal of the Physical Society of Japan, JPSCP.6.030134, 2015.*
2. **V. Vedia**, H. Mach, L. M. Fraile, J. M. Udías, S. Lalkovski. Enhanced time response of 1-inch LaBr$_3$(Ce) crystals by leading edge and constant fraction technique. *Nuclear Instruments and Methods in Physics Research Section A: Accelerators, Spectrometers, Detectors and Associated Equipment, 795:144150, 2015.*
3. **V. Vedia**, M. Carmona-Gallardo, L. M. Fraile, H. Mach, J. M. Udías. Performance evaluation of novel LaBr3(Ce) scintillator geometries for fast-timing applications. *Nuclear Instruments and Methods in Physics Research Section A: Accelerators, Spectrometers, Detectors and Associated Equipment, 857:98-105, 2017.*
4. **V. Vedia**, L. M. Fraile, H. Mach, A. Aprahamian, C. Bernards, J. A. Briz, B. Bucher, C. J. Chiara, Z. Dlouhy, D. Ghiă, P. Hoff, U. Köster, W. Kurcewicz, R. Lică, N. Mărginean, R. Mărginean, B. Olaizola, V. Paziy, J.-M. Régis, M. Rudigier, T. Sava, G. Simpson, M. Stănoiu, L. Stroe, J. M. Udías y W. B. Walters. Search for the $^{73}$Ga ground-state doublet splitting in the $\beta$-decay $^{73}$Zn. *Phys. Rev. C, 96:3034311, 2017.*
5. L. M Fraile, H. Mach, **V. Vedia**, V. Paziy, E. Picado, J. M Udías. Fast timing study of a CeBr$_3$ crystal: time resolution below 120 ps at $^{60}$Co energies. *Nuclear Instruments and Methods in Physics Research Section A: Accelerators, Spectrometers, Detectors and Associated Equipment, 701:235 - 242, 2013.*

6. L. M Fraile, H. Mach, E. Picado, **V. Vedia**, J. M. Udías. Study of the time response of a LuAG(Pr) crystal for fast timing applications.*Nuclear Instruments and Methods in Physics Research Section A: Accelerators, Spectrometers, Detectors and Associated Equipment, 713: 27-32, 2013.*

7. J.-M. Régis, J. Jolie, N. Saed-Samii, N. Warr, M. Pfeiffer, A. Blanc, M. Jentschel, U. Köster, P. Mutti, T. Soldner, G. S. Simpson, F. Drouet, A. Vancraeyenest, G. de France, E. Clément, O. Stezowski, C. A. Ur, W. Urban, P. H. Regan, Zs. Podolyák, C. Larijani, C. Townsley, R. Carroll, E. Wilson, L. M. Fraile, H. Mach, V. Paziy, B. Olaizola, **V. Vedia**, A. M. Bruce, O. J. Roberts, J. F. Smith, T. Kröll, A.-L. Hartig, A. Ignatov, S. Ilieva, M. Thrauf, S. Lalkovski, D. Ivanova, S. Kisyov, W. Korten, M.-D. Salsac, M. Zielińska, N. Mărginean, D. G. Ghită, R. Lică, C. M. Petrache, A. Astier, y R. Leguillon. B(E2; $2^+ \to 0^+$) value in $^{90}$Kr. *Phys. Rev. C, 90:067301, 2014.*

8. I. Marroquín, M. J. G. Borge, A. A. Ciemny, H. de Witte, L. M. Fraile, H. O. U. Fynbo, A. Garzn-Camacho, A. Howard, H. Johansson , B. Jonson, O. S. Kirsebom, G. T. Koldste, R. Lică, M. V. Lund, M. Madurga, C. Mazzocchi, C. Mihai, M. Munch, S. A. Nae, E. Nacher, A. Negret, T. Nilsson, A. Perea, J. Refsgaard, K. Riisager, E. Rapisarda, C. Sotty, M. Stanoiu, O. Tengblad , A. E. Turturica, **V. Vedia**. Multi-particle emission from $^{31}$Ar at ISOLDE. *Acta Phys. Polon. B, 47:747, 2016.*

9. R. Lică, H. Mach, L. M. Fraile, A. Gargano, M. J. G. Borge, N. Mărginean, C. O. Sotty, **V. Vedia**, A. N. Andreyev, G. Benzoni, P. Bomans, R. Borcea, L. Coraggio, C. Costache, H. De Witte, F. Flavigny, H. Fynbo, L. P. Gaffney, P. T. Greenlees, L. J. Harkness-Brennan, M. Huyse, P. Ibañez, D. S. Judson, J. Konki, A. Korgul,T. Kröll, J. Kurcewicz,S. Lalkovski, I. Lazarus, M. V. Lund, M. Madurga, R. Mărginean, I. Marroquín, C. Mihai, R. E. Mihai, A. I. Morales, E. Nacher, A. Negret, R. D. Page, J. Pakarinen, S. Pascu, V. Paziy, A. Perea, M. Perez-Liva, E. Picado, V. Pucknell, E. Rapisarda, P. Rahkila, F. Rotaru, J. A. Swartz, O. Tengblad, P. Van Duppen, M. Vidal, R. Wadsworth, W. B. Walters, N. Warr. Fast-timing study of the $l$-forbidden $1/2^+ \to 3/2^+ M1$ transition in $^{129}$Sn. *Phys Rev C, 93:044303, 2016.*

10. V. Guadilla, A. Algora, J.L. Tain, J. Agramunt, J. Ǎystö, J.A. Briz, D. Cano-Ott, A. Cucoanes, T. Eronen, M. Estienne, M. Fallot, L.M. Fraile, E. Ganioglu, W. Gelletly, D. Gorelov, J. Hakala, A. Jokinen, D. Jordan, A. Kankainen, V. Kolhinen, J. Koponen, M. Lebois, T. Martinez, M. Monserrate, A. Montaner-Pizá, I. Moore, E. Nácher, S. Orrigo, H. Penttilä, Zs. Podolyak, I. Pohjalainen, A. Porta, P. Regan, J. Reinikainen, M. Reponen, S. Rinta-Antila, B. Rubio, K. Rytkönen, T. Shiba, V. Sonnenschein, A.A. Sonzogni, E. Valencia, **V. Vedia**, A. Voss, J.N. Wilson, A.-A. Zakari Issoufou. First experiment with the NUSTAR/FAIR Decay Total Absorption $\gamma$-Ray Spectrometer (DTAS) at the IGISOL IV facility. *Nuclear Instruments and Methods in Physics Research Section B: Beam Interactions with Materials and Atoms, 376:334337, 2016.*

11. G. Bocchi, S. Leoni, B. Fornal, G. Colo, P.F. Bortignon, S. Bottoni, A. Bracco, C. Michelagnoli, D. Bazzacco, A. Blanc, G. de France, M. Jentschel, U. Köster, P. Mutti, J.-M. Régis, G. Simpson, T. Soldner, C.A. Ur, W. Urban, L.M. Fraile, R. Lozeva, B. Belvito, G. Benzoni, A. Bruce, R. Carroll, N. Cieplicka Orynczak, F.C.L. Crespi, F. Didierjean, J. Jolie, W. Korten, T. Kröll, S. Lalkovski, H. Mach, N. Mărginean, B. Melon, D. Mengoni, B. Million, A. Nannini, D. Napoli, B. Olaizola, V. Paziy, Zs. Podolyák, P.H. Regan, N. Saed-Samii, B. Szpak, **V. Vedia**. The mutable nature of particle-core excitations with spin in the one-valence-proton nucleus $^{133}$Sb. *Physics Letters B, 760:273-278, 2016.*

12. M. V. Lund, A. Andreyev, M. J. G. Borge, J. Cederkäll, H. De Witte, L. M. Fraile, H. O. U. Fynbo, P. T. Greenlees, L. J. Harkness-Brennan, A. M. Howard, M. Huyse, B. Jonson, D. S. Judson, O. S. Kirsebom, J. Konki, J. Kurcewicz, I. Lazarus, R. Lică, S. Lindberg, M. Madurga, N. Mărginean, R. Mărginean, I. Marroquin, C. Mihai, M. Munch, E. Nacher, A. Negret, T. Nilsson, R. D. Page, S. Pascu, A. Perea, V. Pucknell, P. Rahkila, E. Rapisarda, K. Riisager, F. Rotaru, C. Sotty, M. Stanoiu, O. Tengblad, A. Turturica, P. Van Duppen, **V. Vedia**, R. Wadsworth y N. Warr. Beta-delayed proton emission from $^{20}$Mg. *Eur. Phys. J. A, 52:304 , 2016.*

13. R. Lică, G. Benzoni, A. I. Morales, M. J. G. Borge, L. M. Fraile, H. Mach, M. Madurga, C. Sotty, **V. Vedia**, H. De Witte, J. Benito, T. Berry, N. Blasi, A. Bracco, S. Cerutik, V. Charviakova, N. Cieplicka-Ory ńczak, C. Costache, F. C .L. Crespi, J. Creswell, G.Fernández-Martínez, H. Fynbo, P. Greenlees, I. Homm, M. Huyse, J. Jolie, V. Karayonchev, U. Köster, J. Konki, T. Kröll, J. Kurcewicz, T. Kurtukian-Nieto, I. Lazarus, S. Leoni, M. Lund, N. Marginean, R. Mărginean, C. Mihai, R. Mihai,A. Negret, A. Orduz, Z. Patyk, S. Pascu, V. Pucknell,P. Rahkila, J.M. Régis, F. Rotaru, N. Saed-Sami,V. Sánchez-Tembleque, M. Stanoiu, O. Tengblad, M. Thuerauf, A. Turturica, P. Van Duppen and N. Warr. Beta decay studies of n-rich Cs with the ISOLDE Decay Station,Focus on Exotic Beams at ISOLDE: A Laboratory Portrait. *Journal of Physics G: Nuclear and Particle Physics, 2016.*

14. E. Picado, M. Carmona-Gallardo, J. Cal-González, L.M. Fraile , H. Mach, J. M. Udías, **V. Vedia**. Efficiency measurement and Monte Carlo simulations of a $CeBr_3$ scintillator. *Applied Radiation and Isotopes, 120:71-75, 2016.*

15. V. Guadilla, A. Algora, J.L.Taín, J.Agramunt, J.Aystö, J.A.Briz, A . Cucoanes, T. Eronen, M. Estienne, M. Fallot, L .M. Fraile, E. Ganiolu, W. Gelletlya, D. Gorelov, J. Hakala, A. Jokinen, D. Jordan, A. Kankainen, V. Kolhinen, J. Koponen, M. Lebois, T. Martinez, M. Monserrate, A. Montaner-Piz, I. Moore, E. Nácher, S. E. A. Orrigo, H. Penttilä, I. Pohjalainen, A. Porta, J. Reinikainen, M. Reponen, S. Rinta-Antila, B. Rubio, K. Rytk"unen, T. Shiba, V. Sonnenschein, E. Valencia **V.Vedia**, A. Voss, J. N. Wilson, A.-A. Zakari-Issoufou. Characterization of a cylindrical plastic $\beta$-detector with Monte Carlo simulations of optical photons. *Nuclear Instruments and Methods in Physics Research Section A: Accelerators, Spectrometers, Detectors and Associated Equipment, 854:134-138, 2017.*

16. P. Spagnoletti, G.S. Simpson, R. Carroll, J.-M. Régis, A. Blanc, M. Jentschel, U. Köster, P. Mutti, T. Soldner, G. de France, C.A. Ur, W. Urban, A.M. Bruce, F. Drouet, L.M. Fraile, D.G. Ghit a, S. Ilieva, J. Jolie, W. Korten, T. Kroll, S. Lalkovski, R. Lică, H. Mach, N. Mărginean, V. Paziy, Zs. Podolyak, P.H. Regan, M. Scheck, N. Saed-Samii, G. Thiamova, C. Townsley, A. Vancraeyenest, **V. Vedia**, A. Gargano and P. Van Isacker. Seniority Two-Body E2 Operator. *Phys. Rev. C, 95:021302(R), 2017*

17. R Lică, G Benzoni, A I Morales, M J G Borge, L M Fraile, H Mach, M Madurga, C Sotty,**V Vedia**, H De Witte, J Benito, T Berry, N Blasi, A Bracco, F Camera, S Ceruti, V Charviakova,N Cieplicka-Oryczak, C Costache, F C L Crespi, J Creswell, G Fernández-Martínez, H Fynbo,P Greenlees, I Homm, M Huyse, J Jolie, V Karayonchev, U Köster, J Konki, T Kröll,J Kurcewicz, T Kurtukian-Nieto, I Lazarus, S Leoni, M Lund, N Mărginean, R Mărginean,C Mihai, R Mihai, A Negret, A Orduz, Z Patyk, S Pascu, V Pucknell, P Rahkila, J M Regís,F Rotaru, N Saed-Sami, V Sánchez-Tembleque, M Stanoiu, O Tengblad, M Thuerauf, A Turturica,P Van Duppen and N Warr. $\beta$-decay studies of n-rich Cs isotopes with the ISOLDE Decay Station. *Journal of Physics G: Nuclear and Particle Physics, 44, 5, 2017.*

18. V. Guadilla, A. Algora, J.L. Tain, J. Agramunt, D. Jordan, A. Montaner-Pizá, S.E.A. Orrigo, B. Rubio, E. Valencia, J. Suhonen, O. Civitarese, J. ystö, J.A. Briz, A. Cucoanes, T. Eronen, M. Estienne, M. Fallot, L. M. Fraile, E. Ganioglu, W. Gelletly, D. Gorelov, J. Hakala, A. Jokinen, A. Kankainen, V. Kolhinen, J. Koponen, M. Lebois, T. Martínez, M. Monserrate, I. Moore, E. Nácher, H. Penttilä, I. Pohjalainen, A. Porta, J. Reinikainen, M. Reponen, S. Rinta-Antila, K. Rytkönen, T. Shiba, V. Sonnenschein, A.A. Sonzogni, **V. Vedia**, A. Voss, J.N. Wilson, and A.-A. Zakari-Issoufou. Study of the $\beta$-decay of $^{100}$Tc with Total Absorption $\gamma$-Ray Spectroscopy. *Phys. Rev C, 961:014319, 2017.*

19. R. Lică, G. Benzoni, T.R. Rodríguez, M.J.G. Borge, L.M. Fraile, H. Mach, A.I. Morales, M. Madurga, C.O. Sotty, **V. Vedia**, H. De Witte, J. Benito, R.N. Bernard, T. Berry, A. Bracco, F. Camera, S. Ceruti, V. Charviakova, N. Cieplicka-Orynczak, C. Costache, F.C.L. Crespi, J. Creswell, G. Fernandez-Martínez, H. Fynbo, P.T. Greenlees, I. Homm, M. Huyse, J. Jolie, V. Karayonchev, U. Köster, J. Konki, T. Kröll, J. Kurcewicz, T. Kurtukian-Nieto, I. Lazarus, M.V. Lund, N. Mărginean, R. Mărginean, C. Mihai, R. E. Mihai, A. Negret, A. Orduz, Z. Patyk, S. Pascu, V. Pucknell, P. Rahkila, E. Rapisarda, J.M. Regis, L.M. Robledo, F. Rotaru, N. Saed-Samii, V. Sánchez-Tembleque, M. Stanoiu,2 O. Tengblad, M. Thuerauf, A. Turturica, P. Van Duppen, and N. Warr. Evolution of deformation in neutron-rich Ba isotopes up to A=150. *Phys. Rev. C, 97:024305, 2018.*

20. S. Ansari, J.-M. Régis, J. Jolie, N. Saed-Samii, N. Warr, W. Korten, M. Zieliska, M.-D. Salsac, A. Blanc, M. Jentschel, U. Köster, P. Mutti, T. Soldner, G.S. Simpson, F. Drouet, A. Vancraeyenest, G. de France, O. Stezowski, C.A. Ur, W. Urban, P.H. Regan, Zs. Podolyk, C. Larijani, C. Townsley, R. Carroll, E. Wilson, H. Mach, L.M. Fraile,V. Paziy, B. Olaizola, **V. Vedia**, A.M. Bruce, O.J. Roberts, J.F. Smith, M. Scheck, T. Kröll,

A.-L. Hartig, A. Ignatov, S. Ilieva, S. Lalkovski, N. Mărginean, T. Otsuka, N. Shimizu T. Togashi and Y. Tsunoda. Study of lifetime and phase transition in neutron-rich 98,100,102 Zr. *Phys. Rev. C, 96:054323, 2017.*

21. M. Jentschel, A. Blanc, G. de France, U. Köster, S. Leoni, P. Mutti, G. Simpson, T. Soldner, C. Ur, W. Urban, S. Ahmed, A. Astier, L. Augey, T. Back, P. Baczyk, A. Bajoga, D. Balabanski, T. Belgya, G. Benzoni, C. Bernards, D.C. Biswas, G. Bocchi, S. Bottoni, R. Britton, B. Bruyneel, J. Burnett, R.B. Cakirli, R. Carroll, W. Catford, B. Cederwall, I. Celikovic,N. Cieplicka-Oryczak, E. Clement, N. Cooper, F. Crespi, M. Csatlos, D. Curien, M. Czerwiński, L.S. Danu, A. Davies, F. Didierjean, F. Drouet, G. Duchne, C. Ducoin, K. Eberhardt, S. Erturk, L.M. Fraile, A. Gottardo, L. Grente, L. Grocutt, C. Guerrero, D. Guinet, A.-L. Hartig,C. Henrich, A. Ignatov, S. Ilieva, D. Ivanova, B.V. John, R. John, J. Jolie, S. Kisyov,M. Krticka, T. Konstantinopoulos, A. Korgul, A. Krasznahorkay, T. Kröll, J. Kurpeta, I. Kuti,S. Lalkovski, C. Larijani, R. Leguillon, R. Lică, O. Litaize, R. Lozeva, C. Magron, C. Mancuso, E. Ruiz Martínez, R. Massarczyk, C. Mazzocchi, B. Melon, D. Mengoni, C. Michelagnoli, B. Million, C. Mokry, S. Mukhopadhyay, K. Mulholland, A. Nannini,D.R. Napoli, B. Olaizola, R. Orlandi, Z. Patel, V. Paziy, C. Petrache, M. Pfeiffer, N. Pietralla, Z. Podolyak, M. Ramdhane, N. Redon, P. Regan, J.M. Régis, D. Regnier, R. J. Oliver, M. Rudigier, J. Runke, T. Rzaca-Urban, N. Saed-Samii, M.D. Salsac, M. Scheck, R. Schwengner, L. Sengele, P. Singh, J. Smith, O. Stezowski, B. Szpak, T. Thomas, M. Thrauf, J. Timar, A. Tom, I. Tomandl, T. Tornyi, C. Townsley, A. Tuerler, S. Valenta, A. Vancraeyenest, V. Vandone, J. Vanhoy, **V. Vedia**, N. Warr, V. Werner, D. Wilmsen, E. Wilson, T. Zerrouki and M. Zielinska. EXILLa high-efficiency, high-resolution setup for $\gamma$-spectroscopy at an intense cold neutron beam facility. *Journal of Instrumentation, 12, 2017.*

22. O. S. Kirsebom, O. Tengblad, R. Lica, M. Munch, K. Riisager, H. O. U. Fynbo,M. J. G. Borge, M. Madurga, I. Marroquin, A. N. Andreyev, T. A. Berry, E. R. Christensen, P. Daz Fernndez, D. T. Doherty, P. Van Duppen, L. M. Fraile, M. C. Gallardo, P. T. Greenlees, L. J. Harkness-Brennan, N. Hubbard, M. Huyse, J. H. Jensen, H. Johansson, B. Jonson, D. S. Judson, J. Konki, I. Lazarus, M. V. Lund, N. Marginean, R. Marginean, A. Perea, C. Mihai, A. Negret, R. D. Page, V. Pucknell, P. Rahkila, O. Sorlin, C. Sotty, J. A. Swartz, H. B. Srensen, H. Tornqvist, **V. Vedia**, N. Warr, and H. De Witte. First Accurate Normalization of the $\beta$-delayed $\alpha$ Decay of $^{16}$N and Implications for the $^{12}$C($\alpha$, $\gamma$)$^{16}$O Astrophysical Reaction Rate. *Phys. Rev. Lett. 121142701, 2018.*

## Submitted scientific publications

1. V. Sánchez-Tembleque, **V. Vedia**, L. M. Fraile, S. Ritt, J. M. Udías. Optimizing Time-Pickup Algorithms in Radiation Detectors with a Genetic Algorithm. *Nuclear Instruments and Methods in Physics Research Section A: Accelerators, Spectrometers, Detectors and Associated Equipment, 2018*

2. M. Piersa, A. Korgul, L. M. Fraile, J. Benito, E. Adamska, R. Álvarez, A. E. Barzakh, G. Benzoni,T. Berry, M. J. G. Borge, M. Carmona, K. Chrysalidis, G. Correia, C. Costache, T. Day Goodacre, D. V. Fedorov, V. N. Fedosseev, G. Fernández-Martínez, A. Fijalkowska, M. Fila, D. Galaviz, R. Grzywacz, C. Henrich, A. Illana, Z. Janas, K. Johnston, V. Karanyonchev, M. Kicińska-Habior, R. Lică, H. Mach, M. Madurga, I. Marroquín, B. Marsh, C. Martínez, C. Mazzocchi, K. Miernik, C. Mihai, B. Olaizola, S. Paulaskalas, J.-M. Régis, S. Rothe, V. Sánchez-Tembleque, G. Simpson, Ch. Sotty, L. Stan, M. Stănoiu, M. Stryjczyk, A. Turturica, J. M. Udías, **V. Vedia**, A. Villa, and W. B. Walters. $\beta$-decay of $^{133}$In: $\gamma$ emission from neutron-unbound states in $^{133}$Sn. *Physical Review C, 2018.*

3. T. A. Berry, Zs. Podolyák, R. J. Carroll, R. Lică, H. Grawe, N. K. Timofeyuk, T. Alexander, A. N. Andreyev, S. Ansari, M. J. G. Borge, J. Creswell, L. M. Fraile, C. Fahlander, H. O. U. Fynbo, W. Gelletly, R.-B. Gerst, M. Gorska, A. Gredley, P. Greenlees, L. J. Harkness-Brennan, M. Huyse, S. M. Judge, D. S. Judson, J. Konki, J. Kurcewicz, I. Kuti, S. Lalkovski, I. Lazarus, M. Lund, M. Madurga, N. Mărginean, R. Mărginean, I. Marroquín, C. Mihai,R. E. Mihai, E. Nácher, S. Nae, A. Negret, C. Nita, S. Pascu, R. D. Page, Z. Patel, A. Perea, V. Pucknell, P. Rahkila, E. Rapisarda, P. H. Regan, F. Rotaru, C. M. Shand, E. C. Simpson, S. Stegemann, T. Stora, Ch. Sotty, O. Tengblad, A. Turturica, P. Van Duppen, **V. Vedia**, R. Wadsworth, P. M. Walker, N. Warr, F. Wearing, and H. De Witte. Investigation of the n=0 selection rule in Gamow-Teller transitions: the $\beta$-decay of $^{207}$Hg. *Physical Review Letters, 2018.*

## Conference proceedings and other publications

1. L.M Fraile, H. Mach, B.Olaizola, V. Paziy. E.Picado, J.J. Sánchez, J.M. Udías, J.J Vaquero and **V. Vedia**. Assessment of New Photosensors for Fast Timing Applications with Large Scintillator Detectors. *IEEE Conference Records ISSN 1082-3654, 72-74 (2011), Nuclear Science Symposium and Medical Imaging Conference (NSS/MIC).*

2. **V. Vedia**, L.M. Fraile, H. Mach, B.Olaizola, V. Paziy. E.Picado and J.M. Udías. Time resolution of a 1-inch cylindrical CeBr$^3$ crystal at $^{60}$Co energies. *AIP Conference proceedings 1541,195 (2013), International scientific meeting on Nuclear Physics, La Rábida.*

3. **V.Vedia**, H.Mach, L.M.Fraile, J.M.Udıas. Optimization of the Time Response of LaBr$_3$(Ce) crystals, and its Dependence on Ce Concentration. *ARIS 2014 (Advances in Radioactive*

*Isotope Science), Tokyo, Japn, 2014 Journal of the Physical Society of Japan, vol 6, 30 June 2015.*

4. L. M. Fraile, B. Olaizola, V. Paziy, J. M. Udías, **V. Vedia** *et. al.*. Technical Report for the Design, Construction and Commissioning of FATIMA, the FAst TIMing Array. *Technical Design Report, TDR, FAIR/NUSTAR/HISPEC-DESPEC/FATIMA. FAIR, Facility for Antiproton and Ion Research in Europe, http://www.fair-center.eu/*
5. M. Rudigier, S. Lalkovski, E.R. Gamba, A.M. Bruce, Zs. Podolyak, P.H. Regan, M. Carpenter, S. Zhu, A.D. Ayangeakaa, J.T. Anderson, T. Berry, S. Bottoni, I. Burrows, R. Carroll, P. Copp, D. Cullen, T. Daniel, L. Fraile, M. Carmona Gallardo, A. Grant, J.P. Greene, L.A. Guegi, D. Hartley, R. Ilieva, S. Ilieva, R.V.F. Janssens, F.G. Kondev, T. Kröll, G.J. Lane, T. Lauritsen, I. Lazarus, G. Lotay, G. Fernandez Martinez, V. Pucknell, M. Reed, J. Rohrer, J. Sethi, D. Seweryniak, C.M. Shand, J. Simpson, M. Smolen, E. Stefanova,**V. Vedia**, O. Yordanov. Fast timing measurement using a $LaBr_3$(Ce) scintillator detector array coupled with Gammasphere. *Zakopane Conference on Nuclear Physics, 2016 Institute of Nuclear Physics of the Polish Academy of Sciences*
6. V. Guadilla, A. Algora, J.L. Taín, J. Agramunt, J. Aystö, J. A. Briz, A. Cucoanes, T. Eronen, M. Estienne, M. Fallot, L. M. Fraile, E. Ganioglu, W. Gelletly, D. Gorelov, J. Hakala, A. Jokinen, D. Jordan, A. Kankainen, V. Kolhinen, J. Koponen, M. Lebois, T. Martinez, M. Monserrate, A. Montaner-Pizá, I. Moore, E. Nacher, S. Orrigo, H. Penttila, I. Pohjalainen, A. Porta, J. Reinikainen, M. Reponen, S. Rinta-Antila, B. Rubio, K. Rytkonen, T. Shiba, V. Sonnenschein, A. A. Sonzogni, E. Valencia, **V. Vedia** , A. Voss, J. N. Wilson, A. -A. Zakari-Issoufou. Study of the $\beta$-Decay of Fission Products with the DTAS detector. *Conference on Nuclear Physics, 2016 Institute of Nuclear Physics of the Polish Academy of Sciences.*
7. **V.Vedia**, M. Carmona-Gallardo, L. M. Fraile, H. Mach y J. M. Udías. Performance Evaluation of $LaBr_3$(Ce) crystal Geometries Designed for Fast Timing Applications. *2015 IEEE Nuclear Science Symposium and Medical Imaging Conference (NSS/MIC), San Diego, CA, 2015, pp. 1-2.*
8. V. Sánchez-Tembleque, L.M. Fraile, **V. Vedia**, M. Carmona, K. Kamada, Y. Shoji, A. Yoshikawa, J.M. Udías. Evaluation of new inorganic scintillator for high performance ToF PET application. *2015 IEEE Nuclear Science Symposium and Medical Imaging Conference (NSS/MIC), San Diego, CA, 2015, pp. 1-4.*
9. L.M. Fraile, J.M Udías, A. Martín Ortega, **V. Vedia**. Digital processing of scintillator signals for fast timing applications. *2015 IEEE Nuclear Science Symposium and Medical Imaging Conference (NSS/MIC), San Diego, CA, 2015, pp. 1-4.*
10. V. Sánchez-Tembleque, **V. Vedia**, M. Carmona-Gallardo, L. M. Fraile, S. Ritt, J.M. Udías. Digital strategies for time and energy measurement for ultra fast scintillators. *2016 IEEE Nuclear Science Symposium, Medical Imaging Conference and Room-Temperature Semiconductor Detector Workshop (NSS/MIC/RTSD), Strasbourg, 2016, pp. 1-2.*